

Real-Time Sound Synthesis of Aeroacoustic Sounds using Physically Derived Models

Rod Selfridge

Submitted in partial fulfilment of the requirements of the
Degree of Doctor of Philosophy

School of Electronic Engineering and Computer Science
Queen Mary University of London
United Kingdom

2018

Statement of Originality

I, Roderick Selfridge, confirm that the research included within this thesis is my own work or that where it has been carried out in collaboration with, or supported by others, that this is duly acknowledged below and my contribution indicated. Previously published material is also acknowledged below.

I attest that I have exercised reasonable care to ensure that the work is original, and does not to the best of my knowledge break any UK law, infringe any third party's copyright or other Intellectual Property Right, or contain any confidential material.

I accept that the College has the right to use plagiarism detection software to check the electronic version of the thesis.

I confirm that this thesis has not been previously submitted for the award of a degree by this or any other university.

The copyright of this thesis rests with the author and no quotation from it or information derived from it may be published without the prior written consent of the author.

Details of collaboration and publications: see Chapter 1, Section 1.5.

Signature: Rod Selfridge

Date: 31/08/18

Revised date: 25/05/19

Abstract

This thesis examines the use of a novel synthesis approach to reproduce aeroacoustic sound effects. This requires research into the field of fluid dynamics to understand the principles which lead to a number of fundamental aeroacoustic tones. Previous research has shown that these fundamental tones can be represented by compact sound sources.

Three compact sound source synthesis models are developed representing three different fundamental aeroacoustic tones, the Aeolian tone, the cavity tone and the edge tone. A number of semi-empirical equations, ones where simplifications, generalisations or observations are considered, are found which provide mathematical relationships between the defining fluid dynamic parameters. Often these equations have been developed prior to computers being able to solve the complex fluid dynamic equations. Frequently, these equations were developed to assist scientists and engineers reduce the aeroacoustic noise. In this instance, the equations are used to replicate the aeroacoustic sounds.

The methodology of developing a compact sound source synthesis model for each of the aeroacoustic tones is presented and how this relates to the chosen noise shaping synthesis technique. Objective evaluation shows the semi-physical synthesis models perform well when compares to previously published results.

Following the development of the compact sound source synthesis models, three sound effect models are developed. These provide examples of how the synthesis models can be used to provide procedural audio sound effects. These are swinging objects, like a sword or a club; a propeller; an Aeolian harp. Evaluation of these are carried out, with subjective evaluation indicating equal or better performance than an alternative synthesis method.

The uniqueness of the implementations presented from this research is that combines the low computational requirements of a signal-based model while the parameterisation draws from equations obtained from aeroacoustic research.

Acknowledgements

I would like to thank everyone within the Media and Arts Technology Doctoral College and within C4DM at Queen Mary University of London. Their patience and cooperation through all the unforeseen challenges and circumstances are greatly appreciated. I would particularly like to convey the upmost gratitude to Professor Josh Reiss. Without him voicing his belief in me, his guidance, flexibility, support and feedback, my progress through this PhD research would have been simply impossible.

My gratitude also goes to the other supervisors: Dr Andy Farnell and Dr Andrew McPherson. Andy's passion to teach and learn along with his kindness and humanity has been a great comfort, encouragement and support. The questioning and examining of my research by Andrew has made this research much stronger as a result. This work was supported by EPSRC EP/G03723X/1.

Acknowledgment and thanks goes to Dr Eldad Avital whose knowledge and expertise in aeroacoustics provided me with great technical support and guidance, ensuring I understood the fluid dynamics involved and applied the theory appropriately. The Audio Engineering Research Group members (past and present) have all assisted in my professional development giving feedback on research, presentations and academic articles, all providing a great boost.

Deepest thanks to my Mum who has provided constant love, support and guidance throughout all my choices. My deepest gratitude also to my Dad who provided constant love and support, sadly passing away before he could see me complete this goal. Thanks to my brothers, their families, Norman, my in-laws and Dharma who have all given me great encouragement while working towards completing the PhD. (Dharma's contribution - *uyhhgnho9i90*). Thanks to my wider friends who have always encouraged me and especially to those kind enough to volunteer as proof readers.

And finally to my wife, Louise. Thank you for your love, support and patience as I follow my goals. Throughout the time of this research you overcome far greater challenges, never complaining, constantly inspiring and encouraging me to achieve. UrOCK!x

Contents

| | | |
|----------|-----------------------------------------------------------------|-----------|
| 1 | Introduction | 15 |
| 1.1 | Motivation | 15 |
| 1.2 | Aims and Objectives | 16 |
| 1.3 | Research Questions | 17 |
| 1.4 | Thesis structure | 18 |
| 1.5 | Associated publications | 19 |
| 2 | Background | 21 |
| 2.1 | Introduction | 21 |
| 2.2 | Applications | 22 |
| 2.2.1 | Traditional Applications | 22 |
| 2.2.2 | Video Games | 22 |
| 2.2.3 | Procedural Audio | 22 |
| 2.3 | Realising Sound Effects | 23 |
| 2.3.1 | Sound Effect Libraries | 23 |
| 2.3.2 | Creating Sound Effects | 24 |
| 2.4 | Traditional and State of the Art Synthesis Techniques | 25 |
| 2.4.1 | Sample-Based Synthesis Techniques | 25 |
| 2.4.2 | Abstract Synthesis Techniques | 26 |
| 2.4.3 | Physical Model Synthesis Techniques | 28 |
| 2.4.4 | Physically Inspired Synthesis Techniques | 31 |
| 2.5 | Summary | 32 |
| 3 | Fundamental Aeroacoustic Tones | 33 |

| | | |
|----------|----------------------------------------------------------------|-----------|
| 3.1 | Introduction | 33 |
| 3.2 | Aeroacoustics | 35 |
| 3.3 | Compact Sound Sources | 37 |
| 3.4 | Examples of Fundamental Aeroacoustic Sound Sources | 40 |
| 3.5 | Summary | 41 |
| 4 | Aeroacoustic Compact Sound Sources | 43 |
| 4.1 | Introduction | 43 |
| 4.2 | Aeolian Tone | 45 |
| 4.2.1 | Introduction | 45 |
| 4.2.2 | State of the Art | 46 |
| 4.2.3 | Aeroacoustic Principles of the Aeolian Tone | 46 |
| 4.2.4 | Implementation of Aeolian Tone Compact Sound Source | 53 |
| 4.2.5 | Evaluation of Aeolian Tone Model | 62 |
| 4.2.6 | Concluding Comments on Aeolian Tone Model | 68 |
| 4.3 | Cavity Tone | 70 |
| 4.3.1 | Introduction | 71 |
| 4.3.2 | State of the Art | 71 |
| 4.3.3 | Principles of Cavity Tone | 72 |
| 4.3.4 | Implementation | 78 |
| 4.3.5 | Evaluation of Cavity Tone Model | 85 |
| 4.3.6 | Concluding Comments on Cavity Tone Model | 89 |
| 4.4 | Edge Tone Model | 92 |
| 4.4.1 | Introduction | 92 |
| 4.4.2 | State of the Art | 93 |
| 4.4.3 | Aeroacoustic Principles of the Edge Tone | 93 |
| 4.4.4 | Implementation of the Edge Tone Compact Sound Source | 99 |
| 4.4.5 | Evaluation of Edge Tone Model | 107 |
| 4.4.6 | Discussion | 112 |
| 4.4.7 | Concluding Comments on Edge Tone Model | 114 |
| 4.5 | Summary | 116 |

| | |
|------------------------------------------------------------------------|------------|
| 5 Aeroacoustic Sound Effects | 117 |
| 5.1 Introduction | 117 |
| 5.2 Swords and Swinging Objects | 118 |
| 5.2.1 Introduction | 118 |
| 5.2.2 State of the Art | 119 |
| 5.2.3 Method | 119 |
| 5.2.4 Implementation | 121 |
| 5.2.5 Swinging Model Evaluation | 124 |
| 5.2.6 Discussion on Swinging Object Synthesis Model | 133 |
| 5.2.7 Concluding Comments on Swinging Object Synthesis Model | 136 |
| 5.3 Propeller | 137 |
| 5.3.1 Introduction to Propeller Sounds | 137 |
| 5.3.2 State of the Art in Propeller Sounds | 137 |
| 5.3.3 Method | 138 |
| 5.3.4 Implementation | 141 |
| 5.3.5 Results | 146 |
| 5.3.6 Discussion on Propeller Sound Synthesis Model | 152 |
| 5.3.7 Concluding Comments on Propeller Sound Synthesis | 154 |
| 5.4 Aeolian Harp | 155 |
| 5.4.1 Introduction | 155 |
| 5.4.2 Background and Related Work | 156 |
| 5.4.3 Physical Principles of the Aeolian Harp | 157 |
| 5.4.4 Implementation | 161 |
| 5.4.5 Evaluation | 163 |
| 5.4.6 Concluding Comments on Aeolian Harp | 171 |
| 5.5 Summary | 173 |
| 6 Conclusion | 174 |
| 6.1 Future Developments | 177 |
| 6.1.1 Existing Sound Effect Models | 177 |
| 6.1.2 Potential Models | 179 |

| | | |
|-------|--------------------------|-----|
| 6.1.3 | Methodology Extension | 180 |
| 6.2 | Summary of contributions | 180 |

List of Figures

| | | |
|------|------------------------------------------------------------------------------------|----|
| 2.1 | Taxonomy of Synthesis Techniques | 25 |
| 3.1 | Diagram illustrating a typical flow gradient | 35 |
| 3.2 | Wind Tunnel at Queen Mary University, 1909 | 37 |
| 3.3 | Typical mesh structure used with CFD and CAA simulations | 38 |
| 3.4 | Sound radiation pattern from a compact sound sources | 39 |
| 4.1 | Diagram illustrating the flow of air around a cylinder | 47 |
| 4.2 | Diagram illustrating the coordinates system for Aeolian tone | 48 |
| 4.3 | Position of 8 compact sources and coordinates used in sword model | 49 |
| 4.4 | Ideal radiation patterns for perpendicular dipole sources | 49 |
| 4.5 | Strouhal number as a function of Reynolds number | 50 |
| 4.6 | Laminar and turbulent conditions | 52 |
| 4.7 | Relationship between the inverse Q values and Reynolds number for the Aeolian tone | 56 |
| 4.8 | Flow diagram of compact sound source for the Aeolian tone | 62 |
| 4.9 | Typical mesh for a 2D cylinder | 65 |
| 4.10 | Simulation of Aeolian tone showing vortex shedding | 66 |
| 4.11 | Fluent CFD and synthesis model time plots | 67 |
| 4.12 | Fluent CFD and synthesis model magnitude plots | 68 |
| 4.13 | Fluent CFD and synthesis model spectrograms | 69 |
| 4.14 | Sword with a grooved profile | 71 |
| 4.15 | Basic components of cavity used in tone generation | 73 |
| 4.16 | Diagram showing coordinates of a cavity | 73 |
| 4.17 | Diagram showing cavity in Wake mode | 73 |

| | | |
|------|---------------------------------------------------------------------------------|-----|
| 4.18 | Diagram showing open cavity | 74 |
| 4.19 | Diagram showing closed cavity | 74 |
| 4.20 | Diagram showing first resonant depth mode | 76 |
| 4.21 | Far field cavity tone spectrum gains | 83 |
| 4.22 | Relationship between Reynolds number and Q values for cavity tone | 84 |
| 4.23 | Flow diagram showing cavity tone synthesis process | 86 |
| 4.24 | Output from the cavity synthesis model | 89 |
| 4.25 | Directional output from cavity synthesis model | 90 |
| 4.26 | Diagram of an edge tone flow | 94 |
| 4.27 | Diagram of parabolic jet profile | 95 |
| 4.28 | Diagram of top hat jet profile | 96 |
| 4.29 | Example of ideal mode changes - varying airspeed | 97 |
| 4.30 | Example of ideal mode changes - varying nozzle exit-to-wedge distance | 98 |
| 4.31 | Example of multiple labels for a single point | 103 |
| 4.32 | Flow diagram showing edge tone synthesis process | 107 |
| 4.33 | Mode changes in edge tone when varying airspeed | 108 |
| 4.34 | Mode changes in edge tone when varying airspeed | 109 |
| 4.35 | Mode changes in edge tone - varying nozzle exit-to-wedge distance | 110 |
| 4.36 | Mode changes in edge tone - varying nozzle exit-to-wedge distance | 111 |
| 4.37 | Sound pressure level with increasing airspeed u | 112 |
| 5.1 | Computer generated character with a sword | 122 |
| 5.2 | Position of 8 compact sources and coordinates used in sword model | 123 |
| 5.3 | Box plots showing plausibility results for the broom handle | 128 |
| 5.4 | Box plots showing plausibility results for the baseball bat | 128 |
| 5.5 | Box plots showing plausibility results for the golf club | 128 |
| 5.6 | Box plots showing plausibility results for the wooden sword | 129 |
| 5.7 | Box plots showing plausibility results for the metal sword | 129 |
| 5.8 | Magnitude spectrum of physical model of grooved sword | 133 |
| 5.9 | Sources of aeroacoustic noise associated with propellers | 138 |

| | | |
|------|--------------------------------------------------------------------------------------------------------|-----|
| 5.10 | Local coordinates of spinning propeller | 139 |
| 5.11 | Thrust sound source radiation patterns | 139 |
| 5.12 | Torque sound source radiation patterns | 140 |
| 5.13 | Thrust and torque combined sound source radiation patterns | 140 |
| 5.14 | Vortex sound source radiation patterns | 141 |
| 5.15 | Time plots of recorded and synthesised propeller powered aeroplane sounds | 147 |
| 5.16 | Magnitude plots of recorded and synthesised propeller powered aeroplane sounds | 149 |
| 5.17 | Spectrograms of recorded and synthesised propeller powered aeroplane sounds | 150 |
| 5.18 | Mean plausibility rating for different propeller aircraft samples | 151 |
| 5.19 | Plausibility rating for different propeller aircraft samples | 151 |
| 5.20 | Pure Data GUI for propeller sound effect | 153 |
| 5.21 | Propeller powered plane within game engine | 154 |
| 5.22 | Aeolian harp at South Carolina | 156 |
| 5.23 | Ideal lock-in conditions and model output at 6th harmonic | 158 |
| 5.24 | Implementation of hysteresis curve showing maximum vibration amplitude in the lock-in region | 159 |
| 5.25 | Example frequency spectrum of Aeolian harp while in lock in | 160 |
| 5.26 | Pure Data GUI for Aeolian Harp sound effect | 164 |
| 5.27 | Time plots of an Aeolian harp | 166 |
| 5.28 | Spectrograms of an Aeolian harp | 167 |
| 5.29 | Magnitude Spectrums of an Aeolian harp | 168 |
| 5.30 | Time plots of an Aeolian harp | 169 |
| 5.31 | Spectrograms of an Aeolian harp | 170 |
| 5.32 | Magnitude Spectrums of an Aeolian harp | 171 |
| 5.33 | Mean perceptual rating of Aeolian harp sounds | 172 |
| 5.34 | Boxplot for Aeolian harp sounds | 173 |
| 1 | Basic coordinates for Aeolian tone intensity equation derivation | 196 |

List of Tables

| | | |
|------|--------------------------------------------------------------------------------------|-----|
| 2.1 | Number of sound effects in common libraries | 23 |
| 4.1 | Values for constants in Eq.(4.3) | 50 |
| 4.2 | Acoustic intensity values for Aeolian tone harmonics | 57 |
| 4.3 | Comparison of measured, simulated and synthesis results | 63 |
| 4.4 | Values of the ratio L/θ_0 for different L/d values | 79 |
| 4.5 | Q values with corresponding Reynolds numbers | 84 |
| 4.6 | Comparison of measured, computed, theoretical, and synthesis model results | 88 |
| 4.7 | Values for coefficients of edge tone frequency prediction Eqn 4.80 | 98 |
| 4.8 | Comparison of equations for predicting edge tone frequency | 100 |
| 4.9 | Coefficient values for edge tone frequency prediction Eqn. 4.87 | 101 |
| 4.10 | Example labels for red point given in Figure 4.31 | 103 |
| 4.11 | Confusion matrix of the decision tree select current mode | 104 |
| 4.12 | Mode selection for different Reynolds values | 104 |
| 5.1 | Table highlighting different synthesis methods for swing sounds | 120 |
| 5.2 | Diameter and radius for pre-set swinging objects | 125 |
| 5.3 | Shapiro-wilk test results for swinging objects | 130 |
| 5.4 | Measure of difference for the metal sword samples | 130 |
| 5.5 | Measure of difference for the broom pole samples | 131 |
| 5.6 | Measure of difference for the baseball bat samples | 131 |
| 5.7 | Measure of difference for the golf club samples | 131 |
| 5.8 | Measure of difference for the wooden sword samples | 132 |
| 5.9 | Swinging objects identified from Wii Controller | 132 |

| | | |
|------|------------------------------------------------------------------------------|-----|
| 5.10 | Swinging objects identified from Wii Controller | 133 |
| 5.11 | Aircraft models and relevant data | 142 |
| 5.12 | Approximate values for atmospheric absorption | 144 |
| 5.13 | Shapiro-wilk test results for propeller powered plane sound effect | 152 |
| 5.14 | Measure of difference for the propeller powered plane sound effect | 152 |

*“It doesn’t matter how beautiful your theory is,
it doesn’t matter how smart you are. If it
doesn’t agree with experiment, it’s wrong”*

Richard P. Feynman

Chapter 1

Introduction

1.1 Motivation

Sound effects, dialogue and music are the three core elements of sound design in the vast majority of audio / visual media. Sound effects are often used to add realism, comedy, tension or general dramatic emphasis depending on context. Today numerous libraries of pre-recorded sound effects, called samples, are available for a sound designer to adapt and mix into the overall audio scene.

The use of pre-recorded sampled sound effects is popular in films and television where the listener is limited to hearing the sound effect only once as the story unfolds. This is defined as linear media. Games, on the other hand, often require skill and learning until a certain level of mastery is achieved before the game progresses. Unlike linear media, games are non-linear media may require a similar sound effect but in a new and unique context [96]. Under these circumstances, a continually repeating the exact same sound effect seems unnatural and detracts from the playing experience instead of enhancing it.

It is not practical to have a sampled sound effect for each unique circumstance in games due to the high memory this would require. One method for varying pre-recorded samples would be to layer a number of similar effects through intelligent mixing, delays, filtering etc., a limited number of variations can be achieved.

An alternative to using pre-recorded samples is to use a sound effect that is synthesised. A synthesised sound effect has the advantage of having the ability to be adapted through audio effects or other parameters to give the unique sound required. The disadvantages of synthesised sound effects are that they often do not capture the same perceptual quality of a recorded sample and for certain synthesis techniques, are not easily adaptable with evolving conditions.

The motivation for this research was to design and implement synthesis sound effect models based on equations obtained from the physics behind the processes that generate the sounds. It was also an intention to implement the synthesis models so that they operate and adapt in real-time, enabling them to work smoothly within non-linear media like games or virtual reality.

Since a real-time synthesised sound effect can be generated when required it is possible to manipulate the sound produced to react in concert with an evolving environment. This is a highly desirable attribute when deciding on which sound effect to use as it offers an inherent flexibility and the opportunity for a more realistic experience.

The approach described in this thesis is to design sound effects based on equations found in fluid dynamics, the study of fluid flow and its interactions with boundaries. The focus of the thesis is on sounds generated in air, either from its interaction with complex flows or with boundaries and objects. This field is known as Aeroacoustics.

By researching this field, we are able to identify key equations enabling the design and implementation of sound effects which obey sound physics principles with the advantage of being able to operate within fast changing non-linear media. The methodology used throughout can be applied to other fields within physics to produce a wide library of flexible and robust sound effects.

1.2 Aims and Objectives

The aim of this thesis is to identify equations and parameters from fluid dynamics that enable the design and implementation of aeroacoustic sound effects. The models should be able to operate in real-time while parameter changes do not break the physical rules imposed. The models should produce good outcomes when evaluated objectively, comparing acoustic properties to previously published theoretical, experimental and simulated results. Similarly, when compared perceptually to other synthesis methods and pre-recorded samples a plausible sound effect is desired.

To achieve this a number of different sound synthesis techniques are examined, identifying key properties. Research into the fundamental principles of a number of aeroacoustic tones has been undertaken to identify key parameters and relationships. Real-time synthesis models of the fundamental tones are developed based on fluid dynamic equations or those defined through examination of properties by the author. The models are evaluated against previously published results based on experimentation, theory and simulation. Examples are given to show how the synthesis models of the fundamental aeroacoustic tones can be used to produce practical sound effects for use as procedural sound effects in video games or for film and television.

1.3 Research Questions

What equations derived from fluid dynamics predict aeroacoustic sounds?

Fluid dynamics is a well-established field of research. The mathematical prediction of flows, pressures and resulting sounds generated is complex. Research was undertaken to identify equations that are either derived from simplifications made to the fundamental equations or based on proven experimental results.

The prediction of aeroacoustic noise is important in the design and construction of a number of items. Prior to computers being able to perform computations on large equations engineers and scientists required simpler equations to predict these sounds and inform their designs.

Can these be used in a real-time sound synthesis model?

To enable the models to operate in real-time without specialist hardware, equations that avoid complex computations are sought. The required synthesis properties vary depending on the technique preferred, which in turn specifies which equations are of value.

What additional properties are not available from equation and how can these be predicted?

Often the fluid dynamic principles are not fully understood or studies into the properties required for the synthesis models are not available. Different techniques are available to predict unknown parameter values to be used for the synthesis model while remaining true to aeroacoustic principles.

How accurate are the synthesis models compared to previously published results?

Numerous studies into aeroacoustic tones have been carried out. These include experimental, theoretical and computational simulation. Comparing the synthesis models to these studies give an indication on how accurate they are.

Can example sound effects be produced, what range of objects can these model and how perceptually plausible are these?

It is important to demonstrate how the synthesis models can be used to design real-time sound effects. Meaningful parameters allow users to interact fully with the models as well as allowing ease of integration with a game engine to give a fully procedural sound effect. Comparing the sound effects to alternative synthesis models and actual recordings shows where the designed sound effects perform well and where they perform poorly.

Where do the sound synthesis models not capture all the physical qualities of real sounds?

Since synthesis models are based on simplified equations it is accepted that full fluid dynamic characteristics cannot be captured. Objective and subjective evaluation against real recordings can identify where the synthesis models fail to replicate the physical processes found in the natural sounds. Any shortcomings provide a foundation for future research.

1.4 Thesis structure

Chapter 2 provides a definition of sound effects and how these are used within media. An explanation is given as to the difference between sampled sounds and synthesised ones. Different synthesis techniques are described, giving examples of state of the art applications.

Chapter 3 introduces the field of aeroacoustics, why it is important and how the sounds generated can be calculated computationally. The concept of compact sound sources is introduced as well as a number of the fundamental aeroacoustic tones that have been observed.

Chapter 4 describes how three of the major fundamental aeroacoustic tones can be modelled as compact sound sources. The aeroacoustic processes and conditions required for each tone to materialise are described.

A synthesis model for each of the tones are developed and established from equations and characteristics obtained from aeroacoustic research. Objective evaluation of each of the synthesis models is carried out, comparing the models' output on previously published experimental and computational results.

Original Contributions:

The thesis' primary original contribution is the first synthesis models of compact sound sources, using noise shaping techniques based on aeroacoustic research and operating in real-time. The sound sources modelled are the Aeolian tone, cavity tone and the edge tone.

Chapter 5 illustrates how the synthesis models of the compact sound sources can be used to create sound effect models. The physical behaviour of objects has been examined as well as how the compact sound sources can be used in conjunction with other physical sound generating processes to construct more complex models.

Original Contributions:

A novel real-time synthesis model of a sword and other swinging items, including a golf club and baseball bat was developed allowing users to adjust highly relevant parameters to create the sound effect desired. Perceptual evaluation illustrates that these models are almost as plausible as swinging the real objects.

Additional sound sources are added to the synthesis models of the compact sound source to produce the first real-time synthesis model of a propeller powered aeroplane. Evaluation results indicate that the synthesis model performs well but some characteristics are not captured. The model offers a high degree of parameter control allowing the modelling of any propeller powered aircraft and full control of the flightpath in relation to an observer.

The use of the compact sound sources and mechanical vibrations are examined in the novel implementation of a real-time synthesis model of an Aeolian harp. This model examines the interactions between two different sound generating phenomenon to produce the unique sounds.

Chapter 6 discusses the approach taken to produce the sound synthesis models, offers future directions and concluding comments.

1.5 Associated publications

Portions of the work detailed in this thesis have been presented in national and international scholarly publications, as follows (journal publications highlighted in bold):

1. R Selfridge, JD Reiss, EJ Avital and X Tang. Physically Derived Synthesis Model of a Aeolian Tone, 141st Audio Engineering Society Convention, LA, USA, Sept 29 - Oct 2, 2016 [130].

Winner of Best Paper Award.

Chapter 4: Section 4.2 on an Aeolian tone synthesis model.

R Selfridge role: Research, develop, implement, and evaluate the synthesis model. X Tang role: Assisted in CFD comparisons.

2. R Selfridge, D Moffat, JD Reiss. Real-Time Physical Model For Synthesis of Sword Swing Sounds. Proceedings of the 14th Sound and Music Computing Conference, Espoo, Finland, July 5 - 8, 2017 [131].

Winner of Best Paper Award.

Chapter 5: Section 5.2 on a swinging objects synthesis model.

R Selfridge role: Research, develop, implement, and evaluate the synthesis model. D Moffat role: Evaluation of the synthesis model.

3. R Selfridge, D Moffat, JD Reiss, and EJ Avital. Real-Time Physical Model of an Aeolian Harp. 24th International Congress on Sound and Vibration, London, UK, July 23 - 27, 2017 [134].

Chapter 5: Section 5.4 on an Aeolian harp synthesis model.

R Selfridge role: Research, develop, implement, and evaluate the synthesis model. D Moffat role: Evaluation of the synthesis model.

4. R Selfridge, D Moffat, and JD Reiss. Physically Derived Sound Synthesis Model of a Propeller. In Proceedings of Audio Mostly, London, United Kingdom, August 23 - 26, 2017 [132].

Winner of silver prize, Audio Engineering Society Design Competition, 141st Audio Engineering Society Convention.

Chapter 5: Section 5.3 on a propeller synthesis model.

R Selfridge role: Research, develop, implement, and evaluate the synthesis model. D Moffat role: Evaluation of the synthesis model.

5. R Selfridge, JD Reiss, and EJ Avital. Physically Derived Synthesis Model of a Cavity Tone, 20th International Conference on Digital Audio Effects (DAFx-17), Edinburgh, UK, September 5 - 9, 2017 [135].

Chapter 4: Section 4.3 on a cavity tone synthesis model

R Selfridge role: Research, develop, implement, and evaluate the synthesis model.

6. R Selfridge, JD Reiss, and EJ Avital. Physically Derived Synthesis Model of a Edge Tone. 144th Audio Engineering Society Convention, Milan, Italy, May 23 - 26, 2018 [136].

Chapter 4: Section 4.4 on a edge tone synthesis model.

R Selfridge role: Research, develop, implement, and evaluate the synthesis model.

7. R Selfridge, D Moffat, and JD Reiss. Sound synthesis of objects swinging through air using physical models. **Applied Science - Special Edition on Sound and Music Computing 2017**, Vol. 7, Issue 11, p1177 [133].

Chapter 5: Section 5.2 on a swinging objects synthesis model.

R Selfridge role: Research, develop, implement, and evaluate the synthesis model. D Moffat role: Evaluation of the synthesis model.

8. R Selfridge, D Moffat, EJ Avital and JD Reiss. Creating Real-Time Aeroacoustic Sound Effects Using Physically Informed Models. **Journal of the Audio Engineering Society**, Vol. 66, no. 7/8, pp. 1-14, (2018 July/August.).

Chapter 4: Section 4.2 on an Aeolian tone synthesis model.

R Selfridge role: Research, develop, implement, and evaluate the synthesis models. D Moffat role: Evaluation of the synthesis models.

Chapter 2

Background

This chapter describes sound effects, why we use them, different methods of creating them and current state of the art in synthesising them.

2.1 Introduction

Audio in typical media like films, video games, television, radio, etc., can be broadly divided into three categories. These are:

- Dialogue / voice
- Music
- Sound effects

The majority of the research carried out in this thesis focuses on sound effects, although techniques and principles describe can often cross over categories and cover a range of audio applications. These are highlighted when applicable.

Sound effects cover a large range of sounds and can be as sonically diverse as an audience clapping to a policeman's whistle. They are added to media for a variety of reasons. The sounds can be magnified for artistic emphasis or to highlight tension. A common use of this is a ticking clock when the protagonist is running out of time. A sound effect can draw and focus the audience's attention to something before an event, for example, the footsteps of approaching foe in a video game.

Other uses for sound effects can include signalling contrasting emotions, changing intended perception, for example turning a dramatic scene into one of comedy. Evoking memory and emotions can be achieved by the right sound effect. Sound designers require a great deal of skill to add sound effects which will maintain a bond between the audience / participant and the content. The current trends is towards greater immersion as virtual reality and augmented reality reinforce the importance of plausible sound effects.

2.2 Applications

2.2.1 Traditional Applications

In traditional media, film and television, sound effects are added in post-production by a sound designer. Normally these sounds are difficult to capture during filming or they may not be the desired sounds and effects are dubbed into the audio mix as required.

The art of producing original sound effects is known as Foley. Basic examples of Foley are using coconut shells to mimic the sound of a horse's hoof, snapping carrots to mimic breaking bones, etc. These are performed by a Foley Artist.

2.2.2 Video Games

Early video games used basic synthesis effects to indicate a score or event. Due to memory limitations this had to be generated in real-time. The software on early games platforms had access to simple wave oscillators and envelopes to generate all sound. This included the music, composition of which became an art form in itself, pushing the boundaries of what could be created.

The synthesised sound effects in early games were generally repetitive and synthetic but more options became possible when memory to store pre-recorded samples became available. Pre-recorded samples are still static, equivalent to a photograph, these are the same each time played. The use of intelligent mixing and audio processing could enable variations.

2.2.3 Procedural Audio

State of the art in sound design looks towards a concept called Procedural Audio, which may be described as a “non-linear, often synthetic sound, created in real time according to a set of programmatic rules and live input” [48] - Andy Farnell, Computer Scientist and Author. It has

also been described as “real-time sound creation using synthesis techniques such as physical modelling with deep links into game system” - Paul Weir, Sound Designer¹

An important aspect of procedural audio is not only to synthesis a plausible sound but to model the behaviour, including forces, directions, and geometry and basing behaviours on states and variables within the game engine. Due to the range of states and variables within media like games, an equivalent range of different sounds produced from a single procedural audio sound effect each time it is triggered is desirable.

2.3 Realising Sound Effects

2.3.1 Sound Effect Libraries

A sound effect library is a collection of sounds that users can search to find the desired effect for their purposes. Traditional libraries are pre-recorded sounds delivered via a hard drive or similar. Online libraries are now available, including synthesised sounds, the quality of which can range from professional to low quality. As such, the price of sound effects libraries can vary from free up to thousands of pounds. Often the provenance of a sound effect is unknown making an academic evaluation of it challenging.

Typical categories for a sound effects library can include Animals, Cloth, Collision, Environment, Footsteps / Applause, Miscellaneous, Sci-Fi, Sports, Textures, Tools, Vehicles / Engines, Water and Weapons. The number of sound effects available within a library varies extensively and a number of examples are shown in Table 2.1.

Table 2.1: Number of sound effects in common libraries

| Library | Number of samples | Memory Required |
|-----------|--------------------------|-------------------------------|
| BBC | 29420 | 38Gb |
| Adobe | 10000+ | 8.2Gb |
| SoundSnap | 250000 (including loops) | Not available (online source) |
| Sony | 1200 | 5Gb |
| Freesound | 230000+ | Not available (online source) |
| Zapsplat | 19500 | Not available (online source) |

¹https://www.youtube.com/watch?v=FY_JaEFmIwI&t=1289s

2.3.2 Creating Sound Effects

As indicated in previous sections, the two options to obtain a sound effect is to record an example of the sound, including a Foley representation, or to synthesise the sound to generate a new sound that represents the sonic qualities desired.

Recorded

Recorded sound effects are generally obtained by field recordings using specialist microphones. This could require travel to specific locations and waiting for specific events, hence why pre-recorded high-quality libraries can be greatly sought after. Foley sound effects require a skilled practitioner to perform and capture the sound to obtain a sample.

The advantages of recorded samples are that the exact sounds can be captured with the highest possible quality. Once a sample is captured it is always available, i.e. it does not require any processing or calculation to be realised; the audio is complete and can be used at any time.

The disadvantages of pre-recorded sound samples are that they are static sonic moments which cannot evolve or adapt to changing conditions. This can have a consequence of ear fatigue where an individual can get over exposed to a sound, diminishing its impact.

There is obviously a disadvantage if the desired sound is not available in a sound effect library and requires to be recorded. For example, an Icelandic sound designer wanting to record a specific lion roar will have to consider cost of travel, time spent obtaining the sample as well having to be lucky enough to find a lion that will roar in the desired manner at the correct time. Under these conditions a synthesis model able to replicate the sound effect has a great advantage.

Synthesised Sound Effects

A synthesised sound effect is one generated artificially which aims at either creating an accurate replication of a sound, creating hyper-real versions of sounds or creating brand new ones. The reasons for synthesising a sound might be that the pre-recorded sound is not available in any library, as in the lion example. It may be that a user requires control over the sonic content which would be more achievable with a parameterised synthesise model compared to a sample. If procedural audio is desired, then a synthesis model with such adaptive parameters would be of great benefit.

The main disadvantages of synthesised sound effects can be the perceptual quality which, depending on synthesis technique, can vary from almost indistinguishable from a recorded sample

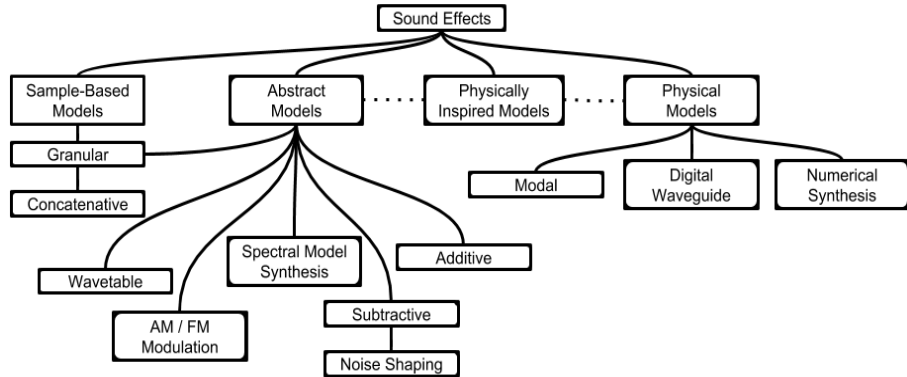


Figure 2.1: Taxonomy of Synthesis Techniques

to an extremely poor representation. Some techniques also require offline calculations to be processed before a sound is available to be heard. This would be entirely unsuitable if the sound effect occurred even a few hundred milliseconds after the event triggering.

2.4 Traditional and State of the Art Synthesis Techniques

There are a number of techniques available to synthesise a sound effect. This section gives a review of the most common, but it is appreciated that the list here is not exclusive. Some techniques are more successful at certain groups of sounds. The techniques described are also not exclusive to sound effects and some have been employed to synthesise vocals and musical instruments. A taxonomy of the techniques described is given in Fig. 2.1. As seen in Fig. 2.1, there are four broad approaches to implementing a synthesis model; sample-based, abstract, physical models and physically inspired models but we can see that techniques can fall under more than one approach.

2.4.1 Sample-Based Synthesis Techniques

These synthesis techniques are ones where pre-recorded samples are manipulated to produce the desired sound. Granular and concatenative synthesis techniques are the main sample-based techniques. Sample-based synthesis methods, like signal-based ones, are generally not computationally complex. Since the models are based on a corpus of samples each grain or clip is fixed but due to the small size and number of samples they can be successfully manipulated to synthesise a number of sounds.

Granular Synthesis

Granular synthesis is based on taking a number of short sound clips, typically milliseconds in length, and adding them together to make a longer sound effect. Choice of grains can be made on to obtain the correct spectral content over time. Grains can also be generated from wavelets which also can be defined as signal-based.

A granular synthesis of drilling sounds was presented in [99] where a signal was analysed, the time and envelope of drill impacts estimated with some impacts extracted. The final output was generated from stored impact noises with random rules based on the analysis of drilling sounds.

Concatenative Synthesis

Granular and concatenative synthesis are similar in approach. The sound clips used in concatenative synthesis are much longer and this technique is often used for voice synthesis where a sound clip can be a formant, plosive or other part of speech. In [6] a low-quality synthesis process based in noise shaping (section 2.4.2), was devised to obtain a fast synthesis process. This was driven by animation and the output mapped to high quality samples with similar sonic qualities which were then concatenated to produce a real-time high-quality sound effect.

2.4.2 Abstract Synthesis Techniques

There are a wide variety of abstract synthesis techniques and only a few of the fundamental ones are covered in this overview. Abstract-based techniques often make use of filters, noise signals, oscillators and similar tools that are commonly used in signal processing. They do not relate to the physics behind the sounds, rather aim to either replicate the signal of a desired sound or implement new ones.

The main advantage of abstract synthesis methods is that they are generally computationally lighter than their physical model counterparts. Complexity can vary from a few oscillators in a simple additive model up to many harmonics in a frequency modulation (FM) model. When abstract models become more complex the ability to parameterise the models becomes increasingly challenging to relate to the effects being modelled. Abstract models can also sound very synthetic compared to recorded samples which can affect their plausibility when applied in certain media.

Additive and Subtractive Synthesis

Additive and subtractive synthesis techniques are two of the most common and easy to understand abstract approaches. In additive synthesis a number of oscillators representing a sinusoidal tone are added together to generate the desired frequency content, harmonics etc. to form a Fourier series. Although simple to understand and implement, additive models can become extremely complex to control once the number of oscillators is increased. The ability to change the sound properties is not always intuitive and parameterisation can be non-trivial.

A flute sound was synthesised in [158] where signal-based analysis / synthesis techniques were used to capture perceptual effects along with physical modelling techniques. A modified additive synthesis method for a trumpet was presented in [84] that used a source filter model to add in-harmonic partials to achieve a more natural sound.

Instead of adding frequency components by means of an oscillator, subtractive synthesis starts with a rich frequency spectrum and reduces the frequency components until the required frequencies are left. Often the initial source for this is a noise source and by use of filtering the frequency content of the sound can be adjusted, known as noise shaping. Again, this technique is simple to understand but, like additive, can become complex if there is a number of filters to control and parameterisation can be non-trivial.

A number of environmental sound textures were presented in [153] using this technique, including the sound of winds which are similar to our model. Sound effects from engines to winds were presented in [49] in which noise shaping was the fundamental technique. The whistling wind sounds presented in [49] again similar to our model.

Spectral Modelling Synthesis

Spectral Modelling Synthesis or (SMS) is a technique where the desired target pre-recorded sound sample is analysed prior to the synthesis process. The analysis is separated into two components, a deterministic and a stochastic. The deterministic component is more tonal in content and modelled by oscillators at the desired frequencies. The stochastic component is more noise-like and the spectrum envelope is generated by noise shaping. SMS works well the more deterministic the sound being analysed. It is limited in reproducing the sound it is given to analyse and difficult to parameterise and adapt the model once developed.

The sound of vehicle pass-by noise was synthesised in [54] where engine noise and tyre noise characteristics were modelled. SMS techniques are used as a comparison synthesis technique to the sound effects developed in this thesis.

Modulation Techniques

Amplitude and frequency modulation techniques can increase the number of frequency partials at a relatively low computational cost [34]. FM synthesis involves creating a signal based on the frequency modulation equation [34]:

$$FM = A \sin(2\pi f_c t + I \sin 2\pi f_m t)$$

where A is the gain of the signal, f_c the carrier signal frequency, I the modulation index and f_m the modulating signal frequency. Increasing I increases the bandwidth of the FM signal with the amplitude of the carrier and sidebands can be determined by Bessel functions of the first kind. These have been extensively used for synthesis of musical instruments as well as in [154] where a synthesis model of animal vocal chords has been developed.

Wavetable

Another abstract approach is to use a wavetable, where a time waveform of the desired sound to be synthesised is obtained. A single period of the waveform can be stored in a buffer then read at a variable rate. This produces a high-quality sound in some instances as it is essentially a pre-recorded sound being played by looping through one period. This technique could also be described as sample-based when using pre-recorded sounds.

When the read rate is altered then there is scope for possible discrepancies and the quality depends on the size of the buffer and methods of interpolation for the varying read speed. An example of wavetable synthesis was given in [53] which reduced interpolation errors using sample integration techniques.

2.4.3 Physical Model Synthesis Techniques

Physical models are ones where the algorithms used to generate the synthesised sounds are based on the physics of the sound generating processes. Developing these algorithms requires an understanding of the different components that generate and shape the sounds produced. The first physical model was given in [82] for the voice. For musical instrument synthesis this could be the dimensions of a vibrating structure, the excitation method, coupling between vibrating structures or terminating boundaries.

One of the main advantages of physical modelling is that the parameters exposed to the user routinely relate directly to the actual objects that are being synthesised. Parameters like length,

density, tension, force, speed and thickness are all examples of typical parameters exposed to the user. This often makes the control of a physical model more intuitive than say an FM synthesis model where changing parameters to obtain a desired sound may be more complex.

One of the main disadvantages associated with physical models is the requirement for a high number of computations to calculate the output sounds. This obstacle is naturally reducing as computational power is constantly increasing.

Modal Synthesis

A technique known as modal synthesis is similar to additive synthesis in that a number of partials are added together to obtain the desired sound. The difference is that the partials are the resonant vibrations and the interactions between structures are simulated [2]. The vibration frequencies can be available in closed form or can be calculated through techniques such as Finite Element Method (FEM). Modal synthesis for musical instruments was described in [102] which can be extending to contact forces [163, 87] and bubble/water sound effects [88].

Digital Waveguides

A common and successful technique for physical modelling is by the use of digital waveguides. A digital waveguide is usually a digital representation of a string or a tube as illustrated by [138] for reed-bore and bow-string instruments. The main principle is that the standing wave of a resonant vibration can be modelled as a pair of travelling waves moving in opposite direction. The length of the string or tube is modelled by two separate delay lines and an excitation signal is added to the system.

The delay lines are connected by filters which represent losses at either end of the string or tube. This has been extended to include fractional delay lines, body modelling, estimation of parameters and methods of control for a number of plucked stringed instruments in [149].

Modelling by this means has been developed to include filters to replicate the loss generated by the bridge of a stringed instrument or shape of the bell on a wind instrument. Different excitation signals have been used to increase the accuracy of the models.

A flute sound was synthesised in [158] where a digital waveguide was used to capture the most relevant physical characteristics while signal-based analysis / synthesis techniques was used to capture perceptual effects. To capture the unusually wide vibrato effect of a Korean geomungo [83] used a time-varying loss filter.

A digital waveguide has been used to replicate an animals vocal tract in [154]. This was successfully implemented to replicate sound effects of a lion's roar and wolf's growl.

Direct Numerical Synthesis

An alternative method of physical modelling is to discretise a space and time representation of the physical object, most often used for musical instruments. This was initially described in [69] and [70] and illustrated for a piano string in [29]. Direct numerical synthesis for musical instrument synthesis has been expanded and developed in [16] for strings and [61, 62, 63] for flue instruments. These techniques do not depend on specific assumptions and appropriate for non-linear problems. As well as musical instruments, the finite-difference time-domain has been shown to be a suitable method for modelling room acoustics [15].

The geometry of the instrument and space being modelled is mapped out in a mesh structure and equations solved for each point or volume on the mesh. The resolution of the mesh and the size of the discrete time step determines the number of calculations required but these often extremely large values and can require offline processing. The numerical solutions obtained by Giordano in [61, 62, 63] were computationally complex; the author states that with their current computing resources one second of sound would take several months of calculation [63]. It should be noted that Giordano's research was into the acoustics of the musical instruments rather than to create a playable synthesis model.

Often specialised hardware has been employed which are more optimal for the computations required than standard computer processors, for example Field Programmable Gate Arrays (FPGAs) or Graphical Processing Units (GPUs). GPUs were used in [17] for three-dimensional simulation of a timpani. Real-time synthesis from two-dimensional simulations of a trumpet, clarinet and flute using a GPU were presented in [4], extending to experimental instrument designs. This was extended to speech synthesis in [160]. Similarly FPGAs have also been used for acoustic modelling [103] and modelling musical instruments [110].

Lumped Models

A physical representation of a physical object can be given by lumped models. In these models the different components that make up a system can be modelled separately; numerically, experimentally or analytically. It was introduced in [24] in the CORDIS synthesis system. Here components were modelled as discrete mass-spring networks where masses were connected by springs and damping components, the behaviour of which can be defined by Newton's laws and the dynamics by differential equations.

Aeroacoustic Models

Physical modelling of aeroacoustic musical instruments is an active area of research and relevant to work presented in Section 4.4. The voice, as modelled in [82] is an aeroacoustic system as are woodwind, brass and flue instruments. In [138] presents a synthesis method for reed instruments while [25] examines the modelling of brass instruments focusing on the coupling with synthesised human lips.

Flue instruments like the recorder and pipe organ have also been the focus of attention with the work of Coltman [35] and Fletcher [51]. Significant progress was made on the modelling of flue instruments by Verge [151] and [152]. Here he identified a number of mechanisms that combined to produce and influence the oscillations in the resonator and how these in turn interacted with the excitation of the jet system. He identified how sounds were influenced by blowing pressure, shape and position of the labium.

In [152] a physical model was developed including models for the jet oscillation, resonator, vortex shedding at the labium and the noise generated by turbulence. The physical model gave excellent results when compared to the experimental findings published in [151].

A study into the aeroacoustics of panpipes is given in [7] and [8], indicating the difference between these musical instruments compared to instruments like the flute. The use of a physical model of the closely related Ouldémé flute was introduced in [39] but to the best of the author's knowledge the research presented in [7] and [8] have yet to be implemented into a similar physical model of the panpipes.

2.4.4 Physically Inspired Synthesis Techniques

As shown in Fig. 2.1, physically inspired models lie in-between signal-based models and physical models. The models have some understanding of physical processes and behaviours but to a lesser extent than full physical models. An advantage of some of the approximations of the laws of physics often made are that the models often require considerably less calculations. This makes them easier to implement in real-time which is often a goal, especially if procedural audio sound effects are desired.

The synthesis techniques used in physically inspired models are often the same as those used in signal-based methods but with appreciation of behaviour and physics. Parameterisation varies greatly between models as does the relevance of the parameters to the physical processes occurring to generate the sounds.

A wide range of physically inspired sound effects were presented in [49]. The models presented

used signal-based synthesis techniques with a focus on the behaviour of models and creating models that complied with the definitions of procedural audio.

The example of a motor given in [49] was built on in [68] where the range of sounds available from a single model was examined. It was found that a motor from a hand drill to a small boat, including motors of intermediate sizes, could be successfully synthesised from one synthesis model.

Procedural audio models of environmental sound effects were presented in [153]. Wind, rain and fire sound effects were generated from a number of different sound atoms. Physically informed model of jackhammer sounds was presented in [109] where parallel digital waveguide models were driven by pulses at pre-defined time intervals.

2.5 Summary

The concept of sound effects has been introduced, explaining what classes of sounds constitute effects for the purposes of this thesis. It can be seen that sound effects are classified into a number of groups of different sounds based on genre as well as split into sounds that are actual recordings and those that are synthesised.

Synthesised sounds can be further split into sample-based models, signal-based models, physical models and physically inspired models. Common techniques for each synthesis approach are described, giving examples of each. It can be seen that some techniques are better suited to some types of sounds compared to others.

With the number of techniques described and the different types of sound effects required, the next section introduces the concept of aeroacoustics and what sound effects these cover.

Chapter 3

Fundamental Aeroacoustic Tones

3.1 Introduction

Aeroacoustics is a sub-field within the broader area of fluid dynamics which in turn is a sub-field of engineering. In fluid dynamics the flows, energy, forces, and pressure of fluids are studied in order to understand the stresses and strains that might be placed on structures. The failure to appreciate these flows can lead to structural failure, an example being the Tacoma Narrows Bridge in the USA which collapsed in 1940 due to the stresses placed on it by the wind.

The fundamental equations governing fluid dynamics are known as the Navier / Stokes equations [106, 139]. These allow us to predict the pressures and forces generated by the movement of fluids. The equations are the conservation of mass and conservation of momentum and stated in Appendix 6.2.

When the fluid involved is air and an acoustic response is obtained the sound is known as aeroacoustic. The swooshing sound when a sword sweeps through the air is a classic example of an aeroacoustic sound effect and one we modelled, (section 5.2). The study of aeroacoustics became increasingly important in the first half of the 20th century when vehicles started to move at vastly increased speeds. If a loud aeroacoustic sound was generated by a fast-moving vehicle it could have a great influence over passenger comfort.

The top speed of trains in Japan had to be limited due to the aeroacoustic sound generated by the pantograph connecting the train to the electric cables above, [56]. More importantly, if the acoustic pressure pulses were of sufficient strength causing vibration, the structural integrity can fail.

The birth of air travel, both military and commercial has driven a number of aeroacoustic studies. A number of sound sources due to a spinning propeller is examined in section 5.3. There is noise associated with the trailing edge of an aircraft wing or aerofoil. This is due to the combining of moving air at two different speeds at the trailing edge of the aerofoil. Turbulence and shockwaves from a jet engine have also been studied in an attempt to minimise these.

Aeroacoustic tones are also generated when weapon bays are opened, or the wheels extended for take-off and landing. For other vehicles, the pantographs on trains can produce aeroacoustic noise. Similarly, radio antenna, wing mirrors and sun roofs can all produce aeroacoustic sounds in cars.

There are a number of musical instruments in which air is a key component of the sound producing mechanism. In woodwind instruments the air from a player blowing into a mouthpiece forces a one or two wooden reeds to vibrate which in turn generates a standing wave in a tube whose frequency depends on the tube length and if open or closed at the opposite end. Brass instruments are similar except it is the players lips that vibrate rather than a reed.

Unlike reed instruments and brass instruments, flue instruments rely on an aeroacoustic vibration to excite a standing wave in the tube. The recorder, flute, piccolo and pipe organ are all examples where air striking a fixed edge is used to generate tones. Other aeroacoustic instruments includes whistles and panpipes. The bullroarer is an aboriginal device used for communication but operates using aeroacoustic sounds generated when a piece of wood attached to a rope or string, is swung around the head at high speeds. Another instrument in which air is the driving component is the Aeolian harp, which is studied in more depth in section 5.4.

Swords and swinging weapons all can generate an aeroacoustic sound when used. A number of items of sports equipment can make similar sounds. These are also studied in section 5.2.

Other aeroacoustic sounds can be generated from a wide number of interactions like a ricocheting bullet, boiling kettle and bicycle spokes. The wind can generate aeroacoustic sounds when blowing around telegraph wires, past door wells, through gaps in a window or even when blowing through trees. One of the most striking examples of this is found in the *Acacia Drepanolobium* tree in Australia.

A key element of the flow of air with respect to aeroacoustics is something called a Shear Layer. Shear layers are areas of the flow where there is velocity variation in directions perpendicular to the normal. An example of this is illustrated in Fig. 3.1.

Shear layers can be generated by flow coming into contact with a boundary or plate. One of the fundamental principles of fluid mechanics is the non-slip condition which states that the molecules in contact with the boundary have zero velocity. If the flow in a tube is moving at any velocity there must be a thin boundary near the tube walls where the velocity decreases to zero.

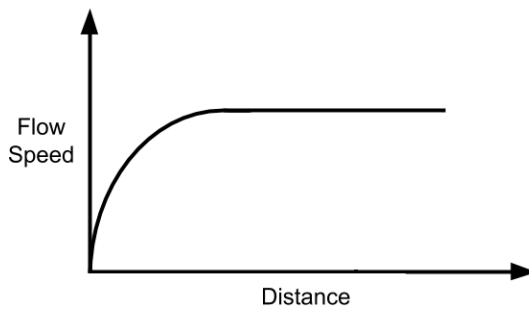


Figure 3.1: Diagram illustrating a typical flow gradient at distances away from a boundary

A shear layer is also formed when two flows at different velocities come into contact, as in the trailing edge of an aerofoil. Similarly, two flows of different temperature also have a shear layer between them when they come into contact.

3.2 Aeroacoustics

The desire to have sound synthesis models operating in real-time has been a barrier to implementing sound effect models based on the physics. The equations are often complex, intimidating and require specialist hardware to enable the number of calculations to occur at audio rate. There are also a number of different aeroacoustic processes that can generate sound; the sound generated from a human whistle is very different than that generated by a helicopter rotor. This thesis does not cover all of the aeroacoustic sound generating processes but looks at a number of significant ones, providing a framework for the research and design of real-time aeroacoustic sound effects based on the physical processes involved.

Physical modelling of aeroacoustic sounds has mostly been focused on replicating musical instruments or designing new ones. There is an obvious market for accurate synthesis models of these to allow composers, musicians and sound designers the ability to play musical instruments either through a midi controller or similar. As stated in section 2, there has been very little research carried out in relation to the design of physical models in relation to sound effects and the implementation and perception of these.

Some previous work has been carried out to synthesise aeroacoustic sounds based on signal-based synthesis models. Usually, signal-based models do not require complex calculations and hence a lower computational requirement. This generally means that real-time operation on non-specialist hardware is achievable.

Signal-based models of aeroacoustic sounds are regularly implemented as a noise shaping model. These models are relatively simple to implement and can give perceptually pleasing results. As

in most signal-based synthesis models, parameters are set based on the perceptual evaluation of the designer rather than on fluid dynamic principles. This can lead to situations where adjusting parameters produces unrealistic results.

In 1952, Lighthill defined the Navier / Stokes momentum equation in a form of the wave equation [89, 90], (Appendix A). This defines aeroacoustic sound sources and stress tensors as a function of small scale pressure perturbations and the airspeed. This is known as Lighthill's Acoustic Analogy.

Following on from Lighthill's acoustic analogy, a number of significant developments have been made by researchers but it is appreciated that there are still a significant questions within aeroacoustic not yet answered. One of the most important advances was to incorporate the effect of boundary conditions in order to be able to predict the sound sources caused by these. This was achieved through the use of Green's functions (Appendix B).

Often results observed from wind tunnel experiments could not be easily defined by theory. Prior to computers, engineers required a means of predicting the sound sources and how best to influence them. This requirement meant that a number of equations known as semi-empirical were defined. Semi-empirical equations are ones where assumptions and generalisations have been made to simplify calculations or in accordance with results obtained through experiments. In practice this often meant that predicting aeroacoustic sounds was based on equations which have been defined from a mixture of theory and experimental observations.

Experimental observations are more often than not conducted in wind tunnels. A classic picture of the wind tunnel at Queen Mary University of London in 1909 is shown in Fig 3.2. Wind tunnels allow engineers to test or examine circumstances within an environment which is controlled to the best of their ability.

Wind tunnels usually operate over a range of airspeeds with different tunnels for subsonic and supersonic measurements. For aeroacoustics, there is the added problem of being able to measure the sounds generated. This requires the user to minimise the reflections from the tunnel walls and sounds generated by the measurement instruments. Often the sound absorbing material for the walls is only valid over a limited frequency range. A consequence of these issues mean that great care has to be taken in planning a wind tunnel experiment to measure aeroacoustic sounds, if not, the possibility of erroneous sensor readings is high.

With the advent of modern computing new software packages became available to engineers, enabling similar experiments to those traditionally carried out in a wind tunnel. The development of this area of research is known as Computational Fluid Dynamics (CFD). CFD when applied to aeroacoustics is known as Computational Aeroacoustics, (CAA).

To run a CFD simulation the domain of interest has to be mapped by a mesh of discrete points

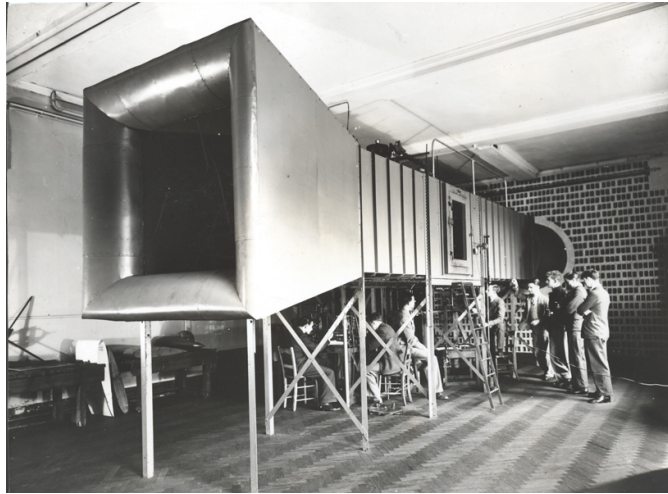


Figure 3.2: Picture of Queen Mary University of London’s wind tunnel in 1909.

enveloping the object being studied. A typical mesh for an aerofoil is shown in Fig. 3.3. Numerical methods are then employed to calculate the flow properties at each of the mesh points. Techniques involve finite difference method, finite volume method and finite element method. See [14] for a description of these methods in relation to musical instruments.

Discrete finite methods give an approximation of the fundamental equations. Differences in conditions are measured spatially within the mesh as well as over time. The spatial approximation can vary in level of detail, going from 1st order to 2nd order and so on. Smaller time steps will give more detail over time.

A further consideration when using a discrete mesh to solve a fluid dynamics problem is the boundary conditions imposed at the edges of the mesh. If careful management of these conditions are not carried out large errors in results can occur. Computational simulations often take an extremely long time to calculate results due to the complexity of the calculations required. Varying the time steps, mesh size and order of detail can all effect the computation time.

3.3 Compact Sound Sources

A compact sound source is a hypothetical concept of different small sound producing objects which are used to model actual sounds generated. A number of different compact sound sources are used to describe different sound propagations. In this work we concentrated on the main three - monopoles, dipoles and quadrupoles.

This study focuses on listening to the aeroacoustic sounds in the far field. The far field is described

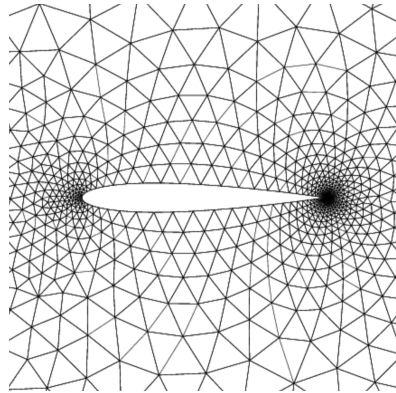


Figure 3.3: Typical mesh structure used with CFD and CAA simulations

as the region away from the sound source where $kr \gg 1$, where k is the wave number defined as ω/c and r is the distance between source and listener [71]. In this region the waves can be treated as plane in the area local to the listener.

The directivity of the sound sources are important as when modelling the behaviour of the object being modelled this adds realism, along with Doppler and panning, as a source moves in relation to the observer (or vice-versa). This can be seen in Section 5.3, where the combination of sources produces a maximum at an azimuth of approximately 120 degrees from a spinning propeller.

A monopole is the most basic compact sound source. Under ideal conditions, it can be described as a pulsating sphere, much smaller than the acoustic wavelength. A monopole radiates omnidirectional spherical sound pulses away from its centre. A diagram of the sound pattern from an ideal monopole is shown in Fig. 3.4a.

A dipole is the equivalent of two monopoles separated by a small distance. Each side of the dipole is in opposite phase to the other. The dipole can be thought of as a sphere pulsing from side to side and is again much smaller than the acoustic wavelength. A diagram of the sound pattern from an ideal dipole is shown in Fig. 3.4b.

A quadrupole is the equivalent to two dipoles or four monopoles and has two configurations. A longitudinal quadrupole is equivalent to two dipoles in opposite phase in which their axes are aligned. A lateral quadrupole can be considered as four monopoles at the corners of a rectangle. The sound pattern from a longitudinal quadrupole is shown in Fig. 3.4c and from a lateral quadrupole in Fig. 3.4d.

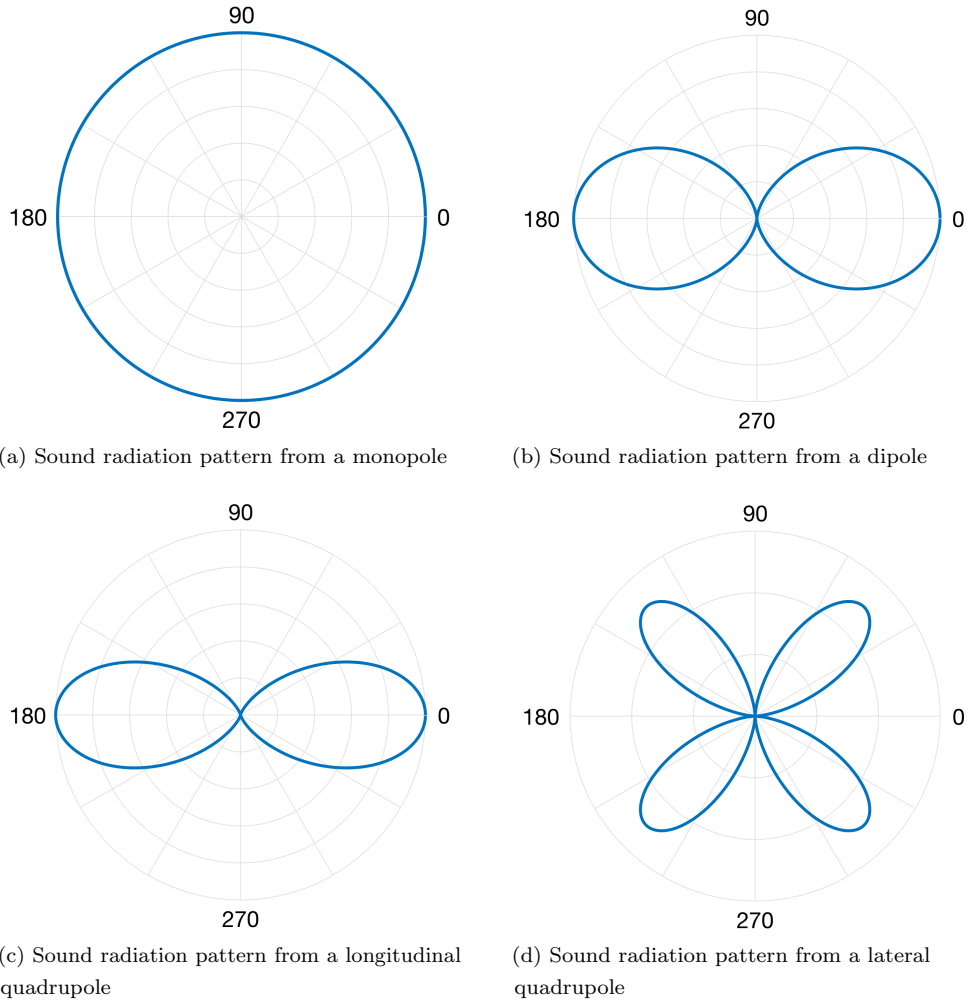


Figure 3.4: Sound radiation pattern from a compact sound sources

It was shown by [38] and confirmed in [59] that aeroacoustic sounds, in low flow speed situations, could be modelled by the summation of compact sound sources, namely monopoles, dipoles and quadrupoles. It should be noted that the monopole is considered the most efficient of the sources, followed by the dipole and then the quadrupole [30]. The far field sound power Π of a monopole is given as [125]:

$$\Pi = \frac{Q^2 \rho c k^2}{8\pi} \Rightarrow \Pi \sim \omega^2 \quad (3.1)$$

where Q is the complex source strength, representing the volume of fluid displaced by the source, ρ the fluid density, c is the speed of sound. The wave number k is given by $k = 2\pi/\lambda$, where λ is

the source wavelength, given by $\lambda = c/f$ where f is the frequency. The far field sound power Π of a dipole is given as [125]:

$$\Pi = \frac{Q^2 \rho c k^4 d^2}{6\pi} \Rightarrow \Pi \sim \omega^4 \quad (3.2)$$

Since the dipole power varies with ω^4 it is less efficient than a monopole with identical source strength Q at radiating low frequency sounds [125]. Similarly, for the sound power radiated by both the quadrupole sound sources $\Pi \sim \omega^6$, making it less efficient still, (for the same source strength) [125].

3.4 Examples of Fundamental Aeroacoustic Sound Sources

There are a number of conditions that produce aeroacoustic sounds which can be modelled by compact sound sources. Details of the major ones are given here.

Aeolian Tone

The Aeolian tone is the sound generated as air passes around an object. The majority of research into this sound has been based on flow around a cylinder due to this being a common shape in structures but other shapes have also been researched. As the air passes the object vortices are shed causing a tone to be produced. The dipole is the dominant sound source for the Aeolian tone. This is explained in more detail in Section 4.2.

Cavity tone

This is the sound generated as air flows over an open cavity. Examples of these being weapons bays of aircraft or wheel wells when landing gear is extended. This causes something called a hydrodynamic feedback loop which is common when discrete aeroacoustic tones are heard. The dipole is the dominant source in shallow cavities and the monopole in deeper ones. This is explained in more detail in Section 4.3.

Edge Tone

This is the sound generated when a planar jet strikes an edge or wedge. This is similar to the driving mechanism in flue instruments as described in Section 3.2. The dipole is the dominant

sound source for this aeroacoustic tone. Vortices are shed and a hydrodynamic feedback loop are present which is explained in more detail in Section 4.4.

Hole Tone

This tone is very similar to the edge tone. A circular jet of air strikes a plate with a circular hole of similar dimensions to the jet. Pressure pulses generated at the hole interact with the jet causing a hydrodynamic feedback loop. The monopole is the dominant source for this tone.

Pipe Tone

This sound is generated from a cylindrical cavity which has a small circular, squared edge hole at one end and is open at the other. Air can flow in from the hole side or sucked from the open cavity side, but no sound is generated if air flows in the opposite direction. In this manner it is known as acoustic diode. The monopole is the dominant source for this tone.

Screech Tone

This tone is generated due to instability in a supersonic jet flow. Interaction between shock pulses and instabilities create a hydrodynamic feedback loop which can produce very high intensity screech tones. The monopole is the dominant source for this tone. If the nozzle is square, then a dipole source is dominant.

Turbulence

Turbulence itself, due to the interaction of shear layers caused by its motion can generate sound. This is more broadband in nature rather than a discrete tone and the lateral quadrupole source dominates.

3.5 Summary

In this section the fundamental concept of aeroacoustics has been introduced, explaining why it is important to understand for engineers and scientists designing items, objects or structures that interact with air. This includes a basic description of the shear layer which has a strong influence on any sounds produced.

An outline of classic wind tunnel experiments are explained as well as the modern CFD techniques. The idea of compact sound sources is developed, indicating the acoustic propagation pattern of the three main sources. A number of fundamental aeroacoustic tones are outlined, including indicating the major compact sound source associated with each. The sound synthesis of compact sound sources are now described for three different aeroacoustic tones.

Chapter 4

Aeroacoustic Compact Sound Sources

4.1 Introduction

In Chapter 3 the concept of compact sound sources was introduced along with the idea that they can be used to represent fundamental aeroacoustic tones. This chapter focuses on how to apply semi-empirical equations to implement compact sound source models for three different aeroacoustic tones; the Aeolian tone, the cavity tone and the edge tone.

On planning how to implement each compact sound source, a number of considerations were common to them. Firstly, it was important that all design decisions, where available, were informed by equations or experimental results obtained from fluid dynamics research.

Previous research and implementation of aeroacoustic sounds has used a number of different synthesis techniques. Examples in [19] included granular and noise shaping techniques for a sword; [49] used noise shaping for wind; and [43] used sound textures from compact sound sources obtained from offline CFD calculations for a sword.

One of the main focus of this research was to avoid complex computations that require offline processing. The method chosen to implement all of the compact sound sources was noise shaping, (Section 2.4.2). It is shown in the following sections, that a common requirement for all synthesis models was to determine:

- the fundamental tone frequency

- the acoustic intensity
- which compact sound source was dominant
- the bandwidth around the tone
- if any harmonic content

Since this work was focused on physical models, operating in real-time, which could be controlled by a game engine and animations within a virtual world, parameterisation of the sound synthesis models was also an important consideration. In nature, the parameters that determine the aeroacoustic sounds generated are airspeed, shape of the object, trajectory, distance and angles from the listener, therefore these are what were used in the models developed in this research. The limitations of each models were also considered.

The choice of implementation software was based on a number of factors. These were computational efficiency, repeatability, open source licence, current state of the art in sound effect design and ease for others to understand. With these considerations the graphical programming language Pure Data was used to implement the compact sound sources.

4.2 Aeolian Tone

Nomenclature

c = speed of sound ($m s^{-1}$)

d = diameter (m)

f = frequency (Hz)

u = air flow speed ($m s^{-1}$)

R_e = Reynolds number (dimensionless)

S_t = Strouhal number (dimensionless)

r = distance between listener and sound source (m)

θ° = elevation angle between listener and sound source

φ° = azimuth angle between listener and sound source

ρ_{air} = mass density of air ($kg m^{-3}$)

μ_{air} = dynamic viscosity of air ($Pa s$)

M = Mach number (dimensionless)

l = correlation length of cylinder (diameters)

b = length of cylinder (m)

I = acoustic intensity (W/m^2)

Q = peak frequency / bandwidth at -3dB (dimensionless)

χ = scaling factor

Γ = wake scaling factor

B = empirical constant

4.2.1 Introduction

When air flows around an object and an aeroacoustic tone generated it is known as the Aeolian tone. The object most frequently studied is a cylinder due to its uniform structure and common use in design. This sound generated by air flowing around a cylinder was the focus of this research.

When a golf club is in mid swing or when a sword is swooshing through the air the Aeolian tone can be generated. It is also one of the major sound sources for a spinning propeller. When an aircraft has its landing gear extended Aeolian tones can be generated as air flows around the rods and poles. The spiral which used to be placed around car antenna was to prevent this sound from causing a nuisance while the car was travelling. The Aeolian tone can also be heard from telegraph wires in a strong wind or even certain types of trees and plants.

4.2.2 State of the Art

A number of studies have focused on creating sound effect models which have the Aeolian tone as the underlying fundamental sound although few attempts to replicate the compact sound source. [91] is one of many studies into the Aeolian tone which used CCA techniques to solve Euler Equations (simplified Navier / Stokes). In [43] offline CFD calculations were used to obtain the acoustic output from each compact source in the model. Sound textures were generated from the CFD outputs which were then summed to give the overall sound output.

[43] is the only aeroacoustic sound effect to the best of the author's knowledge to generate sound by modelling the compact sound sources. This differs from those presented here as these calculations were performed offline to create sound textures summed for playback. If the speed of air flow was increased the playback speed was increased. This changes the pitch of the tone but loses accuracy for other parameters.

Models described in this thesis allow for real-time acoustic output from the compact sound sources but is based on equations obtained through study into the Aeolian tone. It is believed that this is a unique approach to modelling sound effects.

4.2.3 Aeroacoustic Principles of the Aeolian Tone

As stated in Chapter 3, understanding shear layers is important to understanding how aeroacoustic tones are often generated. One condition where a shear layer exists is when air is in contact with a boundary and this occurs as air flows around a cylinder. The change in velocity of air from point of contact with the boundary to the free flow causes the air to spiral in the form of an eddy.

These spirals get bigger as the air continues round the cylinder and eventually disconnect from the cylinder and continue to flow downstream. This is known as vortex shedding and a trail of vortices is known as a Karmen vortex street [161]. An illustration of this can be seen in Fig 4.1.

To assist in modelling an Aeolian tone compact sound source, a coordinate system was used. This is shown in Fig. 4.2, where 0° azimuth and elevation are directly in front of the source. Distance r , length of the cylinder b and cylinder diameter d are given in metres, and airflow in metres per second.

With respects to sound effect synthesis the input parameter, seen in Fig. 4.2 could be the airspeed u , given as a scalar value. This could be the speed of wind through a fence or is equivalent to the speed of an object through stationary air, for example the speed of a sword swinging. The Aeolian tone compact sound source is 3 dimensional with the acoustic intensity requiring the azimuth and elevation angles between source and listener [64].

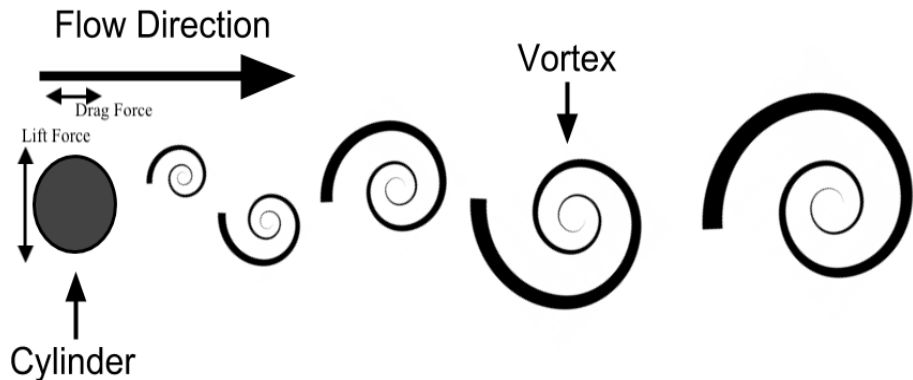


Figure 4.1: Diagram illustrating the flow of air around a cylinder

In Section 5.2 an aeolian compact sound source is applied to synthesis the sound of a swinging object. A model for this is shown in Fig. 4.3 where we can see the representation of the cylinder as a discrete number of compact sound sources.

As each vortex is shed from the back of the cylinder there is a pressure change at the side, depending on which side the vortex was formed. The pressure changes as vortices are shed generates oscillating lift and drag forces. The lift force is perpendicular to the flow and has a frequency given by each time a pair of vortices is shed from opposite sides of the cylinder.

The drag force is normal to the flow and has a frequency defined by the time between each vortex shed. The drag frequency is therefore twice that of the lift. A diagram illustrating the oscillating lift and drag forces is given in Fig. 4.4. It can be seen from this that the lift force is dominant and noted that the oscillating lift and drag forces can each be modelled by dipole compact sound sources.

The first major study into Aeolian tones was carried out by the Czech physicist, Vincenc Strouhal in 1878. In his experiments he spun an arm which had a cylindrical wire at the end. He was able to measure the tone frequency for a known airspeed and cylinder diameter. Strouhal defined the equation:

$$S_t = \frac{f_l d}{u} \quad (4.1)$$

where S_t is a dimensionless value called the Strouhal number and u is the speed of air flowing around the object (or speed of the object through air), f_l is the fundamental frequency associated with a lift force and d is the diameter of the cylinder. This equation defines the tone frequency as a dimensionless number based on the airspeed u and characteristic dimension, on this occasion the diameter d . It is not based on the Navier - Stokes equations or simplifications.

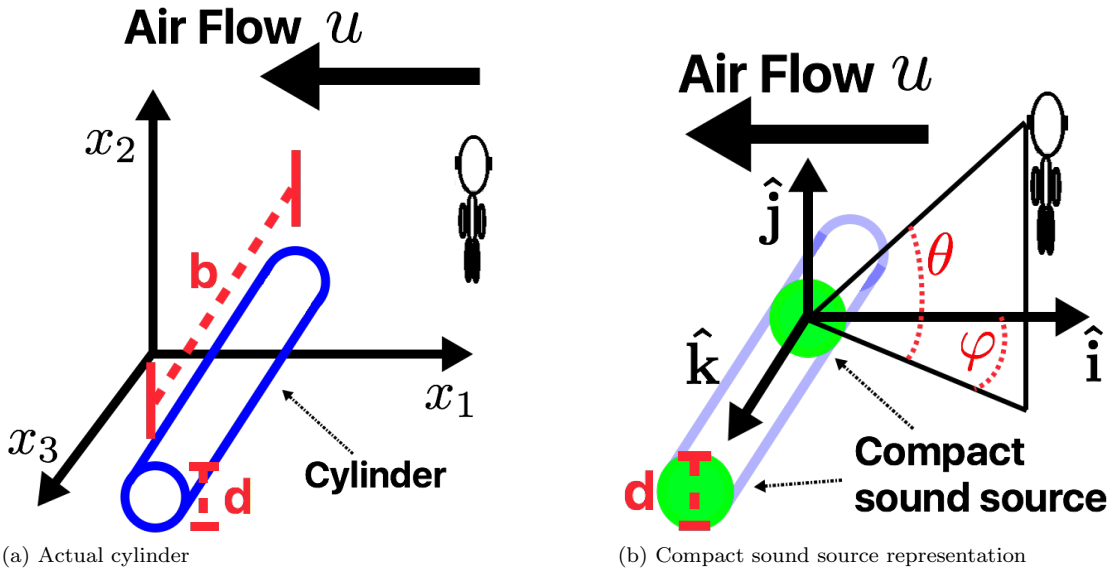


Figure 4.2: Diagram illustrating the coordinates system used thoughtout our model

When concluding his findings, Strouhal believed the Strouhal number had a constant value of 0.2 for the Aeolian tone. This is close to being correct, but it has subsequently been established that the Strouhal number has a weak dependence on another dimensionless value known as the Reynolds number.

The Reynolds number R_e is a dimensionless measure of the ratio between the inertia and viscous force in a flow. It is defined by the following equation:

$$R_e = \frac{\rho_{air} L u}{\mu_{air}} \quad (4.2)$$

where ρ is the mass density of air, approximately $1.225 \text{ kg} / \text{m}^3$ at sea level and 15° . μ is the dynamic viscosity of air, approximately $1.81 \times 10^{-5} \text{ kg/(ms)}$ at 15° . L is a characteristic dimension of the object being examined. For the Aeolian tone this is the cylinder diameter d .

The value of the Reynolds number allows us to deduce how turbulent the flow around the cylinder will be. The higher the Reynolds number the higher the turbulence with smaller and more diffuse vortices.

It can be seen from Eqn. 4.1 that if we know the Strouhal number, airspeed and diameter of the cylinder, we can determine the frequency of dipole associated with the lift. The airspeed and diameter are parameters of our sound synthesis model and are set by the user. Therefore, all that is left to find is the correct value for the Strouhal number. Using a value of 0.2 would produce a

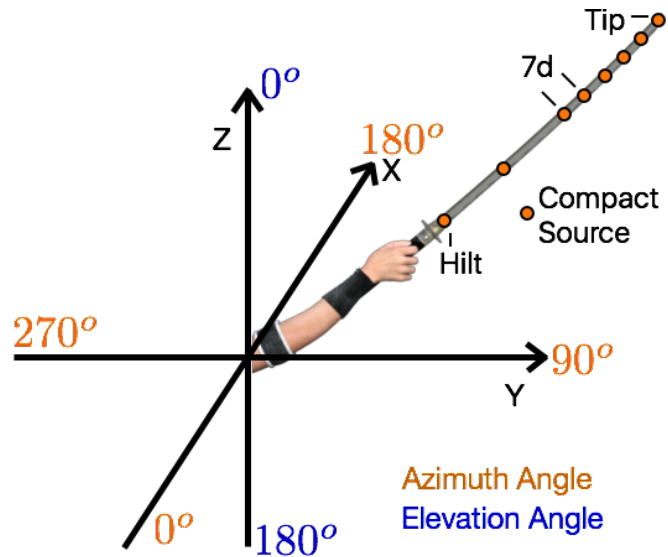


Figure 4.3: Position of 8 compact sources and coordinates used in sword model

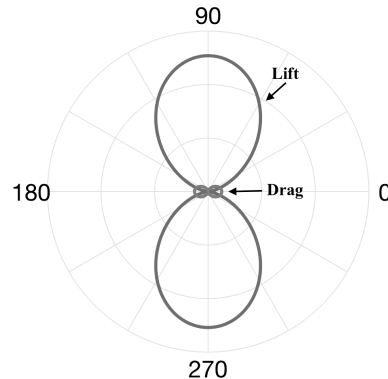


Figure 4.4: Ideal radiation patterns for perpendicular dipole sources

reasonably accurate model but it was decided that in order to be as accurate as possible a more exact value for the Strouhal number would be obtained.

An experimental study in [50] defined a piecewise relationship between the Strouhal number and the Reynolds number. Wind tunnel experiments on cylinders of length to diameter ratios varying from 50 to 400, was carried out. Reynolds numbers were varied from 47 up to 2×10^5 . Eqn. 4.3 gives a piecewise estimate of the Strouhal number:

$$S_t = \lambda + \frac{\tau}{\sqrt{R_e}} \quad (4.3)$$

Table 4.1: Values for constants in Eq.(4.3), reproduced from [50]. † Linear interpolation between published values. ‡ interpolated from [56].

| R_e range | λ | τ |
|----------------------------------|-----------|-----------|
| [47,180) | 0.2684 | -1.0356 |
| [180, 230) | 0.2437 | -0.8607 |
| [230, 240) | 0.4291 | -3.6735 |
| [240, 360) | 0.2492 † | -0.8861 † |
| [360, 1300) | 0.2257 | -0.4402 |
| [1300, 5000) | 0.2040 | +0.3364 |
| [5000, 2×10^5) | 0.1776 | +2.2023 |
| $[2 \times 10^5, 1 \times 10^6]$ | 0.5760‡ | -175.956‡ |

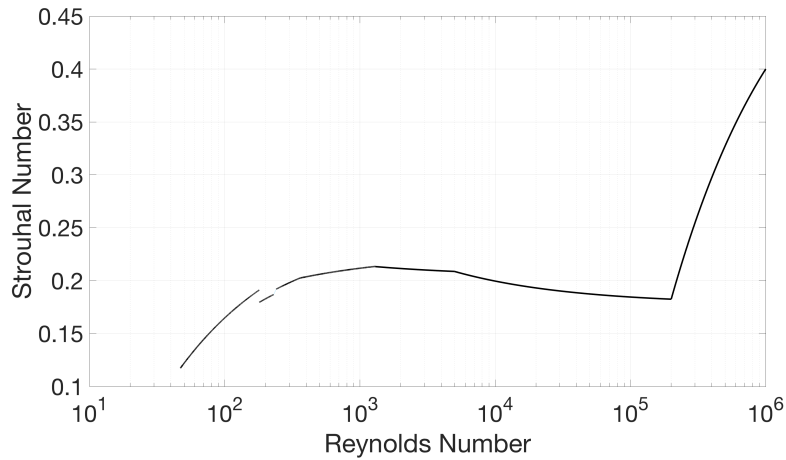


Figure 4.5: Piecewise approximation of Strouhal number as a function of the Reynolds number. Calculated by constants provided in [50]

where the values of λ and τ are obtained from Table 4.1. It should be noted that two of the results were interpolated from published results in order to give a more complete range, [50] and [56]. These values are plotted in Fig. 4.5 and shows the Strouhal number increasing to 0.4 at high Reynolds numbers.

Now the Strouhal number has been obtained, Eqn. 4.1 is defined for the frequency of the oscillating lift force as in Eqn 4.4.

$$f_l = \frac{S_t u}{d} \quad (4.4)$$

Values for Strouhal number, airspeed and diameter are then applied to obtain the fundamental lift frequency. The drag force acts normal to the air flow and oscillates each time a single vortex is shed. Therefore the frequency of the drag oscillation is twice that of the lift frequency [33]. This can be calculated by adapting Eqn. 4.4 as given in Eqn. 4.5.

$$f_d = \frac{2S_t u}{d} \quad (4.5)$$

The acoustic intensity of the Aeolian tone was defined in [64]. Goldstein's derivation for acoustic intensity starts from the equation given by Lighthill's acoustic analogy. Using Ffowcs Williams-Hawkins' equation (Appendix C) to provide a solution incorporating boundary conditions and Green's functions to give a complex summation of partial derivatives, Goldstein was able to define an equation for acoustic intensity.

Goldstein [64] assumes the cylinder is rigidly supported and defines the acoustic intensity as (see Appendix D):

$$\overline{I_l(t)} \sim \frac{\sqrt{2\pi}\kappa^2 S_t^2 l b \rho u^6 \sin^2 \theta \cos^2 \varphi}{32c^3 r^2 (1 - M \cos \theta)^4} \left\{ \exp \left[-\frac{1}{2} \left(\frac{2\pi M S_t l}{d} \right)^2 \sin^2 \theta \sin^2 \varphi \right] \right\} \quad (4.6)$$

where κ is a numerical constant which lies between 0.5 and 2. Goldstein states that the variation in κ is due to sensitivity to turbulence in the oncoming airflow. The variable b is the cylinder length, u the airspeed around the cylinder, θ the elevation angle, φ the azimuth angle, c the speed of sound and r the scalar distance between compact sound source and observer. The value M is known as the Mach number and is the ratio of flow speed to the speed of sound given by

$$M = u/c \quad (4.7)$$

The value l in Eqn. 4.6 is called the correlation length. This is a dimensionless parameter and describes the span-wise length that the vortex shedding is perfectly correlated but is random with respects to points outside [47]. This means that the vortices are being shed in phase. The value of l represents the distance between areas of the cylinder where the shedding is in phase or correlated. It is stated in units of diameters.

In [64] the acoustic intensity is derived from the perturbations of the fluid density based on a period of the vortex shedding. The relationship between pressure and acoustic intensity is given by [64] as:

$$I = \frac{P^2}{\rho_{air} c} \quad (4.8)$$

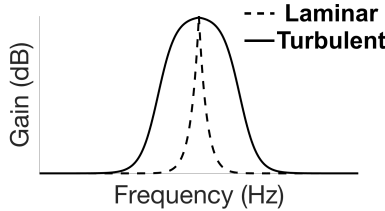


Figure 4.6: Illustration of Aeolian tone fundamental under laminar and turbulent conditions

The value of the fluid density perturbations is integrated over the fluctuation period of the vortex shedding. The period of the lift frequency is given by Eqn. 4.9:

$$T = \frac{2\pi}{f_l} \quad (4.9)$$

An assumption is made that the distance and angle between the source and the listener is constant. The time averaging period T_p is given by [64]:

$$T_p = \frac{2\pi}{f_l}(1 - M \cos \theta) \quad (4.10)$$

where the Doppler Factor $(1 - M \cos \theta)$ incorporates the variation due to airspeed and elevation angle between source and observer.

Due to the nature of vortices, the acoustic sound produced are rarely a pure sine tone. The peak frequency are centred around the calculated lift frequency but varies based on diffuse nature of the fluid as it travels downstream. The bandwidth of an Aeolian tone is closest to a pure tone when the airflow is laminar (small Reynolds number). The more turbulent the flow the more diffused the vortices become, and the tone shifts towards a wider band of frequencies, centred around the fundamental. This is illustrated in Fig. 4.6.

An experimental study was carried out by [107] in which the bandwidth around the fundamental lift frequency was measured for a range of Reynolds numbers. The Reynolds numbers, with respect to the diameter, ranged from 0 to 237000, with the bandwidth measured.

Harmonics to the fundamental lift dipole are described in [59] and [56]. These were at frequencies of 3 times the fundamental lift frequency and 5 times the fundamental lift frequency. The normalised gains for these harmonics are given in [66]. When carrying out CFD simulations on the Aeolian tone, the author also witnessed a harmonic of the fundamental drag tone at twice the drag frequency.

It is believed that the amplitude of the harmonics and fundamental tones has a dependency on

the turbulence intensity of the incoming free stream of air. Case studies of different turbulence intensities were presented in [107] but the difference appeared minimal.

As well as the dipole sources attributed to the oscillating lift and drag forces, there are quadrupoles associated with the diffuse wake in turbulent flows. These can produce wideband noise modelled by lateral quadrupole compact sound sources. The acoustic intensity of wake quadrupoles varied with u^8 , [47].

It is noted that the frequency spectrum of the wake noise has very little content below the fundamental lift dipole frequency, [47]. Above the fundamental lift frequency, the spectrum has a roll-off of $1/f^2$, [113].

To the author's knowledge, there has been no specific study into the acoustic intensity of sounds generated by Aeolian tone wakes but there have been numerous studies into wakes generated by subsonic jet turbulence, [64, 105, 9]. [64] states the radiated sound from a jet is greatly influenced by a Doppler factor of $(1 - M \cos \theta)^{-5}$. It is also understood that wake noise has much less energy than a jet. The acoustic intensity of the wake $\overline{I_w(t)}$ has been approximated as:

$$\overline{I_w} \sim \Gamma \frac{\sqrt{2\pi}\kappa^2 S_t^2 l b \rho_{air} u^8}{16\pi^2 c^5 (1 - M \cos(\pi - \theta))^5 r^2} \left(1 + B \cos^4(\theta) - \frac{B+3}{4} \sin^2(2\theta) \sin^2(\varphi) \right) \quad (4.11)$$

where Γ is a scaling factor between the wake noise and lift dipole noise. B is an empirical constant given in [105] as [-1,3]. The range of the value for B accounts for the possible range of combinations between longitudinal and lateral quadrupoles in the jet turbulence. The value of π was included in the denominator of the first component in Eqn. 4.11 as the Aeolian tone and wake derivations in [64] were made with the air flowing in opposite directions.

4.2.4 Implementation of Aeolian Tone Compact Sound Source

Using Pure Data, a number of parameters were sampled at audio rate of 44100 Hz. The sampled airspeed was given as $u[n]$, where n is the discrete time variable. The airspeed u is a scalar value given in metres per second. This leads to the values for Reynolds number, Strouhal number, lift and drag frequencies, and acoustic intensities being calculated at audio rate, $R_e[n], S_t[n], f_l[n], f_d[n], \overline{I_l[n]}$.

Discrete frequency calculations

The first step in the obtaining the dominant lift dipole frequency is to obtain a value for the Reynolds number $R_e[n]$. A discrete implementation of Eqn. 4.2 is given in Eqn. 4.12 below.

$$R_e[n] = \frac{\rho_{air} d u[n]}{\mu_{air}} \quad (4.12)$$

Values for λ and τ are obtained from Table 4.1. A discrete value for the Strouhal number $S_t[n]$ was then calculated, Eqn. 4.13.

$$S_t[n] = \lambda + \frac{\tau}{\sqrt{R_e[n]}} \quad (4.13)$$

The discrete lift frequency $f_l[n]$ was given from Eqn. 4.14 and the discrete drag frequency $f_d[n]$ from Eqn. 4.15.

$$f_l[n] = \frac{S_t[n] u[n]}{d} \quad (4.14)$$

$$f_d[n] = \frac{2S_t[n] u[n]}{d} \quad (4.15)$$

Discrete Acoustic Intensity Calculation

A discrete implementation of the time averaged acoustic intensity equation $\overline{I_l[n]}$, Eqn. 4.16 is shown below.

$$\begin{aligned} \overline{I_l[n]} &\sim \frac{\sqrt{2\pi}\kappa^2 S_t[n]^2 l b \rho u[n]^6 \sin^2 \theta \cos^2 \varphi}{32c^3 r^2 (1 - M[n] \cos \theta)^4} \\ &\left\{ \exp \left[-\frac{1}{2} \left(\frac{2\pi M[n] S_t[n] l}{d} \right)^2 \sin^2 \theta \sin^2 \varphi \right] \right\} \end{aligned} \quad (4.16)$$

Previous theoretical research carried out in [111] set the constant κ to 1 and neglected the exponent. [64] confirms that for low Mach numbers the exponent can be neglected. Following these, the value of κ was set to 1 and the exponent section neglected to give the simpler Eqn. 4.17.

$$\overline{I_l[n]} \sim \frac{\sqrt{2\pi}\kappa^2 S_t[n]^2 l[n] b \rho u[n]^6 \sin^2 \theta \cos^2 \varphi}{32c^3r^2(1 - M[n] \cos \theta)^4} \quad (4.17)$$

Values for the correlation length l were given in [111] ranging from 17d to 3d, depending on the Reynolds number. [108] published a plot showing similar values, highlighting the difference between other previously published results. It was noted that the overall trend was that the correlation length decreases as the Reynolds number increases. Based on the results published in [108], a relationship between the Reynolds number and the correlation length $l[n]$ was derived, Eqn. 4.18.

$$l[n] = 10^{1.536} R_e[n]^{-0.245} d \quad (4.18)$$

All parameters for Eqn. 4.17 could now be determined and the time averaged acoustic intensity calculated. [33] found that the drag dipole acoustic intensity was approximately one tenth of the lift dipole. The drag dipole time averaged acoustic intensity $\overline{I_d[n]}$ was therefore given by Eqn. 4.19.

$$\overline{I_d[n]} = 0.1 \frac{\sqrt{2\pi}S_t^2 l[n] b \rho_{air} u[n]^6 (\sin(\theta + \frac{\pi}{2}))^2 (\cos \varphi)^2}{32c^3r^2(1 - M \cos \theta)^4} \quad (4.19)$$

The time averaging period T_p was given in [64] as:

$$T_p[n] = \frac{2\pi}{f_l}(1 - M[n] \cos \theta) \quad (4.20)$$

Bandwidth

In signal processing, the relationship between the spectrum value at the frequency peak and the bandwidth given where the spectrum value is -3dB is known as the Q value, where $Q = f_l[n]/\Delta f_l[n]$. The Q value is particularly used when describing the characteristics of a filter and this is highly relevant to our noise shaping implementation.

The data relating to the bandwidth of the Aeolian tone was published in [107] although this was limited to Reynolds numbers under 237000. A linear relationship was found to relate to lower data portion of the data and a quadratic relationship to the upper. The data is shown in Fig. 4.7. Equation 4.21 is the linear equation (red line in Fig. 4.7) which represents the lower and Eqn. 4.22 the upper (blue line in Fig. 4.7).

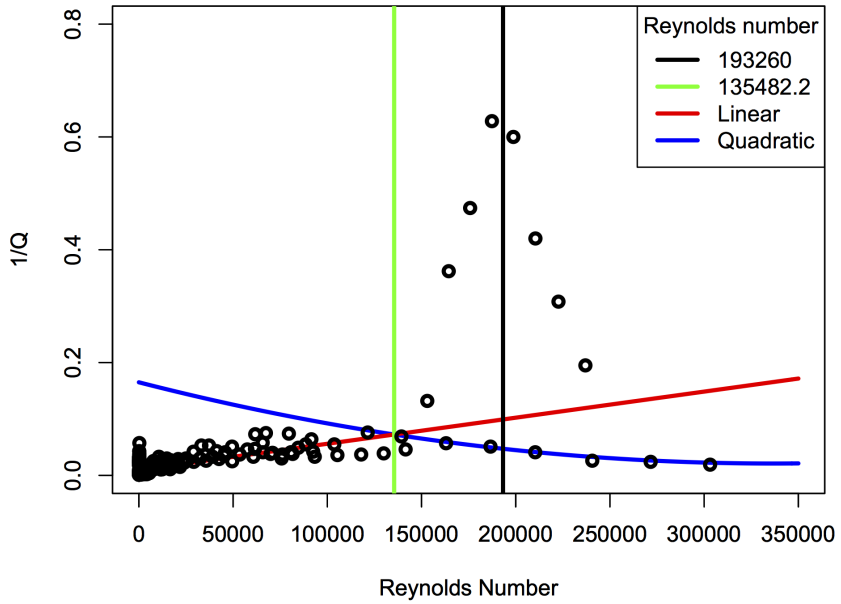


Figure 4.7: Relationship between the inverse Q values and Reynolds number for the Aeolian tone

$$\frac{1}{Q[n]} = 4.624 \times 10^{-7} R_e[n] + 9.797 \times 10^{-3} \quad (4.21)$$

$$\frac{1}{Q[n]} = 1.27 \times 10^{-12} R_e[n]^2 - 8.552 \times 10^{-7} R_e[n] + 0.165 \quad (4.22)$$

For this implementation a threshold between the two equations was chosen to be 193260. This minimises the error between area where the inverse Q values go high and the remaining values around a Reynolds number of 200000. This spike in inverse Q values are where the Reynolds number is in a region called critical flow [107]. An alternative option for future development could be using a threshold of Reynolds number of 135482.2, the crossing point of the two lines. A method of predicting if the flow regime was critical or not could assist with maybe a second quadratic predicting the inverse Q values for these.

Harmonics Calculations

The values for the normalised harmonic gains given in [66] are calculated as shown in Table 4.2. The value for the drag dipole harmonic was visible in simulations and implemented.

Table 4.2: Acoustic intensity values for Aeolian tone harmonics

| Harmonic | Acoustic Intensity |
|-----------|---------------------------------------------------|
| 3 x f_l | $I_{l3} = 10^{0.6 \log_{10} \overline{I_{l1}}}$ |
| 5 x f_l | $I_{l5} = 10^{0.1 \log_{10} \overline{I_{l1}}}$ |
| 2 x f_d | $I_{d2} = 10^{0.125 \log_{10} \overline{I_{d1}}}$ |

Digital Filters and z-Transform

The digital filters used to implement the sound effect are all classed as *Linear Time Invariant* (LTI). A linear filter is one in which no new spectral components are added by the filter. A time invariant filter is defined as one whose transfer function coefficients remain constant over the duration of the impulse response [137]. This provides the opportunity to define the filter transfer function in the discrete time $[n]$ and z-domain (z). The z-transform of a filter $H(z)$ is given by:

$$H(z) = \frac{Y(z)}{X(z)} \quad (4.23)$$

where $Y(z)$ and $X(z)$ are the z-transform of the filter output and input respectively. A typical signal becoming nonzero at time zero ($n = 0$) therefore we can describe the z-transform from the unilateral equation given in Eqn. 4.24.

$$X(z) = \sum_{n=0}^{\infty} x[n]z^{-n} \quad (4.24)$$

for example, the difference equation:

$$y[n] = 6x[n] + 2x[n - 1] - x[n - 2]$$

has the z-transform:

$$Y(z) = 6X(z) + 2X(z)z^{-1} - X(z)z^{-2}$$

$$Y(z) = X(z)(6 + 2z^{-1} - z^{-2})$$

therefore the z-transform $H(z)$ is given by:

$$H(z) = \frac{Y(z)}{X(z)} = 6 + 2z^{-1} - z^{-2}$$

Wake Noise Calculations

As previously stated, the wake noise associated with the Aeolian tone has a frequency profile of $\frac{1}{f^2}$ above the fundamental lift frequency. A noise profile of $\frac{1}{f^\alpha}$ is known as coloured noise and can be produced by inputting white noise to a filter with the transfer function given in Eqn. (4.25), [81].

$$H_{\text{coloured}}(z) = \frac{1}{1 - \frac{\alpha}{2}z^{-1} - \frac{\frac{\alpha}{2}(1-\frac{\alpha}{2})}{2!}z^{-2} + \dots} \quad (4.25)$$

White noise has a profile of a constant gain value across the frequency spectrum. When $\alpha = 2$ this noise is called brown noise. In our implementation Eqn. (4.25) was approximated as:

$$H_{\text{brown}}(z) = \frac{1}{1 - \frac{\alpha}{2}z^{-1}} \quad (4.26)$$

The value of 1 in the denominator when $\alpha = 2$ proved to be unstable. A value of 0.99 was used instead. The spectrum was plotted and analysed and did not show any significant difference than a $\frac{1}{f^2}$ roll-off.

The brown noise profile was therefore given as in Eqn. 4.27:

$$N[z] = H_{\text{brown}}[z]W[z] \quad (4.27)$$

where $W[z]$ is a white noise source and $N[z]$ is the brown noise output. To ensure little wake content below the fundamental lift frequency, the brown noise was passed through a high pass filter. By setting the cut off frequency as the fundamental lift frequency, the wake content below this was minimised.

The filters used in the implementation were realised using the standard recursive filters within Pure Data. A one pole low-pass filter is given by [116]:

$$H_{lp} = \frac{1-p}{1-pz^{-1}} \quad (4.28)$$

where p is a pole and given by $p = 1 - \omega$, where $\omega = 2\pi(f_l[n]/f_s)$, $f_l[n]$ is the cut-off frequency and f_s is the sampling frequency. The numerator is multiplied by $1 - p$ to give a normalised output. A single one pole, one zero high-pass filter with the transfer function given in [116] as $1 - H_{lp}$:

$$H_{hp}[z] = 1 - \frac{1 - p}{1 - pz^{-1}} = p \left(\frac{1 - z^1}{1 - pz^1} \right) \quad (4.29)$$

The cascade transfer function for the two high pass filters is given in Eqn. 4.30:

$$H_{hp}[z] = p^2 \left(\frac{1 - 2z^{-1} + z^{-2}}{1 - 2pz^{-1} + p^2z^{-2}} \right) \quad (4.30)$$

This transfer function gives a roll off of ≈ 35 dB/dec. The wake profile required was therefore obtained from Eqn. 4.31:

$$G[z] = H_{hp}[z]N[z] \quad (4.31)$$

An inverse Z-transform of the output gives the wake discrete time signal $g[n]$. The time averaged acoustic intensity of the wake was given by a discrete implementation of Eqn. 4.11 as shown in Eqn. 4.32.

$$\begin{aligned} \overline{I_w[n]} &\sim \Gamma \frac{\sqrt{2\pi}\kappa^2 S_t[n]^2 l[n] b \rho_{air} u[n]^8}{16\pi^2 c^5 (1 - M[n] \cos(\pi - \theta))^5 r^2} \\ &\left(1 + B \cos^4(\theta) - \frac{B+3}{4} \sin^2(2\theta) \sin^2(\varphi) \right) \end{aligned} \quad (4.32)$$

Final Output

The dipole outputs for the Aeolian tone were achieved from a white noise source filtered by a bandpass filter centred around the relevant frequency and the correct gain applied. The outputs relating to the fundamental lift and drag dipoles and harmonics are then summed together before being output to the digital to analogue converter.

For the dipole compact sound sources, a cascade of two LTI bandpass voltage-controlled filters were used. Pure data uses a two-pole bandpass filter [116], with complex-conjugate poles, p_1 and p_2 :

$$\begin{aligned} p_1 &= (1 - \beta)(\cos \omega + i \sin \omega) \\ p_2 &= (1 - \beta)(\cos \omega - i \sin \omega) \end{aligned} \quad (4.33)$$

where β is the bandwidth of the peak at -3dB and ω is the centre frequency in radians. Relating this to the complex-conjugate pair given in [137] as:

$$\begin{aligned} p_1 &= x_p + iy_p \\ p_2 &= x_p - iy_p = \overline{p_1} \end{aligned} \quad (4.34)$$

we can see that x and y can be given as:

$$\begin{aligned} x_p &= (1 - \beta) \cos \omega \\ y_p &= (1 - \beta) \sin \omega \end{aligned} \quad (4.35)$$

The pole radius R is given in [137] as:

$$R = \sqrt{x_p^2 + y_p^2} \quad (4.36)$$

and the poles' respective angles θ given as:

$$\theta = \tan^{-1} \left(\frac{y_p}{x_p} \right) \quad (4.37)$$

The transfer function of a two-pole bandpass function is expressed in [137] as:

$$H[z] = \frac{b_0}{(1 - Re^{i\theta}z^{-1})(1 - Re^{-i\theta}z^{-1})} \quad (4.38)$$

The bandpass filter used in pure data as given by [116] is multiplied by $\beta(\beta + 2\omega)$ giving:

$$\begin{aligned}
H[z] &= \frac{\beta(\beta + 2\omega)}{(1 - Re^{i\theta}z^{-1})(1 - Re^{-i\theta}z^{-1})} \\
&= \frac{\beta(\beta + 2\omega)}{1 - 2R\cos(\theta)z^{-1} + R^2z^{-2}}
\end{aligned} \tag{4.39}$$

In this implementation, two bandpass filters were placed in series to give:

$$H_{bp}[z] = H[z]H[z] \tag{4.40}$$

Noise Shaping

For the fundamental lift dipole frequency, the centre frequency of the bandpass filter was set to $f_l[n]$ and the Q value was calculated from the reciprocal of the percentage value obtained from a discrete implementation of Eqn. 4.21 or Eqn. 4.22. The fundamental lift dipole output thereafter given by:

$$X_{l1}[z] = H_{bp}[z]W[z] \tag{4.41}$$

where $W[z]$ is the same white noise source as used in Eqn. 4.27. Equation 4.41 gives the output of the bandpass filter in the z domain and the discrete time output can be obtained from an inverse Z transform of this, giving $x_{l1}[n]$.

The model replicating the fundamental drag dipole was implemented in the same manner except with the bandpass filter centre frequency set at the fundamental drag frequency, giving a discrete time signal output of $x_{d1}[n]$. Note, there was no information found in relation to the tone bandwidth for the drag dipole and harmonics. For simplicity if was also set at the same Q value calculated for the fundamental lift frequency.

The dipoles modelling the lift and drag harmonics were obtained in a similar manner, with centre frequencies at $3f_l[n]$, $5f_l[n]$, and $2f_d[n]$, giving discrete signal outputs of $x_{l3}[n]$, $x_{l5}[n]$ and $x_{d2}[n]$.

The gain value for the lift dipole was set proportional to the time-averaged acoustic intensity as given in Eqn. 4.17. The gains for the drag dipole were obtained from Eqn. 4.19 and the harmonics from Eqns. given in Table 4.2. The gain for the wake output $g[n]$ was calculated from Eqn 4.32.

Since all the sources are combined to give one compact sound source modelling the Aeolian tone, a single white noise source was used for all the dipoles. It was believed this is valid since the dipoles representing the fundamental and harmonic sources are at the same location.

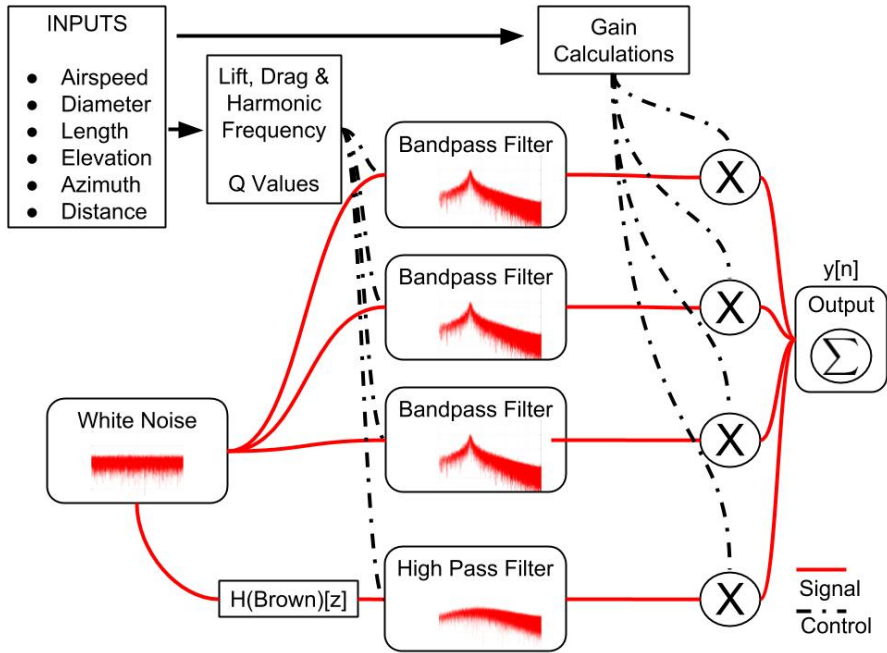


Figure 4.8: Flow diagram of compact sound source for the Aeolian tone

The final discrete time output is given in Eqn. 4.42:

$$y[n] = \chi \left[\sum_{k=1}^3 \overline{I_{l(2k-1)}} x_{l(2k-1)}[n] + \sum_{j=1}^2 \overline{I_{d(j)}} x_{d(j)}[n] \overline{I_w g}[n] \right] \quad (4.42)$$

where χ is a user defined variable gain to allow the sound effect to be set to the required overall gain while maintaining an authentic gain relationship between the sound sources. It should be noted that allowing the user to define an overall gain value χ , would allow all constants in Eqns. 4.17, 4.19 and 4.32 to be factored out. Therefore the approximation of setting $\kappa = 1$ valid as long as it is constant across the equations. A diagram illustrating the synthesis process is given in Fig. 4.8.

4.2.5 Evaluation of Aeolian Tone Model

Numerous studies have published results pertaining to the Aeolian tone at different cylinder diameters and airspeeds. For comparison to the frequency prediction method employed by our model, the diameter and airspeed conditions were replicated. The frequency results are shown in Table 4.3.

Table 4.3: Comparison of known measured results, ones we have simulated using Fluent CFD and our synthesis model - (* read from a graph, ** computed answer); (a) [11], (b) [145], (c)[91], (d) [143] (e) [47], (f) [60]. (Frequencies are in Hz)

| Publication | [11] | | | [145] | [91] | [143] | | | [47] | | | | [60] |
|----------------------------------|-------|--------|-------|-------|-------|-------|--------|--------|--------|--------|--------|--|------|
| Air speed (m/s) | 20 | 40 | 15 | 69 | 69 | 69 | 68.58 | 42.67 | 16.6 | 26.7 | 32.3 | | |
| Diameter (m) | 0.004 | 0.004 | 0.006 | 0.019 | 0.019 | 0.019 | 0.0127 | 0.0127 | 0.0254 | 0.0254 | 0.0254 | | |
| Published Frequency | 1000 | 2000* | 508 | 617** | 643 | 1000* | 650* | 150* | 210* | 240* | | | |
| Real-Time Model Frequency | 1038 | 1988 | 515 | 674 | 674 | 1008 | 635 | 125 | 197 | 238 | | | |
| % Error | 3.8 | 0.6 | 1.38 | 9.24 | 4.82 | 0.8 | -2.31 | -16.67 | -6.19 | 0.83 | | | |
| Fluent CFD Frequency | 1113 | 1635 | 590 | 837 | 837 | 1148 | 703 | 145 | 245 | 304 | | | |
| % Error | 13.3 | -18.25 | 16.14 | 35.66 | 30.17 | 14.8 | 8.15 | -3.33 | 16.67 | 26.67 | | | |

Discrepancies between the published results for frequency measurements and values simulated by our model can be seen. Some of these discrepancies could be attributed to the measurements made in the wind tunnels. As previously stated in Section 3.2, it is not trivial to eliminate unwanted noise within wind tunnels, especially from the instrumentation added to measure the actual desired sound. Some of the results shown in Table 4.3 are historical dating back to the 1950s and 1960s where instrumentation might not have been as precise as those available today.

It is possible that the piecewise linear relationships between the Reynolds number and the Strouhal number, taken from [50] are incorrect. [50] states the error is up to ± 0.003 in the Strouhal number which relates to approximately $\pm 1.5\%$. The air in a wind tunnel also has a property called free stream turbulence which is the turbulence of the air prior to reaching the cylinder. The effects of this are not replicated in the synthesis model which may affect results. The synthesis model was based on a smooth cylinder which is static, but wind tunnel measurements can be affected by surface roughness and possible movement of the cylinder.

As an exercise to compare results obtained through CFD simulations, the conditions given in the publications used for Table 4.3 were replicated using the commercial package, Fluent. This provided an opportunity to compare measured, theoretical and simulated results together as well as providing an appreciation for CFD as a technique. It should be noted that CFD simulations can yield much more information than that used for the comparison, e.g. what happens during transients and exact values for the pressure perturbations that are heard in the far field.

The settings for the CFD calculations were as follows:

- Unsteady Reynolds Averaged Navier Stokes (URANS)
- 2-dimensional model
- Shear-Stress Transport model (SST)
- 2nd order upwind numerical scheme
- Ffowcs-Williams Hawkings acoustic analysis method [155] (Appendix C)

URANS has been shown to provide good qualitative and quantitative agreements with Aeolian tone experiments, able to show a frequency spike at shedding frequencies [76]. Because there is no analytical theory to predict how turbulent flows evolve a model is required. A number of different models have been developed and improved as computational fluid dynamic simulators have developed. The Shear-Stress Transport model is one that combines two models; using a preferred option for flow near a boundary and a preferred alternative for free stream flow. This has been shown to give good results in conjunction with URANS simulations [98].

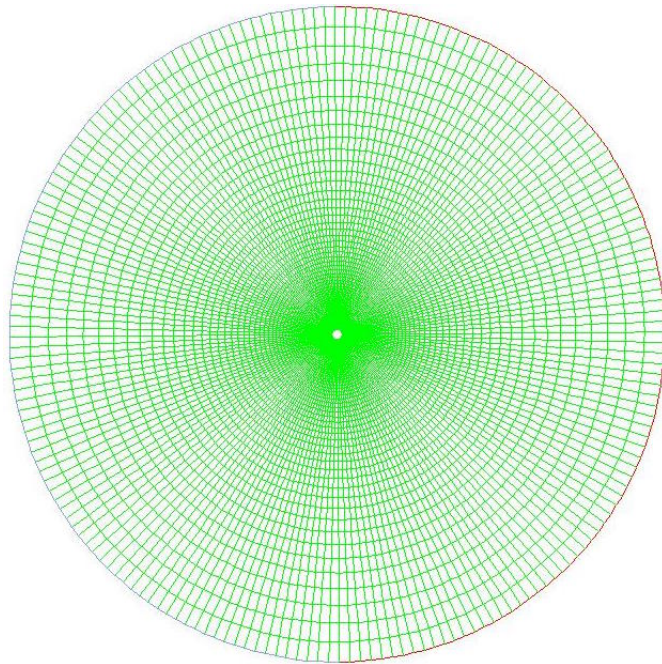


Figure 4.9: Typical mesh for a 2D cylinder

A mesh with 73728 elements was created for the simulation and shown in Fig. 4.9. The acoustic receiver was positioned at a distance of 12 metres with an elevation angle of 90° above the cylinder, perpendicular to the flow. Figure 4.10 shows the velocity vectors for a typical simulation. Vortex shedding can clearly be seen behind the 2-dimensional circle.

The results for the CFD simulations are also shown in Table 4.3. It can be seen that the differences in these results and the published measurements was significantly larger than those given by our model.

The absolute error was calculated by Eqn. 4.43. The average absolute error for the synthesis model based on the semi-empirical equations was 4.66%. The average absolute error for the CFD simulations was 18.11%. The % error values in Table 4.3 indicates that the CFD calculations consistently overestimate the frequency values whereas our model estimates were more equally balanced between less than or greater than published values.

$$\text{Absolute error} = \frac{|(f_{\text{predicted}} - f_{\text{published}})|}{f_{\text{published}}} \cdot 100 \quad (4.43)$$

There are a number of reasons for the differences between the CFD result and those obtained from the semi-empirical model. The equations the model was based on may take into consideration experimental observations which are possibly not replicated by the CFD simulation. Therefore, it

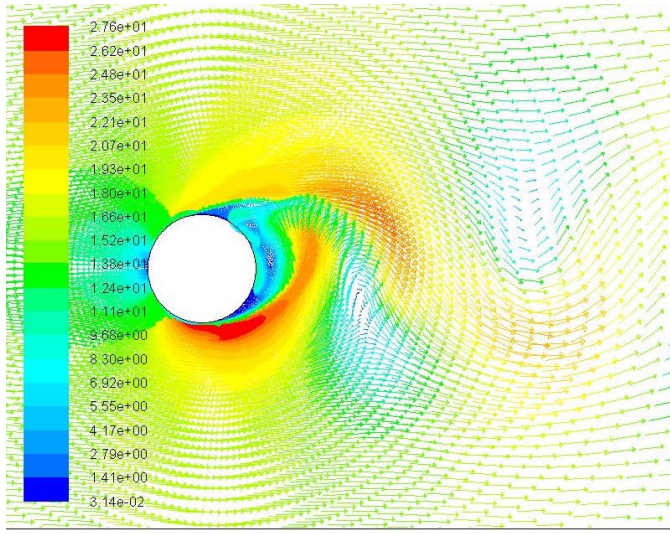


Figure 4.10: Simulation of Aeolian tone showing vortex shedding

might be expected that the semi-empirical model is closer to results obtained through experimental measurements.

How the CFD software computes the interaction at the boundary of the cylinder and the main flow domain may introduce errors. When simulating in 2-dimensions it is not possible to fully simulate the turbulence which is a 3-dimensional phenomenon.

To illustrate this further, the CFD output file was converted to a sound file and analysed using signal processing techniques. The time plot, magnitude spectrum and spectrogram are shown in Figs 4.11, 4.12 and 4.13 respectively. Figs 4.11, 4.12 and 4.13 are replications of conditions set in [145]. It can be seen from Fig. 4.12 particularly that the tones due to the lift, drag as well as their harmonics are virtually pure sine waves.

The simulations in Fluent are carried out in 2-dimensions and therefore not able to simulate the turbulent structure cascade and just captures the tones. It is for this reason that the wake noise roll-off was also not visible. This indicates that compared to a 2-dimensional simulation, the synthesis model has some aspects that are more authentic than a 2-dimensional simulation.

There is a marked difference between the CFD calculated time plot and the synthesised one, Fig. 4.11. This is believed to be due to a combination of reasons but the wider bandwidth surrounding the peak frequencies in the synthesised model introduces additional components seen in the time plot. It can also be seen that between the peak frequencies in the CFD generate plots, Fig 4.12a the magnitude response goes down to below 0dB. In Fig. 4.12b there is a considerable frequency content between the peaks that is about 0dB.

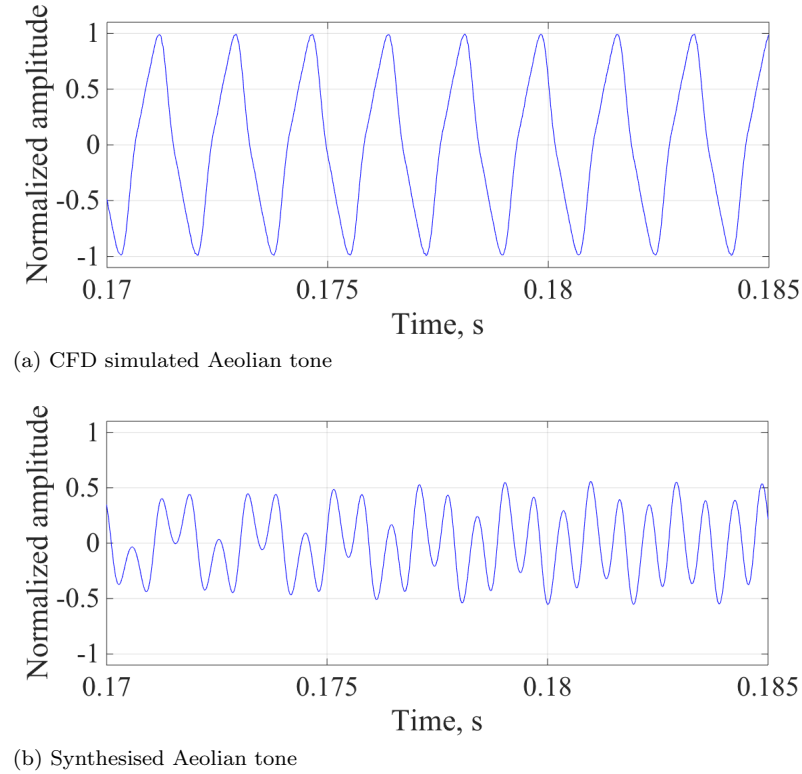


Figure 4.11: Fluent CFD and synthesis model time plots, $u = 15 \text{ m/s}$, $d = 0.006 \text{ m}$

Another difference between the simulated results and the result from our synthesis model was the number of harmonics visible. The simulated version in Fig 4.12 show harmonics up to the 7th. This was replicated up to only 5th harmonic in the synthesis model. This was also replicated with respect to the drag tone harmonics. One possible reason is that the minor harmonics might be masked by the wake noise.

A difference in frequency of the fundamental tone and harmonics can clearly be seen when comparing Figs. 4.12a and 4.12b. Even harmonics are also visible, but this was not the case in the synthesised model which was based on ideal dipoles. The partials representing the 6th and 7th harmonics are seen to be small in relation to the others and it was decided not to include them at this stage to maintain computational efficiency.

The reasons above highlights the difference between the exact replication of the pressure fluctuations of the 2 dimensional simulation and the simplified version of the shaped noise. For the purposes of procedural audio sound effects, the exact details given in a CFD simulation may more detail than the synthesis model is able to process in real-time. This comparison does give a useful insight into the accuracy of the equations used and how applying them includes some of the physical properties but a detailed CFD simulation has the ability to reveal additional detail.

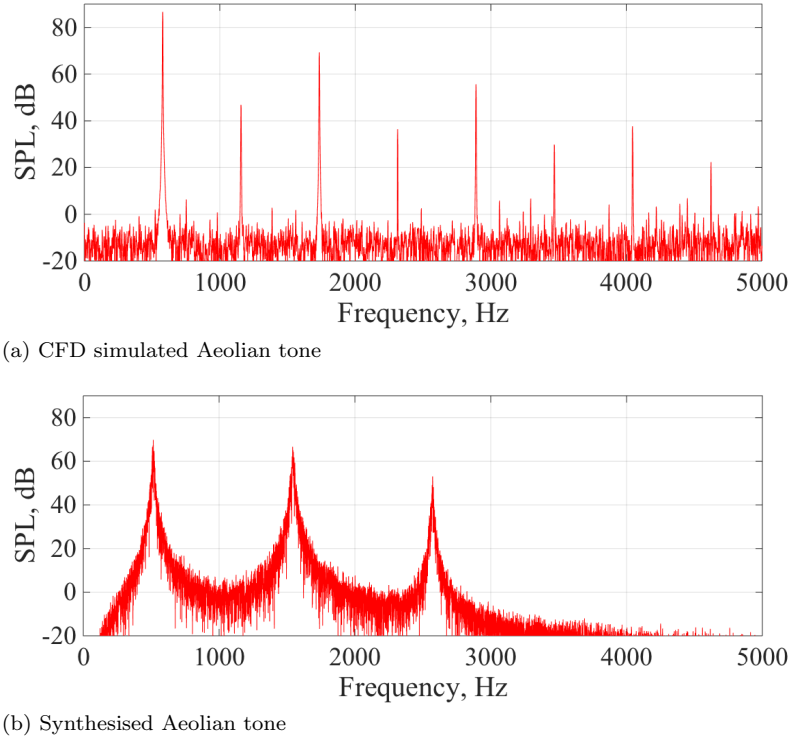


Figure 4.12: Fluent CFD and synthesis model magnitude plots, $u = 15 \text{ m/s}$, $d = 0.006 \text{ m}$

4.2.6 Concluding Comments on Aeolian Tone Model

Presented in this section is a real-time synthesis model of an Aeolian tone compact sound source. The semi-empirical model is defined by equations which are obtained by simplifications from theoretical equations or experimental observations. The model has been designed to replicate sounds close to what would occur in nature. Unlike other models which aim to replicate this sound, this model operates in real-time but accounts for physical properties such as airspeed, diameter and the relationship between source and listener.

The compact sound source model can be used as an integral component of wider aeroacoustic sound effects. Examples of these are demonstrated in Chapter 5 including, swords, propellers and an Aeolian harp. This compact sound source could also be used in the development of helicopter rotors, fans and similar. A demo of the Aeolian tone synthesis model can be downloaded at <https://code.soundsoftware.ac.uk/projects/aeolian-tone>.

It was noted in this section that some of the assumptions require the airspeed to be in the region of low Mach number and $< 343 \text{ m/s}$ (speed of sound). It is possible to synthesise the sounds generated by the interaction of the wind and wire fences and poles at airspeeds far greater than it is possible to record. The airspeeds can be increased beyond the highest wind speeds

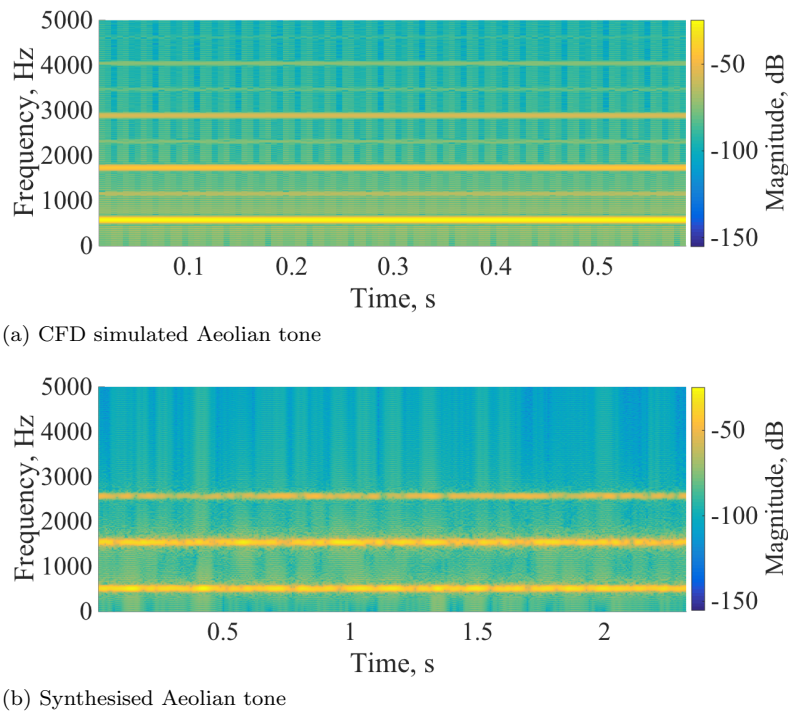


Figure 4.13: Fluent CFD and synthesis model spectrograms, $u = 15 \text{ m/s}$, $d = 0.006 \text{ m}$

recorded to generate original sound effects. If this is the case, it would make sense to re-include the exponential component of Eqn. 4.16.

The implementation of the model has set values for air density and viscosity, but these could also be adjusted to suit an adapting environment with varying temperature or even an alien atmosphere.

Discrepancies between our model and previously published results have been highlighted and the real-time synthesis model performs well at predicting the fundamental frequencies. The 2-dimensional simulations using the CFD package Fluent had a greater number of discrepancies than the synthesis model. It also took a significant time to compute, with a number of hours required to get less than a second's worth of data.

Performing a 3-dimensional simulation increases the computation time considerably but would give the CFD software the ability to simulate turbulence, increasing the accuracy of any data produced.

Further improvements to this model would include decreasing the assumptions made in the governing equations. It would be beneficial to examine more oval shapes and blunt objects like square as these would increase the accuracy of the sound effects modelled.

4.3 Cavity Tone

Nomenclature

c = speed of sound (m/s)

f = frequency (Hz)

ω = angular frequency = $2\pi f$ (rads/revolution)

u = air flow speed (m/s)

R_e = Reynolds number (dimensionless)

S_t = Strouhal number (dimensionless)

r = distance between listener and sound source (m)

ϕ = elevation angle between listener and sound source

φ = azimuth angle between listener and sound source

ρ_{air} = mass density of air (kg m^{-3})

μ_{air} = dynamic viscosity of air (Pa s)

M = Mach number, $M = u/c$ (dimensionless)

L = length of cavity (m)

d = depth of cavity (m)

b = width of cavity (m)

κ = wave number, $\kappa = \omega/c$ (dimensionless)

δ = shear layer thickness (m)

δ^* = effective shear layer thickness (m)

δ_0 = shear layer thickness at edge separation (m)

θ_0 = shear layer momentum thickness at edge separation (m)

C_2 = pressure coefficient (dimensionless)

I = acoustic intensity (W/m^2)

Q = peak frequency / bandwidth at -3dB (dimensionless)

λ = mode number

α = constant representing the difference in phase (dimensionless)

K = ratio of the convection velocity of the vortices to the free stream flow (dimensionless)

γ = ratio of specific heats (dimensionless)

A = area of the cavity mouth (m^2)

ζ = cavity end correction (m)

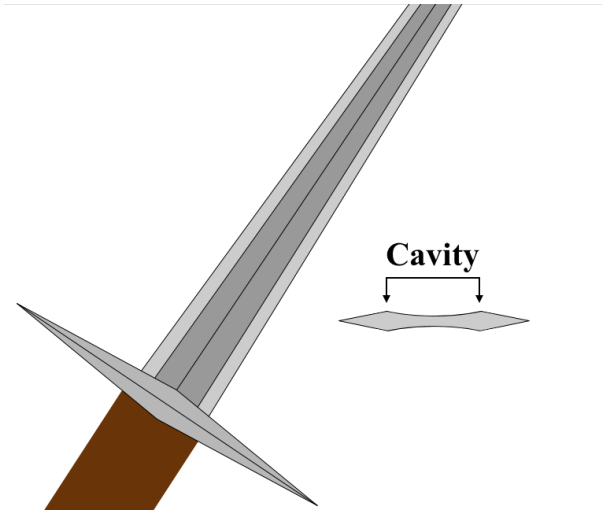


Figure 4.14: Sword with a grooved profile can produce the cavity tone

4.3.1 Introduction

The cavity tone is the name given to the acoustic tone produced as air passes over a cavity. Examples of this tone have been witnessed most clearly in aircraft where cavities in the structure, often temporary, appear during flight. This can be when a weapons bay is opened for deployment or when wheels are extended for take-off and landing.

The cavity tone has also been heard when a sword with a grooved profile is swung through the air. An example of this type of profile is shown in Fig. 4.14. It can also be present when wind blows passed windows and doors and the correct fluid dynamic conditions are met.

4.3.2 State of the Art

The cavity tone was included in research by [43] into real-time aeroacoustic sounds. Like the Aeolian tone model, the sounds generated are obtained from off-line CFD calculations and played back in real-time as sound textures.

The sounds of an aircraft were analysed and re-synthesised by [13]. They identified tonal sounds in the analysis were due to cavities in the wheel wells when landing gear extended. This was synthesised using a pure sine wave with time varying amplitude and frequency.

In [49] the cavities in walls were synthesised to give a general wind type sound. In this case the cavities were microscopic cavities in the faces of walls or larger doorways. These sounds were labelled as howls and obtained from noise filtering. Exact dimensions and number of the cavities

were unknown, and the sound triggered when the wind speed passed above a threshold.

The model presented here is for a cavity tone compact sound source. This model operates in real-time like that of [49] but exact dimensions and relevant parameters are given to the user. The parameters and ability to set dimensions is similar to the work of [43] but the model does not employ any CFD calculations.

4.3.3 Principles of Cavity Tone

Basic Fluid Dynamics

Consider air flowing with a flat plane as a boundary at one side. It is known there is a small shear layer parallel to the plane due to the non-slip condition [28]. When the air reaches a cavity the boundary layer separates from the plane at the cavity leading edge creating a shear layer between the free-flowing air above the cavity and the air within the cavity.

Shear layer instabilities travel with a certain velocity away from the leading edge and as this happens, instabilities within it grow. These are Kelvin-Helmholtz instabilities [124] which are convected downstream towards the trailing edge. When the instabilities reach the trailing edge of the cavity it strikes the trailing edge and a pressure pulse is created. The pressure pulse travels upstream towards the leading edge where the air is separating from the plate. The pressure pulse interacts with vortices being created at the leading edge and re-enforces this process creating what is known as a aeroacoustic or hydrodynamic feedback system [120].

When the aeroacoustic feedback system is complete, the pressure pulse generated at the trailing edge can be heard in the far field as a tone. The frequency of the tone is based on the distance between the leading and trailing edge and the wavelength of the pressure pulse [122]. Figure 4.15 illustrates the flow over a cavity and Fig. 4.16 shows the dimensions used throughout the calculations.

The operation of the cavity tone described above is known as shear mode. The cavity tone can also operate in what is known as wake mode which occurs when the cavity length or depth becomes large compared to the shear layer thickness, or when the Reynolds numbers are raised [124]. In wake mode, large 2-dimensional vortex is shed from the cavity itself. This process is illustrated in Fig. 4.17. Wake mode cavity tones are beyond the scope of this research.

In shear mode operation, a cavity can be described as either open or closed. An open cavity is when the shear layer stretches out and strikes the trailing edge as described above. A closed cavity is when the cavity length is such a length that the shear layer is able to contact the bottom of the cavity before it reaches the trailing edge. Under these circumstances there is no shear layer flapping against the trailing edge, no pressure pulse and hence no tone [126].

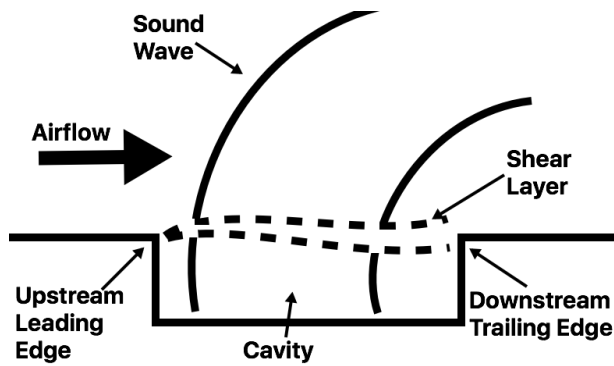


Figure 4.15: Basic components of cavity used in tone generation

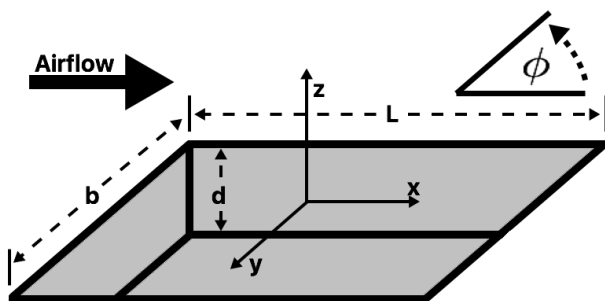


Figure 4.16: Diagram showing coordinates of a cavity

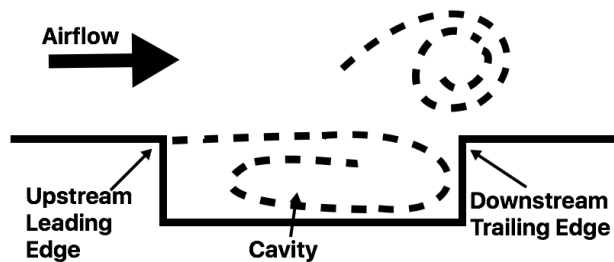


Figure 4.17: Diagram showing cavity in Wake mode

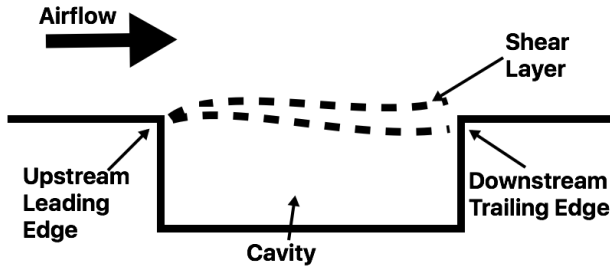


Figure 4.18: Diagram showing open cavity

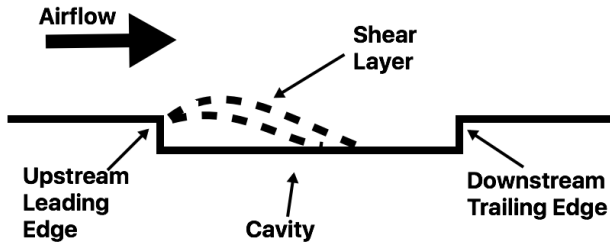


Figure 4.19: Diagram showing closed cavity

The relationship between cavity length between leading and trailing edge, and the depth of the cavity can be used to estimate if the cavity is open or closed. Figures 4.18 and 4.19 illustrate the difference between an open and a closed cavity.

Frequency Prediction

The cavity tone frequency can be described by a dimensionless Strouhal number. Unlike the Aeolian tone, Section 4.2, for the cavity tone the dimension used to describe the relationship between the Strouhal number and frequency is the cavity length L . The cavity tone non-dimensional Strouhal number $S_{t\lambda}$ was calculated from Eqn. 4.44 [122].

$$S_{t\lambda} = \frac{f_\lambda L}{u} \quad (4.44)$$

where f_λ is the predicted cavity tone frequency and u is the speed of air flowing across the cavity. One of the most important studies into predicting the cavity tone frequency was carried out by [122]. In this publication Rossiter defined the semi-empirical equation to calculate the cavity tone Strouhal number $S_{t\lambda}$. This is shown in Eqn. 4.45:

$$S_{t\lambda} = \frac{\lambda - \alpha}{\frac{1}{K} + M} \quad (4.45)$$

where α is a constant representing the difference in phase between the acoustic wave arriving at the leading edge and the vortex being shed. The value of 0.25 was given to α to fit in with observations of the experimental data. The constant K represents the ratio of the convection velocity of the vortices to the free stream flow. The convection velocity is the velocity of the instabilities travelling towards the trailing edge as described above.

In [122] the value of K was set to 0.57. This was again to fit with observed experimental data. The value λ is an integer that represents the mode of operation for the cavity tone. This mode number refers to the number of wavelengths or fraction of wavelengths, in the pressure pulse before it reaches the leading edge. Therefore, each mode has a different frequency. M is the Mach number, calculated as Eqn. 4.7.

In [67] Eqn. 4.45 was extended to include the speed of sound within the cavity. This is shown in Eqn. 4.46:

$$S_{t_\lambda} = \frac{\lambda - \alpha}{\frac{1}{K} + \frac{M}{[1 + \frac{\gamma-1}{2} M^2]^{\frac{1}{2}}}} \quad (4.46)$$

where γ is the ratio of specific heats. A value of 1.4 is given in [67]. Combining and rearranging Eqns. 4.44 and 4.46, we can obtain an equation to predict the frequency of the cavity tone for each mode λ ; modes 1-4 are the most common.

$$f_\lambda = \frac{\lambda - \alpha}{\frac{1}{K} + \frac{M}{[1 + \frac{\gamma-1}{2} M^2]^{\frac{1}{2}}}} \frac{u}{L} \quad (4.47)$$

The cavity tone due to the aeroacoustic feedback loop is a dipole sound source, positioned near the trailing edge. In this thesis, the dipoles represent the sound generated by the aeroacoustic feedback known as Rossiter frequencies. Cavities also have monopole sources representing the resonant modes of the cavity. This is examined in the next section.

Acoustic Intensity

For the cavity tone, the acoustic intensity work of [75] was the most useful for this model. Like Goldstein for the Aeolian tone, [75] started from Lighthill's Acoustic Analogy and through the use of Green's functions defined an equation to predict the acoustic intensity in the far field of the cavity tone.

The work presented in [75] included an end correction value due to inertia in the shear layer. The peak frequency mode was shown to be dependent on the thickness of the shear layer.

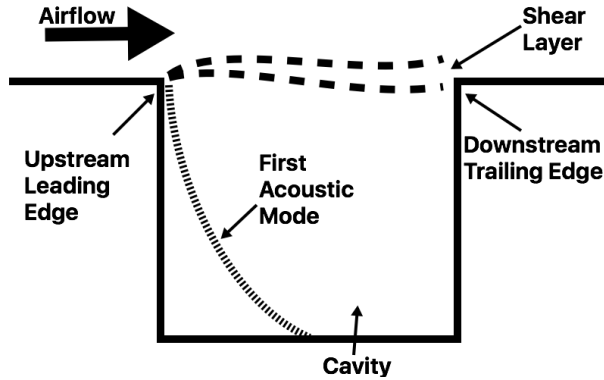


Figure 4.20: Diagram showing first resonant depth mode

The equation published from [75] for acoustic intensity $I(\omega, x)$ is shown in Eqn. 4.48:

$$I(\omega, x) \approx \frac{M^2 (\omega \delta^* / u)^{5/3}}{(1 + M \cos \phi)^2 \{(\omega \delta^* / u)^2 + \tau_p^2\}^{3/2}} \cdot \left| \frac{C_2 \sin(\kappa d)}{\cos\{\kappa(d + \zeta + i(\kappa A/2\pi))\}} + i(\cos \phi - M) \right|^2 \quad (4.48)$$

where ω is the angular frequency ($= 2\pi f$), δ^* is the effective shear layer thickness, u is the air speed, C_2 and τ_p are constants set to 1.02 and 0.12 respectively [75]. A is the area of the cavity mouth given by bL , d is the cavity depth, κ is the acoustic wave number given by ω/c and ϕ is the elevation angle from the flow normal (Fig. 4.16). In the far field the spherical waves can be regarded as plane waves [75]. The end correction, ζ is the effective length which the cavity must be extended to account for the inertia of fluid above the cavity mouth which is also set into reciprocal motion by the cavity resonance. This was given in [75] as Eqn. 4.49.

$$\zeta = \sqrt{\pi A / 4} \quad (4.49)$$

Resonant Mode

Along with the dipoles due to the aeroacoustic feedback system there are also monopoles due to the resonant modes of the cavity. The most significant resonant mode for the cavity is the first mode of the resonance due to the cavity depth. This is illustrated in Fig. 4.20.

If the cavity is sufficiently deep, the resonant monopole due to the depth can be dominant over the dipoles due to aeroacoustic feedback. The complex frequency, relating to the lowest order

mode was calculated when Eqn. 4.50 is true [75]. The terms on the left-hand side are those operated on by the cosine in the denominator of the second term in Eqn. 4.48 [75].

$$\kappa \left(d + \zeta + i \frac{\kappa A}{2\pi} \right) = \frac{\pi}{2} \quad (4.50)$$

Giving [75]:

$$\kappa d \sim \frac{\pi d}{2(d + \zeta)} - \frac{i\pi Ad}{8(d + \zeta)^3} \quad (4.51)$$

The real part of equation 4.51 is the expression for the lowest depth mode for the cavity, augmented by the end correction factor ζ .

Bandwidth

Due to the diffuse nature of vortex shedding at the leading edge, the cavity tone is often not a pure tone but a range of frequencies, peaking at the cavity tone and with a bandwidth which is proportional to how diffuse the vortices are. When examining the bandwidth of the Aeolian tone in Section 4.2, [107] published data relating to the relationship between the fundamental lift frequency and the bandwidth. Unfortunately, nothing of equivalence to this was found by the author which could relate the bandwidth of the cavity tone to the peak Rossiter frequency.

Harmonics

In this study, only the major modes relating to the aeroacoustic feedback system are modelled. During literature research no mention to harmonics of these modes was forthcoming. It was believed that if the air flowing past the cavity is supersonic and contains shock waves that harmonics may be produced. This is beyond the scope of this research.

It is also recognised that further resonant modes may exist due to depth, length or width. These were not examined at this time as it was believed that the 1st depth mode would dominate and hence was the only one included.

4.3.4 Implementation

As with the previous compact sound source model, the cavity tone model was implemented in Pure Data. The airspeed u was sampled at audio rate giving $u[n]$ where $[n]$ is the discrete time variable. For the frequency calculations this gives $R_e[n]$, $S_t[n]$, $f_\lambda[n]$, $f_M[n]$, $M[n]$ as well as the acoustic intensity for all modes, $I(\omega, x)[n]$, all calculated at audio rate.

Conditions of Activation

To determine whether there was any output due to the aeroacoustic feedback system, the model was required to determine whether the shear layer would reach the trailing edge (open) or come into contact with the bottom of the cavity prior to this (closed). It was found in [31] that a cavity would become closed when $L/d > 8$. Another study in [126] found this relationship to be nearer $L/d > 11$. It was believed the variation could be due to the airspeed. For this implementation the two previous stated values were averaged to give a value of $L/d > 9.5$ for all airspeeds. If the ratio exceeded this value, the dipoles would not operate leaving only the monopole of the resonant depth mode.

Frequency Calculations

The Rossiter frequencies for modes 1-4 were calculate using a discrete implementation of Eqn. 4.47 as shown below:

$$f_\lambda[n] = \frac{\lambda - \alpha}{\frac{1}{K} + \frac{M[n]}{[1 + \frac{\gamma-1}{2} M[n]^2]^{\frac{1}{2}}}} \frac{u[n]}{L} \quad (4.52)$$

This gives the first four dominant Rossiter frequencies, $f_\lambda[n]$ which relate to the dipole sources associated with the feedback loop. To calculate the frequency of the dominant depth resonant mode, a solution to the real part of Eqn. 4.51 was found. This is shown in Eqn. 4.53.

$$\kappa d = \frac{\pi d}{2(d + \zeta)} \quad (4.53)$$

The value κ is the wavenumber and given by ω/c , while ω is $= 2\pi f$. Inputting these variables into Eqn. 4.53 and rearranging we can obtain Eqn. 4.54 which predicts the monopole frequency.

Table 4.4: Values of the ratio L/θ_0 for different L/d values from [124] and [140]

| Reference | L/d | L/θ_0 |
|-----------|-------|--------------|
| [124] | 2 | 52.8 |
| | 4 | 60.24 |
| | 4 | 86.06 |
| | 6 | 90.36 |
| [140] | 4 | 82 |

$$f_M = \frac{c}{4(d + \zeta)} \quad (4.54)$$

Shear Layer Thickness

The thickness of the shear layer is important in determining the acoustic intensities of the dipoles. The shear layer thickness can be described in three different ways. The value δ is the shear layer thickness. δ^* is the effective shear layer thickness and the value θ is the momentum thickness of the shear layer.

In [124] and [140], values for the momentum thickness θ were published in relation to the length to depth ratio of the cavity L/d . These are given in Table 4.4.

A linear regression line was calculated for this data giving the relationship as stated in Eqn. 4.55 below:

$$\frac{L}{\theta_0} = 9.39 \frac{L}{d} + 36.732 \quad (4.55)$$

Since the length and depth of the cavity are set by the user, we are able to predict a value for the momentum thickness of the shear layer. Eqn. 4.48 requires the effective thickness of the shear layer. At the leading edge, the relationship between the momentum thickness and the effective thickness is given by a shape factor H [28] as shown in Eqn. 4.56.

$$H = \delta_0^*/\theta_0 \quad (4.56)$$

In [140] a shape factor value of $H = 2.69$ was stated for laminar flow and $H = 1.29$ was for turbulent. An indication of whether a flow was turbulent or not was given by the Reynolds number with regards to the cavity length. In [128] a critical value of 25000 was found as the transition from laminar to turbulent.

We can calculate the value for Reynolds number with respects to the cavity length $R_{eL}[n]$ giving a real-time indication if the flow was laminar or turbulent. The correct shape factor, H was then selected allowing the effective thickness of the shear layer at the leading edge to be calculated.

The growth of the effective shear layer over the cavity had to be taken into consideration. In [28] the shear layer thickness δ_c over a cavity for laminar flow is given by Eqn. 4.57:

$$\delta_c = \left(\frac{xL}{R_{eL}} \right)^{\frac{1}{2}} \quad (4.57)$$

where x is the distance from the leading edge. For turbulent flows [28] states the equation to calculate the shear layer thickness δ_c is

$$\delta_c = \left(\frac{x}{\sigma\sqrt{8}} \right) \quad (4.58)$$

where σ is a parameter called the Görtler Parameter. In [124] the value of σ was found to lie between 5 and 7; it was set to 6 for this implementation. The value of x was set to 0.75L due to the dipoles being positioned near to the trailing edge [124].

To convert the shear layer thickness to the required effective shear layer thickness, a relationship was found in [28] and given as shown in Eqn. 4.59.

$$\delta^* = \frac{1}{1+n} \delta \quad (4.59)$$

[28] set $n = 7$; this value was replicated in this model. This enabled our model to calculate the effective shear layer thickness at the dipole source in laminar or turbulent flows as given by eqn. 4.60.

$$\delta^* = \delta_c^* + \delta_0^* \quad (4.60)$$

Acoustic Intensity Calculations

To calculate the acoustic intensity, a discrete version of Eqn. 4.48 was required. It stated in [75] that this equation also included the intensity produced by the resonant first mode of the depth, which was a monopole source. It was therefore required to separate this equation into components for the dipoles representing the aeroacoustic feedback loop and the monopole representing the

resonant mode. The first component in the squared magnitude brackets on Eqn. 4.48 refers to the monopole and the second term refers to the dipole.

The first step was to separate out the real and imaginary terms within the denominator of the first term within the squared magnitude brackets. This term is given in Eqn. 4.61:

$$\cos \left[\kappa \left(d + \zeta + i \frac{\kappa A}{2\pi} \right) \right] \quad (4.61)$$

Multiplying the internal bracket by κ gives:

$$\cos \left[\kappa(d + \zeta) + i \left(\frac{\kappa^2 A}{2\pi} \right) \right] \quad (4.62)$$

The identity given in Eqn. 4.63 relates to this equation.

$$\cos(a + ib) = \cos a \cosh b - i \sin a \sinh b \quad (4.63)$$

Substituting in the variables of Eqn. 4.63 we can define two variables X and Y as:

$$\begin{aligned} X &= \cos [\kappa(d + \zeta)] \cosh \left(\frac{\kappa^2 A}{2\pi} \right) \\ Y &= \sin [\kappa(d + \zeta)] \sinh \left(\frac{\kappa^2 A}{2\pi} \right) \end{aligned} \quad (4.64)$$

Placing these variables back into the first term within the squared magnitude brackets and multiplied by the complex conjugate of the denominator. The terms in the squared magnitude brackets can then be rewritten as:

$$\left| \frac{C_2 \sin(\kappa d) X}{X^2 + Y^2} + i \left(\frac{C_2 \sin(\kappa d) Y}{X^2 + Y^2} + (\cos \phi - M) \right) \right|^2 \quad (4.65)$$

Using the relationship $|x + iy|^2 = x^2 + y^2$ we can multiply out Eqn. 4.65 to give:

$$\left(\frac{C_2 \sin(\kappa d) X}{X^2 + Y^2} \right)^2 + \left(\frac{C_2 \sin(\kappa d) Y}{X^2 + Y^2} + (\cos \phi - M) \right)^2 \quad (4.66)$$

The second term was multiplied out to give the full representation of Eqn. 4.48 as shown in

Eqn. 4.67 below.

$$I(\omega, x) \approx \frac{M^2(\omega\delta^*/u)^{5/3}}{(1+M\cos\phi)^2\{(\omega\delta^*/u)^2+\tau_p^2\}^{3/2}} \cdot \left[\left(\frac{C_2 \sin(\kappa d) X}{X^2 + Y^2} \right)^2 + 2 \frac{C_2 \sin(\kappa d) Y (\cos\phi - M)}{X^2 + Y^2} + (\cos\phi - M)^2 \right] \quad (4.67)$$

As previously stated the terms with “ $C_2 \sin(\kappa d)$ ” are associated with the monopole and the terms with “ $\cos\phi - M$ ” are associated with the dipole. The middle term in Eqn. 4.67 contains terms relating to both. To minimise error this term was placed along with the other term relating to the monopole. This was because the monopole is the more efficient source and it was believed the error due to the dipole component would be less than adding the monopole component to the dipole terms.

This manipulation enabled Eqn. 4.48 to be defined in terms of the dipole acoustic intensity and the monopole acoustic intensity as shown in Eqns. 4.68 and 4.69.

$$G_D(\omega_{D\lambda}, r, \phi) \sim \frac{M^2(\omega_{D\lambda}\delta^*/u)^{5/3}}{r(1+M\cos\phi)^2\{(\omega_{D\lambda}\delta^*/u)^2+\tau_p^2\}^{3/2}} \left[\left[\cos\phi - M \right]^2 \right] \quad (4.68)$$

$$G_M(\omega_M, r, \phi) \sim \frac{M^2(\omega_M\delta^*/u)^{5/3}}{r(1+M\cos\phi)^2\{(\omega_M\delta^*/u)^2+\tau_p^2\}^{3/2}} \left[\left[\frac{XC_2 \sin(\kappa_M d)}{X^2 + Y^2} \right]^2 + \left[\frac{YC_2 \sin(\kappa_M d)}{X^2 + Y^2} \right]^2 + 2 \frac{YC_2 \sin(\kappa d)}{X^2 + Y^2} (\cos\phi - M) \right] \quad (4.69)$$

where $G_D(\omega_{D\lambda}, r, \phi)$ is the discrete far field acoustic intensity in relation to the dipoles and $G_M(\omega_M, r, \phi)$ is the far field acoustic intensity in relation to the monopole. Both gains were multiplied by the reciprocal of the distance between source and listener, r . Figure 4.21 shows the output from Eqn. 4.48 and the outputs from Eqns. 4.68 and 4.69 separately.

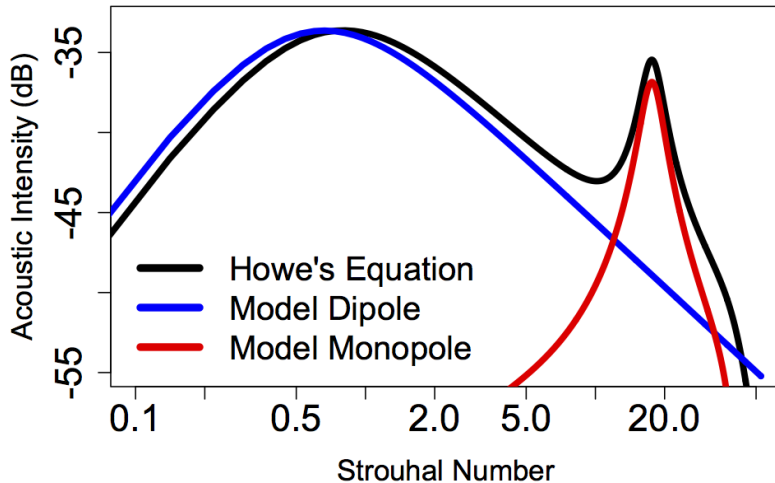


Figure 4.21: Far field cavity tone spectrum gains calculated by Eqn. 4.68 & Eqn. 4.69 as compared to Howe's derivation from [75]. $L = b = 0.03m$, $d = 0.015m$ and $u = 3.43m/s$.

Tone Bandwidth

As stated in Section 4.3.3, no data in relation to the tone bandwidth of the cavity tone was forthcoming from the literature. It is known that the more turbulent the flow the smaller and more diffuse the vortices are. This leads to an increase in complex interactions and a broader width of frequencies around the peak value. In contrast a laminar flow has larger, simpler interactions and the tones can be predicted to be closer to pure tones.

The previous implementation of the Aeolian tone required the prediction of a Q value for use in the bandpass filter used in the noise shaping. Similarly, the Q value was required for this implementation. The measure of turbulent in the flow is given by the Reynolds number and therefore a relationship between the Reynolds number and Q value had to be found.

To achieve this a number of plots published in [3, 46, 159, 112, 93, 123, 86, 104] were examined. The bandwidth and peak frequency value of each plot was measured and converted to a Q value. The results of this are shown in Table 4.5.

A linear regression line was fitted to the natural logarithm of the Reynolds number was defined using this data. This is given in Eqn. 4.70.

$$Q = 87.715 - 5.296 \log(R_{e_L}) \quad (4.70)$$

This line is plotted in Fig. 4.22. It can be seen that the Q value decreases giving a wider bandwidth around the peak frequency as the Reynolds number increases. This matches the

Table 4.5: Q values with corresponding Reynolds numbers measured from plots given in a number of publications

| Reference | Q | R_{e_L} |
|-----------|--------|--------------------|
| [3] | 5 | 5.64×10^5 |
| | 4.5 | 4.52×10^5 |
| | 4.5 | 3.45×10^5 |
| [46] | 25 | 3.10×10^5 |
| [159] | 11.875 | 1.27×10^5 |
| [112] | 6 | 1.47×10^5 |
| | 14 | 3.54×10^6 |
| | 14 | 7.08×10^6 |
| [93] | 6.875 | 2.48×10^6 |
| | 7.875 | 2.95×10^6 |
| [123] | 22.5 | 4.01×10^6 |
| [86] | 76 | 4.51×10^4 |
| [104] | 15 | 6.46×10^5 |

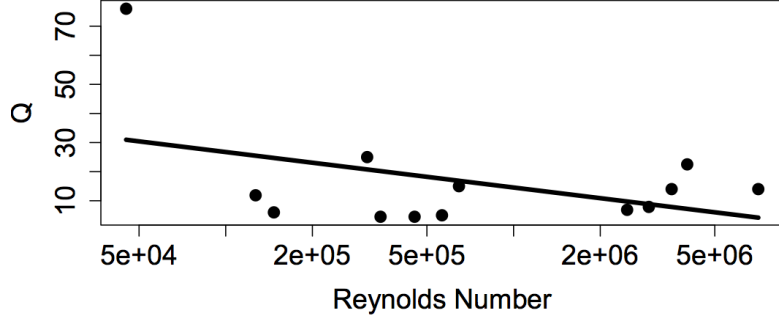


Figure 4.22: Relationship between Reynolds number and Q values for cavity tone

hypothesis that this would be the case. To prevent the value of Q reaching unrealistic values a limit was set so that Q varied between 2 and 90.

Total Output

Each of the dipole mode frequencies was calculated using Eqn. 4.46 and this was set as the centre frequency to four band pass filters. The transfer function for these filters $H_{bp}[z]$ was the same as the ones used for the Aeolian tone, Eqn. 4.4.4, given here for convenience as:

$$H_{bp}[z] = \frac{\beta_1 + \beta_2 z^{-1} + \beta_3 z^{-2}}{1 + \alpha_1 z^{-1} + \alpha_2 z^{-2} + \alpha_3 z^{-3} + \alpha_4 z^{-4}}$$

with the values for the constants $\alpha_{1,2,3,4}$ and $\beta_{1,2,3}$ given in the appendix. White noise $W[z]$ was

applied to the input of each filter giving:

$$B_{D\lambda}[z] = H_{bp}[z]W[z] \quad (4.71)$$

where $B_{D\lambda}[z]$ is the output for each mode. The dipole acoustic intensity $G_D(\omega_{D\lambda}[n], r, \theta)$ given in Eqn. 4.68 was calculated for each mode and output of each bandpass filter multiplied by the corresponding acoustic intensity. A single dipole output is given as:

$$D_\lambda[n] = G_D(\omega_{D\lambda}[n], r, \theta)B_{D\lambda}[n] \quad (4.72)$$

The frequency of the resonant depth mode was calculated from Eqn. 4.54. The same white noise source as used for the monopoles was also applied to a bandpass filter with the centre frequency set at the monopole frequency, $H_{bp}[z]$. This gave the output from the bandpass filter $B_M[z]$ as:

$$B_M[z] = H_{bp}[z]W[z] \quad (4.73)$$

The acoustic intensity relating to the monopole source $G_M(\omega_m[n], r, \theta)$ is given in Eqn. 4.69. The output from the monopole bandpass filter was multiplied by this to give the monopole output as:

$$M[n] = G_M(\omega_m[n], r, \theta)B_M[n] \quad (4.74)$$

Summing all the outputs together gave the final output for the cavity tone as:

$$y[n] = M[n] + D_1[n] + D_2[n] + D_3[n] + D_4[n] \quad (4.75)$$

A flow diagram illustrating the synthesis process for the cavity Tone is shown in Fig. 4.23.

4.3.5 Evaluation of Cavity Tone Model

Figure 4.21 shows the acoustic intensity output from Eqns. 4.68 and 4.69 as compared to the complete equation given in [75]. It can be seen that the dipole peak in our model occurs at a slightly lower value than that of [75]. A possible reason for this is the fact that [75] uses a value of $L\tau_p^2/\pi\sqrt{2}$ for the effective shear layer thickness. This sets the 2nd mode as the dominant peak; our model calculates the shear layer thickness, Section 4.3.4.

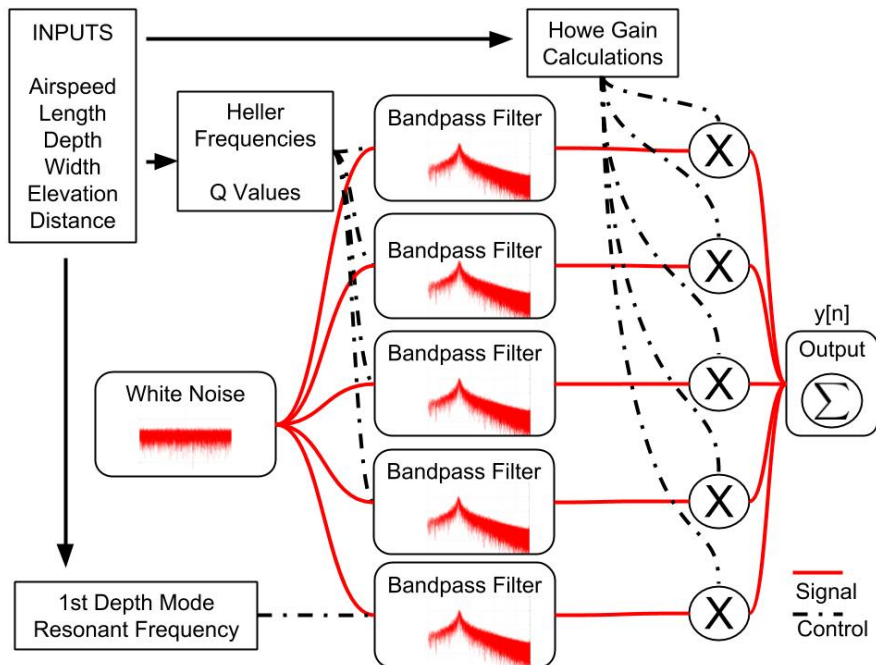


Figure 4.23: Flow diagram showing cavity tone synthesis process

The plot for the monopole acoustic intensity matches well to the plot given in [75]. This indicates that the extra component we added to Eqn. 4.69 which was from multiplying out squared brackets (a dipole component) has not diminished the accuracy of this calculation.

To evaluate the frequency prediction of Heller's equation given in [67] and Eqn. 4.52, a comparison was carried. A number of conditions from previous publications were collated and are presented in Table 4.6. Unlike the evaluation for the Aeolian tone, results from literature included both experimental and simulated along with some theoretical results. Due to time restraints, it was decided preferable to use simulated results from other publications rather than running a fluent simulation to produce my own results.

The emphasis of [3] was to provide benchmark data to validate CAA codes. It was found that the frequency prediction used in this model provided excellent results when compared to this publication. It can be seen that for the lower airspeeds in [3], the published theoretical results are closest to our predictions. For higher airspeeds our theoretical predictions are closer to the measured frequencies than the theoretical calculations carried out in [3].

The reason for this is that it is presumed that [3] used Rossiter's formula, Eqn. 4.45, to predict cavity tone frequency but the synthesis model uses Heller's extension to this equation and this is possibly more accurate as airspeed increases.

A larger sized cavity was examined in [55]. The published results for theoretical, measured and simulated cavity tone frequencies are all quite similar but not identical. This illustrates that no one method is exact. The results predicted by the synthesis model lie within the range of frequencies of the different methods examined in [55]. It should be noted when modelling this cavity that the synthesis model found the resonant depth mode to be the dominant sound. This was not mentioned in [55].

In [162] the cavity tone frequency was published as theoretical value, measured value and simulated value. Again, a difference was present between them. The cavity tone frequencies for these conditions was above the maximum frequency for human hearing. Examining Table 4.6 it can be seen that the synthesis model predicted frequency was closest to the published theoretical results. The measured and simulated results are higher than those predicted by the model.

In order to evaluate the synthesis model's prediction of the resonant depth mode, it was compared to a deep cavity which was examined in [46]. The frequencies relating to the dipole are not published in [46] but the frequency due to the resonant monopole was found to be 225Hz. The synthesis model used Eqn. 4.54 to predict this frequency and obtained a value of 213Hz. The discrepancy may be due to the value of the end correction, $\zeta = \sqrt{\pi A/4}$ used in Eqn. 4.54.

A contrasting low airspeed over a wide cavity was published in [85]. The measurements in [85] were made using a technique called Particle Image Velocimetry. This technique is beyond the scope of this research but the results show a more pronounced error than previously compared publications, especially for the lowest speed of 12m/s. It was stated in [140] that theoretical prediction models are less accurate at very low airspeeds and that measured results are also found to have the greatest variation.

The final comparison was made with a square shaped cavity as examined in [32]. In this case the published data was in the form of a graph which had to be interpreted by the author. It can be seen that the values given by the synthesis model are lower than the published results. The results published in [32] indicated that the third mode of the feedback loop was dominant, but the synthesis model predicts that the resonant monopole would be the dominant sound source. This was in keeping with the findings of [75] who stated that if $L/d > 5/2$ that the resonance can dominate the cavity tone.

Comparing the average frequencies predicted by the synthesis model and the results published in Table 4.6 it was found that the synthesis model predictions were 0.3% lower than theoretical frequencies, 2.0% lower than computed frequencies and 6.4% lower than measured frequencies.

The Aeolian tone model output was compared to the output from a CFD simulation in Figs. 4.11 to 4.13. Similarly, Fig. 4.24 shows the output of the cavity tone model, replicating the theoretical examples given by [75]. The dipole frequencies f_{D1} , f_{D2} , f_{D3} , f_{D4} follow the shape of the

Table 4.6: Comparison of published measured, computed and theoretical results and our cavity tone synthesis model. **Bold** indicates dominant frequency. Ref. = Reference. (* - read from a graph, † - theoretical answer, ‡ - computational answer, ? - Unknown)

| Reference | Airspeed (m/s) | Dimensions (m) | | | | Published Results (Hz) | | | | | Physical Model Results (Hz) | | | | |
|-----------|---------------------------------------------------|----------------|--------|--------|--------|------------------------|-------------|----------|----------|-------|-----------------------------|---------------|----------|------------|-------|
| | | u | l | w | d | f_{D1} | f_{D2} | f_{D3} | f_{D4} | f_M | f_{D1} | f_{D2} | f_{D3} | f_{D4} | f_M |
| [75] | 3.43 | 0.03 | 0.03 | 0.015 | | 114*† | | | | 49 | 113 | 178 | 243 | 2061 | |
| [3] | 89.2 137.2 181.8 230.5 274.4 308.7 | 0.0191 | 0.1016 | 0.0127 | | 4530 | | | | 1739 | 4057 | 6376 | 8695 | | |
| | | | | | | 4063† | | | | | | | | | |
| | | | | | | 5854† | | | | 2506 | 5848 | 9190 | 12532 | | |
| | | | | | | 7339 | | | | 3141 | 7330 | 11519 | 15707 | | |
| | | | | | | 8062† | | | | | | | | | |
| | | | | | | 8809 | | | | 3773 | 8804 | 13835 | 18865 | | |
| | | | | | | 9401† | | | | | | | | | |
| | | | | | | 10027 | | | | 4294 | 10019 | 15745 | 21470 | | |
| | | | | | | 10372† | | | | | | | | | |
| | | | | | | 10925 | | | | 4680 | 10919 | 17159 | 23398 | | |
| [55] | 291.6 | 0.4572 | 0.1016 | 0.1016 | 195 | 419 | 693 | 947 | | 188 | 438 | 689 | 938 | 293 | |
| | | | | | 181† | 422† | 663† | 904† | | | | | | | |
| | | | | | 193‡ | 460‡ | 667‡ | 940‡ | | | | | | | |
| | | | | | 31899 | 71344 | 110789 | | | | | | | | |
| [162] | 514.5 | 0.0045 | ? | 0.0015 | 28469† | 66542† | 104615† | | | 28567 | 66657 | 104707 | 142837 | | |
| | | | | | 32242‡ | 66542‡ | 126567‡ | | | | | | | | |
| | | | | | | | | | | | | | | | |
| [46] | 40 | 0.06 | 0.06 | 0.35 | | | | | 225 | 168 | 391 | 615 | 838 | 213 | |
| | | | | | | 454 | | | 908 | | | | | | |
| | | | | | | 454‡ | | | 908‡ | | | | | | |
| | | | | | | 496 | | | 992 | | | | | | |
| [85] | 12 | 0.03 | 0.6 | 0.015 | | 496‡ | | | 992‡ | 209 | 487 | 766 | 1043 | 640 | |
| | | | | | | 496‡ | | | 992‡ | | | | | | |
| [32] | 31 | 0.15 | 0.15 | 0.15 | 125* | 245* | 375* | | | 84 | 196 | 308 | 420 | 303 | |

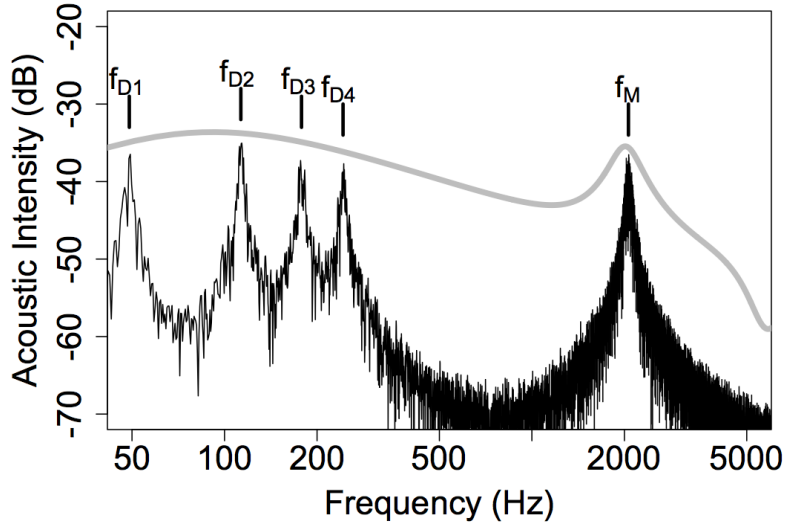


Figure 4.24: Output from the cavity synthesis model. The grey line indicates the value from Eqn. 4.48 for comparison. L and $b = 0.03\text{m}$, $d = 0.015\text{m}$, $u = 3.43\text{m/s}$, $\theta = 30^\circ$.

intensity curve with the second mode dominant, as in [75]. The monopole tone was given at the frequency as calculated by [75].

A further example was modelled in [75] detailing the 2-dimensional sound propagation from the cavity. [75] illustrated the propagation pattern for a number of Strouhal numbers at an airspeed of 34.3m/s. To generate this plot the conditions were matched, frequencies set to the corresponding Strouhal number and the acoustic intensity measured while the elevation varied between 0° and 180° . For this test the acoustic intensity equation was not separated into dipole and monopole components and implemented as Eqn. 4.67.

The result of this is shown in Fig. 4.25. Like the results published in [75], the Strouhal number of 0.5 and 1 give a typical dipole output along the plan of the cavity. At Strouhal number of 1.5 and 2 the monopole output becomes dominant, with a much more omnidirectional output at a Strouhal number of 2. This differs from the results published in [75] where the largest monopole peak was given as $\text{St} = 2.5$. The value of Strouhal number at 2.5 on the synthesis model indicates that it was higher than the dominant resonant mode and therefore did not give the monopole output.

4.3.6 Concluding Comments on Cavity Tone Model

The equation defined by Heller in [67] and implemented by our model performs well for frequency prediction compared to previously published results. This includes results pertaining to

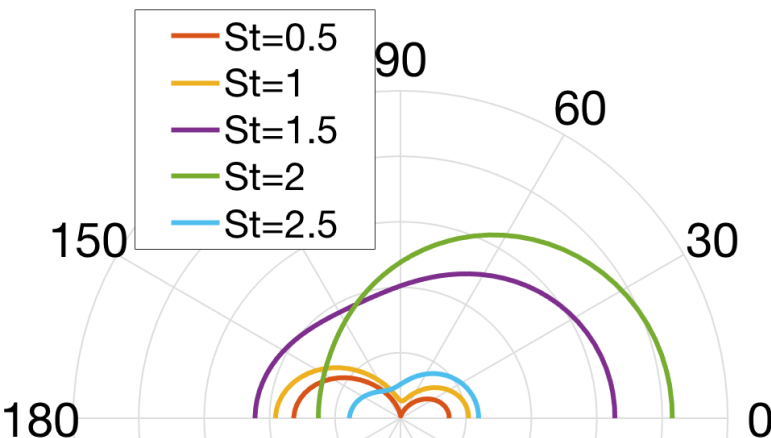


Figure 4.25: Directional output from cavity synthesis model. L and $b = 0.03\text{m}$, $d = 0.015\text{m}$, airspeed = 34.3m/s . St = Strouhal number.

measurements in a wind tunnel, other theoretical models and simulations using CFD packages.

In more than one occasion the papers cited in Table 4.6 publish results from more than one method simultaneously, indicating the difficulty in obtaining the correct value and that it varies depending on method. As highlighted when evaluating the synthesis model for Aeolian tone compact sound source, theoretical models may not capture the complete behaviour of a cavity tone due to the nature of semi-empirical formula.

Computational models may also fail to capture details due to discretisation of the domain or how boundary conditions are modelled. The experimental results from wind tunnels also have potential for errors in instrumentation, noise and human operation.

The acoustic intensity equation given in [75] was the most comprehensive and suitable for the purposes of the synthesis model. In this equation variables C_2 and τ_p were introduced as constants based on the geometry modelled in that publication. These were assigned constant values as indicated in [75] but it is acknowledged that they might not be fixed for all geometries and airspeeds. It is beyond the scope of this research but an area for future development.

Under the same conditions as [75] the synthesis model performs well, matching the acoustic intensity outputs of the dipoles and monopole creating the cavity tone. The final sound effect model provided a further gain to allow the user to increase or decrease the tone as desired but kept the relationships between the independent sound sources intact. This allows the user to set the value as desired.

The directional output of the synthesis model matched that output given by [75] up to a point. For low Strouhal numbers the propagation pattern was virtually identical. The main difference

came when the resonant monopole became dominant. The cause of this cannot be explained by the author and is an area for future research.

Unlike the Aeolian tone, the equations defining the cavity tone are inherently 2-dimensional. The azimuth to the cavity has not been considered. The only place where the width of the cavity was considered was in the calculation of the variable b which was used to calculate A in Eqn. 4.49 and in the acoustic intensity Eqns. 4.68 and 4.69.

The effect of the azimuth is an area of future research as is research into any similar attributes like the correlation length given in the Aeolian tone research, indicating when the vortex shedding is out of phase and a new compact sound source is required. The angle of incident of the air was also not considered in this model. This could have a great influence over the propagation of the shear layer across the top of the cavity, preventing the aeroacoustic feedback loop from occurring. A demo of the cavity tone synthesis model can be downloaded at <https://code.soundsoftware.ac.uk/projects/cavity-tone>.

The compact sound source presented has been derived using semi-empirical models obtained through research of fluid dynamics publications. The sound synthesis model operates in real-time and unlike other models accounts for the angle and distance between source and listener. The user has full control over the size of the cavity to be modelled as well as the airspeed across it. This makes our model unique compared to similar sound effects.

4.4 Edge Tone Model

Nomenclature

c = speed of sound (m/s)

f = frequency (Hz)

ω = angular frequency = $2\pi f$ (rads/revolution)

u = air flow speed (m/s)

R_e = Reynolds number (dimensionless)

S_t = Strouhal number (dimensionless)

r = distance between listener and sound source (m)

ϕ = elevation angle between listener and sound source

ρ_{air} = mass density of air (kgm^{-3})

μ_{air} = dynamic viscosity of air (Pa s)

M = Mach number, $M = u/c$ (dimensionless)

h = nozzle exit-to-wedge distance (m)

δ = nozzle width (m)

λ = mode number

P = pressure (Pa)

I = acoustic intensity (W/m^2)

ξ = shear layer thickness (m)

Q = peak frequency / bandwidth at -3dB (dimensionless)

Λ = scaling factor

4.4.1 Introduction

The edge tone is the sound generated when a planar jet of air from a nozzle comes into contact with a wedge or edge and a number of fluid dynamic conditions are met. Like the previous synthesis models for aeroacoustic compact sound sources, research was undertaken to enable accurate frequency predictions and acoustic intensity. Semi-empirical equations were fundamental to the design of the model.

The edge tone commonly is found as an excitation source for flue instruments. A flue instrument are ones like a recorder, flute, piccolo and pipe organ where air is forced either through a nozzle or from the lips, towards an edge. In musical instruments the edge tone system is coupled to a tube. Once resonant vibrations are established these dominates the sound.

4.4.2 State of the Art

As the edge tone is an integral component of flue instruments, how it was synthesised in musical instrument models is relevant. A flute synthesis model was presented in [158]. The most relevant physical characteristics were modelled using the digital waveguide synthesis technique (see section 2.4.3). To capture perceptual effects a signal-based approach was used. To obtain an excitation signal, the transfer function of the digital waveguide representing the resonator section was obtained. A recorded sample of a flute was then de-convolved with this transfer function. This left a residual which was used as the excitation signal. This excitation signal was then used in the synthesis model as the input to the digital waveguide.

In [40] a real-time synthesis of a physical model of a flute was presented. In this publication, the excitation source and resonator of the tube body were split into lumped models. The approach undertaken for this was similar to ours with noise shaping used as part of the excitation signal.

The edge tone was described in [77] as a special type of impinging tones. Other impinging tones include the hole tone used to indicate a boiling kettle. In the case described in [77] a jet of air impinges on a flat plate rather than a wedge and a tone was produced. These tones are known to occur between the ground and the jet created by vertical take-off and landing (VTOL) aircraft, in transonic wind tunnels and from pressure and velocity probes.

4.4.3 Aeroacoustic Principles of the Edge Tone

Basic Fluid Dynamics

The edge tone is generated when a planar jet from a nozzle, at a certain distance from the nozzle, comes into contact with a wedge. A basic diagram showing this condition is given in Fig. 4.26. As a jet of air exits the nozzle it is inherently unstable. Shear layers exists between the jet moving at a velocity and surrounding air at rest.

When the jet comes into contact with the wedge vortices are shed from alternate sides and an oscillating pressure force is generated. The pressure pulses travel back upstream towards the nozzle exit and at certain frequencies can disturb and re-enforce the inherent instabilities in the jet. This re-enforcement creates a aeroacoustic feedback loop which can produce tones at discrete frequencies. The oscillating pressure pulses can be heard in the far field and are modelled as a dipole compact sound source, located near the wedge tip.

Unlike the cavity tone, where an airflow is moving at some speed over a boundary before reaching the cavity, the edge tone is produced by a jet of air emerging from a nozzle, therefore surrounded by a boundary. As the jet of air travels from the nozzle (and the air over a cavity from the

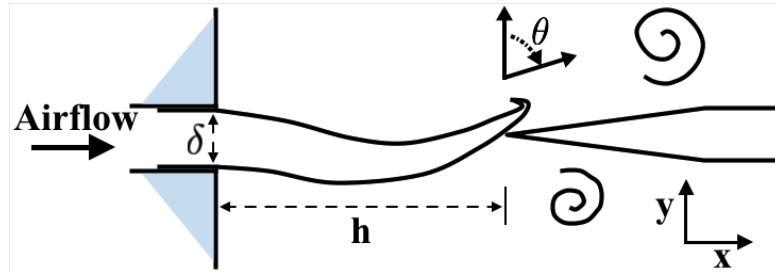


Figure 4.26: Diagram of an edge tone flow showing nozzle exit width δ and nozzle to edge width h

upstream edge) inherent instabilities are entrained and magnified. Unlike the cavity tone, the jet emerging from the nozzle has air at rest above and below, whereas the cavity has air at rest only in the cavity.

Both the cavity tone and the edge tone involve a shear layer impinging on a solid boundary which creates a pressure pulse. It is when the pressure pulse travels back upstream towards either the nozzle or the leading edge and re-enforces the instabilities already present in both shear layers that the aeroacoustic feedback loops are completed. The cavity causes the pressure pulse to be less symmetrical than the jet tone, (see Section 4.3.3, and in particular how the speed of sound in the cavity has to be taken into consideration, Section 4.3.3).

It should also be noted that the airspeed when examining the cavity tone can go much higher than those encountered when researching the edge tone. This is mainly due to the fact that cavities on aircraft have had to be examined compared to the edge tone which is more commonly found in musical instruments and hence lower speeds.

Key variables in Fig. 4.26 that influence the frequency of any tone produced, are the nozzle exit-to-wedge distance h , and the exit width of the nozzle δ . Some studies vary the position of the wedge in relation to the centre of the nozzle exit. This is common in some musical instruments. In this research it was presumed that the wedge was in the centre of the jet, at a position of $\delta/2$.

The airspeed when the jet exits the nozzle is another important factor in determining the edge tone properties. The jet can have different profiles as it exits the nozzle depending on the length of the flue. A parabolic profile is shown in Fig. 4.27. It is created from a flue channel where the length is such that the airspeed at the walls is reduced due to the boundary conditions. If a significant boundary layer has formed on the flue walls the jet profile as it exits the nozzle has a parabolic profile.

The other significant jet profile studied in the literature is that of the top hat. This jet profile is illustrated in Fig. 4.28 and created from a flue channel which is shorter than that which creates the parabolic profile. In the short channel, conditions are such that the boundary layers are not

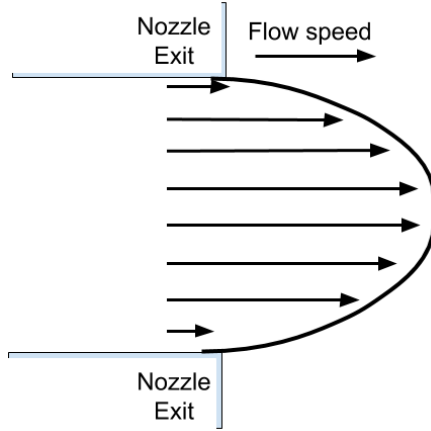


Figure 4.27: Diagram of parabolic jet profile

able to grow to the same extent as a longer flue channel. Therefore when the jet exits the nozzle it has a much flatter profile, described as looking like a top hat.

The fluid dynamics of the edge tone have been studies by numerous researchers. A review in [146] and the references therein provides a comprehensive report of current understanding, yet the complex behaviour is not fully understood.

Observations of the edge tone indicate that the frequency varies with the airspeed u and the distance between the nozzle exit and the wedge, h . There are also a number of stages or modes depending on these parameters. When modes change from one to the other, hysteresis is observed based on either varying u or h . An ideal plot of the hysteresis changes obtained when varying u is shown in Fig. 4.29 and an similar ideal plot for varying h is shown in Fig. 4.30.

Frequency Prediction

Research of the literature indicated that there are a number of semi-empirical equations predicting the frequency of the edge tone. The first notable experimental study was carried out in [22]. The formula stated to predict the edge tone frequency f_λ is given in Eqn. 4.76.

$$f_\lambda = C_\lambda \left(100u - 40 \right) \left(\frac{1}{100h} - 0.07 \right) 0.466 \quad (4.76)$$

where λ is the mode of operation, C_λ are 1, 2.3, 3.8, and 5.4 for mode numbers [1 - 4], u is the air speed flowing out of the nozzle and h is the nozzle-to-wedge distance. This equation has been adapted from imperial to metric units.

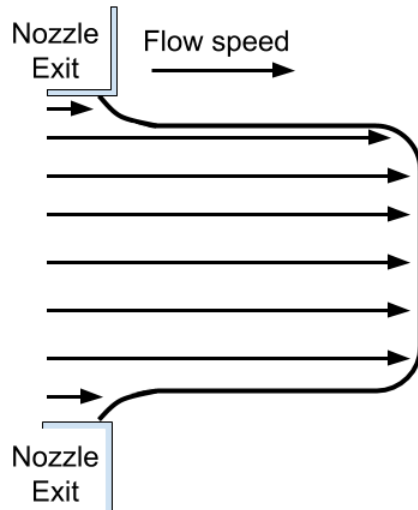


Figure 4.28: Diagram of top hat jet profile

It was found in [22] that the limits of operation of the edge tone were when the ratio of nozzle exit-to-wedge distance over nozzle exit width was between 3.5 and 60. Beyond this no edge tone was detected. It was also noted that the first frequency mode could co-exist with other modes but at a decrease in frequency of approximately 7%.

Research by [72] modelled the edge tone phenomena by vortices travelling in the air jet which were generated by periodic disturbances at the nozzle exit. Through an analysis of the interaction between the vortices and the edge, the oscillating flow at the nozzle exit can be estimated. This in turn enabled an estimate to be made of the phase of the feedback mechanism and thus predict the tone frequency.

Holger et. al.[72] defined Eqn. 4.77 to predict the frequency of the edge tone:

$$f_\lambda = 0.925 \sqrt{\frac{\delta}{h}} (\lambda + C_\lambda)^{\frac{3}{2}} \frac{u}{h} \quad (4.77)$$

where δ is the nozzle height and the coefficients C_λ are 0.4, 0.35 and 0.5 for the first 3 modes respectively; [72] did not consider any higher than mode 3.

Another equation for predicting the frequency of the edge tone was defined in [37] by a linear analytical model. Equation 4.78 gives the frequency prediction equation for modes 1 - 4. It was accepted that results from this equation were much higher than previous equations.

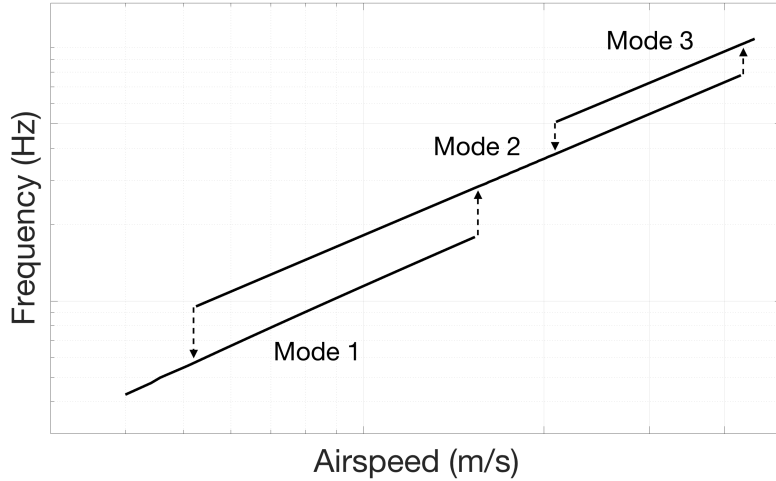


Figure 4.29: Example of ideal mode changes, including hysteresis, as airspeed u varies with fixed h

$$f_\lambda = \frac{\delta/2}{h} 4\pi(\lambda - 0.375)^{\frac{3}{2}} \frac{u}{\delta\pi} \quad (4.78)$$

In [74] a linear analysis was also conducted into the edge tone interactions. This presented the boundaries between the jet and surrounding air as vortex sheets - a plane of vortices. [74] defined Eqn. 4.79 for predicting the edge tone frequency.

$$f_\lambda \approx 0.92 \left(\frac{\delta}{h} \right)^{0.5} (\lambda + 0.54)^{\frac{3}{2}} \frac{u}{h} \quad (4.79)$$

A study by [146, 147] examined the edge tone frequency's dependence on the Reynolds number and the ratio of nozzle exit-to-wedge distance with the width of the nozzle exit. An equation was defined to predict the edge tone frequency and is given in Eqn 4.80.

$$f_\lambda = \left(C_1 - \frac{C_2}{R_{e\delta}} \right) \left(\frac{1}{h/\delta} - C_3 \right) \frac{u}{\delta} \quad (4.80)$$

The values of C_1 , C_2 and C_3 are given in Table 4.7. It should be noted that this was the only study found in the literature that provided different coefficients for the different jet profiles as well as giving coefficients for mode 1 when occurring along with other modes. [147] also found that the mode 1 frequency reduced when co-existing with other modes, similar to the findings of [22].

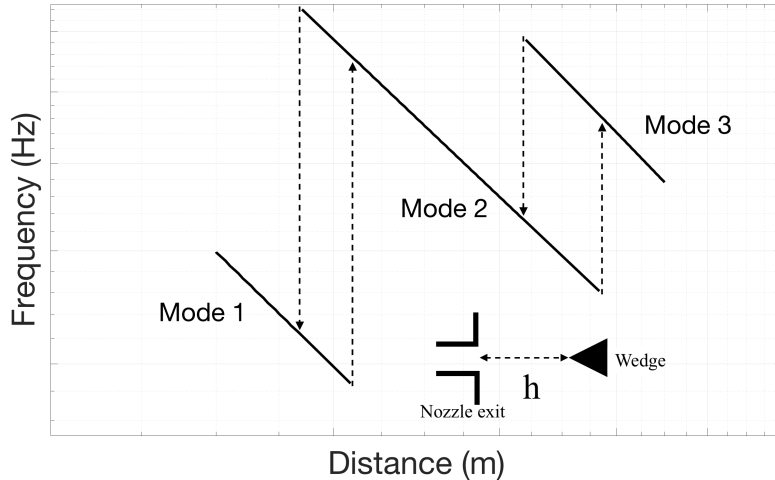


Figure 4.30: Example of ideal mode changes, including hysteresis, as distance h varies with fixed u

Table 4.7: Values for coefficients of edge tone frequency prediction Eqn 4.80

| Profile | Mode λ | C_1 | C_2 | C_3 |
|-----------|----------------------------------|--------|--------|-----------|
| Top Hat | 1 | 0.4837 | 12.31 | 0.005461 |
| | 1 (concurrent with modes 2 or 3) | 0.4167 | 0.2292 | 0.01426 |
| | 2 | 1.066 | 27.11 | 0.004157 |
| | 3 | 1.884 | 19.96 | 0.001261 |
| Parabolic | 1 | 0.5230 | 11.08 | 0.004836 |
| | 1 (concurrent with modes 2 or 3) | 0.5029 | 6.6451 | 0.01417 |
| | 2 | 1.177 | 37.15 | -0.002273 |
| | 3 | 1.972 | 6.954 | 0.007792 |
| | 4 | 2.365 | -55.21 | -0.000999 |

A further point from [146] was that, through 3-dimensional simulations and experiments, the edge tone was found to be a 2-dimensional phenomenon and hence the breadth of the nozzle was not considered.

For Eqns. 4.76 to 4.80 the mode of operation has to be implicitly stated. It is not possible to predict which mode the system is operating in. From these equations alone it is not possible to replicate the hysteresis effects.

Acoustic Intensity

Equation 4.81 was defined in [114] for the far field sound pressure P_λ generated by an edge tone:

$$|P_\lambda| \simeq \frac{\alpha}{2} \left(\frac{\rho_{air} S_{t_\lambda} u^3}{rc} \right) \cos \theta \quad (4.81)$$

where α is a constant assigned the value 4 to fit with observations and ρ_{air} is the mass density of air. The angle θ is the elevation angle from a vector normal to the air flow, from the tip of the wedge (Fig. 4.26). The Strouhal number, S_{t_λ} for this equation relates to the specific mode frequency given by Eqn. 4.82. The dimension in this case is the nozzle width δ .

$$S_{t_\lambda} = \frac{f_\lambda \delta}{u} \quad (4.82)$$

A relationship between sound pressure and acoustic intensity I was given in [64] as:

$$I = \frac{P_\lambda^2}{\rho_{air} c} \quad (4.83)$$

Using this relationship it was possible to define an acoustic intensity for the edge tone as shown in Eqn. 4.84. This gives a dipole propagation pattern as expected.

$$I_\lambda \simeq \frac{4\rho_{air} S_{t_\lambda}^2 u^6 (\cos \theta)^2}{r^2 c^3} \quad (4.84)$$

Tone Bandwidth

Similar to research carried out for the other fundamental compact sound source models, then tone bandwidth is an important feature to capture. A literature review did not find any published data in relation to the edge tone bandwidth. As stated in Section 4.3.4 on the cavity tone, it is known that the bandwidth is small for laminar flow and wider for more turbulent flow due to the more diffused and small-scale vortices generated.

4.4.4 Implementation of the Edge Tone Compact Sound Source

As with the previous compact sound source models, the edge tone model was implemented in Pure Data. The airspeed u was sampled at audio rate giving $u[n]$ were $[n]$ is the discrete time variable. For the frequency calculations this gives $R_e[n], S_t[n]$ as well as the acoustic intensity for all modes, λ , all calculated at audio rate.

Frequency Calculations

In Section 4.4.3, a number of equations have been defined to predict the frequency of the edge tone depending on which mode the system was in. A number of results were published in [22, 115, 45, 10] which had a mixture of wind tunnel measurements at CFD simulations. The jet profiles for these results were either parabolic or no profile was stated.

A total of 851 results were collated from publications [22, 115, 45, 10] which were referred to as data points. Each point had corresponding values for airspeed, nozzle exit width, nozzle exit-to-wedge distance and mode number.

To illustrate the difference between each of the prediction equations the absolute error was measured between the predicted result and the published results. The equation to calculate absolute error is shown in Eqn. 4.85.

$$\text{Absolute error} = \frac{|(f_{\text{predicted}} - f_{\text{published}})|}{f_{\text{published}}} \cdot 100 \quad (4.85)$$

For each of the published data points the values for airspeed, nozzle exit width, nozzle exit-to-wedge distance and mode number were used to predict the edge tone frequency. This predicted frequency was then used to obtain the absolute error for each data point for each equation. Table 4.8 shows the average absolute error over the 851 data points for each equation.

Table 4.8: Comparison of equations for predicting edge tone frequency

| Equation | Absolute error (%) |
|--------------------|--------------------|
| [22] | 11.51 |
| [72] | 47.23 |
| [37] | 255.31 |
| [74] | 58.85 |
| [147] | 22.56 |
| Best fit; Eqn 4.87 | 8.88 |

It can be seen from Table 4.8 that the equation published by Brown [22] gives the best results followed by Vaik [147]. The equation from Crighton [37] gives a massive error when compared to published results. It was accepted that the results were higher than previously published equation but the reason for the large error here is unknown.

Using the data points and variables available, it was decided to use an iterative technique in Matlab to find the best fit equation of a surface to predict the frequency. The parameters used

in [147] of Reynolds number with respect to the nozzle exit width $R_{e\delta}$ and the ratio of nozzle exit-to-wedge distance with the nozzle exit width h/δ , gave an accurate and relevant representation of operating conditions for which the frequency of the edge tone was being predicted. In this prediction model these values were used as the two independent variables and the value of Strouhal Number was used as the dependant variable.

The equation of a surface in a 3-dimensional space is given by Eqn. 4.86.

$$z = C_1 + C_2x + C_3y + C_4x^2 + C_5xy + C_6y^2 \quad (4.86)$$

Substituting in variables for the edge tone to calculate the Strouhal number is given by Eqn. 4.87.

$$S_{t\lambda} = C_1 + C_2R_{e\delta} + C_3\left(\frac{h}{\delta}\right) + C_4R_{e\delta}^2 + C_5R_{e\delta}\left(\frac{h}{\delta}\right) + C_6\left(\frac{h}{\delta}\right)^2 \quad (4.87)$$

To find the best fitting surface for the 3-dimensional space of Strouhal number, Reynolds number and ratio of nozzle width to nozzle-to-wedge distance, a least square cost function was employed. Random weighted vectors were chosen and values with the lowest error from over 200000 iterations were chosen for the coefficients of the new equation. Values for the coefficients C1, C2, C3, C4 & C5 are given for each mode in Table 4.9.

Table 4.9: Coefficient values for edge tone frequency prediction Eqn. 4.87

| Mode | C ₁ | C ₂ | C ₃ | C ₄ | C ₅ | C ₆ |
|------|--------------------------|---------------------------|--------------------------|--------------------------|-------------------------|--------------------------|
| 1 | 119.38 x10 ⁻³ | 32.14 x10 ⁻⁶ | -12.88 x10 ⁻³ | 6.09 x10 ⁻⁹ | -3.83 x10 ⁻⁶ | 436.76 x10 ⁻⁶ |
| 2 | 180.98 x10 ⁻³ | 103.82 x10 ⁻⁶ | -11.10 x10 ⁻³ | -9.41 x10 ⁻⁹ | -8.54 x10 ⁻⁶ | 199.89 x10 ⁻⁶ |
| 3 | 187.38 x10 ⁻³ | 129.94 x10 ⁻⁶ | -7.08 x10 ⁻³ | -13.29 x10 ⁻⁹ | -7.47 x10 ⁻⁶ | 86.48 x10 ⁻⁶ |
| 4 | 187.62 x10 ⁻³ | 181.78 x10 ⁻⁶ | -5.09 x10 ⁻³ | -21.33 x10 ⁻⁹ | -8.20 x10 ⁻⁶ | 47.24 x10 ⁻⁶ |
| 5 | 1.00 | -129.43 x10 ⁻⁶ | -76.38 x10 ⁻³ | 6.84 x10 ⁻⁹ | 7.58 x10 ⁻⁶ | 1.63 x10 ⁻³ |

The absolute error for this prediction equation compared to the 851 published data points was calculated in the same manner as previously. For Eqn. 4.85 the error was found to be 8.88%, as shown in Table 4.8. This was lower than all other previous prediction equations. A comparison to the answer using Matlab's *polyfitn* was carried out. This total error for the equations based on the coefficients generated from this function was 9.65%, slightly greater than the one found by using large number iterations of random weighted vectors to solve a least squares problem.

The value of 1 for the first coefficient of Mode 5 does appear curious but it should be noted that this has been rounded from a value of 1.00212589342061. Using Matlab's *polyfitn* function this

values was found to be 1.152.

The best fit equation, Eqn. 4.87, was used in the implementation of the model for parabolic jet profiles. As mentioned, no data was forthcoming that specifically stated it was from a top hat jet profile. The equation given by [147] does cover jets with this profile and was used under these circumstances giving the user the opportunity to select which jet profile they would prefer.

Missing from all frequency prediction theories was a method for predicting the mode of operation. It was decided to look at the large number of data points accumulated when evaluating the frequency prediction equation to see if mode prediction could be made. It was noted that the data given in [115] also published a number of plots illustrating the mode changes with associated hysteresis. These were given for both increasing and decreasing airspeed and increasing and decreasing nozzle-to-wedge distance.

It was noted in Section 4.3.4 that for the cavity tone, the peak mode depended on the thickness of the shear layer and airspeed. Since the edge tone is generated by a similar aeroacoustic feedback loop it was decided to calculate a similar value for each of the data points. For laminar flow the shear layer thickness ξ is given in [28] as:

$$\xi = h^{2/3} \quad (4.88)$$

For turbulent flow it was given as:

$$\xi = 0.115h \quad (4.89)$$

At the nozzle exit-to-wedge distance, the total thickness of the jet flow, Υ including upper and lower shear layers was given in Eqn. 4.90.

$$\Upsilon = 2\xi + \delta \quad (4.90)$$

For each of the 851 data points the mode number was available from the publications. Since the data published in [115] included information on increasing or decreasing of the airspeed or nozzle exit-to-wedge distance, it was possible to label each data point depending on this information.

To illustrate this, Fig. 4.31 shows a red point in mode 2 at an airspeed of approximately 14m/s. It was hypothesised, that for this point, it was achieved as the airspeed increased through 14m/s, decreased through 14m/s or was static at 14m/s. Each data point was labelled based on the unique conditions it is possible to be reached. If the red point was in one arm of a hysteresis

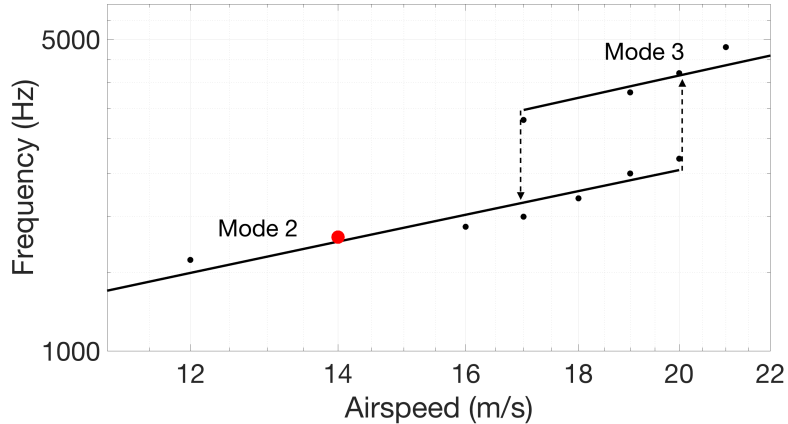


Figure 4.31: Example of multiple labels for a single point, as airspeed u varies with fixed h

loop the it would only be achieved by the condition defined by the hysteresis loop, i.e. decreasing airspeed.

Each data point could be classified by its Reynolds number, jet thickness Υ , airspeed direction, nozzle exit-to-wedge distance direction and the corresponding mode number. If a point, similar to the red point in Fig. 4.31 could be achieved under different conditions then it was treated as a separate data point for each of these conditions. The red point in Fig. 4.31 became three different data points as shown in Table 4.10. This increased the data points from 851 to 1589.

Table 4.10: Example labels for red point given in Figure 4.31

| Reynolds Number Re_h | Jet Thickness Υ (m) | Distance Direction | Airspeed Direction | Mode |
|------------------------|------------------------------|--------------------|--------------------|------|
| 7106.35 | 0.004546893 | Static | Up | 2 |
| 7106.35 | 0.004546893 | Static | Down | 2 |
| 7106.35 | 0.004546893 | Static | Static | 2 |

With 1589 data points it was logical to research the possibility of a machine learning algorithm to predict the mode of operation. The data points were input to the Weka machine learning workbench [73] and a number of algorithms explored.

The most successful prediction model came from a decision tree. This was evaluated using 10 cross fold validation and found to predict the correct mode of operation of the edge tone 82.69% of the time. This was based on feeding into the decision tree the Reynolds number, jet thickness, airspeed direction and nozzle exit-to-wedge distance direction. A confusion matrix, highlighting where the correct predictions are made, and which modes are selected in error is shown in Table 4.11.

Table 4.11: Confusion matrix of the decision tree implemented to select current edge tone mode

| | | Classified as | | | | |
|------|---|---------------|-----|-----|----|----|
| | | 1 | 2 | 3 | 4 | 5 |
| Mode | 1 | 531 | 60 | 2 | 1 | 0 |
| | 2 | 64 | 400 | 49 | 1 | 0 |
| | 3 | 0 | 45 | 287 | 20 | 0 |
| | 4 | 1 | 0 | 24 | 61 | 4 |
| | 5 | 0 | 0 | 1 | 3 | 35 |

The last problem in relation to the frequency prediction was being able to predict if mode 1 edge tones would be heard in conjunction with other modes. Conditions on which this would occur were published in [147]. These conditions are shown in Table 4.12 for only one value of the ratio of nozzle exit-to-wedge distance over the nozzle exit width.

Table 4.12: Mode selection for different Reynolds values. $h : \delta = 10 : 1$; $R_{e\delta}$ = Reynolds number with respect to nozzle width.

| $R_{e\delta}$ | Airspeed direction | Mode |
|----------------------------|--------------------|-------|
| 0 - 85 | up | 0 |
| 85 | | 1 |
| 180 | | 1 & 2 |
| 180 - (360-420) | | 2 |
| (360-420) - (550 - 750) | | 1 & 3 |
| (550 - 750) - (650 - 1000) | | 3 |
| 0 - 85 | down | 0 |
| 85 | | 1 |
| 180 - 400 | | 1& 2 |
| 400 - 900 | | 1 & 3 |
| 900 - 1200 | | 3 |

These conditions were input to the Weka machine learning workbench and a second decision tree generated. The tree predicted whether mode 1 co-existed with other modes. 10-fold cross validation was carried out and based on the information published in [147], predicted if the co-existing mode 1 was present 94.49% of the time correctly.

Edge Tone Bandwidth

With no information forthcoming from the literature in relation to the edge tone bandwidth it was decided worthwhile drawing from its similarities to the cavity tone. This has some justification as the sound generating process of a aeroacoustic loop is similar in both instances. The bandwidth calculation for the cavity tone was based on values obtained from plots given in published data. The equation used to predict the cavity tone bandwidth is given again in Eqn. 4.91.

$$Q_h = 87.715 - 5.296 \log R_{e_h} \quad (4.91)$$

The transition from laminar to turbulent flow was given in [129] to occur at a value of Reynolds number $R_{e_h} = 25000$. Applying this to Eqn. 4.91 gives a value for Q as approximately 34.

For the edge tone, it was also important to consider the Reynolds number with respect to the nozzle exit width. In [141] a value of R_{e_δ} of 3000 was considered laminar for the edge tone. A value of $R_{e_\delta} = 6000$ was considered turbulent in [144]. The highest R_{e_δ} value obtained in the study by [115] was 4000.

An estimated value of $R_{e_\delta} = 5000$ was labelled as the critical values between laminar and turbulent in our model. This was assigned the Q value of 34 to match that obtained when examining R_{e_h} . When $R_{e_\delta} = 50$ it was labelled fully laminar and assigned a Q value of 90.

An equation similar to Eqn. 4.91 was derived to estimate the Q value based on the value of R_{e_δ} . This is shown in Eqn. 4.92.

$$Q_\delta = 137.571 - 12.1602 \log(R_{e_\delta}) \quad (4.92)$$

To allow for both the Reynolds number due to the nozzle exit-to-wedge and the Reynolds number due to the nozzle exit width, the implemented Q value was found by averaging the two.

$$Q = (Q_h + Q_\delta)/2 \quad (4.93)$$

Acoustic Intensity

A discrete implementation of Eqn. 4.84 was used to calculate the acoustic intensity of the edge tone dipole compact sound source.

Final Output

As in the previous compact sound sources, a single pseudo-randomly generated white noise source was used for an individual source. The parameters of operation for a single edge tone compact sound source are the airspeed, nozzle exit width and nozzle exit-to-wedge distance. Any change increase or decrease in airspeed or nozzle exit-to-wedge distance can also be detected.

The accumulated data was fed into the decision tree which predicts the mode of operation for the model. Once this has been identified and the jet profile was set to parabolic, the correct coefficient values for Eqn. 4.87 were chosen from Table 4.9. If mode 1 was coexisting the coefficients from Table 4.7 were applied to Eqn. 4.80 and the frequency of the co-existing mode 1 frequency obtained. If the jet profile was top hat, the coefficient values from Table 4.7 for the correct mode were selected and applied to Eqn. 4.80.

Bandpass filters for each mode were implemented but only active if that mode or co-existing mode were active. The predicted frequency values are used as the centre frequency for the bandpass filter with the transfer function:

$$H_{bp}[z] = \frac{\beta_1 + \beta_2 z^{-1} + \beta_3 z^{-2}}{1 + \alpha_1 z^{-1} + \alpha_2 z^{-2} + \alpha_3 z^{-3} + \alpha_4 z^{-4}}$$

where the coefficient values are calculated from equations given in the Appendix. Noise shaping was employed to generate the edge tone dipole compact sound source, where white noise, $W[z]$ is filtered by $H_{bp}[z]$:

$$X_\lambda[z] = W[z]H_{bp}[z] \quad (4.94)$$

where the discrete time output $x_\lambda[n]$ is given by the inverse z-transform of $X_\lambda[z]$.

The final output is given by Eqn. 4.95 as:

$$y[n] = \begin{cases} \Lambda(x_1[n]^{\ddagger} + x_\lambda[n]), & \text{co-existing modes = true} \\ \Lambda x_\lambda[n], & \text{otherwise} \end{cases} \quad (4.95)$$

where Λ is a user defined variable allowing the gain to be adjusted for artistic purposes. The \ddagger symbol indicates that that mode was co-existing and implemented using coefficients from Table 4.7 and Eqn. 4.80 from [147].

Research carried out in [22] indicated that the tone would only be produced if the ratio of nozzle

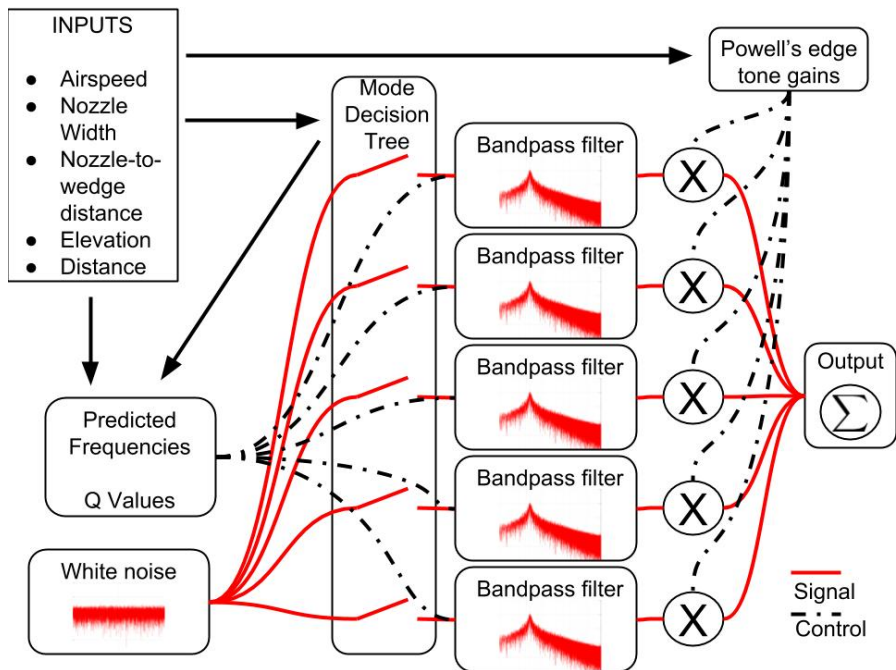


Figure 4.32: Flow diagram showing edge tone synthesis process

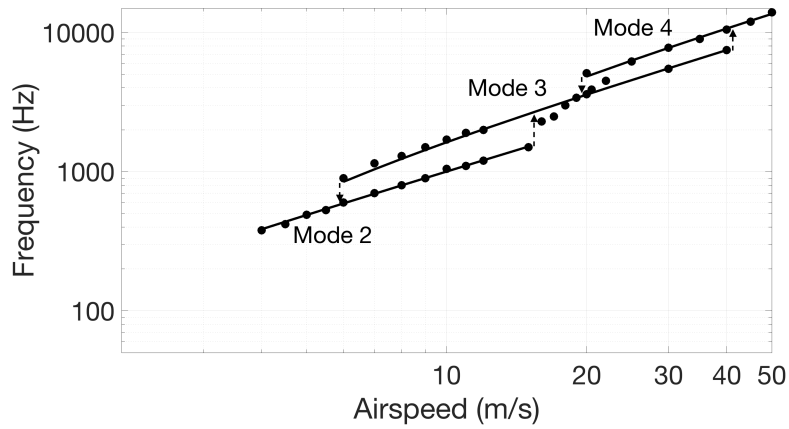
exit-to-wedge distance over nozzle exit width lies between 3.5 and 60. The original 851 results were examined and found the ratio ranges from 2 and 60.6. Limits of operation were placed on the model based on the nozzle exit-to-wedge distance over nozzle exit width being between 2 and 61.

A flow diagram of the edge tone synthesis process is shown in Fig. 4.32. A single white noise source was used for each of the modes represented in the compact sound source model.

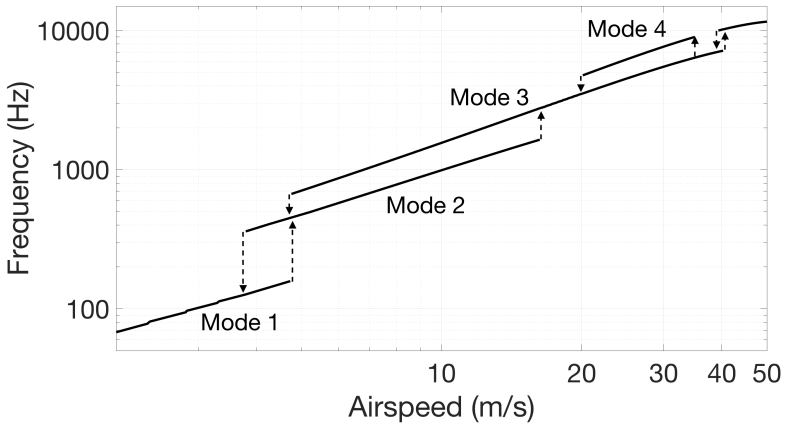
4.4.5 Evaluation of Edge Tone Model

An evaluation of the frequency prediction capabilities of our model to the published results from [115] was carried out, similar to evaluation of the Aeolian tone and the cavity tone. The output, including mode and hysteresis prediction, from our synthesis model were compared. It should be noted that a co-existing mode 1 was not considered in [115] and has been omitted from the results to enable a clearer comparison.

Figure 4.33a shows results from [115] where the airspeed was increased and decreased while all other factors remained constant. The same results under identical circumstances from the compact source model are shown in Fig. 4.33b.



(a) Points from Powell [115] - read from plot, with best fit lines



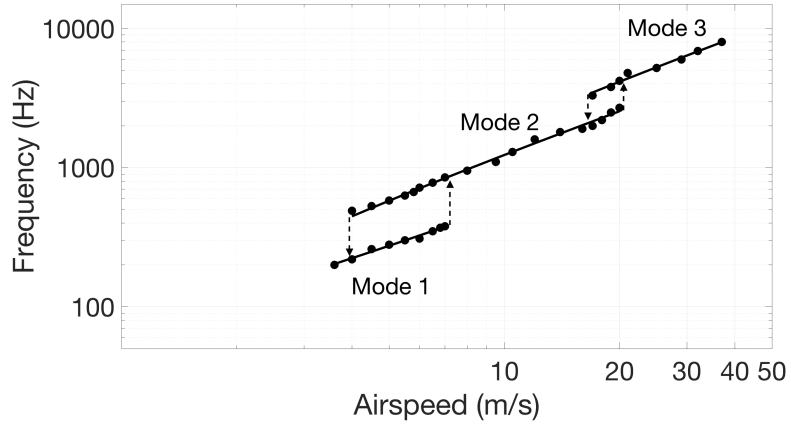
(b) Real-time physically derived model output

Figure 4.33: Mode changes, including hysteresis, in edge tone when varying airspeed u . Nozzle exit width, $\delta = 0.00104\text{m}$; Nozzle exit-to-wedge distance, $h = 0.01\text{m}$.

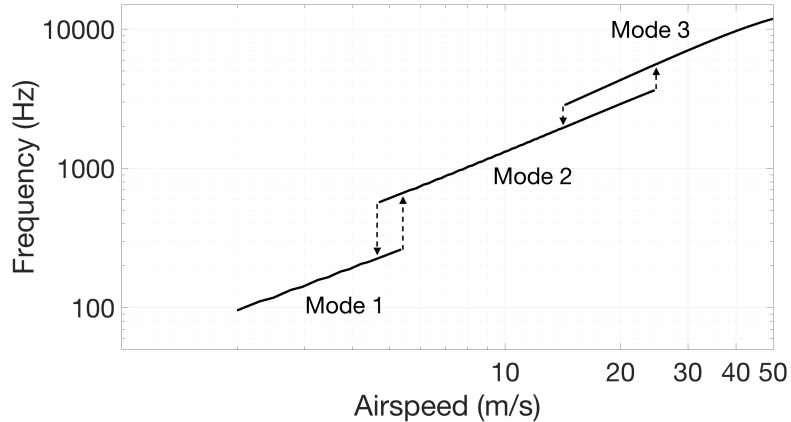
It is acknowledged that the data from [115] was read from plots and hence minor human error may add some noise. Overall it can be seen that the predicted frequency output from the synthesis model gives excellent results compared to wind tunnel results under these particular conditions.

The mode changes in Fig. 4.33a from mode 2 to 3 then to 4 and back can clearly be seen in the synthesis model output in Fig. 4.33b. The hysteresis changes in the model occurred at approximately similar frequencies to those published. An anomaly can be seen in the synthesis model whilst in mode 4 with decreasing airspeed. The prediction model dropped the mode number down to 3 before rising up to 4 again. It was assumed that this error was in relation to the decision tree which had an accuracy of 82.69%.

A second difference seen in the synthesis model was while in mode 2 and the airspeed decreases below 4m/s. The synthesis model predicted a drop down to mode 1 under these circumstances.



(a) Points from Powell [115] - read from plot, with best fit lines



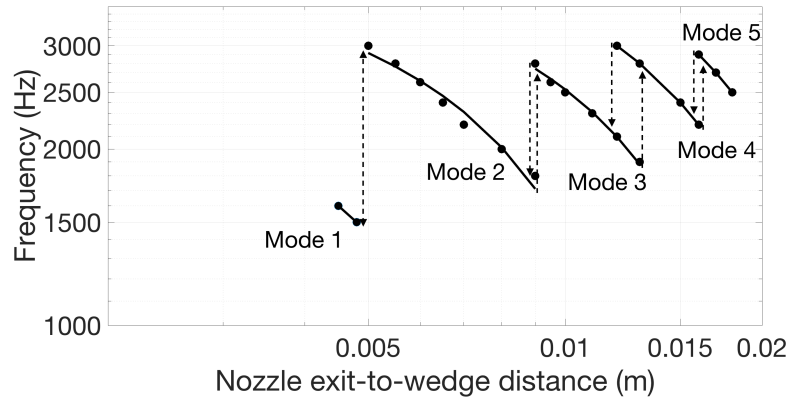
(b) Real-time physically derived model output

Figure 4.34: Mode changes, including hysteresis, in edge tone when varying airspeed u . Nozzle exit width, $\delta = 0.00099\text{m}$; Nozzle exit-to-wedge distance, $h = 0.0075\text{m}$.

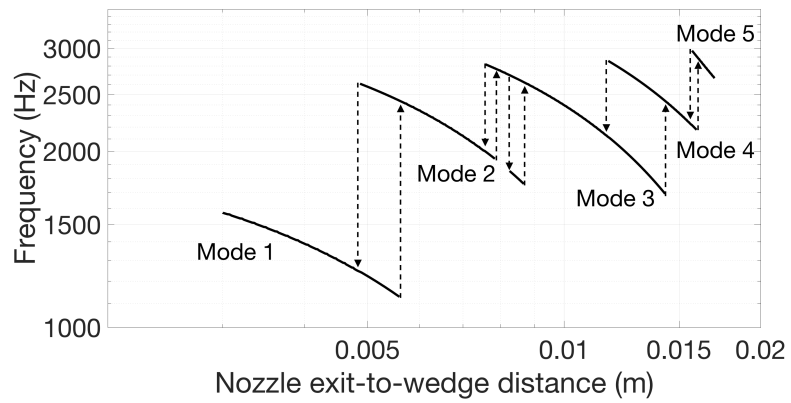
The published data does not incorporate this information, but it is highly plausible that this may occur.

A second comparison where the airspeed was varied is shown in Figs. 4.34a and 4.34b. Although as not as similar to the results shown in Figs 4.33a and 4.33b, the general output from the synthesis model was very good. The main difference on visual inspection was the size of the hysteresis loop from modes 1 to 2. The synthesis model predicted this range of airspeed to be quite narrow while the wind tunnel experiments show it to be wider. The exact opposite was shown in regard to the hysteresis loop relating to the changes from modes 2 to 3.

The output from the synthesis model when predicting edge tone frequency as the nozzle exit-to-wedge distance was varied was also examined. Figure 4.35a shows the wind tunnel results from [115] with fixed nozzle exit width and airspeed. The results from the synthesis model under



(a) Points from Powell [115] - read from plot, with best fit lines



(b) Real-time physically derived model output

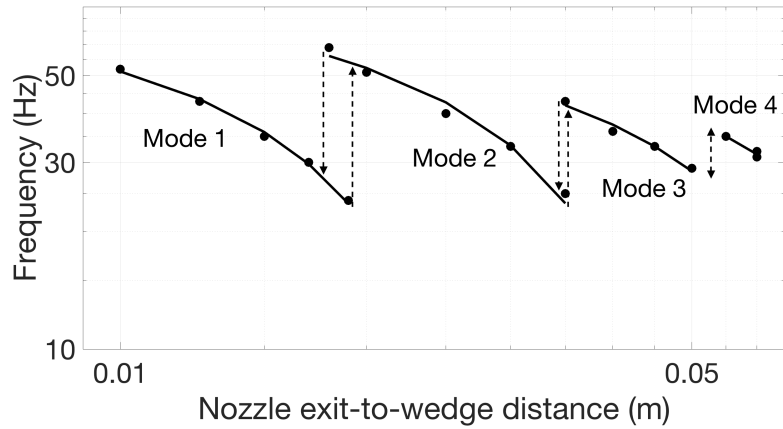
Figure 4.35: Mode changes, including hysteresis, in edge tone when varying nozzle exit-to-wedge distance h . Nozzle exit width, $\delta = 0.00106\text{m}$; Airspeed, $u = 14.48\text{m/s}$.

identical circumstance is shown in Fig. 4.35b.

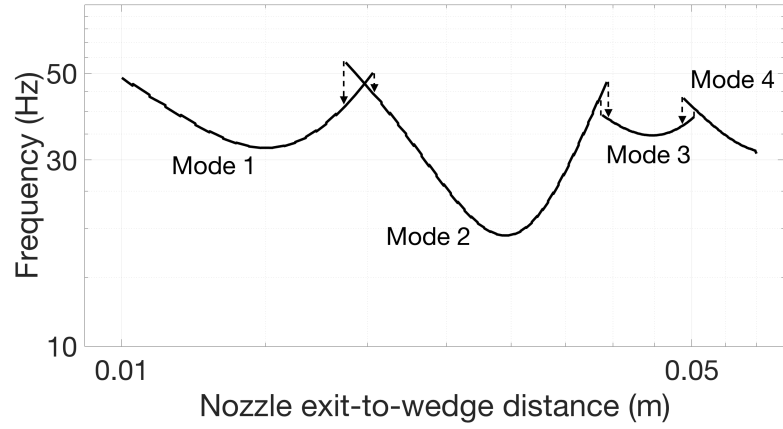
The mode changes and hysteresis for each change can clearly be seen for each model. The hysteresis loops for the synthesis model appear wider than those from the wind tunnel results. An error in mode prediction can be seen in Fig. 4.35b while in mode 2 and when the nozzle exit-to-wedge distance was increased. The prediction model jumped up to mode 3 before returning to mode 2.

The distances for the mode changes, although a wider loop was seen in the synthesis model, occur at approximately the same nozzle exit-to-wedge distance. The predicted frequencies were approximately the same too.

A similar comparison where the nozzle exit-to-wedge distance was varied is shown in Fig. 4.36. On this occasion the airspeed was very low at only 1.45 m/s and the discrepancy between the



(a) Points from Powell [115] - read from plot, with best fit lines



(b) Real-time physically derived model output

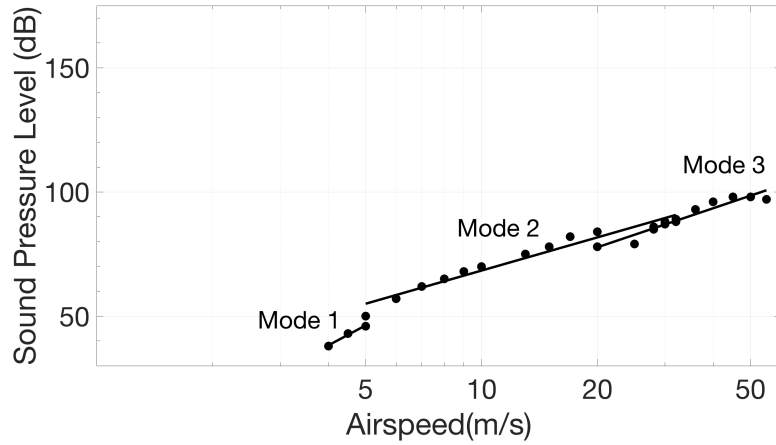
Figure 4.36: Mode changes, including hysteresis, in edge tone when varying nozzle exit-to-wedge distance h . Nozzle exit width, $\delta = 0.00099\text{m}$; Airspeed, $u = 1.45\text{m/s}$.

wind tunnel results and the synthesis model output was far greater.

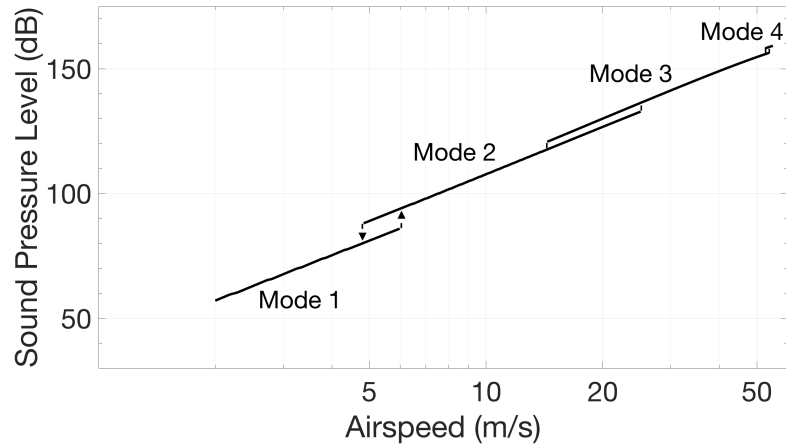
Inspection of Fig. 4.36b, it is seen that the predicted frequency values were not uniform in the synthesis model and instead quadratic in shape. It was hypothesised that this was due to the shape of the best fit plane used to define Eqn. 4.87. Although the frequency values at the beginning of a mode were approximately correct and they decreased as the nozzle exit-to-wedge distance increased, they should not increase as the nozzle exit-to-wedge distance increases.

A final comparison to published data for the Sound Pressure Level (SPL) given in [115] and the output from the synthesis model was undertaken. The variable gain was set to 1 so that it had no influence. The wind tunnel measurements and synthesis model replication are shown in Fig. 4.37.

It can be seen that the SPL increased faster in the synthesis model than those from the measured



(a) Points from Powell [115] - read from plot, with best fit lines



(b) Real-time physically derived model output

Figure 4.37: Sound pressure level with increasing airspeed u . Nozzle height $\delta = 0.000104\text{m}$; nozzle to wedge distance $h = 0.0075\text{m}$; distance $r = 0.2\text{m}$; elevation $\theta = 0^\circ$; user gain $\Lambda = 1$.

results. The reason for this is unknown. The mode changes occur at approximately the same airspeed for both measured and synthesis model, but the synthesis model moved into mode 4 right as the airspeed passes 50 m/s. This was not seen in the wind tunnel results, but it is possible this might have been if the airspeed had been increased more than it was in the experiments.

4.4.6 Discussion

An analysis of the results presented in the previous section indicates that the synthesis model performed very well in comparison to previously published results. The greatest errors seen in the synthesis model were found when operating at low airspeed. This was at the lower limit of the data at which the prediction model was generated. The average airspeed used to obtain the

data which generated the prediction model was 12.76 m/s. When operating around the centre of these data points the model was less prone to error. When operating at 4 m/s as shown in Fig. 4.33b, the model had excellent results.

The general performance of predicting mode changes and the hysteresis loops were found to be very good. It is appreciated that musical instrument models are able to predict hysteresis in the resonant tones, the hysteresis predicted in this model applies solely to the edge tone. To the best of knowledge, this is the first prediction model to obtain the operating mode of the edge tone which can assist greatly with the frequency prediction equations.

The values given in Table 4.8 for the absolute error highlights the difficulty in predicting the frequency of the edge tone. From [147] it was seen that the profile of the jet as it exits the nozzle has an influence over the predicted frequency. Equation 4.80 defined by [147] was the only one found to take this into consideration and this is an area for future research.

Compared to the previous models of the cavity tone and Aeolian tone, design of this model's frequency prediction equation was defined by the author. This was due to the high errors found when comparing the theoretical results to the experimental ones. Definitions for the prediction frequency (Eqn. 4.87) and the prediction model for the current operating mode numbers were completely based on results from experimental data rather than theoretically derived. This is a similar approach to [147] where the parameters used for a best fit equation are identical to the one presented here, Eqn. 4.87.

Future development would be to examine the upper and lower limits of operation of the model with respect to airspeed and nozzle exit-to-wedge distance. Further experimental and simulation values around these operating conditions could be fed into the prediction model to make it more robust in these areas.

Our best fit equation, Eqn. 4.87 was based on parabolic or unknown jet profiles. If this could have been separated into jet profiles a more accurate prediction may have been possible. It was also noted that the equations presented in [22, 72, 37] were limited to modes 1 - 4, 1 - 3, and 1 - 4 respectively. Our prediction equation was able to predict up to mode 5, increasing the range of frequencies it was able to predict compared to previous equations.

Further errors in the prediction equation were found during general operation. Under certain circumstances the best fit equation predicted negative frequency values. This corroborates the results shown in Fig. 4.36b when the frequencies are low the prediction model made the greatest errors. A threshold of 0 Hz was imposed during implementation.

Further tests should be carried out using the solution provided by Matlab's *polyfitn* function. This did not produce any negative results like the best fit equation described here. No tests have been carried out on this function at low airspeed and it might produce more accurate results

under these circumstances. It should be noted that the value of 1 for the first coefficient of Mode 5 for the best fit equation (Table 4.9) was found to have the value of 1.152 using the Matlab function. The remaining coefficients were of similar magnitude.

Although the best fit equation produced the lowest error compared to the other equations, this was only applicable with a parabolic jet profile. When a user selects a top hat profile the synthesis model would implement Eqn. 4.80 from [147]. There was no data to compare this jet profile to and allow a more rigorous evaluation. This was the same for the prediction model for a co-existing mode 1. Although other publications mentioned the phenomena, the actual frequencies were not published.

Figure 4.37 showed that the SPL output from our model increases faster than that measured. This could be due to the value of α chosen in [114]. It should also be noted that [114] identifies that Eqn. 4.81 gives the pressure as *approximately equal to*, indicating it is not an exact equality.

Ideal evaluation of the edge tone compact sound source synthesis model would include more wind tunnel experiments. Under these circumstances the number of models and properties of airspeed and nozzle exit-to-wedge distance could be controlled. Any further experiments would include a systematic recording of the bandwidth to peak frequency relationship. This would enable a more accurate approximation of the Q value used in the bandpass filters.

It is also believed it would be of value to measure and compare the output of the synthesis model to far more extreme conditions, including higher airspeeds and Reynolds numbers past critical and in more turbulent regimes. This would give us a wider range of data points to train equations and decision trees, giving a model that is more accurate.

Additional future developments would include coupling the edge tone synthesis model to a resonator model. The model could be used as an excitation for a synthesis model to replicate flue instruments, like that similar to [148]. The use of the edge tone synthesis model could be compared to the use of the white noise source in the original research. It is known that the transient component of a musical note has a strong influence over timbre and this could have particular perceptual consequences.

4.4.7 Concluding Comments on Edge Tone Model

A number of frequency prediction equations were examined, and absolute errors noted. These appeared to be high and a best fit equation was defined to examine if this error could be reduced. It was then vital to predict the current mode of operation of the edge tone system in order to be able to use any of the prediction equations. No previous attempt at mode prediction was found in the literature and a machine learning approach was undertaken.

When comparing the frequency predictions, mode changes and hysteresis, to wind tunnel measured data, excellent results were observed. Errors in both mode prediction and frequency prediction have been highlighted, along with areas for future development. A demo model of the edge tone compact source can be downloaded at <https://code.soundsoftware.ac.uk/projects/edgetone>.

4.5 Summary

This chapter has described how synthesis models of compact sound sources representing fundamental aeroacoustic tones can be developed. Using semi-empirical equations which have been defined or derived within the field of fluid dynamics the models have intrinsic knowledge of the physics. It is acknowledged that any semi-empirical model defined by semi-empirical equations are subject to the same limits of these equations.

Often the equations used are based on experimental results rather than theory, the definition by Strouhal in Eqn. 4.1 being an example of this which is still highly relevant today. When research of the aeroacoustic literature failed to yield an equation to predict a property required by the synthesis process, previously published results are used to define an equation that captures this behaviour. The calculation of the tone bandwidths which depend on the Reynolds number for all tones is an example of this.

The use of machine learning techniques for prediction of the edge tone mode is a unique approach to solve this problem. Reviewing literature revealed, to the best of the author's knowledge, that a technique for predicting the edge tone mode number has not been established previously.

With synthesis models of compact sound sources established, the use of these to produce real-time sound effects is demonstrated in the next section. This requires developing additional models to capture the geometry of the objects and their behaviour. It is shown that the compact sound sources can be used in conjunction with other sound generating mechanisms to produce highly novel sound effects.

Chapter 5

Aeroacoustic Sound Effects

5.1 Introduction

Having created synthesis models to replicate the compact sound sources of aeroacoustic sounds it is now shown how these can be used to produce real-time sound effects. In this section the compact sound source models are integral to each sound effect. Since the compact sound sources are defined from equations obtained from fluid dynamics they are able to produce sounds based on the relationships of physical properties.

The sound effect models offer a unique level of parameter control without requiring any offline computations or specialist hardware to perform any re-calculations. For each of the sound effects developed, the behaviour of the objects being modelled was important. The more accurate the behaviour of the item being modelled is captured the more accurate the resulting sound synthesis.

Evaluation for each sound effect developed was carried out and results presented, highlighting where the models perform well and where they do not. Explanation is given to attempt to explain any shortcomings of the models.

5.2 Swords and Swinging Objects

Nomenclature

r = distance between listener and sound source (m)

ϕ_1 = initial latitude (radians)

ϕ_2 = final latitude (radians)

λ_1 = initial longitude (radians)

λ_2 = final longitude (radians)

u = air flow speed (m/s)

d = diameter (m)

ANCH = Anchor

SMS = Spectral Modelling Synthesis model

PM = this model

Real = pre-recorded sample

5.2.1 Introduction

When a sword or a sports club is swung through the air it can make a very distinctive swoosh sound. The inclusion of this sound effect can make the visuals more believable and the experience more immersive. These sounds would be expected in a sword fighting sequence in a film or video game, possibly adding a sense of how fast a blade is travelling, leading to heightened sense of danger or excitement.

The sound of a sword swinging through the air or sports object like a golf club or baseball bat, are all produced in a similar manner. Being able to replicate a range of related sounds within a single synthesis model offers a user with a wide range of objects they can produce sounds for. A synthesis model replicating these sounds which can also be attached to objects in a game engine would allow for procedural audio sound effects, varying with each unique condition, and the relationship between source and listener.

Evaluation of the synthesis model was carried out via listening tests as well as a limited objective evaluation. Physical objects examined were a metal sword, wooden sword, golf clubs, baseball bat and a broom handle.

5.2.2 State of the Art

Four different sword models were evaluated in [19]. The research was more focussed on the perception and preference rather than physical accuracy. Users were able to interact with the sound effect models by use of a Wii Controller. The first model was based on white noise being shaped by a bandpass filter. The centre frequency of a bandpass filter varied with the speed of the Wii Controller. A second model extracted the dominant modes from a recording of a bamboo stick being swung through the air. A synthesis model varied the amplitude of the dominant modes with the speed of the Wii Controller being swung.

Acceleration of the Wii Controller was used as a trigger between two samples in a third model. The fourth model used granular synthesis adjusting the speed of playback through the grains proportionally to the speed the Wii Controller being swung.

A sword swoosh was included in research into environmental sounds in [94]. A signal-based approach was used in this instance with an analysis of a signal was carried out in the frequency domain as well as synthesis. This produced a narrow band coloured noise output.

A physical model approach with a number of similarities to the one presented here, was carried out by [43]. In this case offline sound textures were generated using CFD software. The sword body was split into a number of compact sound sources and a texture created for each. During playback the speed of playback for each compact sound source was varied in accordance to the speed of swing of the sword. The individual textures were then summed to give the final output.

Instead of an object moving through the air, similar sound effects have been created to model wind blowing around objects. [49] created Aeolian type sound effects for whistling wind due to a cable. In this model noise shaping with a bandpass filter was used, with the centre frequency set by a second model replicating the behaviour of wind. The bandpass filter had a set Q value and gain set to the airspeed squared. A similar approach was taken by [153] based on shaped noise. The different methods for each of these similar synthesised sound effects is shown in Table 5.1.

In [121] a sword was taken into a wind tunnel and experiments carried out. This found strong tones due to the Aeolian tone and its harmonics but also some cavity tones. It was suspected that the cavity tones were generated by the grooves in the swords profile.

5.2.3 Method

The main sound generated when an object swings through the air is due to vortex shedding which creates the Aeolian tone. Each swinging object was modelled as a discrete number of Aeolian tone compact sound sources as described in Section 4.2. Modelling an object as compact sound sources was proven to be valid by [38] and confirmed by [59].

Table 5.1: Table highlighting different synthesis methods for swing sounds

| Reference | Model | Synthesis method | Parameters | Comments |
|------------------|--------------|-------------------------------------|-------------------------------------------------------|---------------------------------------------------------------------|
| [94] | Sword | Frequency domain signal-based model | Amplitude control over analysis and synthesis filters | Operates in real-time |
| [19] | | Granular | Accelerometer speed | Mapped to playback speed |
| | | Sample-based | | Triggered by threshold speeds |
| | | Noise shaping | | Mapped to bandpass centre frequency |
| | | Physically inspired | | Mapped to amplitude of frequency modes |
| [43] | | Computational Fluid Dynamics | Length, diameter & swing speed | Real-time operation but requires initial offline computations |
| [49] | Wind | Noise shaping | Pre-set values for wind type | Real-time operation with Filter centre frequency & gain $\propto u$ |
| [153] | | | | |

The benefits of this model are that exact replicas of objects can be created if the geometry is known, acoustic properties are informed by the aeroacoustic equations within the compact sound source models and operation was in real-time.

5.2.4 Implementation

Each discrete Aeolian tone compact sound source synthesis model was implemented as described in Section 4.2. The audio output from each compact sound source was summed at the output of the swinging object model.

The concept behind the swinging model was similar to [43] where a number of compact sound sources were placed in a row along the length of the object. An issue that became apparent at the beginning of implementation was that the time averaging process as described in Section 4.2.4, was too long a time compared to a short swing time. This component of the compact sound source was bypassed, and the intensity value calculated instantaneously.

Ideally, the span-wise distance between sources would be set by the correlation length as described in Section 4.2.4. This could not be done due to the following reason. The correlation length is dependent on the Reynolds number which in turn is dependent on the diameter and airspeed. As an object is swung through the air its airspeed varies which in turn varies Reynolds number which means the correlation length is not static. Changing span wise position based on the correlation length can also change the object diameter requiring another re-calculation of the Reynolds number.

To avoid this, [43] set the correlation length to 3 and placed compact sound sources along the entire length of the object. To reduce the computational load, this model was limited to eight compact sound sources. Since two swinging object models were created, the positions of the compact sound source synthesis models are described with their relevant swinging object model.

The first swinging object model allowed the user to adjust the length of the sword as well as the diameter at the top (tip) and bottom (hilt). A linear interpolation was used to calculate the diameter of the object between these two points. The second model was based on a number of pre-set object measurements. Both the models let the user set the top speed of the object during its swing and the position of the observer.

It is possible to map the position, geometry and movement of each compact sound source into a game engine. The speed of each source can be calculated from the difference in position between frames at a known rate. Figure 5.1 shows a still from an example of this implementation. A reference is provided in the caption to the video link showing the game engine controlling the synthesis model in real-time.



Figure 5.1: Computer generated character with a sword. Motion and dimension parameters can be determined by the game engine. (<https://www.youtube.com/watch?v=zVvNthqKQIk>)

In the swinging object models presented, the centre point of swing was set at the centre of a coordinate system as shown in Fig. 5.2. An additional length was added of 0.35m representing the length of an elbow to hand, making the elbow the centre of a swing. The user was able to set the start and stop position of the swing based on azimuth and elevation, and with the elbow set at the centre, the points of a sword always travel on the circumference of a sphere.

Lines traced on spheres are known as Great Circles and their length can be calculated using the Haversine Formula [92]. This is given in Eqn. 5.1.

$$\text{arc length} = 2r \arcsin \left(\sqrt{\sin^2 \left(\frac{\phi_2 - \phi_1}{2} \right) + \cos(\phi_1) \cos(\phi_2) \sin^2 \left(\frac{\lambda_2 - \lambda_1}{2} \right)} \right) \quad (5.1)$$

where ϕ_1 and ϕ_2 are the latitude of the start and finish points and λ_1 and λ_2 are the longitude values. All values are given in radians. The radius r is the distance between the centre of the arc and the tip of the object. The point of maximum speed set as the halfway distance of the arc. The increase and decrease in speed was set to linear acceleration and deceleration for ease of calculation. It was also presumed that each swing starts and finishes at rest.

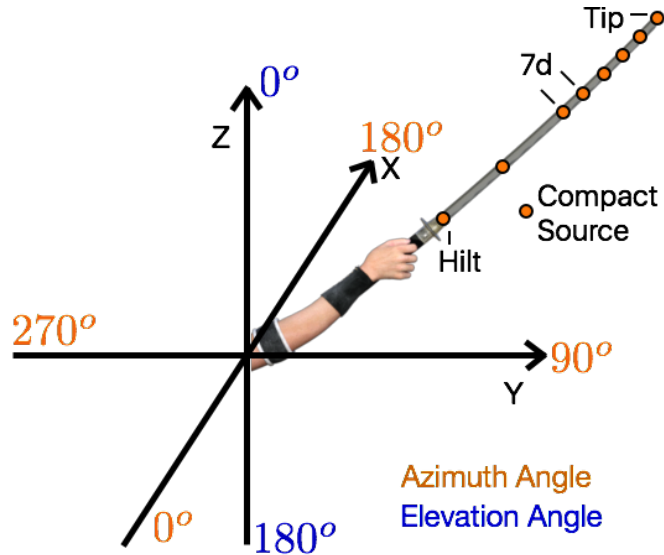


Figure 5.2: Position of 8 compact sources and coordinates used in sword model

To ensure the correct values for elevation and azimuth between source and listener for each compact sound source model, the arc of the sword was considered as a 2-dimensional plane through the 3-dimensional sphere. The 3-dimensional position of the observed was projected onto the plane by use of a projection matrix. By using the points of the source, observer, the observer position as projected onto the plane of the sword sweep, and the origin, the azimuth and elevation angles for each source could be calculated.

The observer's head position was set so that it was always facing the plane of the y-z axes, parallel to the x axis. Stereo panning and Doppler were then added to the sound effect. The addition of Doppler has been shown to increase perception, [101].

Variable Model

In this model the user had the ability to adjust the diameter of the object to be replicated. The user was able to set the thickness of the object at the tip and the thickness at the hilt. The user can also vary the length of the object. There were eight Aeolian tone compact sound source synthesis models used in this model, the position of each varied depending on user choices, within limits.

Figure 5.2 shows the positioning of the eight sources. Six of the eight were placed at the tip. This was done because it was hypothesised that the majority of sound would be produced there. The tip had the greatest speed when the swing was modelled in the manner it was here. Eqn. 4.17 in Section 4.2.4 states that the acoustic intensity is proportional to u^6 . This validates the belief

that the faster moving portion produces the greatest sound.

The remaining two sound sources were placed at the hilt and then halfway between the hilt and the first of the six sources at the tip. These were mainly to capture any details that might be missing from the others.

At the tip the positioning of the sources was equivalent to a correlation length of $7d$. The range of lengths given in [111] was $17d - 3d$ depending on the Reynolds number. As explained it was necessary to fix the position in this model. [43] used a correlation length of $3d$ but it was decided in this model to use $7d$ as the entire length of the object was not going to be covered by eight sources and it was believed this gave a fair balance of coverage whilst still being within the range given by [111].

Pre-set Model

In this model the option to adjust the diameter at the tip and hilt were removed along with being able to adjust the length. Instead a number of fixed objects were measured, and their geometries programmed in as pre-sets. The objects measured were a metal sword, wooden sword, baseball bat, 3 wood golf club, 7 iron golf club and a broom handle.

By measuring the objects, the exact diameter parameter of each compact sound source could be set. Unlike the variable model the correlation length of the sources at the tip were set to $5d$ for the thin objects and $2d$ for the baseball bat. The exact position from the hilt and the source diameter for each object is given in Table 5.2.

Grooved Model

[121] found that a grooved sword profile not only produced tones due to vortex shedding but also the cavity tone due to the groove. To replicate a grooved profile sword, a cavity tone compact sound source synthesis model was placed alongside the Aeolian tone model.

5.2.5 Swinging Model Evaluation

Subjective Evaluation

A subjective evaluation of the swinging objects model was undertaken. This evaluation was separated into two parts. One was a listening test and the other an object recognition test. In total, 26 participants took part in the subjective evaluation, comprising of 18 male and 7 females

Table 5.2: Diameter and radius from the hilt of compact sound sources for the pre-set swinging objects. All values in metres. Correlation Length = $5d$ except for Baseball bat where Correlation Length = $2d$.

| Metal Sword | | Wooden Sword | | Baseball Bat | | 3 Wood Golf Club | | Broom Handle | |
|-------------|----------|--------------|----------|--------------|----------|------------------|----------|--------------|----------|
| Radius | Diameter | Radius | Diameter | Radius | Diameter | Radius | Diameter | Radius | Diameter |
| 0 | 0.0046 | 0 | 0.0117 | 0 | 0.0237 | 0 | 0.0258 | 0 | 0.0270 |
| 0.418 | 0.0046 | 0.307 | 0.0111 | 0.159 | 0.0237 | 0.383 | 0.0124 | 0.313 | 0.0270 |
| 0.777 | 0.0046 | 0.370 | 0.0108 | 0.314 | 0.0246 | 0.767 | 0.0095 | 0.625 | 0.0270 |
| 0.780 | 0.0037 | 0.417 | 0.0105 | 0.371 | 0.0286 | 0.813 | 0.0092 | 0.760 | 0.0270 |
| 0.810 | 0.0029 | 0.465 | 0.0103 | 0.444 | 0.0366 | 0.857 | 0.0089 | 0.895 | 0.0270 |
| 0.821 | 0.0022 | 0.512 | 0.0100 | 0.549 | 0.0504 | 0.900 | 0.0086 | 1.030 | 0.0270 |
| 0.830 | 0.0017 | 0.560 | 0.0098 | 0.672 | 0.0637 | 1.050 | 0.0154 | 1.165 | 0.0270 |
| 0.836 | 0.0013 | 0.607 | 0.0095 | 0.804 | 0.0659 | 1.100 | 0.0388 | 1.300 | 0.0270 |

with one preferring not to say. The age range for participants was from 17 to 71, with a median of 28. Participants were split into two groups; one that completed the listening test before the object recognition and one that completed the object recognition first and then the listening test.

The listening tests were carried out using the Web Audio Evaluation Tool (WAET) [79]. The WAET allowed the page order and sample of each to be presented in a pseudo random manner creating a double-blind test. The magnitude for each sample was loudness normalised in accordance with [23]. Two different headphones were used for each group; AKG K552 Pro closed-back headphones and Beyerdynamic DT150, both closed-back isolating studio headphones.

In the listening test, each participant was presented with five test pages representing five objects: metal sword, wooden sword, baseball bat, golf club and broom handle. The wooden sword, baseball bat, golf club and broom handle pages contained two real samples, two samples from our model and two samples generated from spectral modelling synthesis (SMS) [5], made from analysis of a recording not used in the test. Finally, the test page contained an anchor sound effect.

The metal sword page contained two real samples, one synthesised sample from [19], one synthesised sample from [43], one SMS sample created by a recorded sample not further used, one sample from the synthesis model and one sample from the synthesis model which included the cavity tone. An anchor was also included in this test page.

The sampled recordings for all objects were captured within the Listening Room, EECS Department, Queen Mary University of London. They were recorded on a Neumann U87 microphone which created mono recordings. The mic was placed approximately 20 cm from the midpoint of the swing and at 90 degrees to the plane of the swing.

In order that the natural reverb of the space did not influence the sound the impulse response of the room was measured. This was then applied to the other sounds used in the listening tests, except the samples from [19] and [43]. The anchor for each effect was created using a real-time browser-based synthesis effect¹. The anchor allows comparison on how plausible a synthesis effect is; a low-quality anchor should encourage full use of the scale. This in turn gives a better understanding as to the effectiveness of the synthesis method.

It was decided to rate the sounds presented as part of the listening test in terms of plausibility. The study conducted in [27] stated plausibility was the preferred judgement for physical models, describing a plausible sound as one that listeners thought “was produced in some physical manner”.

The results for all five objects are shown in boxplots in Figs. 5.3 to 5.7. On first examination

¹<http://c4dm.eecs.qmul.ac.uk/audioengineering/RTSFX/app/main-panel/whoosh.html>

it can be seen that the physical model based on the compact sound source synthesis models outperforms alternative synthesis methods on most of the objects. The only object it performed poorly for was the metal sword. The grooved profile sword with added cavity tone performs slightly better but still poor.

The distribution of the plausibility ratings was examined using a Shapiro-Wilk test. This indicated that 29 out of the 36 tests were not normally distributed. This is shown in Table 5.3. To examine similarity between the ratings for each audio source in the listening test, a Mann-Whitney U test was performed. The results of these are shown in Tables 5.5 to 5.14.

Object Recognition

The second part of the subjective evaluation was to invite participants to control the sound synthesis model using a Wii Controller. All parameters were set except the speed of swing which was calculated as the square root of the sum of squared yaw angular velocity and pitch angular velocity. This was then smoothed, scaled for each source and used as the model's airspeed input.

By using the Wii Controller, participants were able to swing a virtual object though the air and were invited to identify the object from the list of five possibilities; metal sword, wooden sword, baseball bat, golf club and broom handle. 14 participants completed the object recognition test prior to the listening test and 12 participants completed it after the listening test. Each participant was presented with all the pre-set objects twice, giving a total of ten tests.

The results from the object recognition tests are shown in Table 5.9 for those who completed the test prior to the listening test and Table 5.9 for those who complete the test after it. A clear difference can be seen from the results between those who completed the tests first and those who completed it second. It is reasonable to conclude that the listening test gave participants a form of informal training for the object recognition test.

Results from Table 5.9 also show that it was more common to choose an incorrect object than the correct one. The model of the wooden sword was never correctly identified whereas the metal sword was correctly identified more than any other object but still less than 50% of the time.

The results from participants who completed the object recognition test second, Table 5.10, shows an increase for all objects being correctly identified. Again, the metal sword was correctly identified more often than the other objects. Although object identification was more often correct than the results shown in Table 5.9, it was still more common for participants to choose one of the other objects being modelled rather than the one being replicated by our synthesis model.

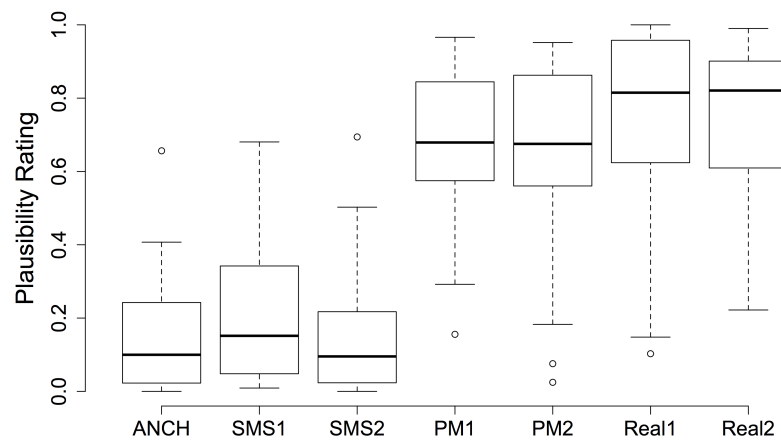


Figure 5.3: Box plots showing plausibility results for the broom handle

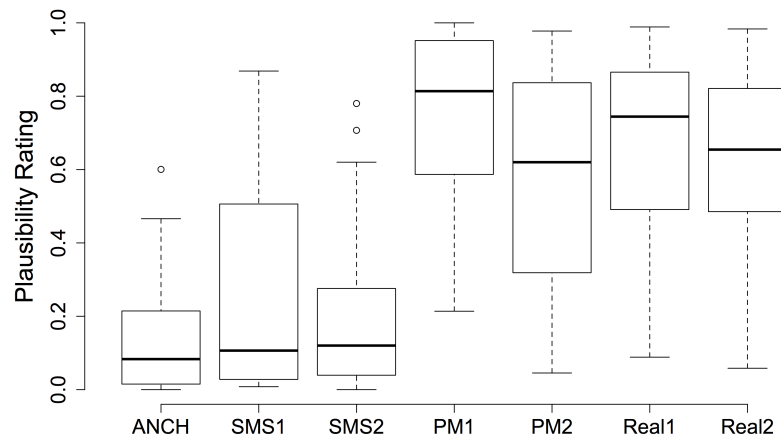


Figure 5.4: Box plots showing plausibility results for the baseball bat

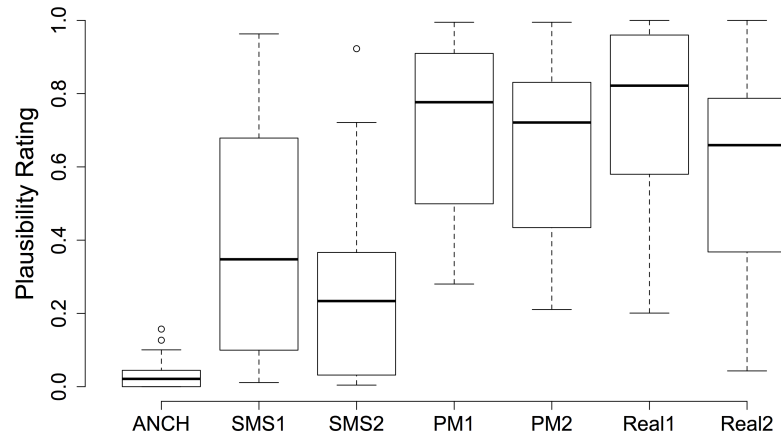


Figure 5.5: Box plots showing plausibility results for the golf club

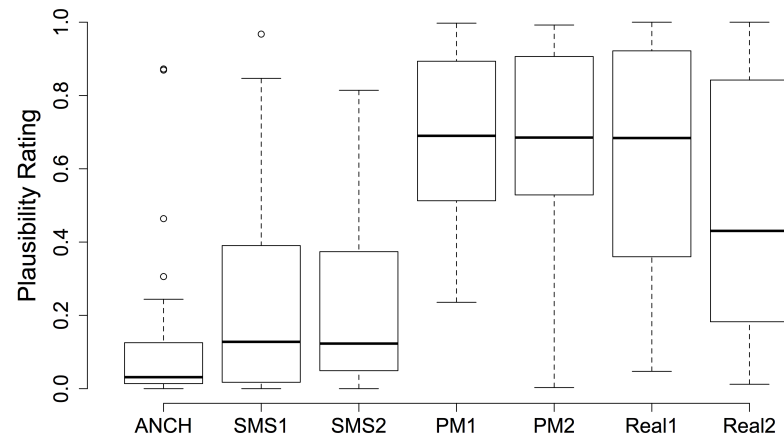


Figure 5.6: Box plots showing plausibility results for the wooden sword

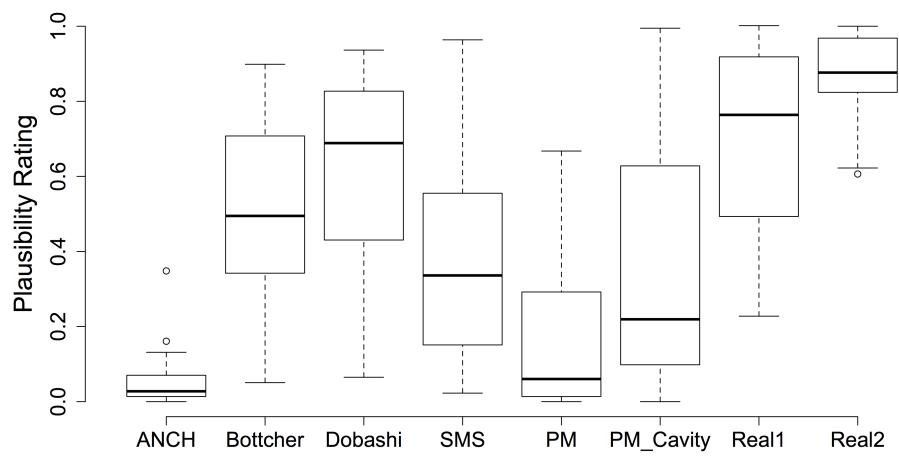


Figure 5.7: Box plots showing plausibility results for the metal sword

Table 5.3: Results for Shapiro-wilk test to the plausibility ratings for swinging objects (**** \Rightarrow $p < 0.0001$, *** \Rightarrow $p < 0.001$, ** \Rightarrow $p < 0.01$, * \Rightarrow $p < 0.05$, - \Rightarrow $p \geq 0.05$)

| | Anchor | SMS1 | SMS2 | PM1 | PM2 | Real1 | Real2 | |
|---------------------|---------------|-------------|-----------------|----------------|------------|-----------------|--------------|--------------|
| Broom Handle | *** | ** | *** | - | ** | *** | *** | |
| Baseball Bat | *** | *** | ** | * | - | * | - | |
| Golf Club | *** | * | ** | * | * | * | - | |
| Wooden Sword | **** | *** | *** | - | * | * | ** | |
| | Anchor | SMS1 | Bottcher | Dobashi | PM | PMCavity | Real1 | Real2 |
| Metal Sword | **** | - | - | * | *** | ** | * | * |

130

Table 5.4: Measure of difference for the metal sword samples (**** \Rightarrow $p < 0.0001$, *** \Rightarrow $p < 0.001$, ** \Rightarrow $p < 0.01$, * \Rightarrow $p < 0.05$, - \Rightarrow $p \geq 0.05$)

| | Anchor | SMS1 | Bottcher | Dobashi | PM | PMCavity | Real1 | Real2 |
|-----------------|---------------|-------------|-----------------|----------------|-----------|-----------------|--------------|--------------|
| Anchor | . | **** | **** | **** | * | **** | **** | **** |
| SMS1 | . | . | - | ** | ** | - | ** | **** |
| Bottcher | . | . | . | - | **** | ** | ** | **** |
| Dobashi | . | . | . | **** | *** | ** | - | **** |
| PM | . | . | . | **** | * | ** | *** | **** |
| PMCavity | . | . | . | . | . | *** | *** | *** |
| Real1 | . | . | . | . | . | *** | *** | ** |

Table 5.5: Measure of difference for the broom pole samples (**** \Rightarrow $p < 0.0001$, *** \Rightarrow $p < 0.001$, ** \Rightarrow $p < 0.01$, * \Rightarrow $p < 0.05$, - \Rightarrow $p \geq 0.05$)

| | Anchor | SMS1 | SMS2 | PM1 | PM2 | Real1 | Real2 |
|---------------|---------------|-------------|-------------|------------|------------|--------------|--------------|
| Anchor | . | - | - | **** | **** | **** | **** |
| SMS1 | . | - | **** | **** | **** | **** | **** |
| SMS2 | | . | **** | **** | **** | **** | **** |
| PM1 | | | . | - | - | - | - |
| PM2 | | | | . | * | - | - |
| Real1 | | | | | . | - | - |

Table 5.6: Measure of difference for the baseball bat samples (**** \Rightarrow $p < 0.0001$, *** \Rightarrow $p < 0.001$, ** \Rightarrow $p < 0.01$, * \Rightarrow $p < 0.05$, - \Rightarrow $p \geq 0.05$)

| | Anchor | SMS1 | SMS2 | PM1 | PM2 | Real1 | Real2 |
|---------------|---------------|-------------|-------------|------------|------------|--------------|--------------|
| Anchor | . | - | - | **** | **** | **** | **** |
| SMS1 | . | - | **** | **** | **** | **** | **** |
| SMS2 | | . | **** | **** | **** | **** | **** |
| PM1 | | | . | * | - | * | |
| PM2 | | | | . | - | - | |
| Real1 | | | | | . | - | |

Table 5.7: Measure of difference for the golf club samples (**** \Rightarrow $p < 0.0001$, *** \Rightarrow $p < 0.001$, ** \Rightarrow $p < 0.01$, * \Rightarrow $p < 0.05$, - \Rightarrow $p \geq 0.05$)

| | Anchor | SMS1 | SMS2 | PM1 | PM2 | Real1 | Real2 |
|---------------|---------------|-------------|-------------|------------|------------|--------------|--------------|
| Anchor | . | **** | **** | *** | *** | **** | **** |
| SMS1 | . | - | ** | ** | *** | * | |
| SMS2 | | . | **** | **** | **** | **** | **** |
| PM1 | | | . | - | - | - | |
| PM2 | | | | . | - | - | |
| Real1 | | | | | . | - | |

Objective Evaluation

The objective evaluation focussed on the sound produced by the katana sword examined in [121]. This sword had a profile with grooves in either side and therefore produced the cavity tone along with the Aeolian tone. To replicate this a cavity tone compact sound source synthesis model was added alongside each of the Aeolian tone compact sound sources.

The sword used in the wind tunnel experiments in [121] had a thickness of 0.005 m. The airspeed was set at 24 m/s. At these values [121] reports a tone around 960 Hz due to vortex shedding. There was also an observed high frequency sound around 6 - 9 KHz believed to be due to the cavity tone. The dimensions of the groove in the sword were not published.

Table 5.8: Measure of difference for the wooden sword samples (**** \Rightarrow $p < 0.0001$, *** \Rightarrow $p < 0.001$, ** \Rightarrow $p < 0.01$, * \Rightarrow $p < 0.05$, - \Rightarrow $p \geq 0.05$)

| | Anchor | SMS1 | SMS2 | PM1 | PM2 | Real1 | Real2 |
|---------------|---------------|-------------|-------------|------------|------------|--------------|--------------|
| Anchor | . | - | * | **** | **** | **** | **** |
| SMS1 | . | - | | **** | **** | *** | ** |
| SMS2 | | . | | **** | **** | *** | ** |
| PM1 | | | . | - | - | - | * |
| PM2 | | | | . | - | . | * |
| Real1 | | | | | . | . | - |

Table 5.9: Swinging objects identified from Wii Controller - Tested before listening test

| Object | Correctly Guessed (%) |
|---------------|------------------------------|
| Wooden Sword | 0 |
| Metal Sword | 36 |
| Broom Handle | 7 |
| Baseball Bat | 11 |
| Golf Club | 21 |

To give a cavity tone between 6 KHz and 9 KHz, (7.5 KHz), a cavity of length 0.0307 m was added. The airspeed and diameter were made identical to those published in [121]. The frequency spectrum from this output is shown in Fig 5.8. The Aeolian tone can clearly be seen at 969Hz, which matches well with the 960Hz wind tunnel result. There was a harmonic to the Aeolian tone at 2907Hz. The cavity tone frequencies were found to be 3213Hz, 7497Hz, 11780Hz, and 16064Hz for modes 1, 2, 3 and 4 respectively.

The frequency for the mode 2 cavity tone lies within the range stated by [121]. This was created by backwards engineering the cavity length, but this seems reasonable. The peaks given in the synthesis model around 3 KHz are from the Aeolian tone harmonic and first mode from the cavity tone. These are of much greater amplitude than those witnessed in [121]. The published data does not cover frequencies as high as the mode 3 and mode 4 cavity tones.

It was also noted in [121] that the two oscillating forces around a sword with a groove will modulate each other. In one wind tunnel experiment the airspeed was ramped from 15 m/s to 30 m/s and extra harmonics were witnessed and attributed to this phenomenon. The magnitude of the individual modulated frequencies varies as airspeed changed.

Our model does not produce any harmonics that are generated by the modulation of the two oscillating forces. The addition of this may increase the perceptual quality of a grooved profile sword model.

Table 5.10: Swinging objects identified from Wii Controller - Tested after listening test

| Object | Correctly Guessed (%) |
|--------------|-----------------------|
| Wooden Sword | 38 |
| Metal Sword | 63 |
| Broom Handle | 42 |
| Baseball Bat | 46 |
| Golf Club | 38 |

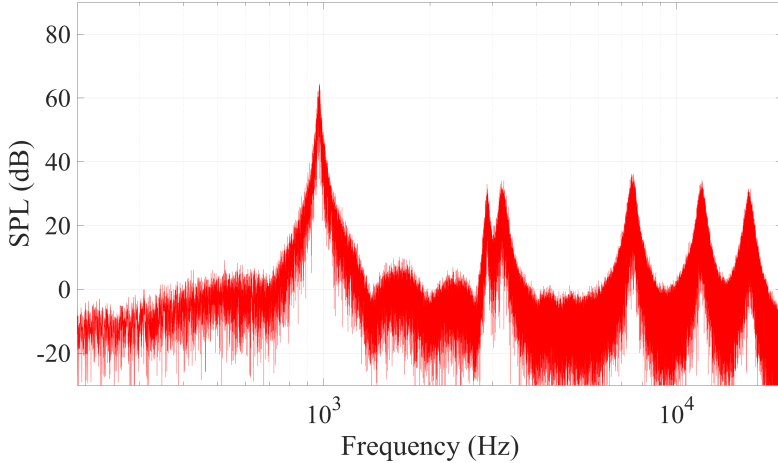


Figure 5.8: Magnitude spectrum of physical model of grooved sword

5.2.6 Discussion on Swinging Object Synthesis Model

Examining results from the listening test it can be seen our model performs well compared to other synthesis models. The model gives exceptional performance for the broom handle, baseball bat, golf club and wooden sword object. The model does poorly for the metal sword model. A number of possible reasons for the poor performance of the metal sword model compared to the other objects are examined.

An obvious difference between the metal sword and the other objects was that the metal sword was the thinnest of all the objects modelled. This could have a detrimental effect on the compact sound source implementation. Thicker objects have a higher Reynolds number and hence a lower Q value in the synthesis model. It may be that the model is not as close to reality for thinner objects.

It is also believed that SMS sounds performed better for thinner objects as this synthesis technique focusses on finding the sinusoidal components which are more prevalent in lower Reynolds number or laminar situations.

The results in Table 5.14 shows that the physical model as significantly different from all other

sounds, especially the real samples and those synthesised by alternative methods. Only one sample from the swinging objects model was compared to the other sounds. This was based on the real sword measured and recorded prior to the experiment. It is believed that further listening tests with different model parameters could provide clearer results.

One point of interest is that the sword modelled by [43] had a diameter of 0.01 m which was substantially thicker than the one modelled here. Replicating this sword too would be advantageous and highlight if listeners prefer thicker sounding sword sounds.

The choice of Γ in Eqn. 4.32, Section 4.2.4, sets the balance between the wake quadrupole and the vortex shedding dipoles. This value was set perceptually for this experiment at 0.2. This was taking into consideration all objects thicknesses from the metal sword to the baseball bat. It could be that this relationship is not static and also varies with the thickness of the sword. If so, this was not captured by this synthesis model.

A further point of interest when examining the metal sword sound, not only was the metal sword the thinnest object it was also the flattest. In Section 4.2.1 it was explained that the Aeolian tone model was based on the shape of a cylinder. The broom handle and baseball bat are cylinder, while the golf club was cylindrical except the head. This could indicate that the synthesis model created performs better for objects that are closer to cylindrical. The wooden sword thickness to width ratio was only 0.37:1 while the metal sword decreases to approximately 0.14:1. This could be a reason why the metal sword model obtained poorer results.

It is also hypothesised that the number of participants who have swung a real sword, hearing the sound produced may well be less than the number of people who have swung a golf club. It has been shown that memory of a sound plays an important role in perception [58]. It was possible that participants have heard a Foley sound effect for a sword more often than the actual sound and this may influence their perception. Since listening test were carried out in the UK participants may not have swung a baseball bat either.

In relation to the object recognition test it is clear that with zero training, participants found it extremely difficult to identify an object from controlling the speed. This was shown by the improvement in object recognition by those participants who completed the listening test first. This is in line with the findings of [117] which found that participant training was the dominant factor in determining whether or not similar tests produced significant results.

A common comment from participants when carrying out the object recognition test was that visual stimulus would have been a benefit. It is anticipated that participants may have given more accurate and closer results if they were all focussing on an image of the same object. A further comment was that some participants would have liked a “none of the above” option. These additions should be considered in any future testing.

Although the Wii Controller was an obvious means of controlling the sound effect, some participants stated they would have preferred to have an item with a similar weight to the object being modelled in their hands. This may increase their sense of belief and like the visual stimulus request, indicates that participants may benefit from multimodal non-visual cues to assist them to identify sounds. This is an area for future research.

The sounds created by the synthesis models were all generated by a single model. With an identical synthesis model, the sonic similarities between each object may be confusing for participants. It is hypothesised that if the object recognition test was carried out with only the metal sword and the baseball bat the results would be far more definite.

The objective comparison with results obtained from wind tunnel measurements [121] and the swinging object synthesis model shows good agreement with the vortex shedding frequency. The difference between measured and the frequency predicted by the synthesis model was only 0.9%.

Including the cavity tone in the synthesis model opens up the possibility of more complex object profiles. Listening tests for the grooved sword model found the sound generated as plausible as the sound generated through SMS. It was also similar to the sound generated by [19] but not as plausible as [43] and the real sample. None of the other blade profiles being modelled have grooved profiles making it an unfair comparison but it does seem to improve the plausibility of the synthesis model. It is difficult to draw an overriding conclusion regarding this.

A future development for this model would be to examine a number of sword profiles which including grooves and how these are modelled using the synthesis model. This could add modulation between the two oscillating forces.

It is known that when the vortex shedding frequency is approximately equal to the vibration frequency of the object the sound is re-enforced. This was examined more in Section 5.4. If this phenomenon was included within the swinging object model the sound may take on a different characteristic and different metals, such as bronze, steal, etc., might produce different sounds and increase the plausibility of the synthesis model.

Another objective evaluation that could be carried out in future research would be to attach an accelerometer to a swinging object while recording the sound. This data could then be used to replicate the speed parameter within the swinging object model. Under these circumstances the acoustic output from the swinging objects model could be compared to the recorded sample and comparisons made.

An improvement that could be made in relation to recording the sounds for the listening test would be to use a stereo microphone. The output from the synthesis model included stereo panning and including this in the examples being compared would have increased accuracy although it is not believed it would have as strong an affect as Doppler. The examination

of spatialisation should be undertaken as part of future evaluations. Recording swing sounds binaurally would be the preferred option.

Future development of this sound effect model could also include increasing the objects to be replicated. These could include hockey sticks, cricket bats, or even tennis racquet, lacrosse sticks and other sporting equipment with a mesh face. Modelling a spherical ball may be possible but the fluid dynamics around a spinning ball may be quite complex. Authenticity of the model may also be increased if the behaviour of the model developed more natural swinging action instead of the fixed radius arc. Often swings are more elliptical and inclusion of this would make the model more realistic.

5.2.7 Concluding Comments on Swinging Object Synthesis Model

This section presented a real-time physically derived synthesis model for swinging objects through the air. The model provides relevant parameters to the users allowing for simple control and replication of an object. It is possible to map object dimensions to graphics and even for the object parameters to be altered in real-time. A demo of the swinging objects synthesis model can be downloaded at <https://code.soundsoftware.ac.uk/projects/physicallyderivedswingingobjects>.

Listening test indicated that the synthesis model was found to be as plausible as actual recordings for all objects except the metal sword. The difficulty in identifying an object from controlling its speed of swing was extremely challenging without any training.

The inclusion of the cavity tone gives an interesting starting point for examining the range of object profiles that can be modelled by combining two compact sound source synthesis models and further examination of this, including any possible interaction was highlighted.

5.3 Propeller

Nomenclature

L = sound pressure level (dB)

P = engine power (horse power)

B = number of blades

D = rotating propeller diameter (m)

M_T = Mach number of the blade tip (dimensionless)

θ = azimuth angle between source and observer (degrees)

r = distance between observer and sound source (m)

Q = peak frequency / bandwidth at -3dB (dimensionless)

N = vortex shedding frequency harmonic number

5.3.1 Introduction to Propeller Sounds

On completion of the swinging objects model one of the next logical extensions was to research and develop a model of a propeller. Many of the characteristics of a spinning propeller are shared with the swinging object, except that the motion is a revolution and additional forces are generated in order to propel a vehicle. For the context of this study, propeller powered aeroplanes were examined and modelled. A propeller powered aeroplane is commonly added sound effect and a model that can replicate the sound of a number of aircraft has definite worth.

5.3.2 State of the Art in Propeller Sounds

The sounds generated by a fan and by helicopter rotors were synthesised in [49]. These sound effects operated in real-time and can be classed as physically inspired. For the fan model a series of narrowband noise pulses are developed and the time between pulses was varied inverse proportionally to a user-defined revolution speed. A similar approach was taken in relation to the rotor model. This has some similarities to the model developed here in so far as the revolution speed was calculated and applied to shape noise.

A study focussing on interior of aircraft for designers to evaluate noise pollution was undertaken in [78]. The approach taken here was to analyse recorded sounds in the Fourier domain and then re-synthesis these back in real-time. The noise of a jet aircraft was synthesised in [13]. Again, analysis of pre-recorded sounds was undertaken and the tonal components in the noise synthesised by use of a sine wave with time-varying amplitude and frequency.

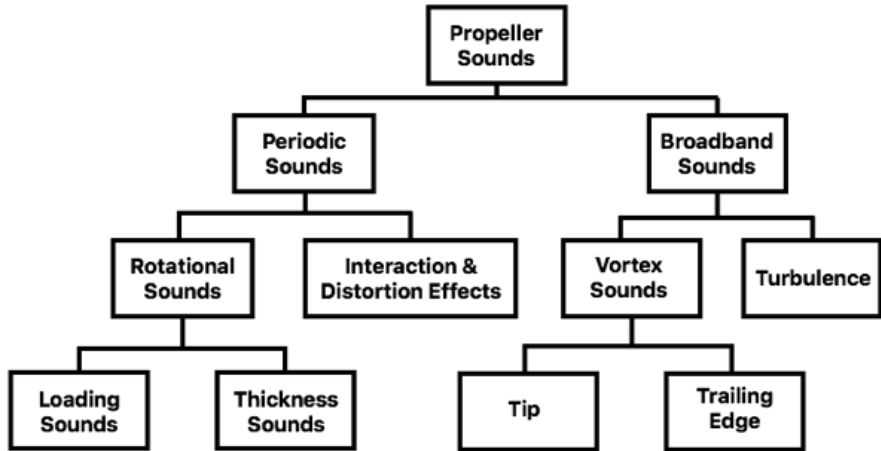


Figure 5.9: Different sources of aeroacoustic noise associated with propellers, rotors and lift fans. Adapted from [95].

The extension of the Kirchhoff integral to produce a multipole expansion replicating the aeroacoustic sound of a propeller was given in [26]. The use of multipoles or compact sound sources was a similar approach to the one given here. The purpose in [26] was to gain an analytical derivation of the sound produced in the far field. Then, by setting the far field noise to acceptable levels at specific observer positions, selective propeller parameters can be ascertained, and the designers reverse engineer the propeller.

5.3.3 Method

A comprehensive review of the sound generated by propellers, rotors and lift fans was given by [95]. This review illustrates the number of different noise sources that contribute to the sounds generated by a spinning propeller as well as helicopter rotors and lift fans used in vertical take-off and landing (VTOL) craft. Figure 5.9 shows a breakdown of these different sound sources.

The interaction and distortion effects refer to AM/FM modulation and blade slap which are associated with helicopter rotors. These were not considered in this study. Similar to the swinging objects model, a virtual coordinate system was devised in order to determine distances and angles required for acoustic calculations. Unlike the swinging objects model, the observer was positioned in the centre of the 3-dimensional coordinates system, facing along the positive x axis. A local coordinates system was also employed for each spinning propeller in order to track its movement with relation to the aircraft and observer. The local coordinate system is shown in Fig. 5.10.

One of the main sources of aeroacoustic noise from a propeller is the loading sounds. This noise is generated by air pressure surrounding the blade and can be split into two components - thrust

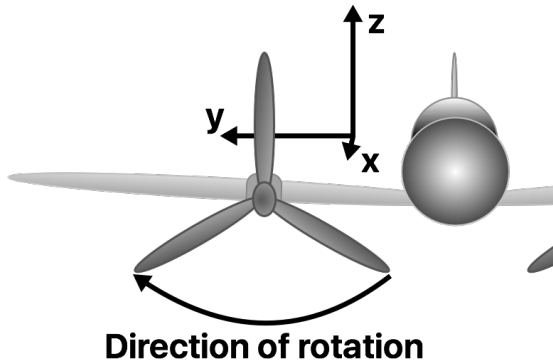


Figure 5.10: Local coordinates of spinning propeller

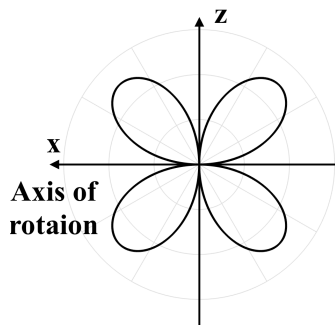


Figure 5.11: Thrust source radiation patterns based on local coordinates

and torque. The thrust component is the pressure force normal to the plane of rotation. This is the force associated with propelling the aircraft forward. The torque component is the pressure component that is within the plane of the spinning propeller.

Viewing the spinning propeller as a disc from a stationary reference point, a pulse is generated at that point each time a propeller blade passes. This is the pulse that [49] referred to when creating the fan sound effect. This pulse generates a harmonic sound source at the blade passing frequency.

A plot of the thrust source radiation pattern is shown in Fig. 5.11. and the plot of the torque sound source radiation pattern is shown in Fig. 5.12. The combination of these plots is given in Fig. 5.13. It can be seen that the maximum sound generated by loading noise is about 120 degrees with respects to the local coordinates system, with 0 degrees directly in front of the propeller. This is consistent with the findings of Gutin's theory [64].

Thickness noise is the sound generated as the blade moves aside air as it rotates. [95] noted that this sound source is small when the blades are moving at a speed on Mach 1. Since this is a minor noise source it was not considered in this model.

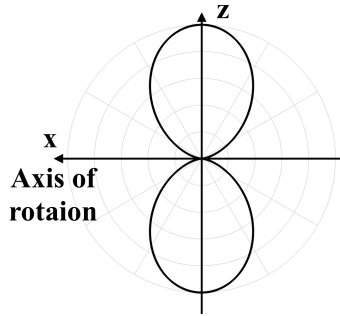


Figure 5.12: Torque sound source radiation patterns based on local coordinates

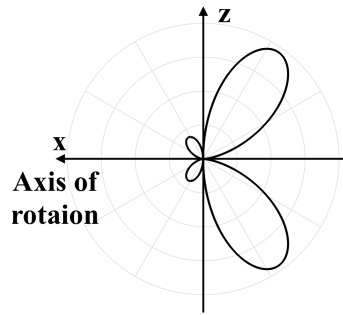


Figure 5.13: Thrust and torque combined sound source radiation patterns based on local coordinates

The vortex sounds are the dominant broadband sources. This sound is created as the blade cuts through the air and vortices are shed, i.e. the Aeolian tone. This component of the sound of a propeller is the one identical to the previous model on swinging objects. The frequency of the vortex shedding is dependent on the speed of rotation or revolutions per minute (RPM) of the propeller blades, as well as the geometry of each blade. The frequency of the vortex shedding was calculated from Eqn. 4.14, given in Section 4.2.4. The acoustic intensity was calculated using Eqn. 4.17, given in Section 4.2.4. The wideband nature of the sound is generated due to each point on the spinning propeller rotating at a different speed, giving a range of frequencies. The vortex sound source radiation pattern is shown in Fig. 5.14. This is the familiar dipole as seen in Fig. 4.4, Section 4.2.3.

Pseudorandom noises from vortices are generated by interactions with air and the spinning propeller. These are known as turbulence sounds. The sources that generate these sounds are inefficient and classed as insignificant compared to the other sound sources. If these sounds interact with the pressure field of a moving propeller blade they can become significant, but they are not replicated in this model.

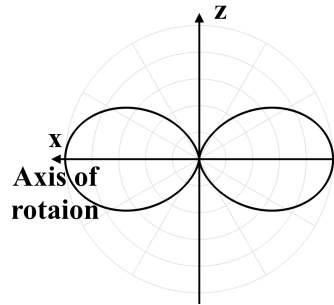


Figure 5.14: Vortex sound source radiation patterns based on local coordinates

5.3.4 Implementation

Aircraft Models

To demonstrate the scope of the model a number of different aircraft were selected to be replicated. The choice of which aircraft was made by considering which aircraft sound recordings were available to enable better evaluation. The data in Table 5.11 shows the different aircraft models which were replicated, along with properties such as engine power and blade profile which are important in calculating the propeller sounds.

Loading Sounds

In the appendix of [95] a generalised propeller noise estimating procedure was given. This was based on a procedure designed by Hamilton Standard, a propeller manufacturer. The procedure outlines a number of systematic steps to provide a reliable estimate for the loading sounds. Some of the steps require simply reading values from plots provided. Since this cannot be done by the software, equations representing the lines given were devised by the author. The values given in each step was the sound pressure level (SPL), given in dBs, the steps requiring imperial units have been converted to metric and each step are outline below:

1. Obtain a reference SPL L_α which relates to the power input to the propeller:

$$L_\alpha[n] = 15.11 \log(P[n]) + 83.57 \quad (5.2)$$

where $P[n]$ is the engine power given in units of horse power.

2. Calculate a correction factor L_β for the number of blades and the blade diameter:

Table 5.11: Aircraft models and relevant data. ‡ - Best estimate based on visual examination of blade images. ⊕ - modified noting blade chord length almost a constant 0.47m [44]. * - profile taken from RAF drawing

| Model | Top Speed (m/s) | RPM | Engine Power (HP) | Blade Radius (m) | Blade Profile ‡ |
|------------------------------|-----------------|-------------------|-------------------|-------------------|--------------------|
| Hercules C13 ^a | 164 | 1020 | 4590 | 2.06 | NACA 16 ⊕ |
| Boeing B17 ^b | 144 | 2500 | 1200 | 1.63 | RAF ^c * |
| Tiger Moth ^d | 48 | 2100 ^e | 130 | 0.99 ^f | RAF * |
| Yakovlev Yak-52 ^g | 79 | 1860 ^h | 360 | 1.20 ⁱ | NACA 16 |
| Cessna 340 ^j | 125 | 2500 ^k | 310 | 0.96 | ARA-D |
| P51 Mustang ^l | 193 | 1280 ^m | 1490 | 1.70 | NACA 16 |

^a en.wikipedia.org/wiki/Lockheed_C-130_Hercules

^b alternatewars.com/SAC/B-17G_Flying_Fortress_SAC_-27_April_1949.pdf

^c i178.photobucket.com/albums/w252/YavorD/PropellorRAFT5291BE2C2D.jpg

^d en.wikipedia.org/wiki/De_Havilland_Tiger_Moth

^e rafjever.org/tigpic027

^f hercprops.com/in-stock/

^g en.wikipedia.org/wiki/Yakovlev_Yak-52

^h airbum.com/pireps/PirepYak-52.html

ⁱ 76.222.206.206/yak52/specs

^j en.wikipedia.org/wiki/Cessna_340

^k aopa.org/go-fly/aircraft-and-ownership/aircraft-fact-sheets/cessna-340

^l en.wikipedia.org/wiki/North_American_P-51_Mustang

^m spitfireperformance.com/mustang/mustangtest

$$L_\beta = 20 \log \frac{4}{B} + 40 \log \frac{4.72}{D} \quad (5.3)$$

where B is the number of blades and D the propeller diameter.

3. Obtain a correction factor based upon the speed of the propeller rotation and the distance between the propeller to what is labelled as *a point of interest*. It was stated in [95] that this distance is 1 foot (or approximately 0.305m), giving:

$$L_\gamma[n] = (25.12M_T[n] - 33.40) \log \frac{0.305}{D} + (34.37M_T[n] - 36.88) \quad (5.4)$$

where $M_T[n]$ is the Mach number relating to the speed of the blade tip.

4. A directional correction was obtained which takes into account the directional characteristics of the loading sound sources in the propeller. This is similar to Gutin's theory of propeller acoustics as illustrated in [64] and shown as a combination of ideal sound sources in Fig. 5.13. The greatest acoustic intensity was given at approximately 120° but it does not reduce to zero as shown in the ideal case, Fig. 5.13. The directional correction is given by:

$$L_\delta[n] = -5.3 \times 10^{-3} \theta^2[n] + 1.19\theta[n] - 62.32 \quad (5.5)$$

where $\theta[n]$ is the azimuth angle between source and observer given in degrees. A minimum value of -20 dB was set to ensure similar results to the measured plot given in [95] which does not provide data for $\theta < 50^\circ$.

5. A further correction factor was required for the spherical attenuation between the source and observer:

$$L_\epsilon[n] = -20 \log(3.375r[n] - 1) \quad (5.6)$$

where r is the distance between observer and source in metres.

6. The correction factors were then added to the initial reference value obtained in step 1.

$$L_\zeta[n] = L_\alpha[n] + L_\beta + L_\gamma[n] + L_\delta[n] + L_\epsilon[n] \quad (5.7)$$

7. The gain for the fundamental and 9 harmonics was then calculated using:

$$H_N[n] = 26e^{(-0.7M_T[n]+0.79)N} - 22 \quad (5.8)$$

where $H_N[n]$ is the gain of each harmonics and N is the harmonic number, $N \in [1, 10]$.

8. The values obtained from step 7 were then individually subtracted from the value obtained in step 6 to give the gains for each of the 10 frequencies (fundamental and 9 harmonics).

Table 5.12: Approximate values for atmospheric absorption for each frequency band, † estimate by authors

| Frequency Bands (Hz) | Attenuation from noise source, $A_N[n]$ (dB per 1000 feet) |
|----------------------|------------------------------------------------------------|
| [0, 90) | 0 |
| [90, 180) | 0.2 |
| [180, 355) | 0.6 |
| [355, 710) | 1 |
| [710, 1400) | 1.8 |
| [1400, 2800) | 3.3 |
| [2800, 5600) | 6 |
| [5600, 11,200) | 11.4 |
| > 11,200 | 20† |

$$L_{N_\psi}[n] = L_\zeta[n] - H_N[n] \quad (5.9)$$

9. An approximate value for atmospheric absorption $A_N[n]$ for each of the harmonics was calculated. The values for this attenuation is given in Table 5.12.

10. The attenuation values based on the harmonic frequency were subtracted from the gain value for each harmonic to give $L_{N_\psi}[n]$.

$$L_{N_\psi}[n] = L_{N_\zeta}[n] - A_N[n] \quad (5.10)$$

This was then converted back to a linear value from decibels to give $G_N[n]$.

$$G_N[n] = 2 \times 10^{-5} \cdot 10^{\frac{L_{N_\psi}[n]}{20}} \quad (5.11)$$

The frequency of each harmonic of the loading sound was calculated from Eqn. 5.12:

$$f_{L_N}[n] = \frac{N \cdot B \cdot \text{RPM}[n]}{60} \quad (5.12)$$

where RPM is the revolutions per minute.

The loading sounds were implemented by means of white noise filtered by 10 variable bandpass filters. The centre frequency of each bandpass filter was set to the frequency value of the corresponding harmonic and gain set to the values calculated in step 10. No information was given as to how tonal the sound was which in turn would influence the bandpass filters Q values.

This was set perceptually at value of 75, giving a narrow passband and tonal quality.

Vortex Sounds

The vortex sounds were generated using the Aeolian tone compact sound source synthesis model. Similar to the swinging objects model, compact sources were placed in a virtual row to replicate each propeller blade. In this instance, each blade was represented by 7 compact sound sources.

One of the main differences between a propeller blade and a cylinder was given in [21], where the Strouhal number was found to be approximately 0.85. This was different than the approximate value of 0.2 which was found by Strouhal and described in Section 4.2.3. Instead of the diameter value as used in Eqn. 4.4, the propeller chord length was used. The harmonic frequency $f_{st_N}[n]$ is calculated using Eqn. 5.13.

$$f_{st_N}[n] = \frac{0.85Nu[n]}{\text{Chord Length}} \quad (5.13)$$

To model each propeller blade, the chord lengths at different positions along span wise length were required. Three different blade profiles were obtained:

- A drawing of a historical RAF blade profile
- Two from [18] labelled
 - NACA 16
 - ARA-D

For all three blade profiles the chord length at different span-wise positions were obtained and Eqn. 4.14 used to calculate the vortex shedding frequency. The speed of each source was calculated from the RPM and radius of the compact sound source to the centre of the propeller. Acoustic intensity was calculated from a discrete implementation of Eqn. 4.17.

It is known that propeller powered aircraft has a noise source due to the motor used for each propeller. Often the motor is a major sound source depending on its characteristics, distance and any masking by aeroacoustic sounds. Perceptually, the lack of a noise source due to, for example, a four-stroke propeller engine, may have a detrimental effect. Different engine design for each aircraft may have a distinctive acoustic pattern depending on the fuel supply mixture, the aircraft era and if the engine is normally aspirated, fuel injected or a turbo.

It was not the intention of this research to replicate the sound of the engine as well as the aeroacoustic sounds but it was believed that not having any engine sound would be detrimental

to the perception of the sound effect. As a compromise, an engine sound from [49] was adapted to work alongside the aeroacoustic noise sources in order to produce a more realistic sound. To replicate minute differences between engine RPM, a small random factor was also added for each propeller.

5.3.5 Results

An exact comparison between recorded samples and the synthesis model was limited. This was because a recorded sound of an aircraft generally does not specify details of the operating conditions to allow the synthesis model to replicate these. Details such as, flight path, aircraft speed, distance, RPM and environmental conditions can all effect the sound produced. It was only really possible to obtain the model of aircraft in the recording from which the engine and propeller details were obtained and detailed in Table 5.11.

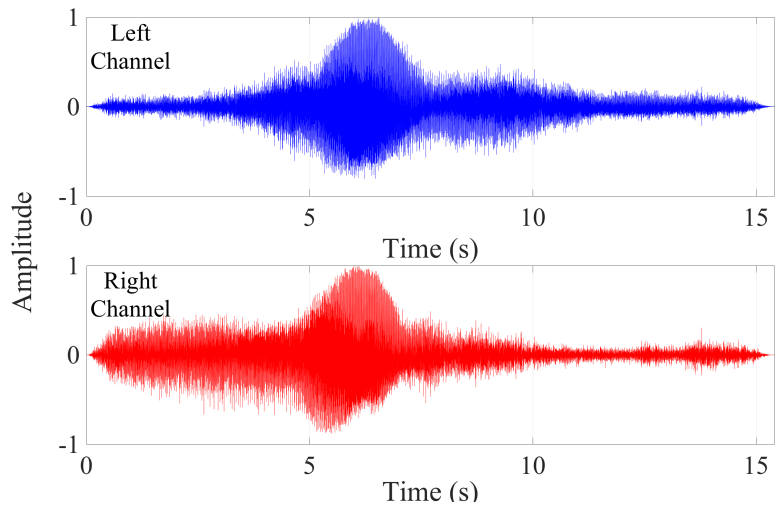
Objective Evaluation

With the caveat of the lack of information as described, an objective evaluation was carried out. This involved comparing a recorded sample and a sample from our synthesis model. The sample taken was of a Cessna, obtained from the BBC Sound Effect Library, (AircraftCessna.BBC.EC1A4b.wav). The Cessna is a small light propeller powered aircraft; the model number of the aeroplane in the recording was unknown.

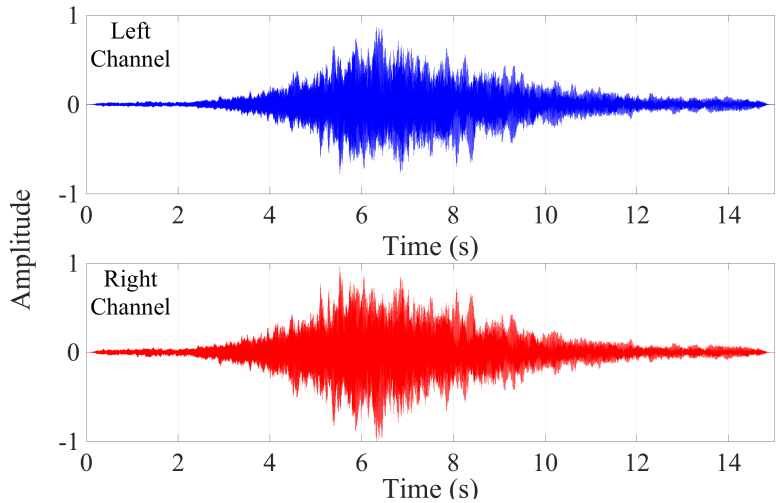
The synthesis model was designed to replicate a Cessna 340. This model has twin propellers, each with three blades. The synthesis model was set to a flight path from south east to north west of the observer on a heading of 319 degrees in the global coordinate system. At the closest point the aircraft was 370 metres from the observer and 1163 metres at the furthest point. The sine-cosine law was used for panning.

The synthesised aircraft travelled at a virtual speed of 100 m/s with propellers spinning at 2200 RPM. The engine power was set at 300 horse power and the blade length for this model of aircraft was 0.96 m.

Time, magnitude and spectrogram plots are shown in Figs. 5.15, 5.16 and 5.17. The time plots in Fig. 5.15a and 5.15b show a similar increase of amplitude as an aircraft passes the observer. The time plots indicate that the aircraft was moving from the right channel (lower red) to the left channel (upper blue).



(a) Time plot of recorded propeller plane



(b) Time plot of synthesised propeller plane

Figure 5.15: Time plots of recorded and synthesised propeller powered aeroplane sounds

The time plot of Fig. 5.15a shows that at the start, the actual recording had a higher average value in the right hand (lower red) channel, than that measured at the start of the synthesis recording, Fig. 5.15b. This area of higher average signal is seen in the left channel (upper right) of Fig. 5.15a after the aircraft has moved to that side of the observe (microphone).

None of this additional content was witnessed in Fig. 5.15b showing the time plot from the synthesis model. The BBC recording had environmental noise in the background, but it is

hypothesised that this would not move across the stereo field with the aircraft. This indicates that there was a component in the recorded sample that was not replicated in the synthesis model.

The rate of increase in amplitude level was different between recorded and synthesised time plots. It is difficult to identify the reason for this as it could be due to the different aircraft speeds or occlusions from structures masking the sounds.

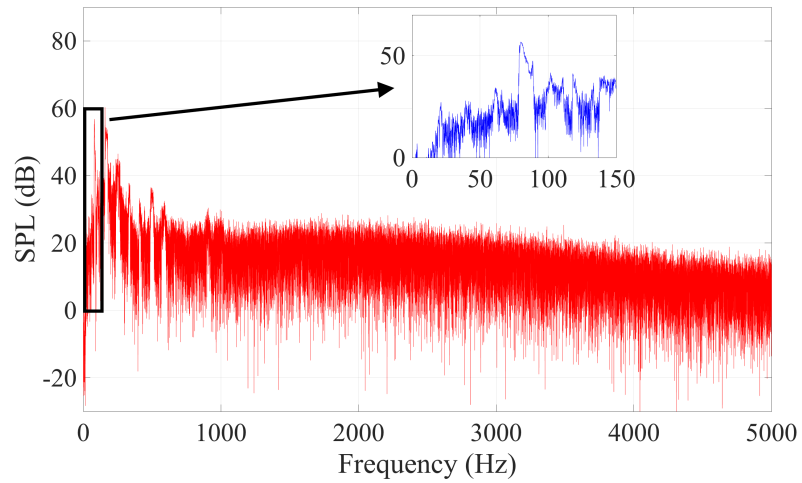
The frequency magnitude plots for recorded and synthesised sounds are shown in Figs. 5.16a and 5.16b. The real recording had an initial peak which decreases rapidly until around 500Hz than much more gradually. Similarly, the synthesised model had an initial peak but a much more gradual decrease until approximately 1000Hz after which there was rapid drop in frequency content. This is believed to be due to the 10 harmonics from the loading sounds being the major source and in the synthesis model these end around 1100Hz.

The noise content above the loading sound was much greater in the recorded sample. This could be due to a number of reasons. There may be environmental noise that adds across the frequency spectrum, the wideband noise from the vortex shedding could be greater than the synthesis model. It may be that the engine sound used in the synthesis model does not produce the frequency content that was within the recorded sound or that there are other components, as highlighted in the time plots, that the synthesis model fails to replicate.

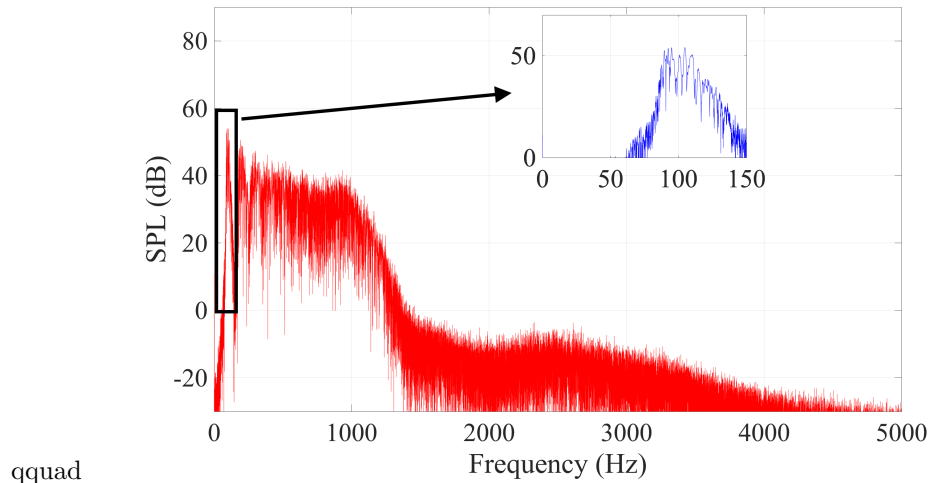
A closer examination of the initial frequency peaks in Fig 5.16, shows the first peak at 80Hz on the recorded sample and 110Hz on the synthesis model. The 80Hz in the recorded sample could relate to a two-bladed propeller rotating at 2400 RPM or a three-bladed propeller rotating at 1600RPM. Only the first four or five harmonic peaks are visible in Fig. 5.16a, with the second harmonic being the most prominent.

The first peak observed in the frequency magnitude plot of the synthesised model was at 110Hz. This equates to a three-bladed propeller with an RPM of 2200 as set prior to recording. In the synthesised sound all ten frequency components of the loading sound are present and decrease as calculated during the implementation process.

With aircraft moving at high speeds such as 100m/s, the Doppler effect has a large influence over the acoustics from the propeller. This was visible for both the recorded and synthesised sounds in Figs. 5.17a and 5.17b. There was additional frequency content in the recorded sound when the aircraft was closest to and passing by the observer, approximately 6 seconds. The increase in spectral content was not replicated by the synthesis model, corroborating that there is definite missing content in the synthesis model as seen in the time plot and frequency magnitude plots.



(a) Magnitude plot of recorded propeller plane

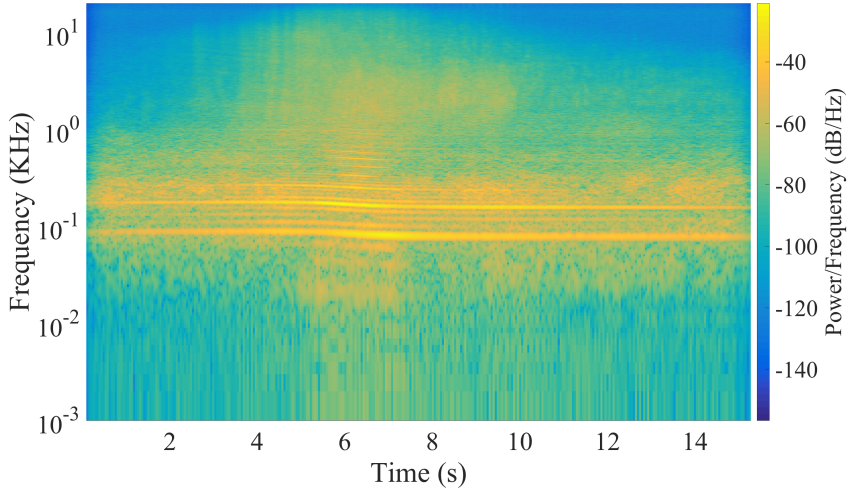


(b) Spectrogram of synthesised propeller plane

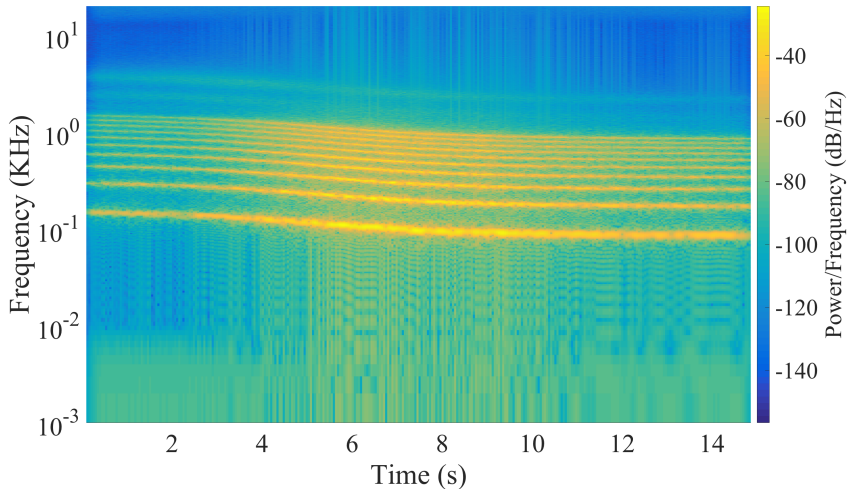
Figure 5.16: Magnitude plots of recorded and synthesised propeller powered aeroplane sounds

Subjective Evaluation

A double-blind listening test was carried out to evaluate the plausibility of the synthesis model. A total of 20 participants took part in the tests, 6 female and 14 male. Participants were aged between 17 and 70.



(a) Spectrogram of recorded propeller plane



(b) Spectrogram of synthesised propeller plane

Figure 5.17: Spectrograms of recorded and synthesised propeller powered aeroplane sounds

The WAET [79] was used to provide the samples to participants, with all samples loudness normalised in accordance with [23] and presentation order randomised. Participants were presented with four test pages, each including two real samples, two samples from our synthesis model, two samples generated by SMS from recordings not otherwise used, and an anchor.

The anchor was generated from a downgraded version of the synthesis model, with only the loading sounds generated by oscillators. The anchor allows a thorough comparison of how

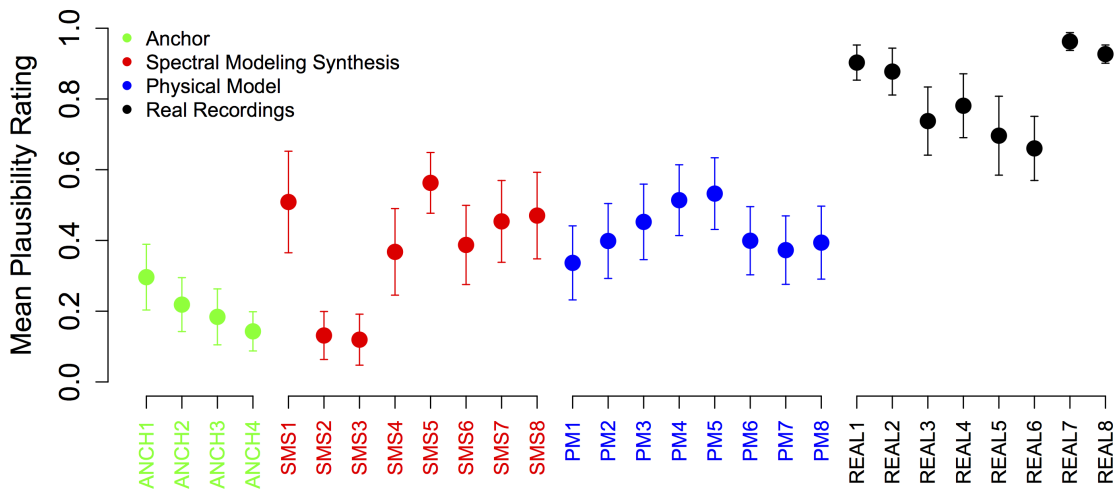


Figure 5.18: Mean plausibility rating for different propeller aircraft samples, including 95% confidence intervals. PM = Physical Model.

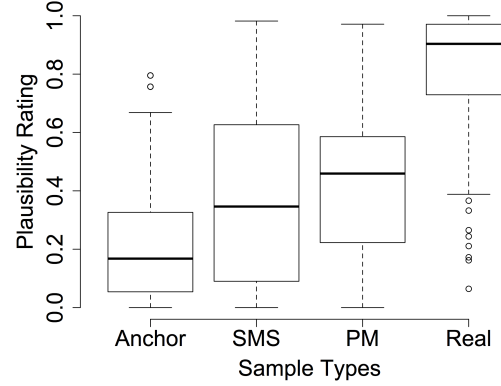


Figure 5.19: Plausibility rating for different propeller aircraft samples

plausible the synthesis model was compared to the recorded sample. The MUSHRA standard expects a lowpass filtered samples as the anchor but it is believed a sample generated from the downgrading of a synthesis sample would have minimal effect on the test.

The mean plausibility rating for all clips is given in Fig. 5.18. It is obvious that the real recordings were rated the most plausible over the synthesis model, alternative synthesis and anchor. Likewise, the anchor is generally the lowest but two of the SMS sound effects are considerably lower than the others created by this method.

There was little difference between the plausibility of both the synthesis methods. A boxplot of the results for each of the sample types is shown in Fig 5.19, which reinforces the results that real samples are the most plausible and the other sample types are hard to distinguish between.

Table 5.13: Results for Shapiro-wilk test to the plausibility ratings for propeller powered plane sound effect ($**** \Rightarrow p < 0.0001$, $*** \Rightarrow p < 0.001$, $** \Rightarrow p < 0.01$, $* \Rightarrow p < 0.05$, $- \Rightarrow p \geq 0.05$)

| Anchor | SMS | PM | Real |
|---------------|------------|-----------|-------------|
| **** | **** | ** | **** |

Table 5.14: Measure of difference for the propeller powered plane sound effect ($**** \Rightarrow p < 0.0001$, $*** \Rightarrow p < 0.001$, $** \Rightarrow p < 0.01$, $* \Rightarrow p < 0.05$, $- \Rightarrow p \geq 0.05$)

| | Anchor | SMS | PM | Real |
|---------------|---------------|------------|-----------|-------------|
| Anchor | . | *** | **** | **** |
| SMS | . | . | - | *** |
| PM | . | . | . | *** |

A Shapiro-Wilk test to the plausibility rating was carried out to examine the distribution of the ratings. Results are shown in Table 5.13 which indicate that results are not normally distributed. The Whittley Mann U Test was carried out to indicate similarity between the sample types. This is shown in Table 5.14 and indicates that both the physical model and the SMS generate samples were similar to each other but significantly different from both the anchors and the real samples.

The results from the listening tests were not unexpected and comments relating to the synthesis model included; “decay too slow”, “echo-like”, “plausible”, “warlike”, “too smooth” and “I would expect more stutter”. The last comment most likely referred to the engine model used.

Obtaining similar results to the SMS samples means that our model performs as well as a synthesis technique that starts with an actual recording and attempts to replicate this. The synthesis model developed here starts with no such information and instead was based upon the physics of operation. An advantage of the synthesis model is that the parameters that can be adjusted include flight path, RPM, engine power and even the aircraft model can be changed, although pre-sets were used for the user interface with this proof of concept model.

5.3.6 Discussion on Propeller Sound Synthesis Model

One of the main challenges when implementing the synthesis model was to balance the three noise sources, loading sound, vortex sounds and engine sounds. No information describing the relative levels was forthcoming and these had to be set perceptually. The relationship between all three possibly changes depending on the motor type, blade and other design factors. Gain sliders were provided in the graphical user interface (GUI), as shown in Fig. 5.21.

The sound from the motor model may have had a large influence over perceptual ratings. This may vary with distance from the aircraft. The synthesis model used was adapted from the

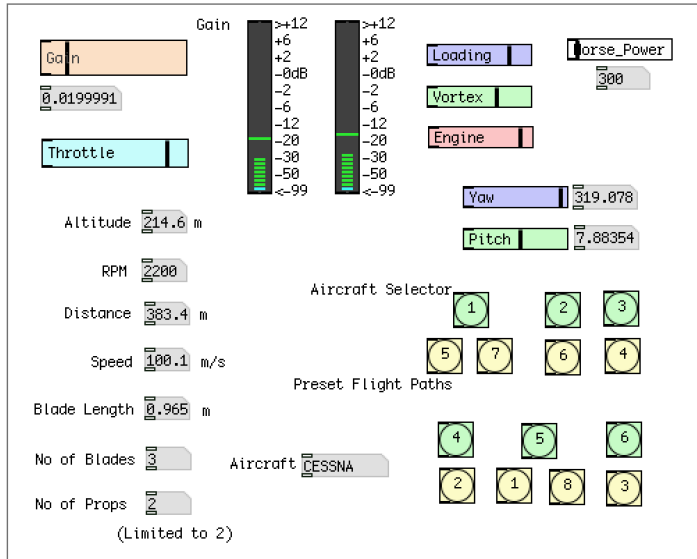


Figure 5.20: Pure Data GUI for propeller sound effect

helicopter motor design from [49] and this may well not capture all the sounds associated with a propeller motor on the aircraft selected. It is hypothesised that development and inclusion of engines matching ones found in the aircraft used in this study would increase the plausibility of the synthesis model greatly.

It was not ideal to compare a sample taken from the synthesis model to one professionally recorded. The specific details of the recorded aeroplanes are unknown, and it was therefore not possible to replicate the scenarios in which the recording took place. The recorded sound would contain acoustic elements like ground reflections which could enhance the sense of realism. Reverb, compression and other audio effects may also have taken place in a post-production scenario; the synthesis sound effects are the equivalent of anechoic chamber recordings. If these details were available, it would be possible to complete more comprehensive objective and subjective evaluation of the synthesis model.

The influence of sound effects heard in films and other media may have a strong influence over a participant's memory of these types of sounds which plays an important role in perception. An improvement to the propeller powered plane model could be to increase the number of compact sound source synthesis models of the Aeolian tone used to replicate the vortex shedding from the propeller blade. This may increase the wideband component seen in the magnitude spectrum of the recorded sound in Fig. 5.16a.

The design process in [95] stops replicating the loading sounds at the ninth harmonic. It may be the case that higher harmonics have perceptual value. There are also other aeroacoustic sound



Figure 5.21: Propeller powered plane within game engine. Full video available at https://www.youtube.com/watch?v=h_WX_O1BVds&t=2s

sources in aircraft that have not been replicated including noise from landing gear, weapons bays, flaps, support rods and instrumentation. The inclusion of these may increase realism.

The design process outlined in [95] required a number of graphs and plots to be implemented as equations. This may have introduced some errors. Further development would include researching alternative interpretations of this data which may be implemented, reducing any errors.

The flight paths used in the listening test were programmed by the author. These always had the aircraft flying in a straight line. Improved behaviour of the aircraft like, banking and diving may increase the realism of the synthesis model. An example of this could be by attaching the synthesis model to a game object which then moves in a more natural manner. This was implemented as a demonstration and a screenshot from the game engine is shown in Fig. 5.21.

5.3.7 Concluding Comments on Propeller Sound Synthesis

Presented was a real-time synthesis model of a propeller sound effect which has been designed based on semi-empirical equations obtained from aeroacoustic literature. The model gives an approximate sound as generated by a spinning propeller from equations used to allow engineers to minimise the propeller noise. A demo of the propeller model can be downloaded at <https://code.soundsoftware.ac.uk/projects/propeller-model>.

The synthesis model performs as well as an alternative synthesis technique when modelling a propeller powered aeroplane. Both synthesis techniques fall short when compared to real recordings in a listening test. It is envisaged the synthesis model would perform better if either a more accurate motor synthesis was employed or if it was evaluated against an electric powered propeller aircraft. The synthesis model has the advantage over the alternative synthesis technique by the fact that any propeller can be modelled once the physical properties are known.

5.4 Aeolian Harp

Nomenclature

l = string length (m)

μ = string linear mass density (kg/m)

T = string tension (N)

η = string harmonic number

f_η = string harmonic frequency (Hz)

f_v = vortex shedding frequency (Hz)

f_d = difference frequency (Hz)

V = reduced velocity (dimensionless)

u = airspeed (m/s)

d = string diameter (m)

m = mass coefficient for string vibration equation

b = damping coefficient for string vibration equation

k = spring coefficient for string vibration equation

ζ = proportional damping variable

α = combined mass-damping parameter

m^* = ratio between the mass density of the string and the mass density of air

$A_{max}(t)$ = maximum vibrating amplitude

$\$ \chi$ = modulation index

Λ = scaling factor

5.4.1 Introduction

The Aeolian harp is a stringed instrument which makes musically pleasing sounds when wind passes over it. An image of an Aeolian harp is shown in Fig. 5.22. Objects like fences and electrical wires can be unintentional Aeolian harps due to wind blowing over them.

The aim of this research was to determine the conditions that cause the Aeolian harp to make a sound and to replicate this in a real-time synthesis model. The model makes use of previously described compact sound source synthesis model for the Aeolian tone and another sound source based on the mechanical properties of each harp.

As stated in Section 4.2.1, Aeolian tone was designed based on a cylinder. In Aeolian harps the cylinders are the strings and shall be referred to as strings here after. The unique sound of the



Figure 5.22: Aeolian harp at South Carolina, by Prof Henry Gurr², reproduced by kind permission.

Aeolian harp is generated when the aerodynamic forces interact with the mechanical properties of the string. A string's vibrating frequency and harmonics are determined by its length, linear mass density and tension [52].

Section 4.2.3 describes the Aeolian tone frequency based on vortex shedding and determined by airspeed and diameter. When the frequency of the vortex shedding is approximately the same as the vibration frequency or a harmonic, the unique sound of the Aeolian harp is produced. Aeolian harps typically have a number of strings which produce musically engaging sounds as the wind rises and falls.

5.4.2 Background and Related Work

Historically there have been a number of stringed instruments that used air as an excitation force. The Aeolian Monochord was an instrument in which air was blown over a portion of the string like a bow by either the mouth or bellows. The lengths of the strings were adjusted by the fingers. An Anemocorde is a modified Aeolian harp with a keyboard and pedals. For this instrument, air was pushed over the strings by bellows.

For stringed instruments the timbre of the sound generated is strongly influenced by the excitation

²Further details of Prof Gurr's work can be found at - <http://web.usca.edu/math/faculty-sites/henry-gurr/aeolian.dot>

method [36]. For strings the excitation is most commonly striking, plucking or friction (bowing). Examples of plucking and friction models are given in [149] and [42] respectively. The model presented here differs from the more common excitation method as it was excited by the wind.

An electro/acoustic stringed instrument was presented in [97], called the magnetic resonator piano. In this research the strings of a piano are excited by electromagnetic actuators rather than traditional methods. This has some common ground with the synthesis model being presented here as it uses a force with no mechanical contact with the strings to excite them.

Digital audio effects and synthesis techniques were used in Jean-Claude Risset's musical piece Avel, a study of the wind [119]. In this musical piece the sound of an Aeolian harp was evoked by the use of a harp and flute rising and falling to stylise the wind.

5.4.3 Physical Principles of the Aeolian Harp

As stated in the introduction, there are two processes that interact to produce the sound of the Aeolian harp. The Aeolian tone was described in Section 4.2 and generated as wind blows around a string causing vortex shedding. The oscillating fundamental lift frequency is the major aeroacoustic source and in this section referred to as the Strouhal frequency. This frequency is calculated using Eqn. 4.14 in Section 4.2.4.

The natural harmonic frequencies of a vibrating string f_η depend on the length l , linear mass density μ , tension T and harmonic number η . It is calculated from Eqn. 5.14:

$$f_\eta = \frac{\eta}{2l} \sqrt{\frac{T}{\mu}} \quad (5.14)$$

When the Strouhal frequency approaches one of the natural harmonic vibration frequencies of a string a phenomenon called vortex induced vibration occurs [127]. Once this phenomenon is established, the frequency of vortex shedding remains approximately constant over a range of wind airspeeds. While vortex shedding remains approximately constant when vortex induced vibration is present, when the airspeed varies, the frequency of vortex shedding is different from that calculated in Eqn 4.14 in Section 4.2.4. This phenomenon is known as lock-in.

Lock-In Calculations

The range of airspeed in which the lock-in phenomenon occurs was determined by a dimensionless parameter called the reduced velocity V and is calculated from Eqn. 5.15 as given in [20].

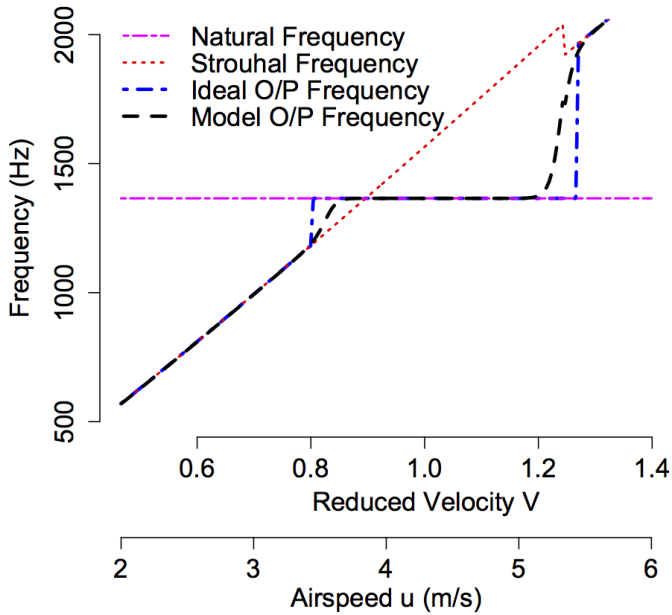


Figure 5.23: Ideal lock-in conditions and model output at 6th harmonic (1365.4Hz). Lock-in at 5th and 7th harmonics removed for clarity. $d = 0.0005m$, $l = 0.61m$, $\rho_m = 2432.2\text{kg/m}^3$, $T = 36.81N$, $\zeta = 0.006$ and $\eta = 1$

$$V = \frac{u}{2\pi d \cdot f_\eta} \quad (5.15)$$

where u is the airspeed and d the string diameter. The difference between the Strouhal frequency, vortex shedding frequency and natural vibrating frequency is shown in Fig 5.23. Note that the minor discontinuity in the Strouhal frequency was due to the piecewise linear method in which the Strouhal frequency was calculated, (Section 4.2.3).

Plots published in [127, 20, 65, 57] show that vortex induced vibrations around the fundamental natural vibrating frequency occur between approximately $V = 0.8$ and 1.27 . To replicate this, these values were chosen as the lower and upper limit for the vortex induced vibrations and hence lock-in in the synthesis models.

It was noted in [127, 20, 65, 57] that there is a hysteresis loop associated with rising and falling airspeed and the region of vortex induced vibration. This is due to there being more than one vortex shedding mode present in the lock-in region. This additional vortex shedding mode is beyond the scope of this research and the reader is referred to [156] for further information.

The hysteresis loop with respect to the vortex induced vibration is shown in Fig. 5.24. The deviation of the string from its position at rest is given by the dimensionless parameter A which

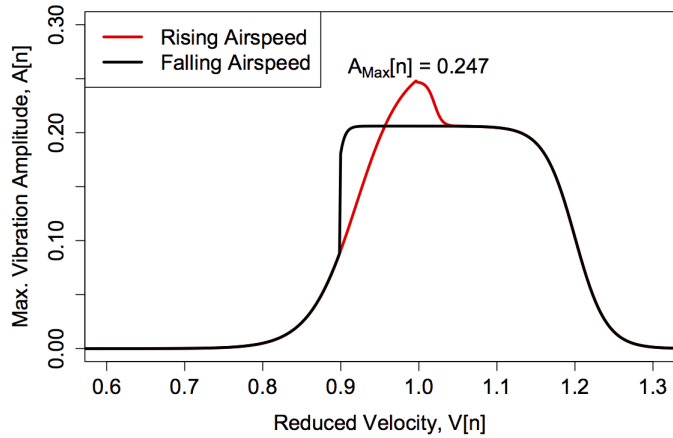


Figure 5.24: Implementation of hysteresis curve showing maximum vibration amplitude in the lock-in region. $\zeta = 0.002$, $d = 6.1 \times 10^{-4}$ m, $l = 0.65$ m, $\rho_m = 6649$ kg/m², $T = 70.78$ N.

is calculated by the distance moved perpendicular to the flow divided by the diameter.

The maximum value for A at its peak in Fig. 5.24 was calculated from the fundamental string vibration equation shown in Eqn 5.16, [142].

$$\frac{\partial^2 x(t)}{\partial t^2} + \frac{b}{m} \frac{\partial x(t)}{\partial t} + \frac{k}{m} x(t) = 0 \quad (5.16)$$

where m , b , and k are the mass, damping and spring coefficients and t is time. The damping can be represented in terms of a proportional damping variable ζ , which is given as a percentage of the critical damping [142]. This is shown in Eqn. 5.17.

$$\frac{b}{m} = 4\zeta\pi f_\eta \quad (5.17)$$

The peak amplitude of the vibrating string is related to the damping through a combined mass-damping parameter α [65]. This is shown in Eqn. 5.18.

$$\alpha = m^* \zeta \quad (5.18)$$

where m^* is the ratio between the mass density of the string and the mass density of air. The relationship between the mass-damping parameter and maximum vibrating amplitude, is dependent on the Reynolds number, (Eqn. 4.12, Section 4.2.4). For laminar flow with low Reynolds numbers the value of $A_{max}(t)$ is calculated from Eqn. 5.19, [65].

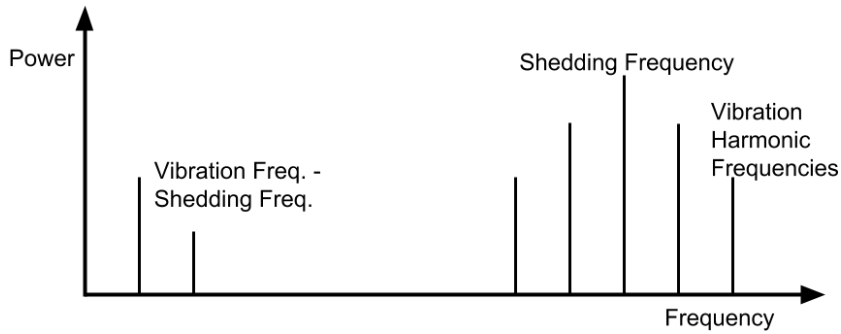


Figure 5.25: Example frequency spectrum of Aeolian harp while in lock in

$$A_{max}(t) = 0.63[1 - 1.29\alpha + 0.59\alpha^2] \quad (5.19)$$

For turbulent flow with high Reynolds numbers the value for $A_{max}(t)$ is calculated from Eqn. 5.20, [65].

$$A_{max}(t) = [1 - 1.12\alpha + 0.30\alpha^2] \log_{10}(0.41R_e^{0.36}(t)) \quad (5.20)$$

Frequency Spectrum

When a string of the Aeolian harp is vibrating in the lock-in region, it has a distinctive frequency spectrum. It was found in [150] that the acoustic output of a string vibrating in lock-in had a central peak at the vortex shedding frequency, f_v and a number of harmonics at $f_{\eta\pm 1}$, $f_{\eta\pm 2}$, etc. During lock-in the values for f_v and f_η are approximately the same. The amplitude of the sideband harmonics decreases with distance from the vortex shedding frequency.

Figure 5.25 illustrates an example of the frequency spectrum of an Aeolian harp string whilst in lock-in. This is similar to a frequency modulated signal of two oscillators. The carrier frequency was equivalent to the vortex shedding frequency f_v . The modulating frequency was a value of a difference frequency given by f_d and calculated from Eqn. 5.21.

$$f_d = f_{\eta+1} - f_v \quad (5.21)$$

It was also shown in [150] that a low frequency signal at the difference frequency was also present and this too had its own harmonic which decreased in amplitude as the harmonic number increased.

When the vortex shedding frequency breaks away from the vibrating frequency the vortex induced vibration ceases as does the lock-in phenomenon. The vortex shedding frequency returns to the Strouhal frequency of Eqn. 4.14 and the string does not produce its distinctive sound.

5.4.4 Implementation

A compact sound source synthesis model was used for each string in the Aeolian harp model. The value for the Strouhal frequency $f_s[n]$ was obtained as described in Section 4.2.4. The fundamental string vibration frequency was calculated from Eqn. 5.14 by setting the harmonic number $\eta = 1$. The number of the harmonic nearest to the Strouhal frequency was then calculated using Eqn. 5.22.

$$\eta[n] = \text{round}\left(\frac{f_s[n]}{f_1}\right) \quad (5.22)$$

The string vibration frequency harmonic nearest the Strouhal frequency was then calculated from Eqn. 5.23.

$$f_\eta[n] = \eta[n]f_1 \quad (5.23)$$

Vibration Magnitude Calculations

A discrete implementation of Eqn. 5.15 enabled the calculation of the reduced velocity. To replicate the plots shown in [127, 20, 65, 57] a number of sigmoid functions were implemented. These were chosen to have similar characteristics to the plot, including the hysteresis property and gave a peak value of 1. This normalised peak value could then be multiplied by the calculated value of $A[n]$ to reproduce the vortex induced vibrations characteristics for that string.

To calculate a value for $A_{max}[n]$ the value of $\alpha[n]$ had to be calculated. An assumption made in this calculation was that the relationship between b/m remained constant for all harmonics. Eqn. 5.17 can then be rewritten as Eqn. 5.24.

$$4\zeta\pi f_\eta[n] = 4\eta[n]\zeta\pi f_1 \quad (5.24)$$

Applying this to Eqn. 5.18 gives Eqn. 5.25 which calculates the mass-damping parameter required to calculate the maximum vibration amplitude.

$$\alpha[n] = m^* \eta[n]\zeta \quad (5.25)$$

The transition between low and high Reynolds number, which determines the equation used to calculate the maximum vibration amplitude, was given to be a value of $R_e = 500$ in [65]. Once the magnitude of the maximum string vibration was calculated, Eqn 5.19 or 5.20, the output from the sigmoid functions (Fig. 5.24) was scaled appropriately. The magnitude of this vibration was assumed to be directly proportional to the amplitude of the sound wave produced by the vibrating string.

Modulation

The difference frequency $f_d[n]$ used as the modulating frequency was calculated from a discrete implementation of Eqn. 5.21. The main acoustic output $y_{FM}[n]$ with the vortex shedding frequency as the carrier is given in Eqn. 5.26.

$$y_{FM}[n] = \cos(2\pi(f_v[n] + \chi \cos(2\pi f_d[n]))) \quad (5.26)$$

where χ is the modulation index which was provided as user input. The low frequency modulated signal at the difference frequency $y_{LFFM}[n]$ was calculated as shown in Eqn. 5.27.

$$y_{LFFM}[n] = 0.1 \cos(2\pi(f_d[n] + \chi \cos(2\pi f_d[n]))) \quad (5.27)$$

where the multiplication factor of 0.1 corresponds to a similar reduction in power shown in [150].

Output Signal

When the string was not in the lock-in region the output was given as the Aeolian tone signal from the Aeolian tone compact sound source. When the string enters the lock-in region the acoustic intensity of the Aeolian tone greatly increases, partially due to the increase in vortex correlation (correlation length in Section 4.2.4) along the length of the string, [57, 12]. To model this a value of $200A_{max}[n]$ was added to the value calculated in Section 4.2.4 based on perceptual observation as no specific value was found within the literature.

The value of the vibration amplitude was applied as a gain to the modulated signal. This gave the discrete output signal $y[n]$ as:

$$y[n] = g[n] + \Lambda A_{max}[n](y_{FM}[n] + y_{LFFM}[n]) \quad (5.28)$$

where the variable Λ is a scaling factor between the modulated output based on the plot by [150] and the Aeolian tone compact sound source, $g[n]$. This was set perceptually to 5×10^{-15} .

To generate a signal representing a scalar windspeed a model from [49] was adapted, allowing a user to control the underlying windspeed and the number of gusts in the wind. An image of the GUI for the Aeolian harp is shown in Fig. 5.26. It can be seen that the user was able to adjust the modulation index, windspeed, gusts and gains. Four pre-set Aeolian harps were provided.

5.4.5 Evaluation

The evaluation of the Aeolian harp was carried out both objectively and subjectively. For the objective test material from Roger Winfield's CD, Windsongs [157], was used. Details of the harps used in [157] was limited but were described as six foot taller or higher, [41]. The string tension, diameter, linear mass density are all unknown.

On Professor Gurr's website³, he compliments the recordings as being of very high quality, but this was achieved by editing recordings taken over a number of months, hence only the best clips were used. Professor Gurr was also of the opinion that the recordings may have been slowed down to achieve the low notes heard.

Other material used in the listening test, both used as examples of real sounds and for SMS synthesis, were obtained from YouTube. The provenance for these recordings cannot be confirmed.

Objective Evaluation

An objective evaluation was carried out to examine and identify similarities and differences in the signal properties. This was intended to highlight where the synthesis model performs well compared to real harps and where the synthesis model falls short. It is conceded that the best objective evaluation would be to compare the synthesis model with a real harp of known dimensions generating sound with a known airspeed. This would allow the model parameters to be as close as possible to those of the actual harp and hence a fairer comparison. It should also be noted that the recording technique used for the real harp was unknown as well as if any audio effects have been added.

³<http://web.usca.edu/math/faculty-sites/henry-gurr/aeolian.dot>

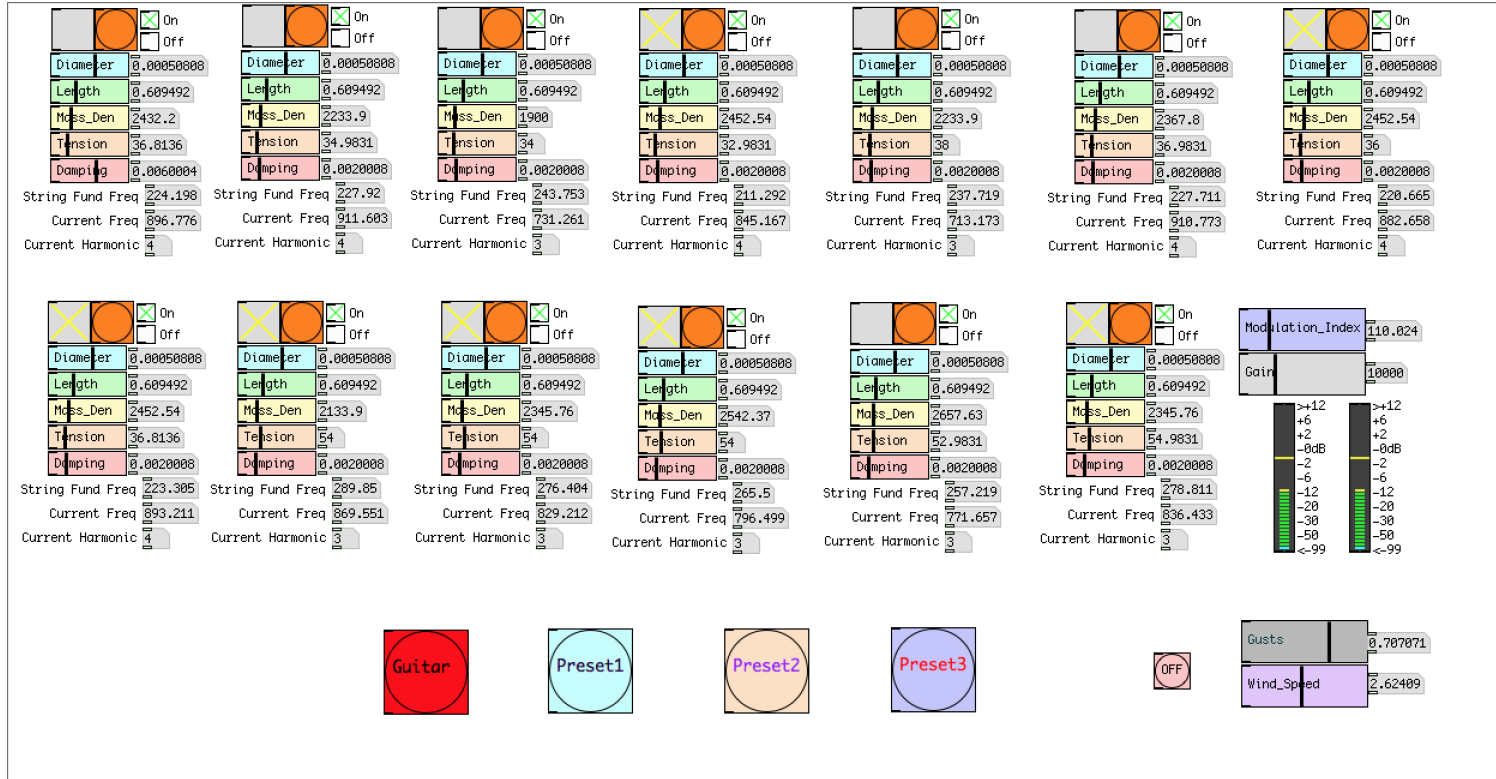


Figure 5.26: Pure Data GUI for Aeolian Harp sound effect

Two separate clips were analysed; the first of two clips that display quite contrasting characteristics and the second where some similarities can be seen. The time, spectrogram and frequency magnitude spectrum for the first sounds can be seen in Figs. 5.27, 5.28 and 5.29. In the time plot of Fig. 5.27a it can be seen that the general signal level was quite low with a much larger signal around 6 seconds. After the main peak the signal level returns to quite low.

In the spectrogram shown in Fig. 5.28a, the peak can be seen around 6 seconds. This was also the area where there was the maximum number of harmonics. The spectrogram shows a clear area where the strings are engaged, around 6 seconds, with similar around 1 second, 4 second and 13 seconds. The spectrogram in Fig. 5.28a has a number of strong components for the length of the recording representing the fundamental vibration of the strings.

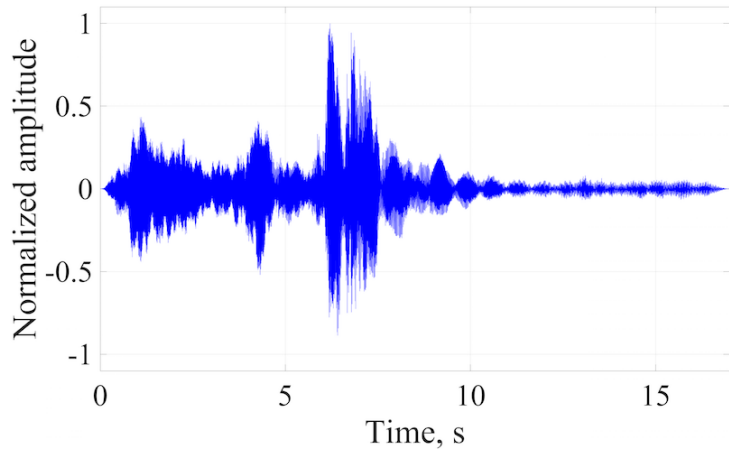
The frequency magnitude spectrum in Fig. 5.29a shows the largest peak around 150 Hz with a number of partials at decreasing decibel levels. The time plot in Fig. 5.27b show two regions where the strings are in lock in, at 0 seconds and around 8 seconds. The regions of lock in last longer than the ones shown in Fig. 5.27a. The real recording time plot has more variety in amplitude between the lock in sections indicating that the number of strings, airspeed and vibration amplitude was different between the regions.

The spectrogram in Fig. 5.28b has similar constant frequency components but these vary when the strings are not vibrating in the lock-in region. In the region where the strings go out of lock in, approximately between 5 and 7 seconds, it can be seen that the frequency values slide down and additional low frequency components appear. The low frequency components are believed to be the output due to the difference frequency f_d as detailed in Section 5.4.3. This was not seen in the real recording and indicates that the gain value applied to this component was possibly too high.

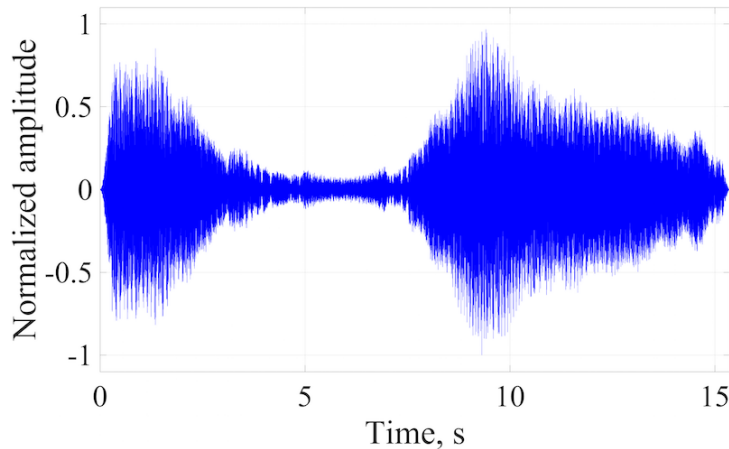
The frequency magnitude spectrum in Fig. 5.29b show a number of partials increasing up to around 800 Hz which then tails off. There was insignificant high frequency content above approximately 1.1 KHz. The number of partials, as seen in the spectrogram, was far less than the recorded signal. This could be due to the number of strings or the modulation index. It is also quite possible that there is a relationship between fluid dynamics and mechanical interactions that varies the number of harmonics which was not captured by the synthesis model.

A second comparison between the signal of a real Aeolian harp and the synthesis model is shown in Figs. 5.30, 5.31, and 5.32. The time plot of the real harp in Fig. 5.30a appears to have modulated properties. These can also be seen in the synthesised time plot in Fig. 5.30b but at a faster rate of change in amplitude.

Fig. 5.31a has the strong harmonics through the spectrogram which were seen in Fig. 5.31b. Areas where the number of harmonics increase, and decrease can be seen which indicate areas



(a) Time plot of recorded Aeolian harp



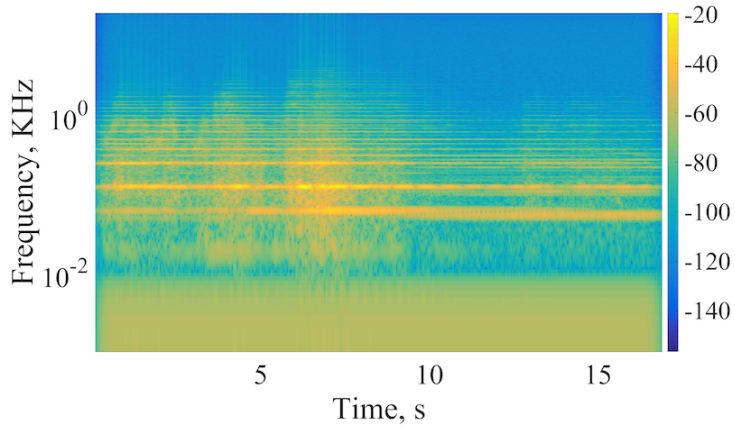
(b) Time plot of physical model of Aeolian harp

Figure 5.27: Time plots of an Aeolian harp

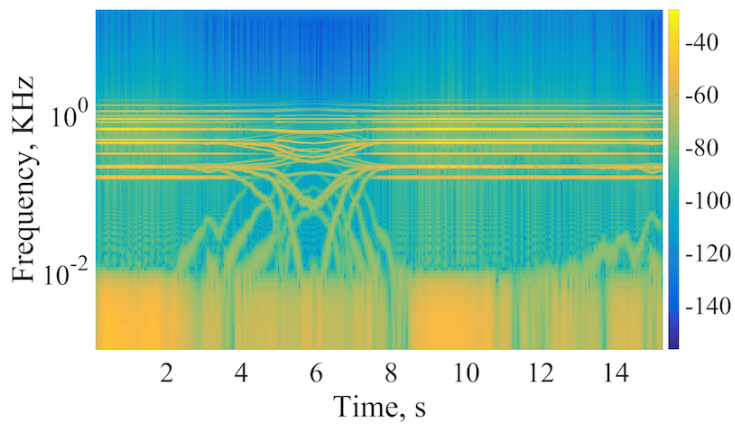
where different strings start to vibrate or fall out of lock-in. The synthesis model has strong partials running through the spectrogram. Where strings go into and fall out of lock in can be seen by the almost vertical lines in the spectrum.

The comparison between real and synthesised spectrograms again shown that there was little high frequency components and varying number of harmonics in the synthesised sounds compared to the real ones. This is corroborated by examination of both the frequency magnitude spectrums of figs. 5.32a and 5.32b. The low frequency components are similar but the high frequency components are clearly different.

Possible reasons for this disparity could be that the frequency modulation of the sound from the real harp creates more sidebands. Alternatively, the physical harp that recordings were



(a) Spectrogram of recorded Aeolian harp



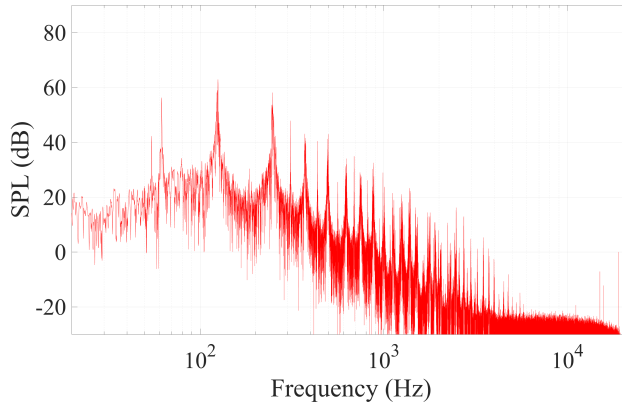
(b) Spectrogram of physical model of Aeolian harp

Figure 5.28: Spectrograms of an Aeolian harp

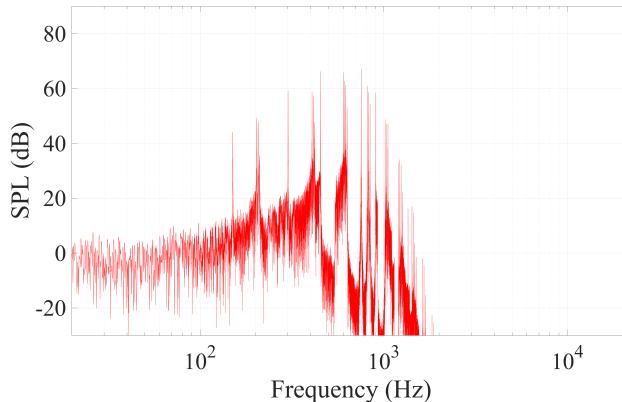
made from has more strings than the synthesised version. It is also possible that there is an interaction between the fluid dynamics and mechanics of the Aeolian harp while in lock in that is not understood. This could be a link between the vibration magnitude and the modulation index. This was not captured by the synthesis model.

Having the ability to adjust the modulation index enables a user to increase the number of harmonics which mitigates the first possible difference to some affect. Up to 13 strings can be implemented as part of the synthesis model which goes some way to mitigating the second difference. Further research is required to investigate if there is any link between the fluid dynamics and mechanics that could cause the number of sidebands to vary that has not been covered in this thesis so far.

Examination of the spectrograms does show that there is a series of fixed harmonic frequency components that are steady over a period of time. This represents areas where a specific string



(a) Magnitude Spectrum of recorded Aeolian harp



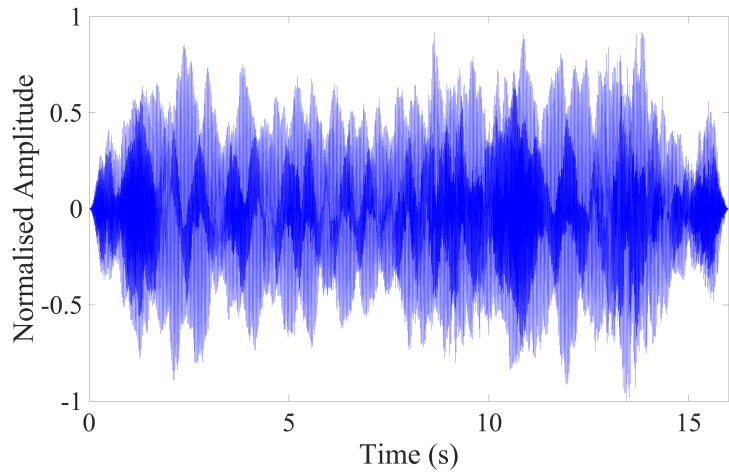
(b) Magnitude Spectrum of physical model of Aeolian harp

Figure 5.29: Magnitude Spectrums of an Aeolian harp

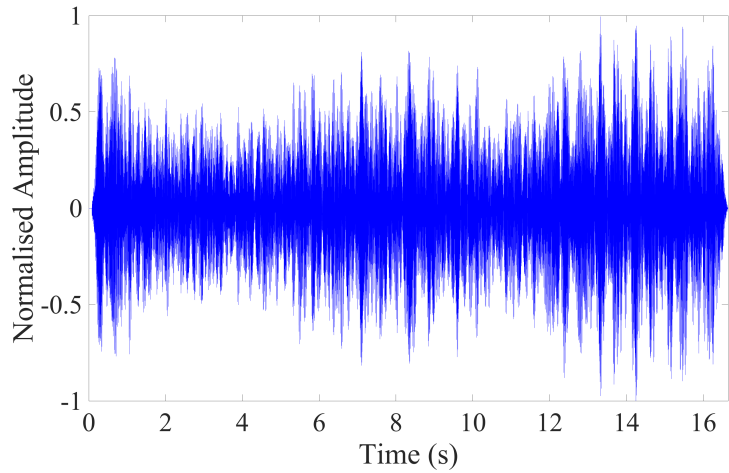
was in lock-in. The output SPL can be seen to vary while in lock-in giving some validity to mapping the vibration amplitude to the gain of the synthesis model. The amplitude was found to vary over a range of lock in airspeeds. (See Section 5.4.3 on reduced velocity.)

Subjective Evaluation

Listening tests were employed to evaluate how plausible sound generated by the synthesis model are. It was anticipated that participants may not be familiar with the sounds generated by an Aeolian harp and training would be required. To facilitate this, a short video describing the basic operation of the harp, along with a number of sound samples was shown to all participants. This can be reviewed at <https://www.youtube.com/watch?v=d6c6-u3MQDk>.



(a) Time plot of recorded Aeolian harp



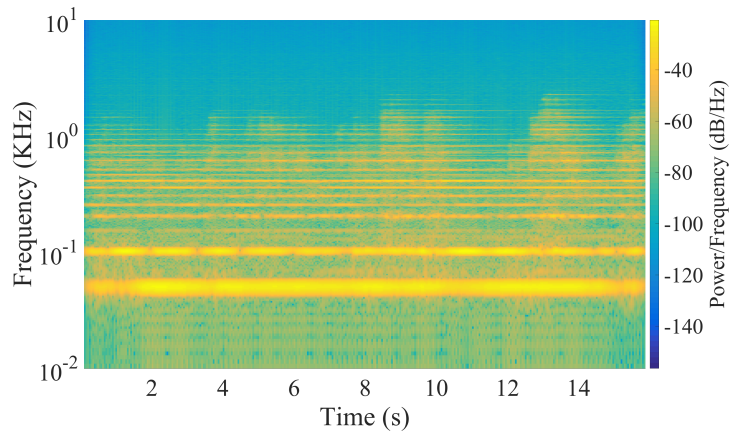
(b) Time plot of physical model of Aeolian harp

Figure 5.30: Time plots of an Aeolian harp

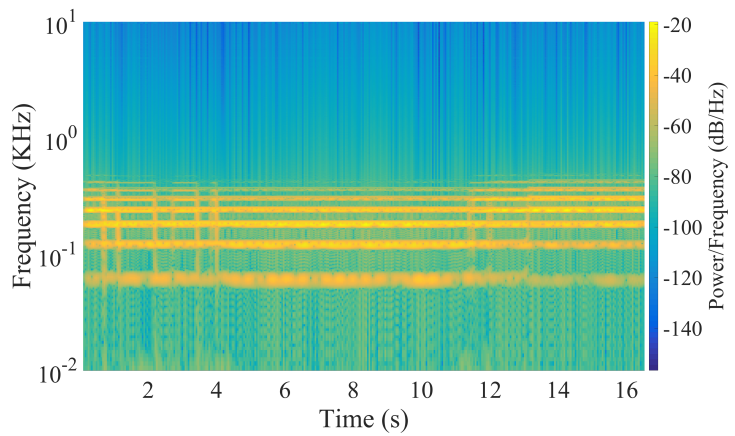
The WAET [79] was used to present the sounds to participants; these were split into four pages. Each page had six sound clips, two recordings of real harps, two clips of the synthesis model and two created from SMS. In total there was 24 clips and the SMS clips were created from real recordings not further used within the test.

There were 32 participants who took part in the listening tests, 22 male and 10 female. Ages ranged from 16 years to 77 years. Only eight participants had previously heard an Aeolian harp.

The mean perceptual rating for all clips is shown in Fig. 5.33. The recordings of real Aeolian harps can be seen to generally being rated higher than both the synthesis sounds. There was little difference between the two synthesis methods. This is seen clearly in the boxplots of the



(a) Spectrogram of recorded Aeolian harp



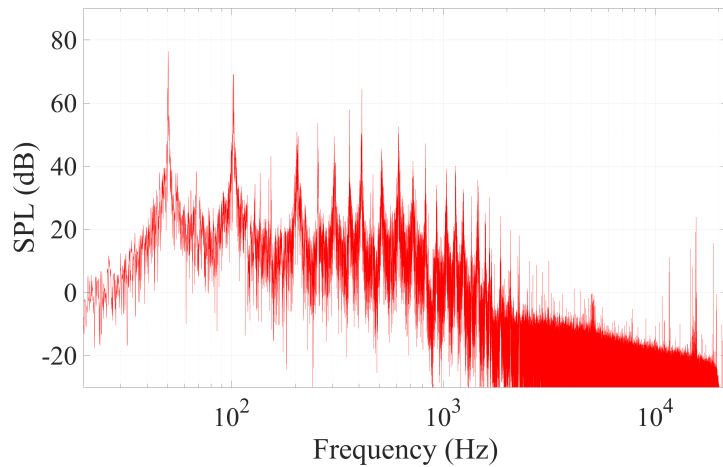
(b) Spectrogram of physical model of Aeolian harp

Figure 5.31: Spectrograms of an Aeolian harp

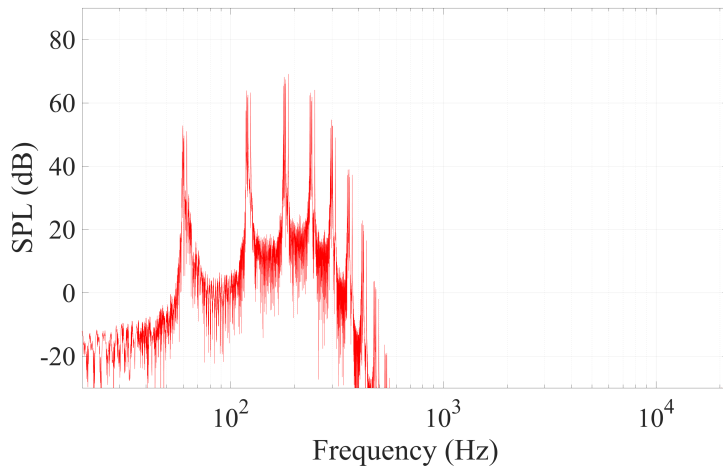
average perceptual ratings shown in Fig. 5.34. Sounds created by the synthesis model and those created from SMS technique have a mean average rating of 0.37 and 0.35 respectively.

Possible reasons for the poorer performance of the synthesis model designed here compared to the real recordings could be due to relationships between the fluid dynamics and mechanical vibrations not captured by the synthesis models. The adapted wind speed generator might not capture some of the subtleties of actual wind that drives the real Aeolian harps. It should be noted that the sounds from the synthesis model were mono but those from the Windsongs CD were stereo, which may have an influence over the perceptual rating of the sounds.

It was found that there was a significant correlation between the rating of the synthesis model clips and the harmonic number of the string vibrations within the lock-in region. The worst performing clip was operating around the 28th harmonic, where an actual Aeolian harp would



(a) Magnitude Spectrum of recorded Aeolian harp



(b) Magnitude Spectrum of physical model of Aeolian harp

Figure 5.32: Magnitude Spectrums of an Aeolian harp

not operate. Although this makes a difference within the synthesis model ratings, it does not make a difference between the real sounds and alternative synthesis sounds overall.

5.4.6 Concluding Comments on Aeolian Harp

A real-time synthesis model of an Aeolian harp has been presented. The synthesis model was based on fundamental equations from fluid dynamics and mechanics of the strings. Objective evaluation highlights that there are some properties not captured by the synthesis model, including the variation of the number of harmonics.

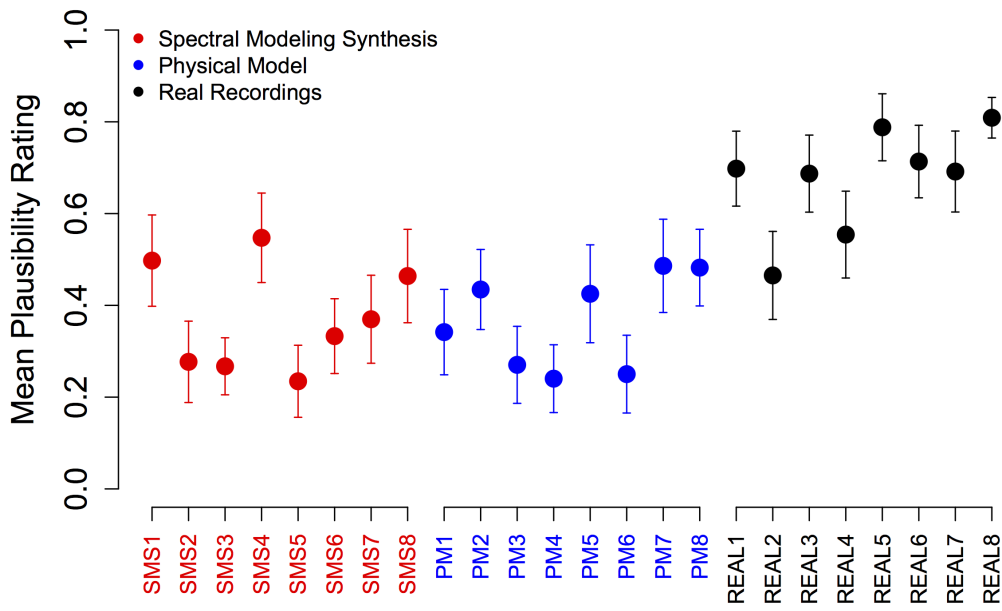


Figure 5.33: Mean perceptual rating of Aeolian harp sounds, including 95% confidence intervals

Subjective evaluation show that the synthesis model was as plausible as an alternative synthesis method but not as plausible as recordings of real Aeolian harps. The advantage of this synthesis model over the alternative technique is that the user is able to select between one and thirteen strings, the length and diameter of each string as well as the linear mass density and tension. This gives users a much greater freedom over harp design.

The user was also given the ability to manipulate the modulation index of the frequency modulated signal which adjusts the number of harmonics in the output signal. The ability to adjust the damping factor reducing the amount of vibration for each string was also provided. A demo of the Aeolian harp can be downloaded at <https://code.soundsoftware.ac.uk/projects/aeolianharp>.

Future development would include investigating if there is any link between the number of harmonics and the vibration amplitude. It would be of value to design a physical Aeolian harp and record sounds while measuring the windspeed. This could give a fairer objective evaluation and possibly highlight properties not captured by the synthesis model. This would also allow research into the different recording techniques that might be employed for real Aeolian harps, whether it is preferred to use contact microphones or even pick-ups like those used in an electric guitar. It is also possible that there is some mechanical and fluid dynamic coupling between adjacent strings which was not captured which may have a strong influence of the acoustics produced by an Aeolian harp.

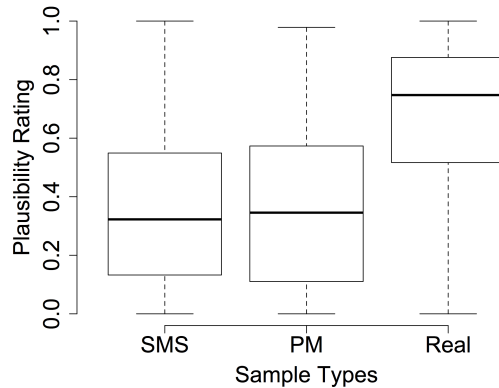


Figure 5.34: Boxplot for Aeolian harp sounds

5.5 Summary

This chapter has presented three different example models that can be designed and developed using synthesis models of compact sound source. The examples shown in this chapter are a very small cross section of the number of possible aeroacoustic sound effects. The models presented illustrate how the aeroacoustic sounds effects can operate in conjunction with other sound generating forces.

The level of control via the parameterisation is believed to be unmatched for similar synthesis models that operate in real-time. It is believed the behaviour of the items modelled has a great influence over the plausibility of the sound effects and is area where future developments or coupling with a game engine may bring further improvements.

Objective evaluation of the objects would have been of higher quality if it was possible to have full control over an actual physical object that was being modelled and controlling all the conditions and parameters of these. This would then enable a synthesis model with all the parameters replicated as close as possible and provide equivalent models to compare.

Evaluation of the sound effects indicates that the synthesis models developed are perceived as plausible as an alternative synthesis method. Areas where the synthesis models fall short of pre-recorded samples have been highlighted and possible explanations given.

Chapter 6

Conclusion

The main achievement of this research was to develop a number of compact sound sources enabling the modelling of fundamental aeroacoustic sounds. Unlike previous approaches, the methods presented have used semi-empirical equations derived from fluid dynamic principles, bestowing the physical properties of these equations onto the synthesis models.

It is believed these semi-physical synthesis models are closer to physical models than physically inspired ones. The knowledge of physics incorporated into the models goes beyond any physically inspired models the author has encountered previously. The compact sound source models make use of equations and theories, some of which would have been state of the art for scientists and engineers prior to the use of computers. It is for this reason that it is believed justified in comparing results from the compact sound sources to previously published experimental and simulated data.

It has been demonstrated how the compact sound sources can be used separately, in combination or along with other sound generating mechanisms. Examples of synthesised sound effects range from simple to complex objects each producing unique aeroacoustic sounds.

The importance of modelling the behaviour of objects being synthesised has been highlighted. Creating a more accurate behaviour for the objects should increase plausibility of each synthesis model.

Calculating the acoustic output due to forces, pressures, flows, geometry, etc., is complex. Often real-time computations require specialist hardware which would be impractical to use in an environment like a game where there often is limited computational power available for sound, including music, sound effects and vocals.

A procedural approach to sound effects, where sounds have a build in authenticity has great appeal in virtual environments. Physical models and physically derived models have a clear benefit over signal-based models due to the understanding of the relationships between parameters, as there is in nature.

The ability to present the users with relevant parameters has great value. Animation and game engine environments often evolve based on the laws of physics therefore sound models that are based on the physics and present physical properties as parameters have great potential.

One issue found when mapping a sound effect to a physical object within a game engine was that often the game object broke the laws of physics due to the fantastic nature of the game. This created unrealistic sounds from the models and often high gain due to the relationship between airspeed and acoustic intensity.

What equations derived from Fluid Dynamics predict aeroacoustic sounds?

A key contribution of this thesis is to describe a methodology for implementing aeroacoustic sound effects using noise shaping synthesis techniques. A literature review of the fundamental principles for the three aeroacoustic tones was undertaken. By implementing the fundamental tones as compact sound sources enables a wide variety of aeroacoustic sound effects to be modelled.

Where possible semi-empirical equations have been implemented to ensure as much knowledge of the physics as possible was built into each model. These equations were defined by engineers usually to enable approximate noise from aeroacoustic sources to be predicted. These could then be used to reduce said noise. In contrast to the original purpose of these equations, they are presented here as the foundations to synthesis models, creating sound effects for interactive media.

Can these be used in a real-time sound synthesis model?

By using semi-empirical equations in the design of each compact sound source synthesis model, real-time implementation was achievable. This is another strength of the models developed in this thesis as complex computations are not required to achieve plausible sound effects. It is believed no other synthesis models can achieve such level of knowledge of physics while maintaining a low computational, real-time performance.

What additional properties are not available from equation and how can these be predicted?

It is acknowledged that not all of the properties required for our sound effects have been studied by the aeroacoustic community. For example, the relationship between Reynolds number and bandwidth of the cavity or edge tone has not been, to the best of our knowledge, fully studied and

the relationship documented. In circumstances where no equation was forthcoming characteristics were modelled based on published experimental results.

Often the relationship between the tone bandwidth and the flow characteristics (Reynolds number) have been implemented by using best-fit equations. The prediction of the edge tone mode has been implemented using machine learning techniques. Both implementations are based on previously published data from the aeroacoustic community.

How accurate are the synthesis models compared to previously published results?

Objective evaluation has been carried out for each of the compact sound source models. The frequency of each of the fundamental tones has been compared to experimental, simulated and other theoretical results.

The results for the Aeolian tone are very close to previously published results, whereas the results for all the edge tone models are not as close. This reflects in some way to the volume of research carried out on the different tones and the level of understanding of the fluid dynamic mechanisms generating the sounds. To improve the prediction of the edge tone frequency a new equations has been introduced, based on previously published data.

The prediction of the dominant mode in the cavity tone was based entirely on flow characteristics and predicts the dominant mode correctly when compared to previously published results, Table 4.6. (It is noted that some studies did not indicate the dominant mode.)

The decision tree established for prediction of the edge tone mode has been shown to have an accuracy of 82.69%. This was found through 10-fold cross validation from previously published data. This is the only mode prediction model known by the author.

Can example sound effects be produced, what range of objects can these model and how perceptually plausible are these?

Three example sound effect models have been developed and subjected to evaluation. These are swinging objects, propeller and Aeolian harps. The swinging object model has been shown to replicate objects successfully from swords to baseball bats. Generally these models were found to be just as plausible as the real sounds with a high level of controllability given to the user. Future developments are given in Section 6.1.1.

The propeller model has been implemented as part of a propeller powered aircraft. Aircraft such as a small Tiger moth from the 1930s to a large Hercules from the 1950s have been modelled. These show the wide range of propeller powered aircraft that can be modelled by the synthesis models. The sound effect models gives users a high level of control which is believed to be unique. Although the sound effect was found to be just as plausible as an alternative synthesis model,

there are still areas for future development for this effect, Section 6.1.1.

A 13 string Aeolian harp model has been developed to replicate a range of actual harps. The string lengths, diameters and tension can be adjusted to any value, although have been set to lie within practical limits in the model. Like the propeler sound effect, the Aeolian harp model was found to be just as plausible as an alternative synthesis model and gives users a unique level of control. Areas for future development have been highlighted, Section 6.1.1.

Where do the sound synthesis models not capture all the physical qualities of real sounds?

The perceptual tests rating the plausibility for the propeller powered aircraft and Aeolian harp show that both models are not as plausible as pre-recorded samples. Results show that there are aspects of the real sounds that are not captured by our model, but all models perform as well as an alternative synthesis technique.

The nature of the semi-empirical equations mean that some approximations have been made and at times the operating conditions are specified. For example, some equations have assumptions that the airspeed was less than Mach 1 and lose accuracy as the airspeed reaches this.

The engine model used in the propeller powered aircraft model could have a strong influence over the sounds produced. This model was a physically inspired model and it is believed that one with greater knowledge of the physics may give higher plausibility ratings for the propeller powered aircraft presented.

6.1 Future Developments

6.1.1 Existing Sound Effect Models

Swinging Objects

The profile of swords could be extended, testing a number of sword cross sections. A synthesis model could be developed which takes into consideration the material the object. This has a close affiliation with the Aeolian harp model where the relationship between the natural frequency and mass density of each string affects the sound produced.

The possibility of a relationship between fundamental tones when generated together was found in [121] where possible modulation was witnessed. Future research into the effects of this on the sound effects could reveal additional frequency partials, creating a more realistic sound.

Increasing the accuracy of the behaviour model for swinging objects could increase the plausibility of the sound effect. In the model presented each swing was replicated by a circular swing with a stationary elbow. Often this is an arc as the elbow moves backwards and forwards rather than staying at a fixed point.

A number of additional models could be examined including:

- Bo Staff
- Tennis racket
- Nunchakus
- Lacrosse sticks
- Garrotte wire

The Aeolian tone compact sound sources would also be able to reproduce the sounds generated when the spokes of a bicycle wheel are spinning.

Propeller model

The objective evaluation of the propeller model would be greatly increased if wind tunnel results or similar were available for a known propeller under controlled conditions. That would allow parameters to be replicated in the synthesis model and provide more exact feedback.

A physical model of each of the engines used by the aircraft used for comparison could increase the plausibility of the propeller powered aircraft models. Current propeller aircraft developments include ones powered by electric motors. These are much quieter than combustion motors and it is envisaged that the synthesis models would fair very well compared with these.

The number of sound sources in the model was limited to loading sounds and vortex sounds, (Fig. 5.9). Increasing the model to include thickness sounds might improve plausibility. The relationship between the loading sounds, vortex sounds and others has not been found. Research into this should improve accuracy in this model.

The pre-recorded samples used for the subjective evaluation generally have the acoustic characteristics of the recording environment imprinted on it. The sound effects produced by the synthesis model are equivalent to being produced in an anechoic chamber. The addition of reverb, ground reflections and other sound effects may have significant effect on the quality of the sound effects.

It may be of value to increase or decrease the number of Aeolian tone representing the vortex sounds. Likewise, the number of harmonics used for the loading noise. This model has proven the

concept, but further computational versus plausibility investigations might improve the model. The material used for propeller blade may also affect the sound produced.

The model of the aircraft presented here has a narrow behaviour as it limits the movement to the aircraft flying in a straight line at a fixed pitch. Increasing the behaviour to include banking and other behaviours could improve the plausibility of the sound effect.

Developing the propeller model to include rotors by adding in the interaction and distortion effects. Horizontal rotors as seen in a helicopter or VTOL aircraft have additional sounds. These are sounds such as blade slap which is generated as each blade moves through the turbulence of the previous blade. Helicopter blades pass through the air at different speeds due to the vehicle movement which changes the vortex shedding frequency as a blade rotates.

Aeolian harp

Further research to identify if there is a link between the vibration amplitude of a string and its modulation index. There may also be interaction between adjacent strings which adds to the plausibility of the sounds.

The objective evaluation of the Aeolian harp model would be improved if recordings of known harps was undertaken, allowing parameters to be set to identical values and results measured.

6.1.2 Potential Models

Compact Sound Sources

As seen in Section. 3.4, a number of different aeroacoustic tones exist. These include the hole tone, pipe tone, screech tone and turbulence. Creating compact sound source synthesis models for these tones opens up a large number of different objects and items which potentially could be modelled.

Synthesis models

The cavity model could be combined with the propeller powered aircraft model to represent the cavities produced when the landing gear is extended or weapons bays opened. This could provide an aural cue in a simulator or video game scenario. Investigation into the sound effects that model sounds produced when car windows or sunroofs are opened is an area for future research.

The turbulent noise from the jet stream was already examined when researching the wake sounds of the Aeolian tone. Sounds generated from a high speed subsonic jet are strongly influenced by these sounds. An initial subsonic jet could be extended to synthesis the sounds of a supersonic jet, including sonic booms and screech tones.

The implementation of a hole tone compact sound source synthesis model would provide the basis for creating synthesis models for objects such as kettles, police whistles and others.

6.1.3 Methodology Extension

An area for future research in relation to this thesis could be to implement the methodology of designing compact sound source synthesis models to other types of sounds. A logical progression may be to investigate if these type of models could be used to implement sound effects generated by water rather than air.

Investigation into extending this further to cover contact sounds, friction sounds, and others would enable the construction of a much wider library of sound effects.

Difficulty can occur when the object being modelled breaks the laws of physics. This was witnessed with the sword model when the sound effect was mapped to the animation then the character swung the sword at speeds higher than physically possible. This caused the sound effect to produce an extremely loud sound but accurate to the relationship between airspeed and acoustic intensity. This indicates that the use of artistic control to balance the accurate and procedural characteristics to the intensity of sounds within a mix of other sounds that might be in a scene.

6.2 Summary of contributions

This thesis has outlined a unique approach to the synthesis of aeroacoustic sound effects. Three compact sound source models have been researched, designed and implemented. All of these models are based on sound equations, in the majority taken directly from research carried out by the fluid dynamics community. Where equations defining direct relationships between parameters and the synthesis model could not be obtained, ones were devised based on previously published experimental results.

Three synthesis models illustrating how the compact sound sources can be used to create sound effect models have been given. These models show how the behaviour of the models have a strong influence over the sounds produced. The interaction between sound producing phenomenon has

been shown as well as directions for future development provided.

When a sound effect is generated by a specific behaviour of the object, the sound produced will be equally specific, based on physical properties. The sound effect models can therefore all be classified as procedural audio effects suitable for implementation in virtual reality or video games as well as linear media.

APPENDIX A

Lighthill's Acoustic Analogy

Lighthill's acoustic analogy is a means of deriving a wave equation with aeroacoustic source terms [118]. Acoustic sources are shown to represent fluid dynamic processes that generate sound. Lighthill's analogy is derived from the fundamental Navier / Stokes equations of mass and momentum conservation [106, 139].

The derivation from the Navier / Stokes to the wave equation of Lighthill's acoustic analogy is given in this appendix. The steps followed are based on the work presented in [118]. The non-homogeneous wave equation is given by:

$$\frac{\partial^2 p'}{\partial t^2} - c_0^2 \nabla^2 p' = q \quad (\text{A.1})$$

where p' is the pressure perturbations (acoustic field), c_0 the speed of sound and q the source term. It shall be shown in Appendix B that p' can be determined from a known q via Green's functions.

The vector and tensor notation of the mass conservation equation is given in Eqn A.2 [118]:

$$\begin{aligned} \frac{\partial \rho}{\partial t} + \nabla \cdot (\rho \vartheta) &= m \\ \frac{\partial \rho}{\partial t} + \frac{\partial}{\partial x_i} (\rho \vartheta_i) &= m \end{aligned} \quad (\text{A.2})$$

where ρ is the fluid density, ϑ is the flow velocity and time t . The value m is a mass source term, generally $m = 0$ where mass is conserved. The momentum conservation equation is given in equation A.3 [118]:

$$\begin{aligned} \frac{\partial}{\partial t} (\rho \vartheta) + \nabla \cdot (\mathbf{P} + \rho \vartheta \vartheta) &= \mathbf{f} + m \vartheta \\ \frac{\partial}{\partial t} (\rho \vartheta_i) + \frac{\partial}{\partial x_i} (\mathbf{P}_{ji} + \rho \vartheta_j \vartheta_i) &= f_i + m \vartheta_i \end{aligned} \quad (\text{A.3})$$

where \mathbf{f} is an external force density, \mathbf{P} is the fluid stress tensor and the mass adds momentum by the amount $m\vartheta$. We can write the mass m as a density ρ_m of volume fraction $\beta = \beta(\mathbf{x}, t)$, with an injection rate [118]:

$$m = \frac{\partial}{\partial t}(\beta\rho_m) \quad (\text{A.4})$$

When there is a source $\beta \neq 0$ and the injected mass displaces the original mass ρ_f by the same amount of volume. Therefore the total fluid density is given by:

$$\rho = \beta\rho_m + (1 - \beta)\rho_f \quad (\text{A.5})$$

Through substitution Eqn. A.2 and eliminating $\beta\rho_m$ we get:

$$\frac{\partial}{\partial t}\rho_f + \nabla \cdot (\rho\vartheta) = \frac{\partial}{\partial t}(\beta\rho_f) \quad (\text{A.6})$$

Take the time derivative of Eqn. A.6:

$$\frac{\partial}{\partial t}\nabla \cdot (\rho\vartheta) = \frac{\partial^2}{\partial t^2}(\beta\rho_f) - \frac{\partial^2\rho_f}{\partial t^2} \quad (\text{A.7})$$

and take the divergence of Eqn A.3:

$$\frac{\partial}{\partial t}\nabla \cdot (\rho\vartheta) = -\nabla^2(\mathbf{P}_{ij} + \rho\vartheta_i\vartheta_j) + \nabla \cdot \mathbf{f} \quad (\text{A.8})$$

In tensor format Eqns A.7 and A.8 can be written as:

$$\frac{\partial^2}{\partial t \partial x_i}(\rho\vartheta) = \frac{\partial^2}{\partial t^2}(\beta\rho_f) - \frac{\partial^2\rho_f}{\partial t^2} \quad (\text{A.9})$$

and

$$\frac{\partial^2}{\partial t \partial x_i}(\rho\vartheta) = -\frac{\partial^2}{\partial x_i \partial x_j}(\mathbf{P}_{ij} + \rho\vartheta_i\vartheta_j) + \frac{\partial}{\partial x_i}\mathbf{f} \quad (\text{A.10})$$

Hence from equation A.9 and equation A.10 it can be seen that:

$$\frac{\partial^2 \rho_f}{\partial t^2} = \frac{\partial^2}{\partial x_i \partial x_j} (\mathbf{P}_{ij} + \rho \vartheta_i \vartheta_j) + \frac{\partial^2 \beta \rho_f}{\partial t^2} - \frac{\partial f_i}{\partial x_i} \quad (\text{A.11})$$

Since only ρ' varies with time, a wave equation for ρ' can be constructed. The term $c_0^2(\partial^2 \rho' / \partial x_i^2)$ is subtracted from both sides of equation A.10 to get equation A.12. c_0 is the speed of sound at the observer.

$$\frac{\partial^2}{\partial t \partial x_i} (\rho \vartheta_i) - c_0^2 \left(\frac{\partial^2 \rho'}{\partial x_i^2} \right) = - \frac{\partial^2}{\partial x_i \partial x_j} (P_{ij} - \rho \vartheta_i \vartheta_j) + \frac{\partial f_i}{\partial x_i} - c_0^2 \left(\frac{\partial^2 \rho'}{\partial x_i^2} \right) \quad (\text{A.12})$$

Making equation A.11 now:

$$\frac{\partial^2 \rho_f}{\partial t^2} - c_0^2 \left(\frac{\partial^2 \rho'}{\partial x_i^2} \right) = \frac{\partial^2}{\partial x_i \partial x_j} (P_{ij} - \rho \vartheta_i \vartheta_j) - c_0^2 \left(\frac{\partial^2 \rho'}{\partial x_i^2} \right) + \frac{\partial^2 (\beta \rho_m)}{\partial t^2} - \frac{\partial f_i}{\partial x_i} \quad (\text{A.13})$$

We can make use of the relationship given in equation A.14:

$$c_0^2 \left(\frac{\partial^2 \rho'}{\partial x_i^2} \right) = \frac{\partial^2 (c_0^2 \rho' \delta_{ij})}{\partial x_i \partial x_j} \quad (\text{A.14})$$

where δ_{ij} is the Kronecker delta. This allows us to define Lighthill's equation:

$$\frac{\partial^2 \rho_f}{\partial t^2} - c_0^2 \left(\frac{\partial^2 \rho'}{\partial x_i^2} \right) = \frac{\partial^2 T_{ij}}{\partial x_i \partial x_j} + \frac{\partial^2 (\beta \rho_m)}{\partial t^2} - \frac{\partial f_i}{\partial x_i} \quad (\text{A.15})$$

Shortened to Eqn. A.16 if $m, f = 0$:

$$\frac{\partial^2 \rho_f}{\partial t^2} - c_0^2 \left(\frac{\partial^2 \rho'}{\partial x_i^2} \right) = \frac{\partial^2 T_{ij}}{\partial x_i \partial x_j} \quad (\text{A.16})$$

This solution illustrates a quadrupole sound source, where T_{ij} is Lighthill's stress tensor, defined by

$$T_{ij} = P_{ij} + \rho \vartheta_i \vartheta_j - (c_o^2 \rho' + p_0) \delta_{ij} \quad (\text{A.17})$$

Using the relationship $P_{ij} = p \delta_{ij} - \tau_{ij}$, equation A.17 can also be written as:

$$T_{ij} = \rho \vartheta_i \vartheta_j - \tau_{ij} + (p' - c_o^2 \rho') \delta_{ij} \quad (\text{A.18})$$

APPENDIX B

Green's Functions

Using the theory of Green's functions allows us to construct an integral equation which combines the effect of sources, propagation, boundary conditions and initial conditions in a simple formula [100]. The free-space Green's function $g(\mathbf{x}, t|\mathbf{y}, \tau)$ is defined as the pulse response of the wave equation and shown in equation B.1 [64]:

$$\frac{\partial^2 g(\mathbf{x}, t|\mathbf{y}, \tau)}{\partial t^2} - c_0^2 \frac{\partial^2 g(\mathbf{x}, t|\mathbf{y}, \tau)}{\partial x_i^2} = \delta(\mathbf{x} - \mathbf{y})\delta(t - \tau) \quad (\text{B.1})$$

where g is the Green's Function. The pulse $\delta(\mathbf{x} - \mathbf{y})\delta(t - \tau)$ is released at the source point \mathbf{y} at time τ and g is measured at the observation point \mathbf{x} at time t . In filter theory this can be thought of as the impulse response, similarly as an impulse response in room acoustics. The Green's Function satisfies the reciprocity relationship $g(\mathbf{x}, t|\mathbf{y}, \tau) = g(\mathbf{y}, -\tau|\mathbf{x}, -t)$ and can be shown to satisfy Eqn. B.2 [71]:

$$\frac{\partial^2 g(\mathbf{x}, t|\mathbf{y}, \tau)}{\partial \tau^2} - c_0^2 \frac{\partial^2 g(\mathbf{x}, t|\mathbf{y}, \tau)}{\partial y_i^2} = \delta(\mathbf{x} - \mathbf{y})\delta(t - \tau) \quad (\text{B.2})$$

Given the wave equation:

$$\frac{\partial^2 \rho'}{\partial t^2} - c_0^2 \frac{\partial^2 \rho'}{\partial y_i^2} = q(\mathbf{y}, \tau) \quad (\text{B.3})$$

where $q(\mathbf{y}, \tau)$ is the sound source. Multiplying Eqn. B.2 by $\rho'(\mathbf{y}, \tau)$ to give:

$$\rho'(\mathbf{y}, \tau) \frac{\partial^2 g(\mathbf{x}, t|\mathbf{y}, \tau)}{\partial \tau^2} - \rho'(\mathbf{y}, \tau) c_0^2 \frac{\partial^2 g(\mathbf{x}, t|\mathbf{y}, \tau)}{\partial y_i^2} = \rho'(\mathbf{y}, \tau) \delta(\mathbf{x} - \mathbf{y})\delta(t - \tau) \quad (\text{B.4})$$

Equation B.3 is multiplied by $g(\mathbf{x}, t|\mathbf{y}, \tau)$:

$$g(\mathbf{x}, t|\mathbf{y}, \tau) \frac{\partial^2 \rho'}{\partial t^2} - g(\mathbf{x}, t|\mathbf{y}, \tau) c_0^2 \frac{\partial^2 \rho'}{\partial y_i^2} = q(\mathbf{y}, \tau) g(\mathbf{x}, t|\mathbf{y}, \tau) \quad (\text{B.5})$$

Subtracting Eqn. B.4 from Eqn. B.5 gives, (where $g(\mathbf{x}, t|\mathbf{y}, \tau)$ is written as g for readability):

$$g \frac{\partial^2 \rho'}{\partial \tau^2} - \rho'(\mathbf{y}, \tau) \frac{\partial^2 g}{\partial \tau^2} - g c_0^2 \frac{\partial^2 \rho'}{\partial y_i^2} + \rho'(\mathbf{y}, \tau) c_0^2 \frac{\partial^2 g}{\partial y_i^2} = \\ -\rho'(\mathbf{y}, \tau) \delta(\mathbf{x} - \mathbf{y}) \delta(t - \tau) + q(\mathbf{y}, \tau) g \quad (\text{B.6})$$

Re-arranging gives:

$$\rho'(\mathbf{y}, \tau) \delta(\mathbf{x} - \mathbf{y}) \delta(t - \tau) = q(\mathbf{y}, \tau) g \\ + \rho'(\mathbf{y}, \tau) \frac{\partial^2 g}{\partial \tau^2} - g \frac{\partial^2 \rho'}{\partial \tau^2} - c_0^2 \left(\rho'(\mathbf{y}, \tau) \frac{\partial^2 g}{\partial y_i^2} - g \frac{\partial^2 \rho'}{\partial y_i^2} \right) \quad (\text{B.7})$$

Equation B.7 is then integrated to \mathbf{y} over volume, V and to τ between t_0 to $t+$.

$$\rho'(\mathbf{x}, t) = \int_{t_0}^{t+} \iiint_V q(\mathbf{y}, \tau) g d\mathbf{y} d\tau + \int_{t_0}^{t+} \iiint_V \left[\rho'(\mathbf{y}, \tau) \frac{\partial^2 g}{\partial \tau^2} - g \frac{\partial^2 \rho'(\mathbf{y}, \tau)}{\partial \tau^2} \right] d\mathbf{y} d\tau \\ - c_0^2 \int_{t_0}^{t+} \iiint_V \left[\rho'(\mathbf{y}, \tau) \frac{\partial^2 g}{\partial y_i^2} - g \frac{\partial^2 \rho'(\mathbf{y}, \tau)}{\partial y_i^2} \right] d\mathbf{y} d\tau \quad (\text{B.8})$$

Partial integration over the time of the second integral and over the space of the third integral in the right-hand side of (B.8) gives:

$$\rho'(\mathbf{x}, t) = \int_{t_0}^t \iiint_V q(\mathbf{y}, \tau) g d\mathbf{y} d\tau - c_0^2 \int_{t_0}^t \iint_S \left[\rho'(\mathbf{y}, \tau) \frac{\partial^2 g}{\partial y_i^2} - g \frac{\partial^2 \rho'(\mathbf{y}, \tau)}{\partial y_i^2} \right] n_i d\mathbf{y} d\tau \\ - \left[\iiint_V \left[\rho'(\mathbf{y}, \tau) \frac{\partial^2 g}{\partial \tau^2} - g \frac{\partial^2 \rho'(\mathbf{y}, \tau)}{\partial \tau^2} \right] d\mathbf{y} \right]_{\tau=t_0} \quad (\text{B.9})$$

where n_i is the outer normal to the surface S . A tailored Green's function is where the boundary conditions eliminates the surface integral to zero [100]. The third integral represents the effect of the initial conditions at $\tau = t_0$. If $t_0 = -\infty$ the solution can be written as:

$$\rho'(\mathbf{x}, t) = \int_{-\infty}^t \iiint_V q(\mathbf{y}, \tau) g d\mathbf{y} d\tau \quad (\text{B.10})$$

The free-field Green's function in cartesian co-ordinates is stated in Appendix B of [100] as:

$$g_\infty(\mathbf{x}, t | \mathbf{y}, \tau) = \frac{1}{4\pi r} \delta(t - \tau - r/c_0) \quad (\text{B.11})$$

where $r = |\mathbf{x} - \mathbf{y}|$.

APPENDIX C

The Ffowcs Williams-Hawkins Equation

An extension of Lighthill's Acoustic Analogy is given in [155] which takes into consideration the effects of solid boundaries. These boundaries have the potential to support multipole sound sources, extending the quadrupole source to include dipoles and monopoles. A simplified description of the process carried out in [155] is given in this appendix and the reader is directed towards this publication for a more detailed derivation. A generalised wave equation is:

$$\frac{\partial^2 \rho'}{\partial t^2} - c_0^2 \frac{\partial^2 \rho'}{\partial x_i^2} = \frac{\partial^2 Q_{ij}}{\partial x_i \partial x_j} \quad (\text{C.1})$$

where Q_{ij} is a generalised source function (equivalent to T_{ij} in Lighthill's Equation, Appendix A, Eqn. A.16). The solution for Eqn. C.1 (using Green's functions) is given in [155] as:

$$\rho' = \frac{1}{4\pi c_0^2} \int_{-\infty}^{\infty} \frac{\partial^n Q_{ij}}{\partial y_i \partial y_j} \frac{\delta(\tau - t + r/c_0)}{r} d\mathbf{y} d\tau \quad (\text{C.2})$$

Equation C.2 can be re-arranged and the derivatives interchanged to give:

$$4\pi c_0^2 \rho' = \frac{\partial^n}{\partial x_i \partial x_j} \int_{-\infty}^{\infty} Q_{ij}(\mathbf{y}, \tau) \delta(\tau - t + r/c_0) \frac{d\mathbf{y} d\tau}{r} \quad (\text{C.3})$$

And integrating over τ to reveal the retard time:

$$4\pi c_0^2 \rho' = \frac{\partial^n}{\partial x_i \partial x_j} \int_{-\infty}^{\infty} Q_{ij}(\mathbf{y}, t - r/c_0) \frac{d\mathbf{y}}{r} \quad (\text{C.4})$$

This equation assumes that the source term Q_{ij} is known in terms of the fixed co-ordinate system \mathbf{y} . It is common for the sources to be in motion and therefore more convenient to reference them with a Lagrangian co-ordinate system η [155], relating to the fixed system \mathbf{y} as follows:

$$\mathbf{y} = \eta + \int^{\tau} c_0 \mathbf{M}(\eta, \tau') d\tau \quad (\text{C.5})$$

where the source convection velocity is $c_0 \mathbf{M}$. When referring to the η frame, the source strength is written as q_{ij} and Eqn. C.3 becomes:

$$4\pi c_0^2 \rho' = \frac{\partial^n}{\partial x_i \partial x_j} \int_{-\infty}^{\infty} q_{ij}(\eta, \tau) \delta(\tau - t + r/c_0) J \frac{d\eta d\tau}{r} \quad (\text{C.6})$$

where r is now a function of τ and

$$J = \exp \int^{\tau} \operatorname{div} c_0 \mathbf{M}(\eta, \tau') d\tau' \quad (\text{C.7})$$

The time variable in Eqn. C.6 is replaced by a length variable λ , which relates to τ by:

$$\left. \frac{\partial \lambda}{\partial \tau} \right|_{\eta} = c_0 \alpha \quad (\text{C.8})$$

where α is a scaling factor, enabling space and time scales to be equated. This enables Eqn. C.6 to be re-written as:

$$4\pi c_0^2 \rho' = \frac{\partial^n}{\partial x_i \partial x_j} \int_{-\infty}^{\infty} q_{ij}(\eta, \lambda) \delta(\tau(\eta, \lambda) - t - r/c_0) J \frac{d\eta d\lambda}{rc_0 \alpha} \quad (\text{C.9})$$

An alternative expression for the radiated sound can be given using generalised function theory given in [80]. A volume integral containing a function and a delta function can be re-written as follows:

$$\int_{-\infty}^{\infty} F(\mathbf{z}) \delta(g(\mathbf{z})) d\mathbf{z} = \int_{\Sigma_k} \left[\frac{F}{|\partial g / \partial z_k|} \right] (\mathbf{z}^*) d\mathbf{z}_k \quad (\text{C.10})$$

where z^* is a point on the hypersurface defined by $g(z^*) = 0$. Using this result, [155] has shown that Eqn. C.9 is equal to:

$$4\pi c_0^2 \rho' = \frac{\partial^n}{\partial x_i \partial x_j} \int \frac{q_{ij}(\eta, \lambda^*)}{|1 - M_r|} \frac{J}{r} d\eta \quad (\text{C.11})$$

where λ^* corresponds to the retard time $\tau^* = t - r/c$. An alternative expression for the source multipoles is now given as:

$$Q_{ij}(\mathbf{y}, \tau) |\operatorname{grad}_{\mathbf{y}} f| \delta(f(\mathbf{y}, \tau)) \quad (\text{C.12})$$

Using this, the equivalent formula to Eqn. C.9 is:

$$4\pi c_0^2 \rho' = \frac{\partial^n}{\partial x_i \partial x_j} \int q_{ij}(\eta, \lambda) |\text{grad}_y f| \delta(f) \delta(g) J \frac{d\eta d\lambda}{rc_0 \alpha} \quad (\text{C.13})$$

where $g = \tau(\eta, \lambda) - t - r/c_0$. Again through the use of generalised functions [80], Eqn. C.13 can be written as:

$$4\pi c_0^2 \rho' = \frac{\partial^n}{\partial x_i \partial x_j} \int \frac{q_{ij}(\eta, \lambda^*)}{r|1 - M_r|} J \frac{|\text{grad}_y f|}{|\text{grad}_\eta f|} dS(\eta) \quad (\text{C.14})$$

This result is now used to obtain a solution to Lighthill's acoustic analogy which is expressed in [155] as:

$$\frac{\partial^2 \rho'}{\partial t^2} - c_0^2 \left(\frac{\partial^2 \rho'}{\partial x_i^2} \right) = \frac{\partial^2 T_{ij}}{\partial x_i \partial x_j} - \frac{\partial}{\partial x_i} \left(p_{ij} \delta(f) \frac{\partial f}{\partial x_j} \right) + \frac{\partial}{\partial t} \left(\rho_0 \vartheta_i \delta(f) \frac{\partial f}{\partial x_i} \right) \quad (\text{C.15})$$

A first form solution to Eqn. C.15 is given in [155], using Eqns. C.11 and C.14 to reduce the integrals. This is shown in Eqn. C.16:

$$4\pi c_0^2 \rho' = \frac{\partial^2}{\partial x_i \partial x_j} \int \left[\frac{T_{ij} J}{r|1 - M_r|} \right] d\eta - \frac{\partial}{\partial x_i} \int \left[\frac{p_{ij} n_j A}{r|1 - M_r|} \right] dS(\eta) \\ + \frac{\partial}{\partial t} \int \left[\frac{\rho_0 \vartheta_n}{r|1 - M_r|} \right] dS(\eta) \quad (\text{C.16})$$

where A is the ratio of the area elements of the surface in the y and η spaces. It can clearly be seen that this version of the equation runs into difficulty when M_r approaches 1. A second derivation available in [155] in which an accurate prediction of the sound sources can be made for supersonic flow rates. This is not be covered in this brief review. The integral representing the volume displaced by the surface is in monopole form. Since the surface is not expanding this is not appropriate in these circumstances and the value of A can be set to 1. Describing the monopole surface as higher order volume sources (See [155] for further details.), Eqn. C.16 can be re-written as:

$$\begin{aligned}
4\pi c_0^2 \rho' = & \frac{\partial^2}{\partial x_i \partial x_j} \int \left[\frac{T_{ij}}{r|1-M_r|} \right] d\eta - \frac{\partial}{\partial x_i} \int \left[\frac{\rho_{ij} n_j}{r|1-M_r|} \right] dS(\eta) \\
& - \frac{\partial}{\partial x_i} \int_{V_0} \left[\frac{\rho_0 \dot{\vartheta}_i}{r|1-M_r|} \right] d\eta + \frac{\partial^2}{\partial x_i \partial x_j} \int_{V_0} \left[\frac{\rho_0 \vartheta_i \vartheta_j}{r|1-M_r|} \right] d\eta
\end{aligned} \tag{C.17}$$

APPENDIX D

Derivation of Aeolian tone acoustic intensity

In this appendix the derivation of Eqn 4.6 is given. Commencing from the Ffowcs Williams-Hawkings Equation derived in Appendix C, this appendix depicts the procedure outlined in [64] and the reader is directed towards this publication for a more detailed derivation.

Simplification of the Ffowcs Williams-Hawkings Equation

The Ffowcs Williams-Hawkings Equation given in Eqn. C.17 is expressed in [64] as:

$$\begin{aligned} \rho' = & \frac{1}{4\pi c_0^2} \frac{\partial^2}{\partial x_i \partial x_j} \int_{v(t_0)} \left[\frac{T_{ij}}{r|1 - (\mathbf{r}/r)M|} \right]_{t=\tau_e} d\eta \\ & - \frac{1}{4\pi c_0^2} \frac{\partial}{\partial x_i} \int_{S(t_0)} \left[\frac{f_i}{r|1 - (\mathbf{r}/r)M|} \right]_{t=\tau_e} dS(\eta) \\ & - \frac{1}{4\pi c_0^2} \frac{\partial}{\partial x_i} \int_{v(t_0)} \left[\frac{\rho_0 a_i}{r|1 - (\mathbf{r}/r)M|} \right]_{t=\tau_e} d\eta \\ & + \frac{1}{4\pi c_0^2} \frac{\partial^2}{\partial x_i \partial x_j} \int_{v(t_0)} \left[\frac{\rho_0 u_i u_j}{r|1 - (\mathbf{r}/r)M|} \right]_{t=\tau_e} d\eta \end{aligned} \quad (D.1)$$

where the values in square brackets are evaluated at η and the retarded time $\tau_e = \tau_e(x, \tau, \eta)$. This is found by solving:

$$g(\tau_e, t, x, \eta) \equiv \tau_e - t + \frac{1}{c_0} |\mathbf{x} - \mathbf{y}(\eta, \tau_e)| = 0 \quad (D.2)$$

The denominator of each integral in Eqn. D.1 is simplified as follows:

$$C^\dagger \equiv 1 - (\mathbf{r}/r)M = 1 - M \cos \theta \quad (D.3)$$

where θ is the elevation angle form the sound source. Applying the chain rule to Eqn. D.2 gives:

$$\left(\frac{\partial g}{\partial x_i} \right) + \left(\frac{\partial g}{\partial \tau_e} \right) \frac{\partial \tau_e}{\partial x_i} = 0 \quad (\text{D.4})$$

Goldstein [64] is able to show that:

$$\frac{\partial \tau_e}{\partial x_i} = - \left[\frac{r_i}{c_0 C^\dagger r} \right]_{t=\tau_e} \quad (\text{D.5})$$

Therefore, applying the chain rule to an arbitrary function f :

$$\frac{\partial f}{\partial x_i} = \left(\frac{\partial f}{\partial x_i} \right)_{\tau_e} - \left(\frac{\partial f}{\partial \tau_e} \right)_x \left[\frac{r_i}{c_0 C^\dagger r} \right]_{t=\tau_e} \quad (\text{D.6})$$

This leads to the specific result:

$$\frac{\partial r}{\partial x_i} = \frac{r_i}{r} - \frac{r_i}{c_0 C^\dagger r} \frac{\partial r}{\partial y_j} \frac{\partial y_j}{\partial \tau_e} = \frac{r_i}{r C^\dagger} \quad \text{at } \tau = \tau_e \quad (\text{D.7})$$

It can be seen that Eqn. D.1 involves first and second order derivatives with respect to x_i . These take the form of $h \equiv [A(\tau)/r|C^\dagger|]$, with dependance on η suppressed for ease of notation. Since A does not explicitly depend on x_i it can be shown from Eqns. D.7 and D.3 that $(\partial h / \partial x_i)_{t_e} = O(r^{-2})$ as $r \rightarrow \infty$. Eqn. D.6 can be shown as:

$$\frac{\partial h}{\partial x_i} = - \left[\frac{r_i}{c_0 r^2 C^\dagger} \frac{\partial}{\partial \tau} \frac{A}{|C^\dagger|} \right]_{t=\tau_e} + O(r^{-2}) \quad (\text{D.8})$$

and

$$\frac{\partial h^2}{\partial x_i \partial x_j} = \left[\frac{r_i r_j}{c_0^2 r^3 C^\dagger} \frac{\partial}{\partial \tau} \frac{1}{C^\dagger} \frac{\partial}{\partial \tau} \frac{A}{|C^\dagger|} \right]_{t=\tau_e} + O(r^{-2}) \quad (\text{D.9})$$

therefore at large values of r (far field region), from [64] Eqn. D.1 can be approximated as:

$$\begin{aligned}
\rho' \sim & \frac{1}{4\pi c_0^4} \int_{v(t_0)} \left[\frac{r_i r_j}{r^3 C^\dagger} \frac{\partial}{\partial \tau} \frac{1}{C^\dagger} \frac{\partial}{\partial \tau} \frac{T_{ij}}{|C^\dagger|} \right]_{t=\tau_e} d\eta \\
& + \frac{1}{4\pi c_0^3} \int_{S(t_0)} \left[\frac{r_i}{r^2 C^\dagger} \frac{\partial}{\partial \tau} \frac{f_i}{|C^\dagger|} \right]_{t=\tau_e} dS(\eta) \\
& + \frac{1}{4\pi c_0^3} \int_{v(t_0)} \left[\frac{r_j}{r^2 C^\dagger} \frac{\partial}{\partial \tau} \frac{\rho_0 a_j}{|C^\dagger|} \right]_{t=\tau_e} d\eta \\
& + \frac{1}{4\pi c_0^4} \int_{v(t_0)} \left[\frac{r_i r_j}{r^3 C^\dagger} \frac{\partial}{\partial \tau} \frac{1}{C^\dagger} \frac{\partial}{\partial \tau} \frac{\rho_0 u_i u_j}{|C^\dagger|} \right]_{t=\tau_e} d\eta
\end{aligned} \tag{D.10}$$

When the surface S is stationary we find:

$$\rho' \sim \frac{x_i x_j}{4\pi c_0^4} \int_v \frac{\partial^2 T_{ij}}{\partial t^2} \left(\mathbf{y}, t - \frac{r}{c_0} \right) dy + \frac{x_i}{4\pi c_0^3 x^2} \int_S \frac{\partial f_i}{\partial t} \left(\mathbf{y}, t - \frac{r}{c_0} \right) dS(y) \tag{D.11}$$

If sources T_{ij} and f_i are constant no sound will be radiated. Accelerative motion of a surface will radiate sound (when sources are constant) but no sound will be radiated for steady state motion of a surface. Goldstein [64] shows that, for a stationary source, equations can be simplified through neglecting the retard times. A similar simplification is shown in [64] for a moving sound source. Supposing δy is a distance across a region, it can be said from mean-value theorem [64] that the relative difference in retard time:

$$\Delta\tau_e \equiv \tau_e(\mathbf{y} + \delta\mathbf{y}) - \tau_e(\mathbf{y}) \simeq \frac{\partial\tau_e}{\partial y_i} \delta y_i \tag{D.12}$$

Again applying the chain rule:

$$\frac{\partial g}{\partial y_i} + \frac{\partial g}{\partial \tau_e} \frac{\partial \tau_e}{\partial y_i} = 0 \tag{D.13}$$

to Eqn. D.2 and eliminating $\partial\tau_e/\partial y_i$ gives:

$$\Delta\tau_e \simeq \frac{1}{c_0(1 - M \cos\theta)} \frac{\mathbf{r}}{r} \cdot \delta\mathbf{y} \tag{D.14}$$

Giving the change in retarded time across the source region as approximately:

$$\Delta\tau_e \simeq \frac{1}{1 - M \cos \theta} \frac{L}{c_0} \quad (\text{D.15})$$

where $L = |\delta y|$ is a characteristic dimension of the source. The time taken for a sound wave to cross the source is given by $\Delta\tau_e$. The characteristic time for source fluctuations T_η and when this is large compared to $\Delta\tau_e$, we can neglect the time variations of the integrals in Eqn. D.10.

$$\frac{L}{c_0(1 - M \cos \theta)} \ll T_\eta \quad (\text{D.16})$$

This gives:

$$\begin{aligned} \rho' \sim & \frac{(r_e)_i(r_e)_j}{4\pi c_0^4 C_0^\dagger r_e^3} \frac{\partial}{\partial \tau_e} \frac{1}{C_0^\dagger} \frac{1}{\partial \tau_e} \left[\frac{Q_{ij}(\tau_e) + v_c \rho_0 u_i(\tau_e) u_j(\tau_e)}{|C_0^\dagger|} \right] \\ & - \frac{(r_e)_i}{4\pi c_0^3 C_0^\dagger r_e^2} \frac{\partial}{\partial \tau_e} \left[\frac{F_i(\tau_e) - v_c \rho_0 a_i^0(\tau_e)}{|C_0^\dagger|} \right] \end{aligned} \quad (\text{D.17})$$

where τ_e is the retard time at the centre of the sound source, u_i and a_i^0 are the velocity and acceleration and r_e is the vector connecting the source and listener at time τ_e . C_0^\dagger is given by:

$$C_0^\dagger \equiv 1 - \frac{u_i(\tau_e)}{c_0} \cdot \frac{\mathbf{r}_e}{r_e} \quad (\text{D.18})$$

The value v_c is the net volume enclosed by the surface S , $Q_{ij} = \int T_{ij} d\eta$ is the integral strength of the external quadrupole sources and $F_i(t) = -\int_s f_i(\eta, t) dS(t)$ is the net force exerted by the fluid on the surface. The first term in Eqn D.17 is associated with a quadrupole source and the second associated with a dipole sound source.

The quadrupole source is smaller than the dipole by a factor of $L/[(1 - M \cos \theta)T_\eta c_0]$ and if neglected gives:

$$\rho' \sim - \frac{(r_e)_i}{4\pi c_0^3 C_0^\dagger r_e^2} \frac{\partial}{\partial \tau_e} \left[\frac{F_i(\tau_e) - v_c \rho_0 a_i^0(\tau_e)}{|C_0^\dagger|} \right] \quad (\text{D.19})$$

Derivation of Acoustic Intensity of Aeolian Tone

We now apply the equations with respect to a rigid cylinder as shown in Fig. 4.2 with length b , diameter d and moving at a constant velocity u in the x_1 direction. Let $F_2(t)$ denote the fluctuating lift force given by:

$$F_2(t) = \int_{-b/2}^{b/2} F_2(t|\eta_3) d\eta_3 \quad (\text{D.20})$$

It was shown in [111] and reproduced in [64] that $F_2(t|\eta_3)$ can be approximated as:

$$F_2(t|\eta_3) = \kappa \frac{\rho_0 u^2}{2} d e^{-i[\Omega t + \Phi(\eta_3)]} \quad (\text{D.21})$$

where κ is a numerical constant which lies between 0.5 and 2. The variation is believed to be due to the sensitivity of force to the amount of turbulence in the flow. d is the cylinder diameter and Φ is the phase on the length of the cylinder and the flow geometry. Since vortex shedding is only in phase over a relatively short length, there is variation in Φ along the length of the cylinder.

The frequency of vortex shedding f_l is given in Section 4.2.3, by Eqn. 4.1, written here as:

$$\Omega = S_t \frac{2\pi u}{d} \quad (\text{D.22})$$

and the characteristic time of the oscillation is given by:

$$T_\eta = \frac{2\pi}{\Omega} \simeq \frac{d}{0.2u} \quad (\text{D.23})$$

Relating Eqn. D.16 to the Aeolian tone shows that any prediction is valid if:

$$\frac{M}{1 - M \cos \theta} \ll \frac{5d}{L} \quad (\text{D.24})$$

where L is a characteristic dimension of the cylinder and the prediction is not valid if b is too large. If this is the case Eqn. D.19 has to be applied to a unit length rather than the cylinder length. The derivations in [64, 111] continue on a unit length basis for Eqn. D.19.

In this derivation the cylinder velocity u is constant, therefore the acceleration $a^0 = 0$. The derivative of C^\dagger with respect to τ_e is neglected as it produces an outcome in higher order terms

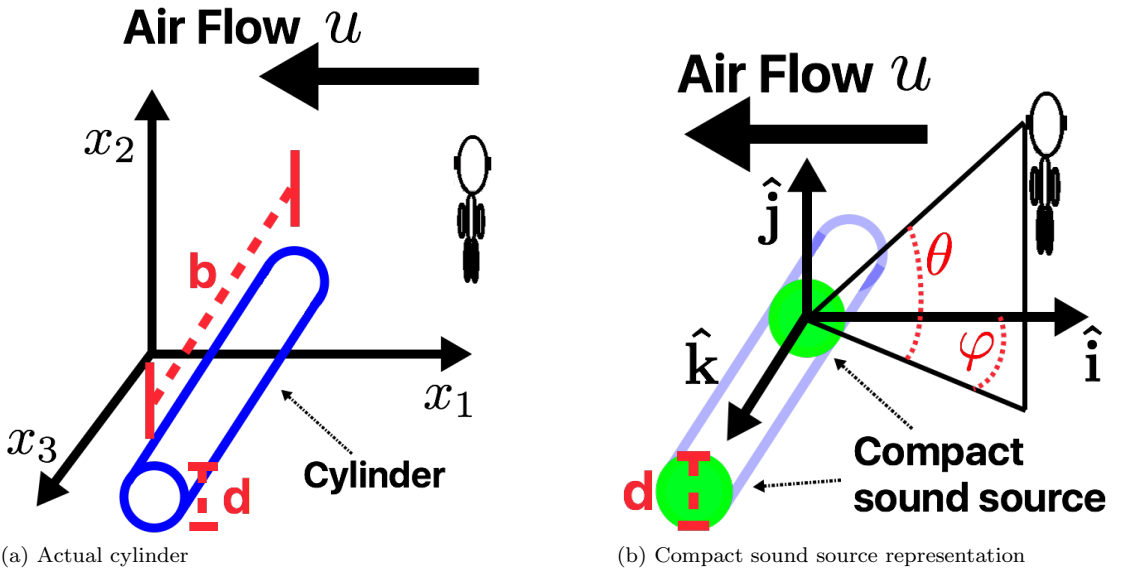


Figure 1: Basic coordinates for Aeolian tone intensity equation derivation - cylinder at emission time τ_e

in r_e^{-1} . Equation D.19 can then be written as:

$$\rho'(\mathbf{x}|\eta_3) \sim \frac{-(r_e)_2}{4\pi c_0^3 r_e^2 [1 - (\mathbf{r}_e/r_e) \cdot \mathbf{M}]^2} \frac{\partial F_2(\tau_e|\eta_3)}{\partial \tau_e} \quad (\text{D.25})$$

where \mathbf{r}_e is given in Eqn. D.26 and $\hat{\mathbf{k}}$ and $\hat{\mathbf{i}}$ are shown in Fig. 1, (Copy of Fig. 4.2, Section 4.2.3):

$$\mathbf{r}_e = \mathbf{x} - \hat{\mathbf{k}}\eta_3 - \hat{\mathbf{i}}c_0 M \tau_e \quad (\text{D.26})$$

$$\tau_e = t - \frac{r_e}{c_0} \quad (\text{D.27})$$

giving the density fluctuations $\rho'(\mathbf{x}|\eta_3)$ at \mathbf{x} due to a unit length of the cylinder. The density fluctuations for the complete cylinder is therefore given by:

$$\rho'(x) = \int_{-b/2}^{b/2} \rho'(\mathbf{x}|\eta_3) d\eta_3 \quad (\text{D.28})$$

The results of Eqn. D.21 can be substituted into Eqn. D.25. Using the results of Eqns. D.26, D.27 and D.22, Eqn. D.25 can be re-written as:

$$\rho'(\mathbf{x}|\eta_3) \sim \frac{i\kappa S_t u^3 x_2}{4\pi c_0^3 r_e^2 [1 - (\mathbf{r}_e/r_e) \cdot \mathbf{M}]^2} e^{i\Omega[t-(r_e/c_0)]} e^{i\Phi(\eta_3)} \quad (\text{D.29})$$

When the distance between source and observer is large, \mathbf{x} is large, therefore:

$$r_e = |x - \hat{\mathbf{k}}\eta_3 - c_0 \hat{\mathbf{i}} M \tau_e| = r_0 - \frac{x_3 \eta_3}{r_0} + O(r_0^{-1}) \quad (\text{D.30})$$

where

$$r_0 = \mathbf{x} - \hat{\mathbf{i}} c_0 M \tau_e \quad (\text{D.31})$$

is the value of r_e at the centre of the cylinder. The result of Eqn. D.30 is substituted for r_e in the exponent of Eqn. D.29 and r_0 is substituted in all other places. This result into Eqn. D.28 gives:

$$\begin{aligned} \rho'(x) \sim & \frac{i\kappa S_t \rho_0 u^3 \sin \theta \cos \varphi}{4c_0^3 r_0 (1 - M \cos \theta)^2} \exp \left(i\Omega[t - r_0/c_0] \right) \\ & \cdot \int_{-b/2}^{b/2} \exp \left(-i \left[\left(\frac{\Omega}{c_0} \right) \eta_3 \sin \theta \sin \varphi + \Phi(\eta_3) \right] \right) d\eta_3 \end{aligned} \quad (\text{D.32})$$

where the relationships below are used in reference to coordinated and dimensions given in Fig. 1:

$$\begin{aligned} \cos \theta &= \frac{\mathbf{r}_0}{r_0} \cdot \hat{\mathbf{i}} \\ \sin \theta \cos \varphi &= \frac{\mathbf{r}_0}{r_0} \cdot \hat{\mathbf{j}} = \frac{x_2}{r_0} \\ \sin \theta \sin \varphi &= \frac{\mathbf{r}_0}{r_0} \cdot \hat{\mathbf{j}} = \frac{x_3}{r_0} \end{aligned} \quad (\text{D.33})$$

The observation point is take to be at a distance that the values of θ and $r_0(t)$ can be considered nearly constant over a period of pressure fluctuation. Setting $r_0(t) = r_0(t_0)$ and $\theta_0 = \theta(t_0)$ at time t_0 during a period, Eqn. D.32 can be written as:

$$\rho'(x) \sim \frac{i\kappa S_t \rho_0 u^3 \sin \theta_0 \cos \varphi}{4c_0^3 r_0 (1 - M \cos \theta_0)^2} \exp \left(-i\Omega \left[\frac{t - t_0}{1 - M \cos \theta_0} - \frac{r_0(t_0)}{c_0} + t_0 \right] \right) \\ \cdot \int_{-b/2}^{b/2} \exp \left(-i \left[\left(\frac{\Omega}{c_0} \right) \eta_3 \sin \theta_0 \sin \varphi + \Phi(\eta_3) \right] \right) d\eta_3 \quad (\text{D.34})$$

which relates to time periods of one period $T_p = (2/\pi)(1 - M \cos \theta)$, Eqn. 4.10 in Section 4.2. We are then able to define the average acoustic intensity:

$$\bar{I} \sim \frac{\kappa^2 S_t^2 \rho_0 u^6 \sin^2 \theta \cos^2 \varphi}{32c_0^3 r_0^2 (1 - M \cos \theta)^4} \\ \cdot \int_{-b/2}^{b/2} \int_{-b/2}^{b/2} \exp \left(i \left[\left(\frac{\Omega}{C_0} \xi \sin \theta \sin \varphi + \Phi(\eta_3 + \xi) - \Phi(\eta_3) \right] \right) d\eta'_3 d\eta'_3 \quad (\text{D.35}) \right)$$

where $\xi = \eta'_3 - \eta_3$ and $\theta \equiv \theta_0$. There are two limiting cases to be considered. The first is when the cylinder length b is small so that the vortex shedding is in phase along the length. It should be noted that the effects of the ends of the cylinder might become important in the acoustic process ($b < 4d$) but is not considered here. If the vortex shedding is in phase then:

$$e^{i[\Phi(\eta_3 - \xi) - \Phi_3(\eta_3)]} \simeq 1 \quad (\text{D.36})$$

Equation D.22 can be re-written to give:

$$\frac{\Omega}{c_0} b \simeq 2\pi(0.2)M \frac{b}{d} \quad (\text{D.37})$$

where $S_t \simeq 0.2$. In low Mach number flow:

$$e^{(i\Omega/c_0)\xi \sin \theta \sin \varphi} \simeq 1 \quad (\text{D.38})$$

over the range of integration. Applying these to Eqn. D.35 gives:

$$\bar{I} \sim \frac{\kappa^2 S_t^2 b^2 \rho_0 u^6 \sin^2 \theta \cos^2 \varphi}{32c_0^3 r_0^2 (1 - M \cos \theta)^4} \quad (\text{D.39})$$

In the second case, the cylinder is considered as long compared to the correlation length l where the vortex shedding is correlated. The variables of integration are changed from η_3 to ξ .

$$\bar{I} \sim \frac{\kappa^2 S_t^2 \rho_0 u^6 \sin^2 \theta \cos^2 \varphi}{32 c_0^3 r_0^2 (1 - M \cos \theta)^4} \cdot \int_{-b/2}^{b/2} e^{i(\Omega/c_0)\xi \sin \theta \sin \varphi} \int_{(-b/2)-\eta_3}^{(b/2)-\eta_3} e^{i[\Phi(\eta_3-\xi)-\Phi(\eta_3)]} d\xi d\eta_3 \quad (\text{D.40})$$

Under this condition the correlation length is small compared to the length of the cylinder and the limits of the inner integral can be taken as $-\infty$ and ∞ . It is feasible to assume that the correlation coefficient:

$$\frac{1}{b} \int_{-b/2}^{b/2} e^{i[\Phi(\eta_3-\xi)-\Phi(\eta_3)]} d\eta_3 \quad (\text{D.41})$$

of the force acting on the cylinder is Gaussian and equal to $e^{-\xi^2/2l^2}$. It is also given that:

$$\begin{aligned} & \int_{-\infty}^{\infty} \left(\exp \left[i \left(\frac{\Omega}{c_0} \right) \xi \sin \theta \sin \varphi - \left(\frac{\xi^2}{2l^2} \right) \right] \right) d\xi \\ &= \sqrt{2\pi} l \exp \left[-\frac{1}{2} \left(\frac{\Omega^2}{c_0^2} \right) l^2 \sin^2 \theta \sin^2 \varphi \right] \end{aligned} \quad (\text{D.42})$$

From this Eqn. D.40 can be written as:

$$\begin{aligned} \bar{I} &\sim \frac{\sqrt{2\pi} \kappa^2 S_t^2 l b \rho_0 u^6 \sin^2 \theta \cos^2 \varphi}{32 c_0^3 r_0^2 (1 - M \cos \theta)^4} \\ &\cdot \left(\exp \left[-\frac{1}{2} \left(\frac{2\pi M S_t l}{d} \right)^2 \sin^2 \theta \sin^2 \varphi \right] \right) \end{aligned} \quad (\text{D.43})$$

In cases of small Mach number the exponential can be neglected, the difference between the short and long cylinders, Eqn. D.39 and D.43, is that b^2 is replaced by $\sqrt{2\pi}lb$ for the long cylinder. Equation D.43 is the same equation used in the implementation of the Aeolian tone, Section 4.2.4, Eqn. 4.16.

Bibliography

- [2] J Adrien. The missing link: Modal synthesis. In *Representations of musical signals*, pages 269–298. MIT Press, 1991.
- [3] KK Ahuja and J Mendoza. Effects of cavity dimensions, boundary layer, and temperature on cavity noise with emphasis on benchmark data to validate computational aeroacoustic codes. 1995.
- [4] A Allen and N Raghuvanshi. Aerophones in flatland: Interactive wave simulation of wind instruments. *ACM Transactions on Graphics*, 34, 2015.
- [5] X Amatriain, J Bonada, A Loscos, and X Serra. Spectral processing. *Digital Audio Effects*, 2002.
- [6] SS An, DL James, and S Marschner. Motion-driven concatenative synthesis of cloth sounds. *ACM Transactions on Graphics*, 31(4):102, 2012.
- [7] R. Auvray, B. Fabre, F. Meneses, P. de la Cuadra, and PY Lagrée. Aeroacoustics of the panpipes. *The Journal of the Acoustical Society of America*, 133(5):3320–3320, 2013.
- [8] R. Auvray, B. Fabre, F. Meneses, P. De La Cuadra, and PY. Lagrée. Specific features of a stopped pipe blown by a turbulent jet: Aeroacoustics of the panpipes. *The Journal of the Acoustical Society of America*, 139(6):3214–3225, 2016.
- [9] EJ Avital, M Alonso, and V Supontisky. Computational aeroacoustics: The low speed jet. *The Aeronautical Journal*, 112(1133):405–414, 2008.
- [10] A Bamberger, E Bänsch, and KG Siebert. Experimental and numerical investigation of edge tones. *Journal of Applied Mathematics and Mechanics*, 84(9):632–646, 2004.
- [11] LA Bazhenova and AG Semenov. Nature of the source of vortex sound flowing around a cylindrical profile. *Acoustical Physics*, 60(6):678–686, 2014.
- [12] PW Bearman. Vortex shedding from oscillating bluff bodies. *Annual review of fluid mechanics*, 16(1):195–222, 1984.

- [13] D Berckmans, K Janssens, H Van der Auweraer, P Sas, and W Desmet. Model-based synthesis of aircraft noise to quantify human perception of sound quality and annoyance. *Journal of Sound and Vibration*, 311(3-5):1175–1195, 2008.
- [14] S Bilbao. *Numerical Sound Synthesis: Finite Difference Schemes and Simulation in Musical Acoustics*. Wiley Online Library, 2009.
- [15] S Bilbao and B Hamilton. Wave-based room acoustics simulation: Explicit/implicit finite volume modeling of viscothermal losses and frequency-dependent boundaries. *Journal of the Audio Engineering Society*, 65(1/2):78–89, 2017.
- [16] S Bilbao and A Torin. Numerical modeling and sound synthesis for articulated string/fretboard interactions. *Journal of the Audio Engineering Society*, 63(5):336–347, 2015.
- [17] S Bilbao and CJ Webb. Physical modeling of timpani drums in 3d on gpgpus. *Journal of the Audio Engineering Society*, 61(10):737–748, 2013.
- [18] PJW Block. Analysis of noise measured from a propeller in a wake. *NASA Technical Report*, 1984.
- [19] N Böttcher and S Serafin. Design and evaluation of physically inspired models of sound effects in computer games. In *Audio Engineering Society: 35th International Conference: Audio for Games*, 2009.
- [20] D Brika and A Laneville. Vortex-induced vibrations of a long flexible circular cylinder. *Journal of Fluid Mechanics*, 250:481–508, 1993.
- [21] D Brown and JB Ollerhead. Propeller noise at low tip speeds. Technical report, DTIC Document, 1971.
- [22] GB Brown. The vortex motion causing edge tones. *Proceedings of the Physical Society*, 49 (5):493, 1937.
- [23] Recommendation ITU-R BS.1534-3. Method for the subjective assessment of intermediate quality level of audio systems. *International Telecommunication Union Radiocommunication Assembly*, 2015.
- [24] C Cadoz, A Luciani, and J-L Florens. Responsive input devices and sound synthesis by stimulation of instrumental mechanisms: The cordis system. *Computer music journal*, 8(3):60–73, 1984.
- [25] M Campbell. Brass instruments as we know them today. *Acta Acustica united with Acustica*, 90(4):600–610, 2004.

- [26] LMBC Campos and FJP Lau. On a generalized multipole expansion with application to propeller design synthesis. *International Journal of Aeroacoustics*, 13(7-8):553–586, 2014.
- [27] N Castagné and C Cadoz. 10 criteria for evaluating physical modelling schemes for music creation. In *6th Digital Audio Effects Conference*, page 7, 2003.
- [28] T Cebeci and P Bradshaw. *Physical and computational aspects of convective heat transfer*. Springer Science & Business Media, 2012.
- [29] A Chaigne and A Askenfelt. Numerical simulations of piano strings. i. a physical model for a struck string using finite difference methods. *The Journal of the Acoustical Society of America*, 95(2):1112–1118, 1994.
- [30] R Chanaud. *Tools for Analysis Sound Sources*. 2010.
- [31] AF Charwat, JN Roos, FC Dewey, and JA Hitz. An investigation of separated flows - part i: The pressure field. *Journal of the Aerospace Sciences*, 28(6):457–470, 1961.
- [32] L Chatellier, J Laumonier, and Y Gervais. Theoretical and experimental investigations of low mach number turbulent cavity flows. *Experiments in fluids*, 36(5):728–740, 2004.
- [33] C Cheong, P Joseph, Y Park, and S Lee. Computation of aeolian tone from a circular cylinder using source models. *Applied Acoustics*, 69(2):110–126, 2008.
- [34] JM Chowning. The synthesis of complex audio spectra by means of frequency modulation. *Journal of the audio engineering society*, 21(7):526–534, 1973.
- [35] JW Coltman. Sounding mechanism of the flute and organ pipe. *The Journal of the Acoustical Society of America*, 44(4):983–992, 1968.
- [36] PR Cook. *Real sound synthesis for interactive applications*. AK Peters Wellesley, 2002.
- [37] DG Crighton. The jet edge-tone feedback cycle; linear theory for the operating stages. *Journal of Fluid Mechanics*, 234:361–391, 1992.
- [38] N Curle. The influence of solid boundaries upon aerodynamic sound. In *Proceedings of the Royal Society of London A: Mathematical, Physical and Engineering Sciences*, volume 231, page 1187, 1955.
- [39] P. de la Cuadra, C. Vergez, and R Caussé. Use of physical-model synthesis for developing experimental techniques in ethnomusicology-the case of the ouldémé flute. In *International Computer Music Conference*, 2002.
- [40] P de La Cuadra, B Fabre, JS Abel, and JO Smith III. A physical model and experimental testbed for real-time simulation of flute-like instruments. *The Journal of the Acoustical Society of America*, 117(4):2414, 2005.

- [41] J DeBlieu. *Wind: How the flow of air has shaped life, myth, and the land*. Counterpoint Press, 2006.
- [42] C Desvages and S Bilbao. Two-polarisation physical model of bowed strings with nonlinear contact and friction forces, and application to gesture-based sound synthesis. *Applied Sciences*, 6(5):135, 2016.
- [43] Y Dobashi, T Yamamoto, and T Nishita. Real-time rendering of aerodynamic sound using sound textures based on computational fluid dynamics. In *ACM Transactions on Graphics*, volume 22, pages 732–740, 2003.
- [44] RE Donham and DJ Osterholt. Utilizing test results to show adding flexibility of propeller blades is more representative than the classical rigid blade propeller whirl flutter analysis. In *Proceedings of International Forum on Aeroelasticity and Structural Dynamics (IFASD)*, pages 18–20, 2007.
- [45] NS Dougherty, BL Liu, and JM Ofarrell. Numerical simulation of the edge tone phenomenon. Technical report, NASA Contractor Report 4581, 1994.
- [46] D Erickson and W Durgin. Tone generation by flow past deep wall cavities. In *25th AIAA Aerospace Sciences Meeting*, page 167, 1987.
- [47] B Etkin, GK Korbacher, and RT Keefe. Acoustic radiation from a stationary cylinder in a fluid stream (aeolian tones). *Journal of the Acoustical Society of America*, 29(1):30–36, 1957.
- [48] A Farnell. An introduction to procedural audio and its application in computer games. In *Audio mostly conference*, volume 23, 2007.
- [49] A Farnell. *Designing sound*. MIT Press Cambridge, 2010.
- [50] U Fey, M König, and H Eckelmann. A new strouhal-reynolds-number relationship for the circular cylinder in the range 47 to 200000. *Physics of Fluids*, 10(7):1547–1549, 1998.
- [51] NH Fletcher. Jetdrive mechanism in organ pipes. *Journal of the Acoustical Society of America*, 60(2):481–483, 1976.
- [52] NH Fletcher and T Rossing. *The physics of musical instruments*. Springer Science and Business Media, 2012.
- [53] A Franck and V Välimäki. Higher-order integrated wavetable and sampling synthesis. *Journal of the Audio Engineering Society*, 61(9):624–636, 2013.
- [54] Y Fu and DT Murphy. Spectral modelling synthesis of vehicle pass-by noise. *InterNoise2017*, 255(1):5997–6006, 2017.

- [55] D Fuglsang and A Cain. Evaluation of shear layer cavity resonance mechanisms by numerical simulation. In *30th Aerospace Sciences Meeting and Exhibit*, page 555, 1992.
- [56] H Fujita. The characteristics of the aeolian tone radiated from two-dimensional cylinders. *Fluid dynamics research*, 42(1):15002, 2010.
- [57] RD Gabbai and H Benaroya. An overview of modeling and experiments of vortex-induced vibration of circular cylinders. *Journal of Sound and Vibration*, 282(3-5):575–616, 2005.
- [58] WW Gaver and DA Norman. *Everyday listening and auditory icons*. PhD thesis, University of California, San Diego, Department of Cognitive Science and Psychology, 1988.
- [59] JH Gerrard. Measurements of the sound from circular cylinders in an air stream. *Proceedings of the Physical Society.*, 68(7):453, 1955.
- [60] JH Gerrard. An experimental investigation of the oscillating lift and drag of a circular cylinder shedding turbulent vortices. *Journal of Fluid Mechanics*, 11(2):244–256, 1961.
- [61] N Giordano. Direct numerical simulation of a recorder. *The Journal of the Acoustical Society of America*, 133(2):1111–1118, 2013.
- [62] N Giordano. Simulation studies of a recorder in three dimensions. *The Journal of the Acoustical Society of America*, 135(2):906–916, 2014.
- [63] N Giordano. Computational study of the piccolo: Evidence for chaotic tones. *The Journal of the Acoustical Society of America*, 140(3):1887–1893, 2016.
- [64] ME Goldstein. Aeroacoustics. *New York, McGraw-Hill International Book Co.,*, 1976.
- [65] RN Govardhan and CHK Williamson. Defining the ‘modified griffin plot’ in vortex-induced vibration: revealing the effect of reynolds number using controlled damping. *Journal of Fluid Mechanics*, 561:147–180, 2006.
- [66] JC Hardin and SL Lamkin. Aeroacoustic computation of cylinder wake flow. *AIAA journal*, 22(1):51–57, 1984.
- [67] HH Heller, DG Holmes, and EE Covert. Flow-induced pressure oscillations in shallow cavities. *Journal of Sound and Vibration*, 18, 1971.
- [68] S Hendry and JD Reiss. Physical modeling and synthesis of motor noise for replication of a sound effects library. In *129th AES Convention, San Francisco*, 2010.
- [69] Lejaren Hiller and Pierre Ruiz. Synthesizing musical sounds by solving the wave equation for vibrating objects: Part 1. *Journal of the Audio Engineering Society*, 19(6):462–470, 1971.

- [70] Lejaren Hiller and Pierre Ruiz. Synthesizing musical sounds by solving the wave equation for vibrating objects: Part 2. *Journal of the Audio Engineering Society*, 19(7):542–551, 1971.
- [71] A Hirschberg and SW Rienstra. An introduction to aeroacoustics. *Eindhoven university of technology*, 2004.
- [72] DK Holger, TA Wilson, and GS Beavers. Fluid mechanics of the edgetone. *The Journal of the Acoustical Society of America*, 62(5):1116–1128, 1977.
- [73] G Holmes, A Donkin, and IH Witten. Weka: A machine learning workbench. In *Intelligent Information Systems, 1994. Proceedings of the 1994 Second Australian and New Zealand Conference on*, pages 357–361. IEEE, 1994.
- [74] MS Howe. Edge, cavity and aperture tones at very low mach numbers. *Journal of Fluid Mechanics*, 330:61–84, 1997.
- [75] MS Howe. Mechanism of sound generation by low mach number flow over a wall cavity. *Journal of sound and vibration*, 273(1-2):103–123, 2004.
- [76] G Iaccarino, A Ooi, PA Durbin, and M Behnia. Reynolds averaged simulation of unsteady separated flow. *International Journal of Heat and Fluid Flow*, 24(2):147–156, 2003.
- [77] MK Ibrahim. Experimental and theoretical investigations of edge tones in high speed jets. *Journal of Fluid Science and Technology*, 8(1):1–19, 2013.
- [78] K Janssens, HD Santos, A Vecchio, and H Van der Auweraer. Real-time synthesis and sound quality evaluation of interior aircraft noise. In *Proc. Forum Acusticum, Budapest, Hungary*, volume 29, 29 Aug - 2 Sept 2005.
- [79] N Jillings, B De Man, D Moffat, and JD Reiss. Web audio evaluation tool: A browser-based listening test environment. *Sound and Music Computing*, 2015.
- [80] DS Jones. *The theory of electromagnetism*. Elsevier, 1964.
- [81] NJ Kasdin. Discrete simulation of colored noise and stochastic processes and $1/f^\alpha$ power law noise generation. *Proceedings of the IEEE*, 83(5):802–827, 1995.
- [82] JL Kelly and CC Lochbaum. Speech synthesis. In *4th International Congress on Acoustics*, page 4, 1962.
- [83] S Kim, M Kim, and WS Yeo. Digital waveguide synthesis of the geomungo with a time-varying loss filter. *Journal of the Audio Engineering Society*, 61(1/2):50–61, 2013.
- [84] G Korvel, V Šimonyte, and V Slivinskas. A modified additive synthesis method using source-filter model. *Journal of the Audio Engineering Society*, 63(6):443–450, 2015.

- [85] V Koschatzky, PD Moore, J Westerweel, F Scarano, and BJ Boersma. High speed piv applied to aerodynamic noise investigation. *Experiments in fluids*, 50(4):863–876, 2011.
- [86] K Krishnamurty. Acoustic radiation from two-dimensional rectangular cutouts in aerodynamic surfaces. 1955.
- [87] TR Langlois, SS An, KK Jin, and DL James. Eigenmode compression for modal sound models. *ACM Transactions on Graphics*, 33(4):40, 2014.
- [88] TR Langlois, C Zheng, and DL James. Toward animating water with complex acoustic bubbles. *ACM Transactions on Graphics*, 35(4):95, 2016.
- [89] MJ Lighthill. On sound generated aerodynamically. i. general theory. *Proceedings of the Royal Society of London. Series A. Mathematical and Physical Sciences*, 211(1107):564–587, 1952.
- [90] MJ Lighthill. On sound generated aerodynamically. ii. turbulence as a source of sound. *Proceedings of the Royal Society of London A: Mathematical, Physical and Engineering Sciences*, 222(1148):1–32, 1954.
- [91] CY Loh and PCE Jorgenson. Computation of tone noises generated in viscous flows. In *Proceedings of the 4th CAA Workshop on Benchmark Problems, NASA/CP-2004-212954*, 2004.
- [92] H Mahmoud and N Akkari. Shortest path calculation: A comparative study for location-based recommender system. In *World Symposium on Computer Applications & Research*, pages 1–5. IEEE, 2016.
- [93] J Malone, M Debiasi, J Little, and M Samimy. Analysis of the spectral relationships of cavity tones in subsonic resonant cavity flows. *Physics of Fluids*, 21(5):055103, 2009.
- [94] D Marelli, M Aramaki, R Kronland-Martinet, and C Verron. Time-frequency synthesis of noisy sounds with narrow spectral components. *IEEE Transactions on Audio, Speech and Language Processing*, 18(8):1929–1940, 2010.
- [95] JE Marte and DW Kurtz. *A review of aerodynamic noise from propellers, rotors, and lift fans*. Jet Propulsion Laboratory, California Institute of Technology, 1970.
- [96] KB McAlpine, M Bett, and J Scanlan. Approaches to creating real-time adaptive music in interactive entertainment: A musical perspective. In *Audio Engineering Society Conference: 35th International Conference: Audio for Games*. Audio Engineering Society, 2009.
- [97] A McPherson. The magnetic resonator piano: Electronic augmentation of an acoustic grand piano. *Journal of New Music Research*, 39(3):189–202, 2010.

- [98] FR Menter. Review of the shear-stress transport turbulence model experience from an industrial perspective. *International journal of computational fluid dynamics*, 23(4):305–316, 2009.
- [99] R Mignot, V Mäntyniemi, and V Välimäki. Granular analysis/synthesis of percussive drilling sounds. In *Proceedings of the 18th Int. Conference on Digital Audio Effects (DAFx-15), Trondheim, Norway, Nov 30-Dec 3, 2015*.
- [100] CL Morfey, CJ Powles, and MCM Wright. Green’s functions in computational aeroacoustics. *International Journal of Aeroacoustics*, 10(2-3):117–159, 2011.
- [101] MJ Morrell and JD Reiss. Inherent doppler properties of spatial audio. In *Audio Engineering Society Convention 129*, 2010.
- [102] JD Morrison and JM Adrien. Mosaic: A framework for modal synthesis. *Computer Music Journal*, 17(1):45–56, 1993.
- [103] E Motuk, R Woods, and S Bilbao. Implementation of finite difference schemes for the wave equation on fpga. In *Acoustics, Speech, and Signal Processing. Proceedings. IEEE International Conference on*, volume 3, page 237, 2005.
- [104] N Murray, E Sällström, and L Ukeiley. Properties of subsonic open cavity flow fields. *Physics of Fluids*, 21(9):095103, 2009.
- [105] RE Musafir. On the sound field of organized vorticity in jet flows. In *13th International Congress on Acoustics*, pages 24–31, 1989.
- [106] CLMH Navier. Mémoire sur les lois du mouvement des fluides. *Mémoires de l’Académie Royale des Sciences de l’Institut de France*, 6(1823):389–440, 1823.
- [107] C Norberg. Effects of reynolds number and a low-intensity freestream turbulence on the flow around a circular cylinder. *Chalmers University, Goteborg, Sweden, Technological Publications*, 87(2):1–55, 1987.
- [108] C Norberg. Flow around a circular cylinder: aspects of fluctuating lift. *Journal of Fluids and Structures*, 15(3-4):459–469, 2001.
- [109] S Oksanen, J Parker, and V Välimäki. Physically informed synthesis of jackhammer tool impact sounds. *Proc. of the 16th Int. Conference on Digital Audio Effects (DAFx-13), Maynooth, Ireland*, 2013.
- [110] F Pfeifle and R Bader. Real-time finite-difference method physical modeling of musical instruments using field-programmable gate array hardware. *Journal of the Audio Engineering Society*, 63(12):1001–1016, 2016.

- [111] OM Phillips. The intensity of aeolian tones. *Journal of Fluid Mechanics*, 1(6):607–624, 1956.
- [112] HE Plumlee, JS Gibson, and LW Lassiter. A theoretical and experimental investigation of the acoustic response of cavities in an aerodynamic flow. Technical report, Lockheed Aircraft Corp, Marietta GA, US., 1962.
- [113] A Powell. Similarity and turbulent jet noise. *The Journal of the Acoustical Society of America*, 31(6):812–813, 1959.
- [114] A Powell. On the edgetone. *The Journal of the Acoustical Society of America*, 33(4):395–409, 1961.
- [115] A Powell et al. An experimental study of low speed edgetones. Technical report, California University Los Angeles, 1964.
- [116] Miller Puckette. *The theory and technique of electronic music*. World Scientific Publishing Company, 2007.
- [117] JD Reiss. A meta-analysis of high resolution audio perceptual evaluation. *Journal of the Audio Engineering Society*, 64(6), 2016.
- [118] Sjoerd W Rienstra and Avraham Hirschberg. An introduction to acoustics. *Eindhoven University of Technology*, 18:19, 2003.
- [119] JC Risset. Examples of the musical use of digital audio effects. *Journal of New Music Research*, 31(2):93–97, 2002.
- [120] D Rockwell and Et Naudascher. Self-sustaining oscillations of flow past cavities. *Journal of Fluids Engineering*, 100(2):152–165, 1978.
- [121] M Roger. Coupled oscillations in the aeroacoustics of a katana blade. *Journal of the Acoustical Society of America*, 123(5):3023, 2008.
- [122] JE Rossiter. Wind tunnel experiments on the flow over rectangular cavities at subsonic and transonic speeds. Technical report, Ministry of Aviation; Royal Aircraft Establishment; RAE Farnborough, 1964.
- [123] C Rowley, D Williams, T Colonius, R Murray, D MacMartin, and D Fabris. Model-based control of cavity oscillations. ii-system identification and analysis. In *40th AIAA Aerospace Sciences Meeting & Exhibit*, page 972, 2002.
- [124] CW Rowley, T Colonius, and AJ Basu. On self-sustained oscillations in two-dimensional compressible flow over rectangular cavities. *Journal of Fluid Mechanics*, 455:315–346, 2002.
- [125] DA Russell, JP Titlow, and Y-J Bemmen. Acoustic monopoles, dipoles, and quadrupoles: An experiment revisited. *American Journal of Physics*, 67, 1999.

- [126] V Sarohia. Experimental investigation of oscillations in flows over shallow cavities. *AIAA Journal*, 15(7):984–991, 1977.
- [127] T Sarpkaya. A critical review of the intrinsic nature of vortex-induced vibrations. *Journal of Fluids and Structures*, 19(4):389–447, 2004.
- [128] H Schlichting. Boundary layer theory. part 2; turbulent flows. 1949.
- [129] H Schlichting et al. *Boundary-layer theory*. Springer, 1960.
- [130] R Selfridge, JD Reiss, EJ Avital, and X Tang. Physically derived synthesis model of an Aeolian tone. In *Audio Engineering Society Convention 141*, 2016.
- [131] R Selfridge, D Moffat, and JD Reiss. Real-time physical model for synthesis of sword swing sounds. In *14th Sound and Music Computing Conference*, 2017.
- [132] R Selfridge, D Moffat, and JD Reiss. Physically derived sound synthesis model of a propeller. In *Proceedings of the 12th International Audio Mostly Conference on Augmented and Participatory Sound and Music Experiences*, page 16, 2017.
- [133] R Selfridge, D Moffat, and JD Reiss. Sound synthesis of objects swinging through air using physical models. *Applied Sciences*, 7(11):1177, 2017.
- [134] R Selfridge, D Moffat, JD Reiss, and EJ Avital. Real-time physical model of an Aeolian harp. *24th International Congress on Sound and Vibration*, 2017.
- [135] R Selfridge, JD Reiss, and EJ Avital. Physically derived synthesis model of a cavity tone. In *Proceedings of the 20th Digital Audio Effects Conference, Edinburgh, UK*, pages 5–9, 2017.
- [136] R Selfridge, JD Reiss, and EJ Avital. Physically derived synthesis model of a edge tone. In *Audio Engineering Society Convention 144*, 2018.
- [137] JO Smith. Introduction to digital filters with audio applications, 2007. URL https://ccrma.stanford.edu/~jos/filters/Elementary_Filter_Sections.html.
- [138] Julius O Smith. Efficient simulation of the reed-bore and bow-string mechanisms. 1986.
- [139] GG Stokes. On the steady motion of incompressible fluids. *Transactions of the Cambridge Philosophical Society*, 7:439, 1848.
- [140] V Suponitsky, EJ Avital, and M Gaster. On three-dimensionality and control of incompressible cavity flow. *Physics of Fluids*, 17(10):104103, 2005.
- [141] V Suponitsky, EJ Avital, and M Gaster. Hydrodynamics and sound generation of low speed planar jet. *Journal of Fluids Engineering*, 130(3):031401, 2008.

- [142] G Takács and B Rohal'-Ilkiv. *Model Predictive Vibration Control: Efficient Constrained MPC Vibration Control for Lightly Damped Mechanical Structures*. Springer Science & Business Media, 2012.
- [143] CKW Tam and JC Hardin. *Second Computational Aeroacoustics (CAA): Workshop on Benchmark Problems*. NASA, 1997.
- [144] FO Thomas and VW Goldschmidt. Structural characteristics of a developing turbulent planar jet. *Journal of Fluid Mechanics*, 163:227–256, 1986.
- [145] T Uda, A Nishikawa, S Someya, and A Iida. Cross-correlation analysis of aeroacoustic sound and flow field using time-resolved piv. In *Proceedings of 15th Int. Symp. on Application of Laser Techniques to Fluid Mechanics*, 2010.
- [146] I Vaik, R Varga, and G Paál. Frequency and phase characteristics of the edge tone, part i. *Periodica Polytechnica. Engineering. Mechanical Engineering*, 58(1):55, 2014.
- [147] I Vaik, R Varga, and G Paál. Frequency and phase characteristics of the edge tone, part ii. *Periodica Polytechnica. Engineering. Mechanical Engineering*, 58(1):69, 2014.
- [148] V Valimaki, M Karjalainen, Z Jánosy, and UK Laine. A real-time dsp implementation of a flute model. In *IEEE International Conference on Acoustics, Speech, and Signal Processing*, volume 2, pages 249–252, 1992.
- [149] V Välimäki, J Huopaniemi, M Karjalainen, and Z Jánosy. Physical modeling of plucked string instruments with application to real-time sound synthesis. *Journal of the Audio Engineering Society*, 44, 1996.
- [150] CW Van Atta and M Gharib. Ordered and chaotic vortex streets behind circular cylinders at low reynolds numbers. *Journal of Fluid Mechanics*, 174:113–133, 1987.
- [151] MP Verge, B Fabre, A Hirschberg, and APJ Wijnands. Sound production in recorderlike instruments. i. dimensionless amplitude of the internal acoustic field. *The Journal of the Acoustical Society of America*, 101(5):2914–2924, 1997.
- [152] MP Verge, B Fabre, A Hirschberg, and APJ Wijnands. Sound production in recorderlike instruments. ii. a simulation model. *The Journal of the Acoustical Society of America*, 101(5):2925–2939, 1997.
- [153] C Verron and G Drettakis. Procedural audio modeling for particle-based environmental effects. In *Audio Engineering Society Convention 133*, 2012.
- [154] W Wilkinson and JD Reiss. A synthesis model for mammalian vocalization sound effects. In *61st International Conference: Audio for Games*. Audio Engineering Society, 2016.

- [155] JE Ffowcs Williams and DL Hawkings. Sound generation by turbulence and surfaces in arbitrary motion. *Philosophical Transactions of the Royal Society of London A: Mathematical, Physical and Engineering Sciences*, 264(1151):321–342, 1969.
- [156] CHK Williamson and R Govardhan. Vortex-induced vibrations. *Annu. Rev. Fluid Mech.*, 36:413–455, 2004.
- [157] R Winfield. Windsongs. Saydisc Records, 1993.
- [158] S Ystad. Sound modeling applied to flute sounds. *Journal of the Audio Engineering Society*, 48(9):810–825, 2000.
- [159] YH Yu. Measurements of sound radiation from cavities at subsonic speeds. *Journal of Aircraft*, 14(9):838–843, 1977.
- [160] V Zappi, A Vasuvedan, A Allen, N Raghuvanshi, and S Fels. Towards real-time two-dimensional wave propagation for articulatory speech synthesis. In *Proceedings of Meetings on Acoustics 171 ASA*, volume 26, page 45005, 2016.
- [161] MM Zdravkovich. Smoke observations of the formation of a karman vortex street. *Journal of Fluid Mechanics*, 37(3):491–496, 1969.
- [162] X Zhang, A Rona, and JA Edwards. An observation of pressure waves around a shallow cavity. *Journal of sound and vibration*, 214(4):771–778, 1998.
- [163] C Zheng and DL James. Toward high-quality modal contact sound. *ACM Transactions on Graphics*, 30(4):38, 2011.